Energy efficiency of CO2 conversion with nanosecond plasma discharges

Jean Maillard

université
PARIS-SACLAY

Energy Efficiency of CO_2 Conversion with Nanosecond Plasma Discharges

Efficacité énergétique de la conversion du CO_2 par décharges plasma nanosecondes

Thèse de doctorat de l'université Paris-Saclay

École doctorale n°579 Sciences Mécaniques et Energétiques, Matériaux et Géosciences (SMEMaG)
Spécialité de doctorat : énergétique
Graduate School : Sciences de l'ingénierie et des systèmes
Référent : CentraleSupélec

Thèse préparée au **Laboratoire EM2C** (Université Paris-Saclay, CentraleSupélec, CNRS), sous la direction de **Christophe LAUX**, Professeur des Universités, et l'encadrement de **Erwan Pannier**, CTO de Spark-Cleantech

Thèse soutenue à Paris-Saclay, le 27 mars 2024, par

Jean MAILLARD

Composition du Jury

Membres du jury avec voix délibérative

Svetlana STARIKOVSKAIA Directrice de recherche, CNRS	Présidente
Paolo TOSI Professor, Trento University	Rapporteur & Examinateur
Paul-Quentin ELIAS Chargé de recherche (HDR), ONERA, Université Paris-Saclay	Rapporteur & Examinateur
Carmen GUERRA-GARCIA Assistant Professor, Massachusetts Institute of Technology	Examinatrice
Olivier GUAITELLA Ingénieur de recherche, Ecole Polytechnique	Examinateur
Richard VAN DE SANDEN Professor, Eindhoven University of Technology	Examinateur

THÈSE DE DOCTORAT

NNT : 2024UPAST043

université PARIS-SACLAY

ÉCOLE DOCTORALE
Sciences mécaniques et énergétiques, matériaux et géosciences (SMEMAG)

Titre : Efficacité énergétique de la conversion du CO_2 par décharges plasmas nanosecondes.

Mots clés : plasmalyse CO_2, décharges Nanosecondes Répétitives Pulsées, spectroscopie d'émission, cinétique chimique, plasmas hors-équilibre, étincelle thermique

Résumé : Afin de contenir la menace du réchauffement climatique sur l'habitabilité de notre planète, les activités humaines doivent se passer d'hydrocarbures fossiles. Pour relever ce défi, on peut utiliser des sources d'énergie bas-carbone pour convertir le CO_2 en CO, puis transformer ce CO en hydrocarbures, dont le bilan carbone d'utilisation est globalement neutre. La dissociation du CO_2 en CO est l'étape critique de ce processus.

Cette thèse étudie les performances énergétiques des technologies plasmas pour convertir CO_2 en CO, et en particulier celles des décharges Nanosecondes Répétitives Pulsées (NRP). Une analyse détaillée des mécanismes cinétiques de dissociation montre que le recyclage de l'oxygène – étape nécessaire pour dépasser 53% d'efficacité énergétique – ne peut pas se produire dans un plasma de CO_2, quelles que soient les conditions de températures électronique, vibrationnelle, et translationnelle, et la composition du gaz. Ce résultat clôt la voie historique de dissociation par plasma froid ($T_g <$ 1000 K), dont le rendement énergétique ne dépasse pas 10% dans les expériences des 10 dernières années. En pratique, les plasmas tièdes ($T_g \sim$ 1000-3000 K) et chauds ($T_g >$ 3000 K) obtiennent les meilleurs performances (30-50% d'efficacité énergétique). Le nouvel enjeu pour les plasmas tièdes est d'obtenir les même efficacités que les plasmas chauds, mais à des températures plus favorables d'un point de vue industriel. Les décharges NRP en régime étincelle sont particulièrement prometteuses en raison de leur capacité à opérer dans des conditions hors-équilibres et à générer des effets hydrodynamiques suceptibles de refroidir rapidement les produits, évitant ainsi la recombinaison du CO en produits indésirables.

La partie expérimentale de cette thèse est dédiée à l'étude détaillée d'une décharge NRP de référence dans le CO_2 à pression atmosphérique. Les effets complexes induits par la décharge NRP sont caractérisés par spectroscopie d'émission à haute résolution spatio-temporelle, par imagerie nanoseconde ainsi que par des mesures électriques.

Sous l'effet des impulsions de tension, une région de faible émission apparaît. Les mesures montrent que son diamètre est de l'ordre de 400 µm et elle présente plusieurs bandes d'émission moléculaire. Elle présente en outre une ionisation modérée – $n_e \sim 10^{16}$-10^{17} cm^{-3} – et est fortement hors-équilibre avec $T_g \approx$ 600-800 K et $T_e \approx$ 20,000 K. Suite à un pulse de tension réfléchi 70 ns après le pulse incident, apparaît un filament d'intense émission, de diamètre de l'ordre de 100 µm. L'analyse des spectres d'émission montre que ce filament est fortement ionisé – $n_e > 10^{18}$ cm^{-3} – et à l'équilibre thermique à $T_g \approx T_e \approx$ 30,000 K. Ces résultats permettent de mieux comprendre plusieurs expériences récentes de la littérature. Sur la base de mesures et de calculs thermodynamiques, il est montré que, dans nos conditions, l'étincelle non-thermique est à l'origine de l'essentiel de la production de CO et que son efficacité énergétique est de l'ordre de 30%.

Afin de comprendre la formation de ces régimes non-thermique et thermique, ainsi que leur efficacité, un modèle thermocinétique 0D des décharges NRP est développé. Ce modèle montre que l'augmentation de température suite au premier pulse explique la formation d'une étincelle thermique au moment de la réflexion.

Enfin, une analyse détaillée de l'efficacité énergétique des régimes d'étincelles non-thermique et thermique est menée. Leurs rendements dépendent fortement des phénomènes de transport induits par l'hydrodynamique de la décharge, qui sont pris en compte à l'aide d'un taux de dilution variable. Une efficacité maximale de 40% est obtenue pour l'étincelle thermique avec un taux de dilution de 10^4-10^5 s^{-1}.

Ainsi, le nouveau régime d'étincelle thermique mis en évidence dans cette thèse pourrait être plus favorable que l'étincelle non-thermique en termes d'efficacité énergétique. Une étude plus approfondie de ce régime est recommandée.

Title: Energy efficiency of CO_2 conversion with nanosecond plasma discharges

Keywords: CO_2 plasmalysis, Nanosecond Repetitively Pulsed discharges, Optical Emission Spectroscopy, chemical kinetics, nonequilibrium plasma, thermal spark

Abstract: To mitigate the threat of global warming to the habitability of our planet, human activities must move away from fossil hydrocarbons. To address this challenge, researchers have proposed to use carbon-free energy sources to convert CO_2 into CO, and to process this CO into hydrocarbons that can be used in a CO_2-neutral energy loop. The dissociation of CO_2 into CO is the critical step in this process. This thesis investigates the energetic performance of plasma technologies to achieve CO production, with the particular focus on Nanosecond Repetitively Pulsed (NRP) discharges.

A detailed analysis of the various kinetic mechanisms of dissociation shows that oxygen recycling – a necessary step to exceed 53% energy efficiency – cannot occur in a CO_2 plasma, whatever the electronic, vibrational, and translational temperature conditions and whatever the gas composition. This result closes the historical path of cold plasma dissociation ($T_g < 1000$ K), whose energy efficiency has not exceeded 10% in experiments over the past 10 years. In practice, warm (T_g~1000-3000 K) and hot ($T_g > 3000$ K) plasmas achieve the best performances (30-50% energy efficiency). The new challenge for warm plasmas is to achieve the same efficiencies as hot plasmas, but at temperatures more suitable to industrial applications. NRP spark discharges are particularly promising thanks to their ability to operate in highly nonequilibrium conditions and to generate strong hydrodynamic effects that can rapidly cool the products, a critical step to avoid the recombination of CO into undesired products.

The experimental part of this thesis focuses on the detailed study of a reference NRP discharge. The intricate effects induced by the NRP discharge are characterized using spatio-temporally resolved optical emission spectroscopy and nanosecond imaging diagnostics, as well as electrical measurements. Many of these measurements are conducted in single shot. Under the effect of the voltage pulses, a low-emission region, with a diameter on the order of 400 µm, appears with several molecular emission bands. This region shows moderate ionization – $n_e \sim 10^{16}$-10^{17} cm^{-3} – and is highly nonequilibrium with $T_g \approx$ 600-800 K and $T_e \approx$ 20,000 K. The reflected voltage, 70 ns after the pulse, produces a filament of intense emission with a diameter of about 100 µm. Analysis of the emission spectra shows that the filament is highly ionized – $n_e > 10^{18}$ cm^{-3} – and in thermal equilibrium at $T_g \approx T_e \approx$ 30,000 K. These findings shed light on several recent experiments in the literature. Based on our measurements and thermodynamic calculations, we estimate that the non-thermal spark is responsible for most of the CO production under our conditions, and that its energy efficiency is on the order of 30%.

To understand the formation of these non-thermal and thermal regimes and their efficiency, we develop a 0D thermokinetic model of NRP discharges. This model shows that, for a given applied electric field, the initial temperature of the plasma determines the degree of thermalization of the spark during the pulse. The formation of the thermal spark after the pulse reflection is explained by the increase in temperature produced by the first pulse.

Finally, a detailed modeling of the energy efficiencies of the non-thermal and thermal spark regimes is conducted. These efficiencies strongly depend on the transport phenomena induced by the hydrodynamics of the discharge, which are taken into account using a variable dilution rate. The model shows that a maximum efficiency of 40% can be obtained with the thermal spark at a dilution rate of 10^4-10^5 s^{-1}.

Thus, the new thermal spark regime evidenced in the present work may be more favorable than the non-thermal regime in terms of energy efficiency, and therefore its further investigation is recommended.

Content

Chapter 1

CO_2 conversion by NRP discharges: towards greener chemistry

1.1 Taking action against global warming

Global warming threatens our planet's habitability

The 2023 assessment report of the Intergovernmental Panel on Climate Change (IPCC 2023) alerts on the disastrous consequences of global warming for human prosperity and life on Earth. These consequences are already here. Beyond striking wildfires, record temperatures, droughts, floods, and tornados, the larger impacts of current warming level are a slowdown of agricultural productivity growth, an overall decrease of the fish catch potential, and a worsening of the freshwater availability experienced by half of the world's population (Calvin et al. 2023).

As the temperature rises, food and freshwater shortages will exacerbate. Additionally, the temperature and humidity conditions will become dangerous for human health. If the temperature rise exceeds 2°C above pre-industrial levels, the temperature-humidity conditions would be mortal for humans for more than 50 days a year in the tropical region (Figure 3.2 of (Calvin et al. 2023)), where 3 billion people currently live.

This dramatic situation results from the emission of greenhouse gases (GHG) such as CO_2, CH_4, or N_2O in human activities. The high absorption coefficient of these gases in the infrared spectrum allows the Earth to keep its warmth by retaining a fraction of its radiative power. An excess of these gases produces a positive radiative forcing, leading the Earth to warm up.

To preserve our planet's habitability, the emissions of GHG induced by human activities must urgently decrease. According to the IPCC (Calvin et al. 2023), to limit warming below 2°C, net-zero emissions of CO_2 must be reached by the end of the century. To achieve this goal, the decarbonization trend must radically accelerate.

Replacing fossil fuels

In 2019, the global use of fossil fuels (for energy production, transportation, and industry) was responsible for approximately 35 $GtCO_2$ (Calvin et al. 2023), which makes up 60% of the total amount of GHG emissions of that year. Replacing these fossil fuels is one of the greatest challenges of our time.

Different solutions are considered. Electrical power can be produced from carbon-neutral sources, such as hydroelectric, solar, wind, geothermal, or nuclear power. Some fossil fuel uses, such as transportation or heat production, can be electrified. However, in some cases, including the chemical industry, hydrocarbons are difficult to replace. Removing CO_2 emissions from these sectors requires the development of carbon-neutral synthetic hydrocarbons.

1.2 CO_2 as a precursor of chemicals

Hydrocarbons could be synthesized in a carbon-neutral manner using biomass (biofuel) and carbon-neutral power (electricity or heat). However, since agriculture currently relies on fossil fuels for both fertilizers and machinery, the actual carbon footprint of such biofuels is far from being neutral, rarely meeting the 65% GHG saving compared to fossil fuels required by the renewable energy directive of the European Union (European Parliament 2018; Jeswani, Chilvers, and Azapagic 2020). Moreover, cultivating biomass raises new issues, including the balance between food and fuel production, deforestation and soil erosion, loss of biodiversity, and freshwater costs.

An alternative is to use CO_2 from an industrial exhaust or the atmosphere as the carbon source. This principle is known as Carbon Capture and Utilization (CCU).

Fuel production from syngas: the Fischer-Tropsch process

The Fischer-Tropsch process is a thermocatalytic process involving several reactions that convert syngas – a mixture of CO and H_2 – to various hydrocarbons, including alkanes, alkenes, and alcohols. Historically, syngas was produced from coal or biomass gasification, but at the cost of huge CO_2 emissions. A low-carbon alternative is to produce syngas from the dry reforming of methane: $CO_2 + CH_4 \rightarrow 2\ CO + 2\ H_2$.

Thus, the thermocatalytic production of hydrocarbons from CO_2 and CH_4, or CO_2 and H_2, has been identified as a possible way to replace fossil fuels with carbon-neutral ones (Appel et al. 2013; Aresta, Dibenedetto, and Angelini 2014; Centi, Quadrelli, and Perathoner 2013). Current research investigates the conversion of CO_2 using porous catalysts, including metal-organic frameworks (Hao et al. 2021; Liang et al. 2021).

Electrolytic reduction of CO_2

Electrolytic reduction of CO_2 is another promising way to convert CO_2 to fuels: CO, formic acid, methanol, ethylene, alkanes, and alcohols could be produced (Weekes et al. 2018). CO production from CO_2 electrolysis is already at the pilot-scale (Masel et al. 2021), and the performance of the process should allow its economic viability (Jouny, Luc, and Jiao 2018).

The principle of CO_2 electrolysis to CO is the following. A few volts are applied between two electrodes. On the cathode side, CO_2 and water vapor flow in. On the anode side, the electrode is immersed in liquid water. An ion-permeable membrane separates the two sides. Under the effect of the voltage, CO molecules and OH^- (or H^+) ions form at the cathode. The OH^- ions cross the membrane and form O_2 and water at the anode. This is illustrated in Figure 1-1.

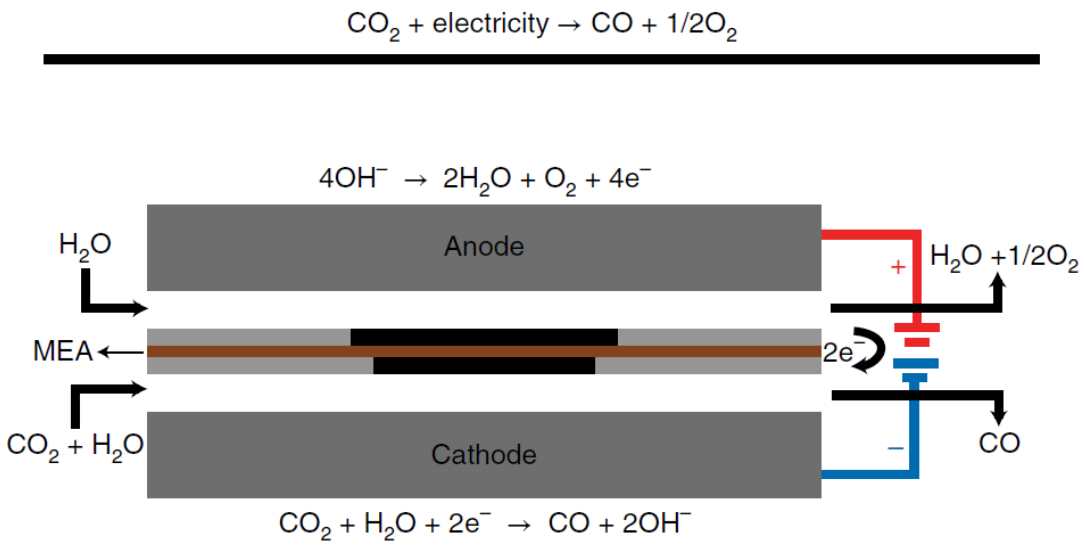

Figure 1-1. Principle of CO_2 electrolysis to CO, using an anion exchange membrane. CO_2 reacts with water and two electrons on the cathode to produce CO and $2OH^-$. The OH^- anions travel through the membrane to the anode and react there to regenerate the water and electrons, and release oxygen. Figure reproduced from (Masel et al. 2021).

The energy efficiency of CO_2 electrolysis, i.e. the ratio of the chemical energy of the CO produced over the total input electrical energy, is seldom given, as electrochemistry papers tend to focus on the Faradaic efficiency, which is the electric charge used for the formation of the desired product over the total charge passed between the electrodes. For the sake of comparison with the plasma processes that will soon be introduced, we recall that the energy efficiency is the product of the Faradaic efficiency and the Voltage efficiency, i.e. the thermodynamic reaction voltage over the actual voltage required for the reaction to occur (Lin et al. 2020). As of 2024, the best laboratory result is a Faradaic efficiency of 95% along with a voltage efficiency of 67% (cell voltage of 2 V compared to the theoretical minimum

of 1.34 V) (Wyndorps, Ostovari, and von der Assen 2021), which yields an energy efficiency of 64%. Compared to most plasma processes, this energy efficiency is high. Another advantage of CO_2 electrolysis to CO is that it does not need a product separation stage, since CO and O_2 are produced separately, which also greatly improve the industrial safety of the process as fuel and oxidizing gases are not mixed.

Nevertheless, CO_2 electrolysis is limited by low current densities. For instance, the 63% energy efficiency results have been achieved at current densities below 0.1 mA/cm^2. To make a viable industrial process, it is generally accepted that current densities above 100 mA/cm^2 are needed (Oloman and Li 2008). Over 100 mA/cm^2, energy efficiencies of 50% (with a Faradaic efficiency of 95% and a cell voltage of 2.5 V) (Ren et al. 2019) and 43% (with a Faradeic efficiency of 80% and a cell voltage of 2.5 V) (Wyndorps et al. 2021) have been achieved.

Currently, the research mainly focuses on the catalyst covering the electrode surfaces: silver, gold, or alloys, organized in different topologies, such as nanoparticles or nanostructured porous films (Masel et al. 2021; Qiao et al. 2014).

Plasmalysis and plasma-catalysis of CO_2

Plasma processes can be used to carry out a wide range of chemical transformations, including pure CO_2 conversion ($CO_2 \rightarrow CO + ½\ O_2$) and Dry Reforming of Methane (DRM, $CH_4 + CO_2 \rightarrow 2CO + 2H_2$). They can operate from ambient temperature to tens of thousands of kelvins, from a few mbars to tens of bars, and provide high densities of reactive species. Moreover, they can reach a high degree of nonequilibrium, i.e., channel the energy into specific modes such as vibrational or electronic excitation. As such, they can achieve high conversion and potentially high energy efficiency for the targeted processes (Fridman 2008).

The high flexibility, versatility, low equipment and operating cost, high conversion, and energy efficiency of plasma processes make them an attractive alternative to thermo- and electro-catalytic processes (Snoeckx and Bogaerts 2017). Powered by low-carbon electricity, they could be a cornerstone of the production of low-carbon fuels.

Many different discharges are being studied: microwave discharges, dielectric barrier discharges, gliding arc discharges, radio frequency discharges, glow discharges, corona discharges, and nanosecond repetitively pulsed discharges. The current trend is to couple the plasma with catalysts (Bogaerts et al. 2020; Chen, Snyders, and Britun 2021).

In this work, we focus on pure CO_2 dissociation in a plasma process. This study is motivated by the potential of this process from an industrial perspective, as well as the fundamental

need to understand CO_2 splitting, which plays a central role in many CO_2 conversion processes.

1.3 CO_2 dissociation by plasma

This section proposes a brief overview of CO_2 dissociation in plasma discharges. A detailed review of the literature is reported in Chapter 2 (Section 2.2).

Energy efficiency

The CO_2 molecule is remarkably stable: its dissociation energy is 5.5 eV. Thus, to minimize the energy and carbon cost of prospective industrial processes, the energy efficiency (EE) of CO_2 dissociation is a major challenge. As the valuable product is CO, the EE is defined as the chemical energy of the CO produced over the total input energy: $\eta = \Delta_r H_0 / E_{CO}$ (see Sec. 2.1.1 for the definition). Record EE up to 80 – 90% were reported in the 80s in microwave (MW) discharges (Azizov et al. 1983; Legasov et al. 1978; Rusanov, Fridman, and Sholin 1981). However, they have never been reproduced since then, the best result being an EE of 58%, obtained by (Montesano et al. 2020) with nanosecond repetitively pulsed (NRP) discharges.

CO_2 can dissociate via different pathways, which are differently solicited depending on the plasma technology. These pathways and their respective energy efficiency will be examined in Chapter 2. There are two approaches for CO_2 conversion by plasmas:

1. In the *thermal* approach, the plasma reaches high temperatures (above 3,000 K), and the energy is evenly distributed between the translation, rotation, vibration, and electronic modes. Several dissociation pathways are activated.
2. In the *non-thermal* approach, the gas temperature is limited (between 300 to 3,000 K), and the energy is channeled into specific modes, such as vibrational or electronic excitation. In this case, the aim is to select the most efficient dissociation pathway.

As will be shown throughout this thesis, the mode-specific temperatures – translational T_g, vibrational T_v, electronic T_e – are the key parameters that determine (i) which dissociation channels are activated, and thus, (ii) the EE. They determine the mechanisms of CO production and depletion.

Thermal plasmas

We report in Figure 1-2 the mole fractions of the main species in atmospheric pressure CO_2 as a function of the gas temperature. As can be seen in this graph, CO is thermodynamically stable between 3,000 and 6,000 K. Producing CO in a process in local thermodynamic

equilibrium (LTE) involves heating the gas, which has an energy cost. Moreover, at these temperatures, a significant amount of O stays atomic. Since O has a much higher formation enthalpy than O_2, it represents a significant additional energy cost.

For obvious practical reasons, CO cannot be stored at 3,000 K and thus must be cooled to ambient temperatures, where its recombination is kinetically frozen. If the cooling is fast enough, no CO molecules are lost via recombination. In this case, the overall EE of the process can reach 50% (Chapter 2). Nevertheless, a slow cooling can lead to significant CO recombination to CO_2, hampering the overall EE.

In practice, thermal plasmas are obtained in different discharges, including MW or arc discharges. In these plasmas, EEs of 30 – 50% have been reported in the last decade (Chapter 2). To achieve the highest EE (50%), the main challenge is controlling the temperature throughout the molecules' journey, from heating to cooling.

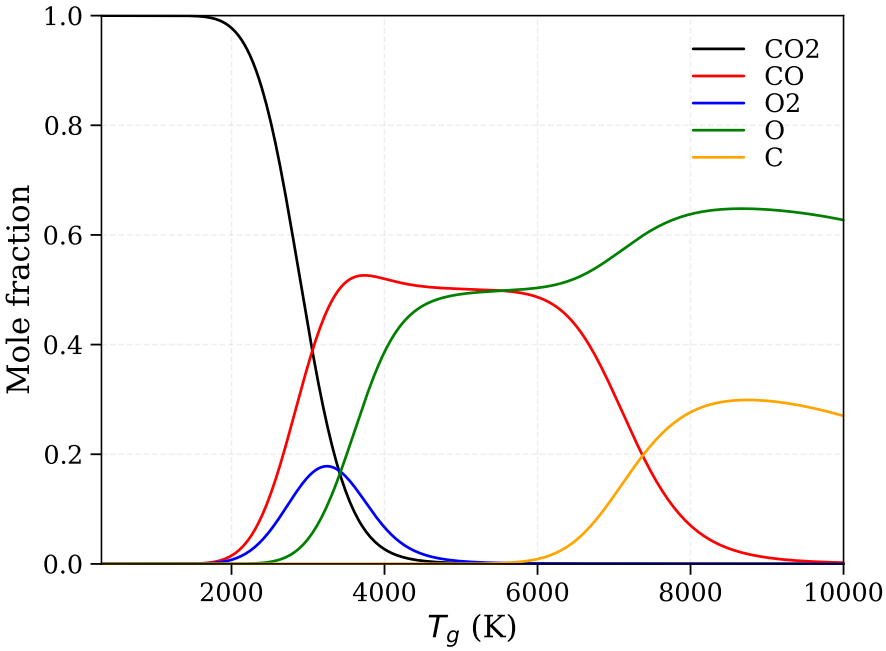

Figure 1-2. Mole fraction of the main species in atmospheric CO_2 at thermodynamic equilibrium. Thermodynamic data from NASA-CEA (McBride, Zehe, and Gordon 2002)

Non-thermal plasmas

In a non-thermal plasma, also called nonequilibrium plasma, the composition converges toward a partial equilibrium, depending on the various temperatures (the translational T_g, vibrational T_v, and electronic T_{el} temperatures of the gas, the translational temperature of the free electrons, T_e). This could potentially allow the conversion of CO_2 into CO and O_2 at a lower energy cost than in the thermal case. Moreover, the dissociation can occur at lower T_g, easing the subsequent cooling phase. From an industrial perspective, lowering T_g is also essential due to the material constraints and the heat losses of a real system.

Non-thermal plasmas can be decomposed into two subcategories: cold and warm plasmas. The 80 – 90% EE allegedly measured in the 80s were obtained in low-pressure MW discharges, at about 100 mbar, with a high degree of nonequilibrium. For instance, (Legasov et al. 1978) reported $T_g \approx$ 600-900 K, while $T_e \approx$ 10,000-20,000 K. (Azizov et al. 1983) reported $T_g \sim$ 100 K and $T_v \sim$ 3,000 K. Nowadays, such nonequilibrium conditions at low T_g are obtained in glow and dielectric barrier discharges, with limited EE results of 5 – 10% as will be reviewed in (Chapter 2).

In warm plasmas, the gas temperature is typically between 1,000 and 3,000 K. At these temperatures, the vibrational and translational modes equilibrate quickly (for instance, at the µs timescale at atmospheric pressure, see Chapter 2). Vibrational-Translational (VT) nonequilibrium may appear, but in practice, it is challenging to maintain (and expensive in energy) (Chapter 2). In these discharges, the electron temperature reaches a few eVs. Typical examples are obtained in NRP, MW and gliding arc (GA) discharges. The 58% EE measured by (Montesano et al. 2020) is obtained using NRP discharges in the spark regime, where T_g, T_v, and T_e are in nonequilibrium during the 20 ns of the pulse, but likely equilibrate in the following microseconds (Chapter 2).

Nanosecond Repetitively Pulsed (NRP) discharges

Among all plasma technologies, NRP discharges stand out for the wide variety of conditions achievable. Due to the high energy deposition at the nanosecond timescale (i.e., faster than the typical electronic and vibrational relaxation times), they can foster high nonequilibrium degrees. As such, they could reach a high EE at reasonable temperatures.

Moreover, NRP discharges generate shock waves, strong gradients of temperature and densities, and recirculation patterns, which overall enable fast cooling of the products (Dumitrache et al. 2019; Tholin 2012; Xu et al. 2014). These effects have been demonstrated to be beneficial to plasma-assisted combustion (Castela et al. 2017; Stepanyan et al. 2017), and could be critical to CO_2 conversion.

Generally, NRP discharges offer a fine control of the temperatures (T_g, T_v, T_e) during the CO production and cooling phases. Last but not least, they can operate at high pressure – they have been tested up to 12 bar in CO_2 (Yong et al. 2023) – which is a critical advantage from an industrial perspective.

1.4 Scope of this work

NRP discharges have been studied in the EM2C laboratory for two decades. Their unique properties – notably, the control of the gas and electron temperatures – show promise for CO_2 conversion, which motivates this work. From an industrial perspective, EE is vital, as

is the conversion degree to CO (van Rooij et al. 2018). Nevertheless, this thesis focuses on the EE only, which we also consider interesting from a fundamental point of view. The general question we will try to answer is: how efficient can NRP discharges be in producing CO from pure CO_2?

This question will be addressed in three parts:

- In Chapter 2, we first provide a detailed review of the literature. Then, we analyze the CO production pathways in a CO_2 plasma and assess their EE. We estimate the maximal EE achievable and identify optimal routes. Finally, we expose the contradictions between the current explanations of the CO production mechanism in NRP-spark discharges.
- In Chapter 3, we first perform a parametric study of the EE in NRP-sparks. Then, using optical emission spectroscopy and ns-imaging, we study the physical conditions in a canonical NRP-spark discharge.
- In Chapter 4, we extend the 0D kinetic model of (Pannier 2019) to simulate non-thermal and thermal spark conditions in CO_2. We assess the kinetic pathways of CO production in each regime and the optimization levers of the EE.
- In Chapter 5, we will summarize the main findings of this thesis, and provide recommendations for future work.

Take-away messages of Chapter 1

- The global warming induced by human activities threatens our planet's habitability.
- CO_2 dissociation to CO by plasma could be an essential step toward the production of synthetic, low-carbon fuels.
- Energy efficiencies of up to 90% for plasma production of CO were reported in the 1980s, but have never been reproduced since.
- Controlling the mode-specific temperatures during CO production and cooling is critical to the energy efficiency of the process.
- NRP discharges allow mode-specific temperature control at atmospheric and industrial pressure, and therefore could offer favorable conditions for CO_2 dissociation.

Chapter 2

Review and analysis of CO_2 plasmalysis

As mentioned in Chapter 1, in order to produce CO at the lowest carbon footprint and financial cost, CO_2 plasmalysis must be energy efficient. That is, it must produce CO at the lowest energy cost possible. To understand how to optimize the energy efficiency, one has to apprehend which reactions are the most efficient, and how they can be promoted. In Section 2.1, we recall the definition of the energy efficiency of CO_2 dissociation to CO in plasma processes, and we list the CO production and loss reactions. In Section 2.2, we review the experimental and numerical works of the literature on CO_2 plasmalysis and the current understanding of the kinetics. In Section 2.3, we discuss the energy efficiency of the main pathways and the energy efficiency achievable in a catalyst-free plasma discharge. Finally, in Section 2.4, we discuss the results of the literature in light of the analysis in Section 2.3.

2.1 Basics

2.1.1 Definitions

Throughout this thesis, the following notations are used to compare the results consistently:

The standard enthalpy (at 298.15 K and 1 bar) of the CO_2 dissociation reaction is written $\Delta_r H°$:

$$CO_2 \rightarrow CO + \tfrac{1}{2}O_2, \qquad \Delta_r H° = 2.93\ eV \qquad \text{Reac. 0}$$

The energy efficiency (EE) for CO_2 dissociation, η, is defined as:

$$\eta = \frac{\Delta_r H°}{E_{CO}} \qquad \text{Eq. 2-1}$$

where E_{CO} is the average energy needed to produce one molecule of CO. The use of the enthalpy at 298.15 K in the expression of the EE is relevant for a process that starts with CO_2 at ambient temperature and whose desired product is CO at ambient temperature. This is the case in most applications.

The conversion degree Φ is defined as the ratio of the number of CO molecules produced over N_0, the initial number of CO_2 molecules in the reactor (or in the inlet flow in the case of a flowing system):

$$\Phi = \frac{N_{CO}}{N_0} \qquad \text{Eq. 2-2}$$

The energy efficiency can be expressed as a function of the conversion degree. For this purpose, it is helpful to introduce the specific energy input (SEI), i.e., the mean energy used per initial CO_2 molecule:

$$SEI = \frac{E_{tot}}{N_0} \qquad \text{Eq. 2-3}$$

where E_{tot} is the total energy deposited. The SEI is a key parameter to compare different plasma dissociation techniques. By combining Eq. 2-2 and Eq. 2-3, Eq. 2-1 can be rewritten in terms of the SEI, the conversion degree, and the dissociation enthalpy:

$$\eta = \frac{\Delta_r H_0 \cdot \phi}{SEI} \qquad \text{Eq. 2-4}$$

2.1.2 CO production and depletion reactions in CO_2 plasmas

In this section, we list the main CO production and loss reactions in a CO_2 plasma. They are summarized in Table 2-1 and Table 2-2. Starting from the CO_2 molecule, 3 elementary processes are possible: either an O atom is ripped out (producing CO and O), either a C atom (producing C and O_2), or an electron (producing CO_2^+ and e^-).

The easiest of the three is the CO-O splitting, whose standard enthalpy of reaction is 5.5 eV. It can be achieved via electron-impact excitation of the vibrational or electronic states of CO_2, or by heavy-particle impact dissociation. The O and CO products can be involved in subsequent reactions, particularly O-CO_2 association which produces an additional CO, and CO-O 3-body recombination which reforms CO_2 back.

The C-O_2 splitting is scarcer and has a reaction enthalpy of 11.5 eV. CO_2 ionisation to CO_2^+ is fast at high reduced electric field and has a reaction enthalpy of 13.8 eV. The latter two processes do not produce CO, but their products may in subsequent reactions, for example, via the Boudouard reaction or CO_2^+ dissociative recombination.

When relevant, we calculate a minimum energy cost of CO production based on the standard enthalpy of reactions. These costs assume that all the energy goes into a particular pathway. They also assume that the products of this pathway are frozen – CO and O, for example, cannot recombine – and that the heat is lost.

Pure vibrational dissociation

CO_2 can be dissociated to CO and O by exciting its vibrational levels up to the top of the dissociation barrier at 5.5 eV. There are two main ways to climb the vibrational ladder. The first one is electron-impact excitation. The electron transfers part of its energy to CO_2 vibration:

$$CO_2(X, v) + e^- \rightarrow CO_2(X, v + n) + e^- \qquad \text{Reac. 1}$$

where v is the quantum number of a given vibrational level, and $n = 1$ for a single-quantum jump or $n \geq 2$ for a multi-quanta jump.

As can be seen in Figure 2-8, the CO_2 ground state in its linear configuration crosses the near-repulsive 1^3B_2 state at 6 eV. With ~115° bond angle, this crossing occurs at 5.5 eV (see the ground state potential energy surface in the supporting information of (Johan A. Schmidt, Johnson, and Schinke 2013)). The transition from CO_2(X) to $CO_2(1^3B_2)$, normally prohibited by their spin difference (Wigner rule), is made possible by spin-orbit coupling (Ibraguimova, Minaev, and Irgibaeva 2014). Thus, when the vibrational energy reaches 5.5 eV, the molecule can go from CO_2(X, v ≥ 21) to $CO_2(1^3B_2)$. Then, it dissociates into ground state CO and ground state O:

$$CO_2(X, v \geq 21) \rightarrow CO_2(^3B_2) \rightarrow CO(X) + O(^3P) \qquad \text{Reac. 2}$$

If the plasma energy is only spent in these reactions, the energy cost of the dissociation through the pure vibrational mechanism is 5.5 eV, i.e. the height of the dissociation asymptote of the triplet state $CO_2(1^3B_2)$.

Electronic dissociation

We will see in section 2.3.1 that after an electron-impact excitation – ie, a vertical excitation in the Franck-Condon region –, the electronic states of CO_2 dissociate directly, or indirectly via a crossing with another state. The correlations between electronic states, excitation energy, and most likely dissociation products are summarized in Table 2-3. To illustrate the electronic dissociation process, we present here the reaction sequence for CO_2's lowest electronic state, the 1^3B_2 triplet i.e. the lowest $^3B_2$ CO_2 state in C_{2v} symmetry. It is first excited by electron impact:

$$CO_2(X) + e^- + 8.3\ eV \rightarrow CO_2(1^3B_2) + e^- \qquad \text{Reac. 3}$$

where the 8.3 eV is the vertical excitation energy of $CO_2(1^3B_2)$ from the ground state (Johan A Schmidt, Johnson, and Schinke 2013). From the Franck-Condon region, this state immediately dissociates:

$$CO_2(1^3B_2) \rightarrow CO(X) + O(^3P) + 2.8\ eV \qquad \text{Reac. 4}$$

Thus, if the plasma energy is only spent in the vertical excitation of $CO_2(1^3B_2)$, the energy cost of dissociation is 8.3 eV.

Dissociation & recombination by collisions with heavy particles

When the gas temperature exceeds 3,000 K, CO_2 dissociation can occur via collisions with heavy species (for convenience in energy bookkeeping, we indicated here and in the following reactions the standard enthalpy of reaction at 1 bar and 298.15 K):

$$CO_2 + M + 5.5\ eV \rightarrow CO + O + M \qquad \text{Reac. 5}$$

However, at temperatures below 3500 K, the inverse process dominates:

$$CO + O + M \rightarrow CO_2 + M + 5.5\ eV \qquad \text{Reac. 6}$$

Taking data from (Kozák et al. 2014; Park et al. 1994), we plot in Figure 2-1 the rate constants of dissociation and 3-body recombination with heavy particles times the total density at P_{atm}. The threshold temperature above which dissociation prevails is about 3500 K.

The activation energy of this reaction is considered to be between 4 and 6 eV (Manion et al. 2008): it is 4.3 eV in (Kozák et al. 2014), 5.5 eV in (Park et al. 1994), and 5.7 eV in (Ibragimova et al. 2000). As we can see, it is approximately equal to the reaction enthalpy. Thus, if the plasma energy were only spent in this reaction, the energy cost would be around 5.5 eV, as for pure vibrational dissociation.

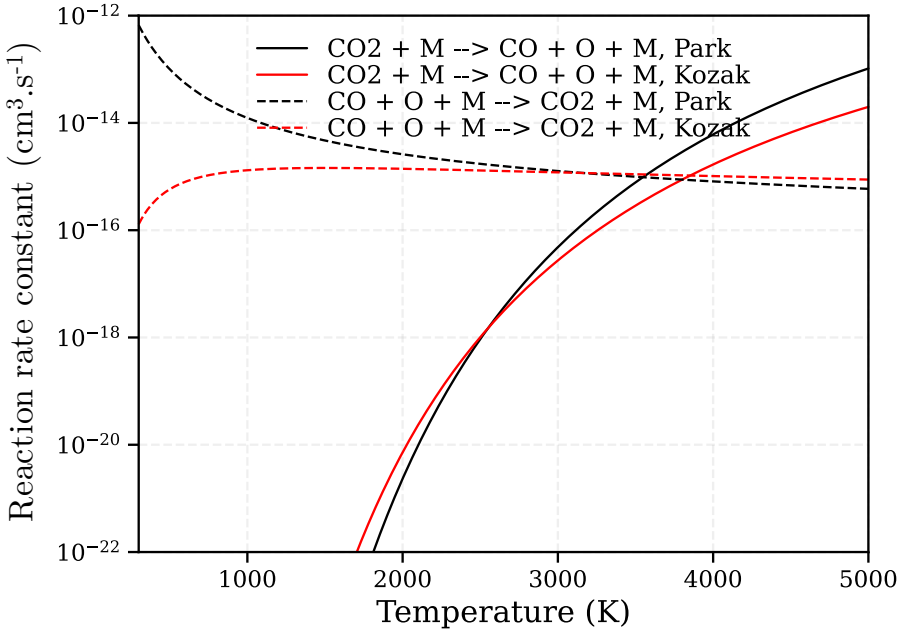

Figure 2-1. Heavy-particle impact dissociation vs three-body recombination rate constants. Data from Park 1994 and Kozak 2014. The 3-body recombination rate constant is multiplied by the gas density at P_{atm}.

O-CO_2 association

Most of the CO_2 dissociation reactions (such as vibrational, electronic, and heavy-particle impact dissociation) produce atomic oxygen. These O atoms can produce an additional CO molecule by association with CO_2. The reaction is:

$$CO_2 + O + 0.35\ eV \rightarrow CO + O_2 \qquad \text{Reac. 7}$$

Figure 2-2 shows the values of the forward and backward rate constants of Reac. 7 from 1000 K to 5000 K given by (Kozák et al. 2014; Park et al. 1994). O-CO_2 association dominates above 1200 K, whereas the reverse process dominates below 1000 K.

The minimum energy cost for producing an O atom from CO_2 is 5.515 eV, the standard enthalpy of Reac. 5. The standard enthalpy of O-CO_2 association is 0.350 eV. Thus, the minimum energy cost for the two reactions is 5.865 eV, which makes 2.93 eV / CO molecule produced. This number equals the standard enthalpy of the global reaction $CO_2 \rightarrow CO + ½\ O_2$ (Reac. 0), which is the minimum energy required to dissociate CO_2.

Actually, since O-CO_2 association has an activation barrier above its reaction enthalpy, the minimum energy cost is likely higher than the latter calculation. The activation barrier is between 0.5 and 1.2 eV according to (Fridman 2008), or 2.3–2.4 eV in the Arrhenius form of the rate constant used by (Kozák et al. 2014; Park et al. 1994). The minimum energy cost to produce CO from pure CO_2 using this reaction would be between 3 and 4 eV / CO molecule.

Later in this Chapter, we will study "O recycling", that we define as the utilization of the chemical energy of the remaining O atoms in an overproduction of CO compared to the equilibrium via the O-CO_2 association reaction. Since O-CO_2 association has a low reaction enthalpy, this overproduction reduces the overall energy cost of CO production, i.e., increases energy efficiency.

Let us emphasize that the denomination "O recycling" has been used in the literature to describe the O-CO_2 association reaction, which in our opinion is an inappropriate use, since *a priori* the O-CO_2 association can occur in a mixture without increasing the energy efficiency[1].

[1] For example, consider the basic case of chemical equilibrium: O-CO_2 association occurs, but is also compensated by its reverse reaction. The O-energy is not reused and the energy efficiency is not increased. Only an overproduction of CO compared to the equilibrium via O-CO_2 association is favorable.

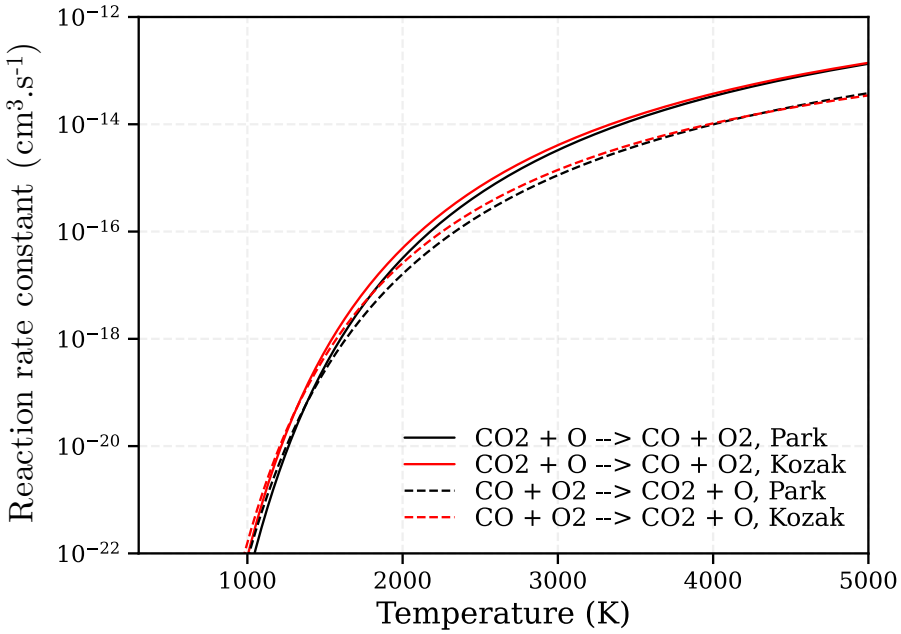

Figure 2-2. O-CO_2 association, forward and backward reaction rate constants. Data from Park 1994 and Kozak 2014.

CO dissociation & recombination

At high electric fields, the CO produced in former reactions can be dissociated by electron impact:

$$CO + e^- + 11.2\ eV \rightarrow C + O + e^- \qquad \text{Reac. 8}$$

CO can also be produced or dissociated by thermal processes.

$$C + O + M \rightarrow CO + M + 11.2\ eV \qquad \text{Reac. 9}$$

$$CO + M + 11.2\ eV \rightarrow C + O + M \qquad \text{Reac. 10}$$

Figure 2-3 shows the rate constants for Reac. 9 and Reac. 10 as given by Park and Kozak. If the gas temperature is less than about 8000 K, C and O recombine into CO. If the gas temperature is above 8000 K, CO dissociation predominates.

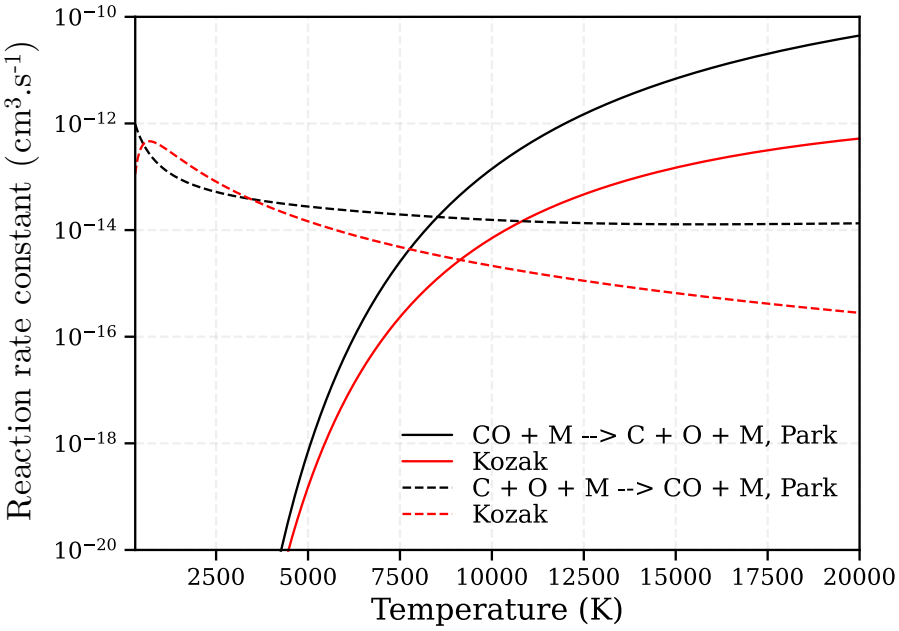

Figure 2-3. CO dissociation by heavy-particle impact: forward and backward rate constants. Data from Park 1994 and Kozak 2014.

Boudouard reaction

The carbon atoms produced in CO dissociation or decomposition of CO_2 to C and O_2 can then form CO in the gaseous version of the Boudouard reaction:

$$CO_2 + C \rightarrow 2\,CO + 5.6\ eV \qquad \text{Reac. 11}$$

Since producing C atoms from CO_2 costs at least 11.5 eV, i.e. the reaction enthalpy of $CO_2 \rightarrow C + O_2$, it costs at least 11.5 eV to produce 2 CO molecules from CO_2 through the Boudouard reaction, which makes 5.75 eV / CO molecule.

CO_2^+ dissociative recombination

CO_2^+ is the main ion in non-thermal CO_2 plasmas. It is produced by electron-impact ionization:

$$CO_2 + e^- + 13.8\ eV \rightarrow CO_2^+ + 2e^- \qquad \text{Reac. 12}$$

The main depletion process of CO_2^+ is via dissociative recombination into CO and O:

$$CO_2^+ + e^- \rightarrow CO + O + 8.3\ eV \qquad \text{Reac. 13}$$

Starting from CO_2, the reactants (electrons and CO_2^+) are produced at a significant energy cost: at least 13.8 eV (through Reac. 12). Thus, this CO production pathway is not expected to be favorable energetically.

Dissociative charge transfer

O atoms can also be ionized by electron impact:

$$O + e^- + 13.6\ eV \rightarrow O^+ + 2e^- \qquad \text{Reac. 14}$$

O^+ is consumed by the ionic equivalent of O-CO_2 association (Reac. 7):

$$CO_2 + O^+ \rightarrow O_2^+ + CO + 1.2\ eV \qquad \text{Reac. 15}$$

Considering the energy cost to produce O^+, this pathway is not energetically favorable either.

Table 2-1. Summary of the main CO production pathways in a CO_2 plasma.

Vibrational dissociation	$CO_2(X, v) + e^- \rightarrow CO_2(X, v + x) + e^-$	Reac. 1
	$CO_2(X, v \geq 21) \rightarrow CO_2(^3B_2) \rightarrow CO(X) + O(^3P)$	Reac. 2
Electronic dissociation	$CO_2 + e^- + 8.3\ eV \rightarrow CO_2(1^3B_2) + e^-$	Reac. 3
	$CO_2(1^3B_2) \rightarrow CO(X) + O(^3P) + 2.8\ eV$	Reac. 4
Heavy-particle impact dissociation	$CO_2 + M + 5.5\ eV \rightarrow CO + O + M$	Reac. 5
O-CO_2 association	$CO_2 + O + 0.35\ eV \rightarrow CO + O_2$	Reac. 7
Atomic 3-body recombination	$C + O + M \rightarrow CO + M + 11.2\ eV$	Reac. 9
Boudouard reaction	$C + CO_2 \rightarrow 2\ CO + 5.6\ eV$	Reac. 11
CO_2^+ dissociative recombination	$CO_2 + e^- + 13.8\ eV \rightarrow CO_2^+ + 2e^-$	Reac. 12
	$CO_2^+ + e^- \rightarrow CO + O + 8.3\ eV$	Reac. 13
Associative charge transfer	$O + e^- + 13.6\ eV \rightarrow O^+ + 2e^-$	Reac. 14
	$CO_2 + O^+ \rightarrow O_2^+ + CO + 1.2\ eV$	Reac. 15

Table 2-2. Summary of the main CO loss mechanisms.

3-body recombination	$CO + O + M \rightarrow CO_2 + M$	Reac. 6
CO electronic dissociation	$CO + e^- + 11.2\ eV \rightarrow C + O + e^-$	Reac. 8
CO heavy-particle impact dissociation	$CO + M \rightarrow C + O + M$	Reac. 10

2.2 Review of CO_2 plasmalysis experiments and current understanding

2.2.1 From the CO_2 laser to the CO_2 plasmalysis craze

The interest of the scientific community in CO_2 plasmas first arose with the development of the CO_2 laser. Harnessing the asymmetric stretch mode of CO_2 vibration and its resonance with N_2 vibration allowed the building of powerful lasers, still widely used in industry. Russian scientists then applied this high degree of vibrational excitation to foster endothermic reactions, such as CO_2 dissociation (Rusanov, Fridman, and Sholin 1981). They reported 80% energy efficiency (EE) in a microwave (MW) discharge at low pressure (Legasov et al. 1978), using the plasma "magic wand" (Fridman 2008) and its vibrational nonequilibrium spell. Azizov *et al.* (Azizov et al. 1983) even reported up to 90% EE in supersonic flow conditions. They explained these outstanding efficiencies through the nonequilibrium excitation of the asymmetric vibrational mode of CO_2, leading to the pure vibrational dissociation mechanism described in Sections 2.1.2 and 2.3.2.

While human activities have been dragging the world into the climate and biodiversity crisis, several studies underlined the potential of plasma technologies to replace fossil fuels with carbon-neutral ones (Ashford and Tu 2017; Lebouvier et al. 2013; Snoeckx and Bogaerts 2017). Thus, driven by a sense of optimism, several groups (Spencer and Gallimore 2013, Belov et al. 2018; Bongers et al. 2017; den Harder et al. 2016; Isa et al. 2020; van Rooij, van den Bekerom, et al. 2015; Silva et al. 2014; Sun et al. 2017) tried replicating the 80s' results, using MW discharges. However, none of them obtained energy efficiencies above 50%.

2.2.2 Down to Earth: vibrational excitation and performances in the current MW discharges

Furthermore, these groups found that vibrational–translational (VT) nonequilibrium does not really enhance CO_2 conversion by MW discharges in the 10 – 1000 mbar range. They attributed it to the following reasons: (i) the mean electron energy in the plasma core is typically about 2-3 eV, favoring electronic excitation over vibrational excitation (Van Rooij et al. 2015; van de Steeg et al. 2020); (ii) the high gas temperature reached in the core – roughly between 2000 and 14,000 K depending on the pressure and input power – induces fast VT relaxation, impeding VT nonequilibrium (Spencer and Gallimore 2013, Bongers et al. 2017; den Harder et al. 2016; van Rooij, van den Bekerom, et al. 2015; van de Steeg et al. 2020; Sun et al. 2017). (iii) The O atoms produced in the dissociation processes are very efficient quenchers, further increasing the VT transfer (Morillo-Candas et al. 2021). Thus,

even if the vibrational distribution function (VDF) is not necessarily Boltzmann in those conditions (Pietanza, Colonna, and Capitelli 2020), the models show that the CO production is dominated by thermal processes, mainly Reac. 5 and Reac. 7 (Van Den Bekerom et al. 2019; Berthelot and Bogaerts 2017; Van De Steeg et al. 2021; Sun et al. 2017; Wolf, Peeters, et al. 2020). In addition, single-temperature kinetic models – where the vibrational and electronic nonequilibrium is not considered – can reasonably account for the measured CO_2 conversion and energy efficiency (Van Den Bekerom et al. 2019; Wolf, Peeters, et al. 2020).

Pulsing the MW power has been attempted to contain the gas temperature increase and favor VT nonequilibrium. Van den Bekerom *et al.* used pulse durations of about 100 µs and duty cycles from 20% to 100% and showed that thermal chemistry is still dominant. Using shorter pulses of a few µs, (Soldatov et al. 2022) achieved significant VT nonequilibrium with $T_g \sim 3000 - 4000$ K, and $T_{v3} \sim 7000 - 8000$ K (where T_{v3} is the temperature of the asymmetric stretch mode of CO_2). However, the benefits remained limited, with an EE below 30%. Overall, these works question the practical feasibility of the pure vibrational pathway and its enhancement by oxygen recycling.

As will be explained in Sec. 2.3 vibrational nonequilibrium, even if attained, is not enough to outperform the EE of thermal processes, which has a maximum near 50%. The energy deposited in a CO_2 plasma is spent not only in CO production, but also in heat and O production. Going beyond an EE of 53% (that corresponds to an energy cost of 5.5 eV per CO molecule) requires recycling oxygen atoms. That is, the chemical energy in the O atoms produced must be reused to dissociate another CO_2 molecule (Reac. 7). Moreover, the CO produced must be cooled fast enough to prevent it from recombining into CO_2.

Thus, optimizing the quenching and transport of excited species is an effective way to increase the energy efficiency. The Eindhoven group has already followed this path, chasing the "super-ideal quenching" (Van De Steeg et al. 2021; Wolf, Peeters, et al. 2020). They explain their EE near 50% with MW discharges by (i) significant oxygen recycling at the interface of the MW hot core and the CO_2 flow and (ii) fast quenching of the CO produced, thus preventing recombination reactions. To further increase the EE, current research is looking at ways to optimize the transport of the excited species from the hot core to the warm surrounding (Mercer et al. 2023), and to model the coupling between plasma kinetics and fluid dynamics (Vialetto et al. 2022).

None of the experiments and models presented in the works mentioned in this section could cross the 50% EE limit. A possible way out could be continuously separating the products to create an underpopulation of CO in the mixture. The addition of a catalyst, for instance, could serve this purpose. As a result, coupling the plasma with catalysts has generated hope and interest in the community (Bogaerts et al. 2020). Due to its high temperature, MW

discharges are not sensed to be the best candidates, but (Chen et al. 2017) gave it a try by adding a catalyst a few cm downstream of the plasma (post-plasma catalysis). Their best results showed a promising 45% conversion and 56% EE in pure CO_2. We did not find more recent attempts to enhance MW discharges with a catalyst. These results have not been reproduced yet.

2.2.3 Glow, DBD, and GA discharges

Meanwhile, other attempts have been made to break the 50% EE barrier. Different kinds of discharges – glow discharges, corona discharges, dielectric barrier discharges (DBD), gliding arc discharges (GA), radio frequency discharges, and nanosecond repetitively pulsed (NRP) discharges, in addition to MW discharges – have been tested, as well as coupling plasma with catalysts (Chen et al. 2021; George et al. 2021). Figure 2-4 summarizes the performances of several types of discharges in terms of conversion degree and SEI. As the conversion degree is proportional to the product of EE times SEI, the diagonals of the graph are the iso-EE lines. Figure 2-5 shows the same results, but this time in terms of conversion degree versus EE. Notably, Salden *et al.* conducted a thorough summary of experimental data from the literature on CO_2 plasmalysis and made it available through the Pioneer database (Salden et al. 2023).

2.2.3.1 Glow discharges

The glow discharge has been mostly studied to validate CO_2 kinetic models, as it offers homogeneous and stable operating conditions. The experiments of (Klarenaar et al. 2017, 2018, 2019; A S Morillo-Candas et al. 2020; Morillo-Candas et al. 2021) allowed to validate the vibrational kinetics (Grofulović et al. 2018; Silva et al. 2018), the neutral kinetics below 1000 K, and to study the kinetics of the first electronic states at moderate reduced electric fields (below 100 Td) (A. F. Silva et al. 2020; Silva et al. 2021). The typical temperatures were $T_g \sim 500\ K$, and $T_v \sim 1{,}000\ K$.

These models indicate that, in low-pressure glow discharges, CO_2 dissociates via direct electron impact, more precisely via the excitation of its electronic pre-dissociative states. This result is confirmed by the measurements of (A. S. Morillo-Candas et al. 2020).

The best CO_2 conversion and EE in a glow discharge were obtained at atmospheric pressure (Renninger, Lambarth, and Birke 2020; Trenchev et al. 2019). Their highest EEs were in the range 20-30%, and the conversion 15-20%. Trenchev *et al.*'s model shows that the VDF is Boltzmann and $T_{v3} = T_g \approx 2000 - 3000\ K$ in the plasma core. The main channel of CO production is then via the reaction of O with hot CO_2. Already, at these temperatures, thermal chemistry becomes dominant. Nevertheless, the latter discharge is not representative of the usual low-pressure glow discharges that are studied in the literature.

2.2.3.2 Dielectric Barrier Discharges (DBD)

CO_2 conversion using DBDs has been extensively studied. Indeed, DBDs are commonly used in industrial processes such as surface treatment so that they can be easily scaled up. Moreover, they operate at atmospheric pressure. They show high nonequilibrium between electrons and heavy particles: typically, $T_e \sim 2-10\ eV$ whereas $T_g \sim 300-500\ K$. Consistently, the models show that the dominant CO production pathway is direct electron-impact dissociation (Aerts, Somers, and Bogaerts 2015; Kozák et al. 2014). However, these studies exhibit poor conversion and EE results: although some points at 15% have been reported (Snoeckx and Bogaerts 2017), the EE is typically only about 5 – 10%.

Due to their low temperature, DBDs are suitable to be coupled with catalysts. Dozens of studies have been carried out, showing some improvements (Chen et al. 2021; George et al. 2021). In particular, a 20% EE was obtained by (Lu et al. 2021). Ray and Subrahmanyam even topped 30% EE (Ray and Subrahmanyam 2016) using TiO_2 packing as a catalyst, although it seems that, in a subsequent study, they could not hit it again (Ray, Chawdhury, and Subrahmanyam 2020). In short, the race is on for DBD catalysis; nevertheless, it is still far from the 50% EE achieved by thermal plasmas.

2.2.3.3 Gliding Arc (GA) discharges

Gliding Arc (GA) discharges yield low CO_2 conversion (below 10%) – but provide some of the highest EE, about 30-40% (Liu et al. 2020). As in the MW discharge, the high temperature prevailing (typically 2000-3000 K) induces fast VT relaxation, impeding the pure-vibrational mechanism. Heijkers *et al.* (Heijkers and Bogaerts 2017) simulated a gliding arc with a 0D kinetic model and showed that the vibrational distribution quickly thermalizes and equilibrates with the translation. They focused on vibrational kinetics, showing a significant contribution of the high vibrational levels to dissociation. However, the vibration being in equilibrium with the translation, they actually described thermal dissociation. Vibration levels indeed play a role in the dissociation process, but as in any gas in thermal equilibrium, their contribution is included in the rate constant of dissociation by heavy particles.

Finally, the combination of GA with catalysts has been primarily tried on methane dry-reforming (Allah and Whitehead 2015; Martin-del-Campo et al. 2021; Zhu et al. 2017), and has been shown to increase the conversion and selectivity toward H_2 and CO. We are aware of only one attempt in pure CO_2 (Zhang et al. 2020), showing improvements of the conversion and EE. However, the EE was still below 30%, far from the 43% record (Nunnally et al. 2011) (set without catalyst).

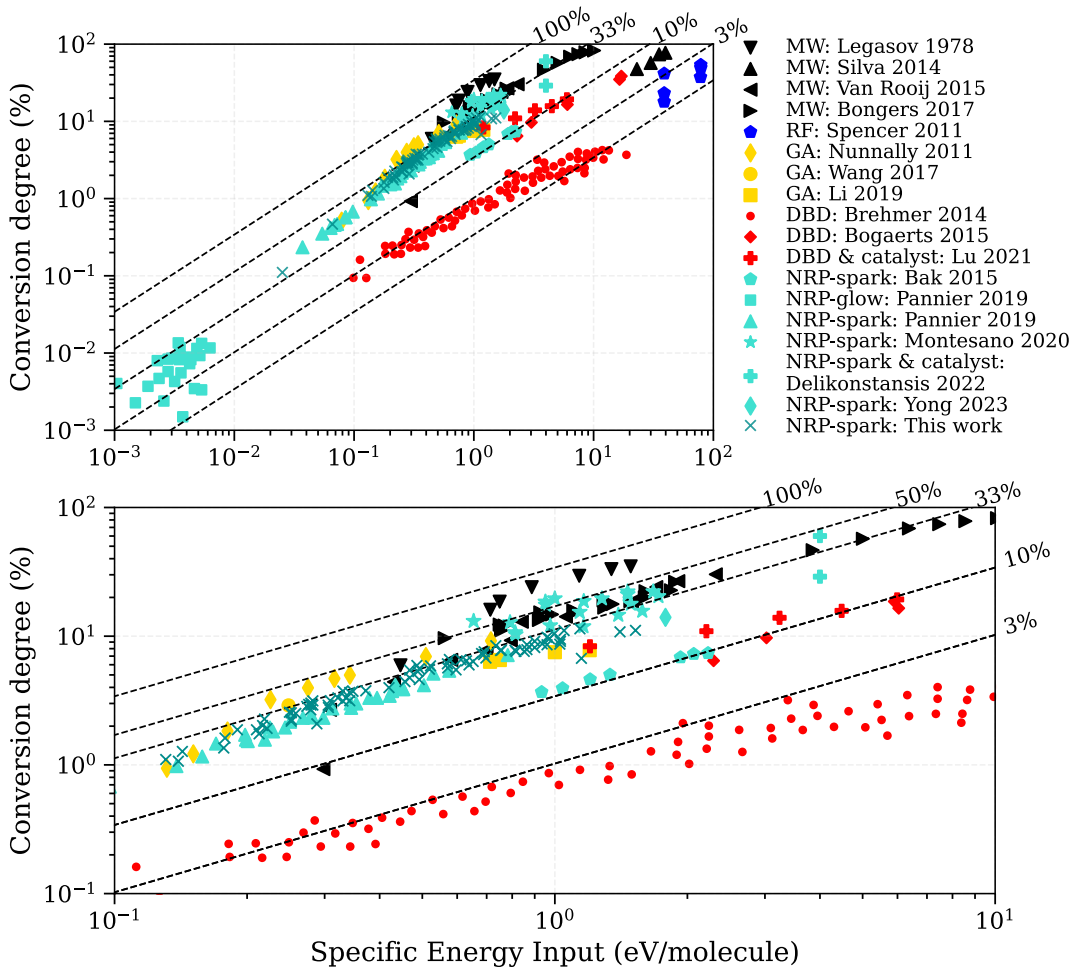

Figure 2-4. Comparison of the conversion and Energy Efficiency (EE) of various discharges. The dotted diagonals are the iso-EE. The warm discharges – MW, GA, NRP-spark – perform much better than the cold discharges – RF, DBD, and NRP-glow. Montesano et al.'s NRP discharges (cyan stars) achieved the best performance since the 80s.

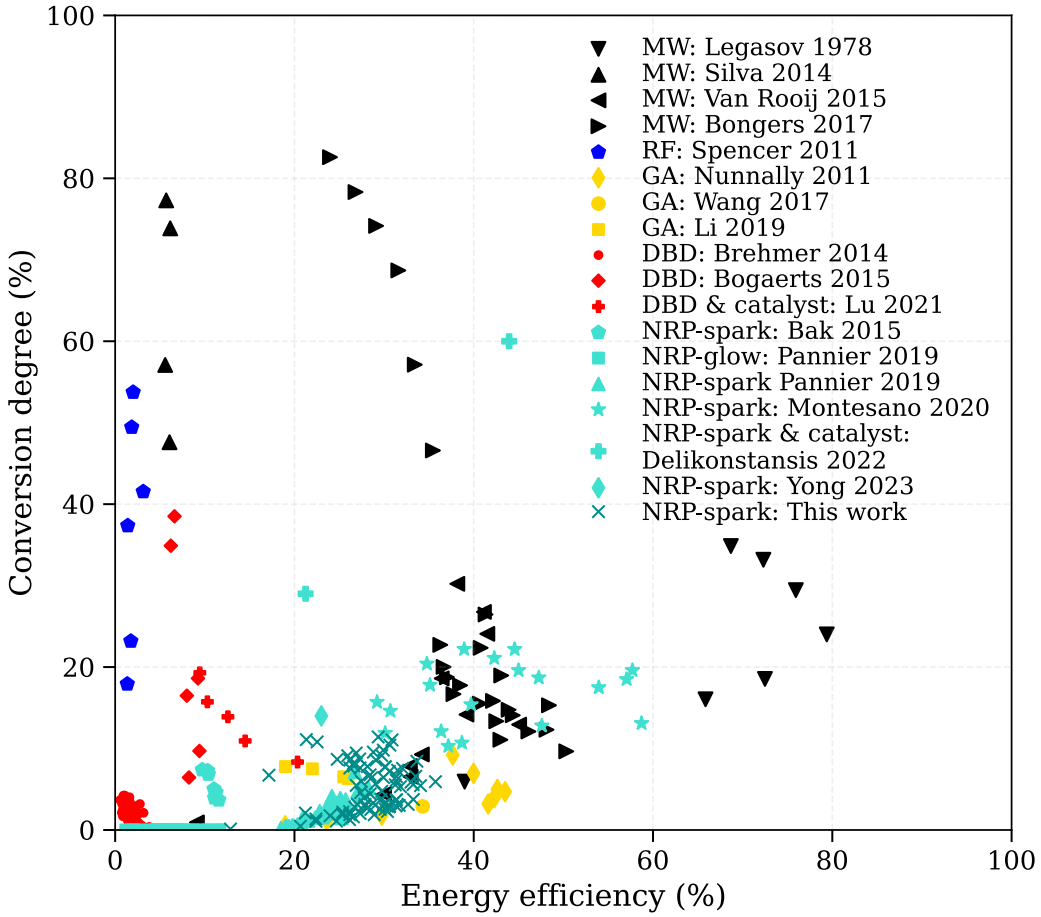

Figure 2-5. Conversion degree vs energy efficiency (EE) achieved in the plasma discharges of the literature.

2.2.4 Nanosecond Repetitively Pulsed (NRP) discharges

2.2.4.1 Basics about NRP discharges

NRP discharges – studied in this work – were introduced at Stanford as a way to produce high electron densities in air at a low energy cost (Kruger et al. 2002). Moreover, they generate highly nonequilibrium plasmas because the energy is deposited at nanosecond timescales, which is faster than typical relaxation times (10 - 100 µs for VT relaxation at atmospheric pressure).

NRP discharges can operate in different regimes: NRP-corona, NRP-glow, and NRP-spark (David Z. Pai, Lacoste, and Laux 2010), to which Minesi *et al.* added the NRP thermal-spark (Minesi et al. 2020).

The NRP-corona and NRP-glow regimes are characterized by low gas heating (typically less than 300 – 500 K), high electron temperatures (typically a few eV), and low ionization degrees (typically less than 10^{13} cm^{-3} (Pai et al. 2009)). They present a high degree of nonequilibrium.

In the NRP non-thermal spark regime, the gas heating is higher than in the corona and glow regimes, typically 1000 – 3000 K, the electron temperature reaches a few eV, the electron density can be as high as 10^{17} cm^{-3}, and it is also highly nonequilibrium.

In the NRP thermal-spark regime, Local Thermal Equilibrium (LTE) is reached quickly during the electric pulse. The temperature rises above 30,000 K, and the gas reaches full ionization with electron densities above 10^{19} cm^{-3} (Minesi et al. 2020).

2.2.4.2 Energy Efficiency

CO_2 conversion by NRP discharges has been relatively little studied. The first attempt to use NRP discharges to produce CO from CO_2 was conducted by Bak *et al.* (Bak, Im, and Cappelli 2015). Operating at high pressure (2 – 5 atm), they reported about 10% EE. In an atmospheric pressure reactor, Martini *et al.* (Luca Matteo Martini et al. 2018) demonstrated up to 30% EE and 20% conversion. Then, Pannier (Pannier 2019) showed that the EE is only about 5% for the NRP-glow discharge at atmospheric pressure, but reaches 30% in the NRP-spark regime. Recently, Montesano *et al.* (Montesano et al. 2020) measured an outstanding 58% EE using bursts of pulses with an in-the-burst frequency of 50 kHz and a carrier frequency of 300 kHz. To our knowledge, these are the best CO_2 dissociation energy efficiency results since the 80s (Rusanov et al. 1981) (see Figure 2-5).

Other measurements with NRP discharges have been performed with varying degrees of success. Pokrovskiy (Pokrovskiy 2021) measured a maximum EE and conversion of 23% and 19% in a capillary discharge at 10 mbar. Pannier *et al.* (Pannier et al. 2022) extended the EE and conversion measurements to high pressures and obtained about 20% EE and 5% conversion at 12 bar. Very recently, Yong et al. (Yong et al. 2023) obtained up to 27% EE (along with a conversion of 4% at this point) at 5 bar, and 14% conversion (along with an EE of 23%) at 6 bar. Finally, Delikonstansis et al. (Delikonstantis et al. 2022) added a catalyst[2] and improved the conversion up to 60% with an EE of 44%.

2.2.4.3 Current understanding of the underlying mechanisms

Predictions from the models

Several 0D kinetic models have been developed to understand CO_2 conversion kinetics (Pietanza et al. 2021), but only a few have addressed NRP discharges (Heijkers et al. 2019; Naidis and Babaeva 2022; Pannier 2019; Pokrovskiy, Popov, and Starikovskaia 2022).

[2] Strictly speaking, the CeO_2/Fe_2O_3 bed they use is more of a catalyzer than a catalyst. As it adsorbs O and O_2, it deactivates. They reactivate it using an H_2 plasma that reduces the oxidized bed. The energy cost of the reactivation process should be included in the energy efficiency calculation.

Pannier adapted Kozak's model (Kozák et al. 2014; Kozák and Bogaerts 2015) to create the first 0D-kinetic model of NRP discharges in CO_2 (Pannier 2019). He paid particular attention to modeling the predissociation of CO_2 electronic states and showed that in the spark regime, two-thirds of the dissociation occurs during the pulse, following electron-impact excitation toward these states. In addition, his model predicted that O-CO_2 association (Reac. 7) and heavy-particle impact dissociation (Reac. 5) accounted for the remaining third of the dissociation at the time scale of about 1 µs. Although a high vibrational excitation was predicted during the 20 ns pulse, the VDF equilibrated at the gas temperature in less than 100 ns. Overall, vibration excitation did not last long enough to have a significant impact on dissociation. These results are reproduced in Figure 2-6, showing the CO_2 conversion to CO as a function of time and the contribution of the different dissociation channels. The simulations predicted an EE of about 20 – 25%.

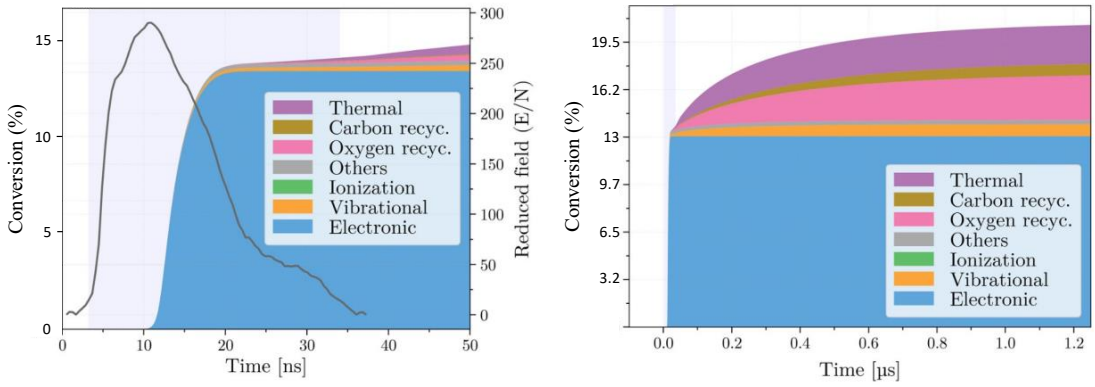

Figure 2-6. CO_2 conversion to CO and reduced electric field (grey line) in a non-thermal spark, from the 0D kinetic model of Pannier (Pannier 2019). The various CO production channels are indicated. Primary channels comprise electron-impact electronic excitation, vibrational excitation, dissociative ionization, and excitation of other molecules. Secondary channels include O-CO_2 association, the Boudouard reaction, and thermal dissociation. The conversion to CO is about 14% at 50 ns after the pulse, and about 20% after 1.2 µs (reproduced with permission from Pannier).

Later, Heijkers *et al.* (Heijkers et al. 2019) simulated the NRP discharge of Martini *et al.* (Luca Matteo Martini et al. 2018). They confirmed that electron-impact dissociation via the electronic states of CO_2 is the dominant dissociation mechanism in those discharges (what they call direct electron dissociation proceeds via predissociative electronic states). They pointed out that vibrational excitation enhances electronic dissociation, lowering the activation energy to the electronic states. This mixed process makes the electronic excitation possible for lower energy electrons. Thus, a larger fraction of the electron distribution is used in the dissociation, which could increase the EE (we will discuss this point in Sec. 2.3.1). Nevertheless, in Heijkers *et al.*'s simulation, electron-impact dissociation occurs

mainly from the lowest vibrational states, which makes little difference in terms of EE compared to electron-impact dissociation from the ground state.

Limits

The current understanding of the CO_2 dissociation pathways in NRP discharges strongly relies on Pannier's and Heijkers's kinetic models. These models have been validated with measurements from 3 µs to 100 µs after the pulse. Heijkers *et al.*'s model has been compared to CET-LIF measurements of the *in situ* conversion and temperature, and to post-discharge measurements of the EE and conversion (Luca Matteo Martini et al. 2018). Pannier obtained the same quantities using IR emission spectroscopy for the *in situ* measurements and a gas analyzer for the post-discharge measurements.

However, because of the ultra-fast heating and dissociation they induce, NRP sparks generate shock waves followed by complex hydrodynamic effects. At 3 µs, they are already significant (Castela et al. 2017; Dumitrache et al. 2019; Xu et al. 2014). A 0D model cannot capture these effects, making the validation incomplete. Pannier's model showed that most CO_2 dissociation occured during the first 20 ns after the pulse (Pannier 2019). Therefore, to validate these models and refine the dissociation mechanisms, the plasma must be characterized at the early instants during and after the pulse. Optical Emission Spectroscopy (OES) is a suitable diagnostic for this task, as the plasma produces intense emission up to about one microsecond after the pulse, as will be seen in Chapter 3.

2.2.5 Summary and open questions

Early work in the 1980s set high expectations for plasma technologies, by reporting energy efficiencies in excess of 80%. In the last decade, these expectations have been disappointed: we have shown in the previous sections that despite numerous attempts from researchers all over the world, using all kinds of discharges, almost no one has been able to reach an energy efficiency (EE) of 50%. A few exceptions could cross this barrier, such as (Montesano et al. 2020), but their results have not yet been reproduced.

In the 1980s, the over 80% EEs were attributed to the nonequilibrium excitation of CO_2 vibration while the gas temperature was maintained below 1,000 K. Since then, it is widely accepted in the community that high T_v and low T_g is the recipe for the best EE. However, the current experimental results not only question the reproducibility of the measurements made at that time, but also, challenge this assumption. In the last decade, the best EE performances have been obtained in plasmas near thermal equilibrium, with T_g exceeding 3,000 K during the process.

The purpose of the following sections (2.3 and 2.4) is to unravel this puzzling situation.

2.3 Energy Efficiency (EE)

As mentioned in Chapter 1, in order to produce CO at the lowest carbon footprint and economical cost, CO_2 plasmalysis must produce CO at the lowest energy cost possible. The enthalpy of the global reaction (Reac. 0) at ambient temperature is 2.9 eV. The closer the energy cost is to this limit, the better the energy efficiency (EE).

In this section, we want to (i) evaluate the maximum value of EE that can be achieved in a plasma discharge without the help of a catalyst, and (ii) identify the kinetic pathway that allows this EE to be achieved.

Since we are looking for an upper bound of the EE, we can simplify the problem without loss of generality, as long as this simplification is favorable to the EE. We divide a (catalyst-free) plasma process to produce CO from CO_2 into 2 steps. A schematic of the process is presented in Figure 2-7. In the first step, energy is added to the system, composed of CO_2. It goes to the electronic, vibrational, rotational, and translational modes of CO_2. It results in the production of CO, O_2, and radicals (including O or C). We name this first step the "discharge stage". In the second step, these radicals react with CO_2, CO, O_2 or themselves to form new products, without additional energy. For example, the O atoms produced during step-1 can produce other CO molecules (Reac. 7, O-CO_2 association), or consume a CO molecule to reform CO_2 (Reac. 6, 3-body recombination of CO). These reactions are more or less promoted depending on the conditions in the gas (pressure, composition, temperatures). We name this second step the "quenching stage". To optimize the EE, we need to understand both stages: the CO formation and depletion pathways at play, their energy cost, and how they can be controled.

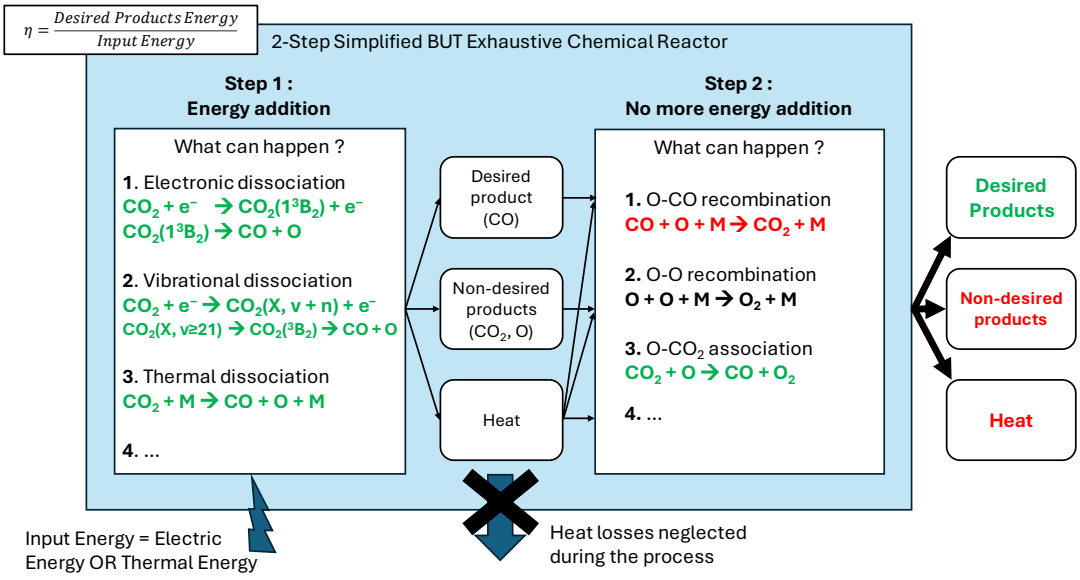

Figure 2-7. Diagram of CO production from CO_2 in a (catalyst-free) plasma process.

In Sec. 2.1.2, the main CO production pathways were listed and, whenever possible, a minimum energy cost for CO production was given. Among the possible reaction pathways, the most favorable to the EE of CO production is by far $CO_2 \rightarrow CO + O$ in step 1, followed by O-CO_2 association ($CO_2 + O \rightarrow CO + O_2$) in step 2. The standard enthalpy of the first reaction is 5.5 eV. Thus, the EE in step 1 alone cannot exceed $\eta = 2.9/5.5 = 53\%$. As explained in Sec. 2.1.2, O-CO_2 association has a standard enthalpy of reaction of 0.35 eV, and thus, combined with Reac. 5, it could allow to reach a cost of 2.9 eV / CO molecule, ie an EE of 100%. This is the 2-step pathway that will be studied in the following of this Chapter.

In the following three sections (Sec. 2.3.1 - 2.3.3), we will study three illustrative cases of the discharge stage (step 1) leading to the formation of CO and O. In Sec. 2.3.1, we study the electronic dissociation pathway. As the fastest dissociation pathway, it suffers little from competing reactions, making it the most relevant pathway to consider independently. In Sec. 2.3.2, we study the pure vibrational pathway and show under which conditions it can dominate over competing processes and be efficient. In Sec. 2.3.3, we consider the EE of CO production in a system at Local Thermodynamic Equilibrium (LTE). In these three sections (and as was done in Sec. 2.1.2), we assume that the products of the pathways studied are frozen, and the heat released is lost.

Then, we focus on the quenching stage (step 2), where the products and heat released in the discharge stage are used in subsequent reactions. In Sec. 2.3.4, we present the different quenching scenarios undergone by the products of the dissociation, and we assess the cooling rate required to freeze the CO content in the mixture (and thus preserve the EE). In Sec. 2.3.5, we study "O recycling", i.e. the use of the chemical energy of the remaining O atoms to produce CO at a reduced energy cost via the O-CO_2 association reaction. The study of O recycling allows us to set an upper bound for the EE. In Sec. 2.3.6, we summarize what we learned in the previous sections and conclude.

2.3.1 Electronic dissociation

To begin with, we present a literature review on CO_2 electronic states to determine whether their excitation by electron impact leads to dissociation. Then, we study the EE of the electronic dissociation pathway alone. Finally, we discuss the EE of a mixed electronic-vibrational pathway.

2.3.1.1 Predissociation of CO_2 electronic states

The electronic states of CO_2 play a major part in CO_2 dissociation by plasma discharges (as illustrated in Sec. 2.2). One of the main questions for us is: do CO_2 electronic states always pre-dissociate following an electron collision? In the literature on CO_2 electronic states, this

affirmation seems to be taken for granted. We have come across statements of the following kind: "It is well established that all the electronically excited valence states in CO_2 are pre-dissociated" (Wright et al. 2017). Most of these affirmations rely on (Okabe 1978), who reviewed photolysis experiments. Even if Okabe appears convinced about the electronic states' pre-dissociation, we could not find in his book a conclusive explanation. Furthermore, some of the quantum yield measurements he reports are not unity, which is inconsistent with the full pre-dissociation assumption.

To elucidate this issue, we have to delve into the bibliography. CO_2 being triatomic, the molecule configuration is much more complex than in the diatomic case. A detailed review of the literature on CO_2 electronic states has been carried out in Pannier's Ph.D. thesis (Pannier 2019), Table 4-1. Starting from there, we will just summarize the best-known states and their energy. Then, we will discuss their pre-dissociation in more detail. The conclusions are summarized in Table 2-3.

Lower states

In CO_2, the electronic ground state is linear ($CO_2(X^1\Sigma_g^+)$), but most of the electronic excited states are bent. The potential energy of these electronic states depends on the two internuclear distances and the bond angle. The D_∞ geometry describes the electronic cloud of a linear molecule. For a bent molecule, the C_{2v} or C_s geometries are used. The potential energy curves of CO_2 low-lying states are represented in Figure 2-8, with the second internuclear distance r_2 at its equilibrium value (2.2 a_0) and the bond angle $\alpha = 179°$. The data for singlet states come from (Grebenshchikov 2013; Lu et al. 2015), and those for the triplet states from (Johan A. Schmidt et al. 2013).

The first triplet state is 1^3B_2, as expressed in C_s geometry. The state is initially mapped to a $^3\Sigma_u^+$ in D_∞ geometry and quickly bends to C_s geometry. The excitation from $CO_2(X^1\Sigma_g^+)$ to $CO_2(1^3B_2)$ is spin-forbidden for a photon. However, in plasmas, the transition is possible under the impact of an electron. Since the interaction time of an electron with a molecule is much shorter than the time for the molecule to vibrate, the Franck-Condon (FC) principle applies (Chen and Chang 2003) and the electron-molecule collision results in a vertical excitation. As can be seen in Figure 2-8, the vertical energy necessary to excite 1^3B_2 from the Franck-Condon region is about 8 eV. The potential energy curve presents a dip and a small energy barrier at $r_1 \sim 2.75$ a_0. Indeed, 1^3B_2 has bound states and reaches its minimal energy 5.5 eV at $\alpha \sim 120°$, $r_1 \sim 2.8$ a_0 (Schmidt, Johnson, and Schinke 2013). However, the 8-eV vertical energy is above the energy barrier on the route to dissociation. Thus, due to the Franck-Condon principle, an electron-impact excitation of 1^3B_2 will systematically lead to its pre-dissociation into CO(X) + O(^{3}P). The same phenomenon happens for the 1^3A_2 state ($^3\Delta_u$). Its energy in the FC region – 8.8 eV – is higher than the energy barrier, leading to pre-dissociation.

The first excited singlet states are 1^1B_2 ($2^1A'$) and 1^1A_2 ($1^1A''$). They lie 9 eV above the ground state, and both have a potential well, whose bottom is at 5.5 eV, reached for $\alpha \sim 120°$ and $\alpha \sim 130°$ respectively (Grebenshchikov 2013; Schmidt et al. 2013). The 1^1B_2 state is known to be responsible for the flame band emission (Raposo et al. 2021). In the case of excitation by electron impact, just like for 1^3B_2 and 1^3A_2, 1^1B_2 and 1^1A_2 vertical energies are higher than the dissociation barrier. They will then pre-dissociate into CO(X) + O(^{1}D).

Higher states

We now turn to the case of the higher states. In the linear configuration plotted in Figure 2-8, we see that, for the singlets 2^1A_2, 2^1B_2, 3^1A_2, and triplets 2^3A_2, 2^3B_2, the energy barrier on the course to dissociation is higher than the vertical energy. The potential energy surfaces (PES) of these states show the same result (Grebenshchikov 2013; Schmidt et al. 2013).

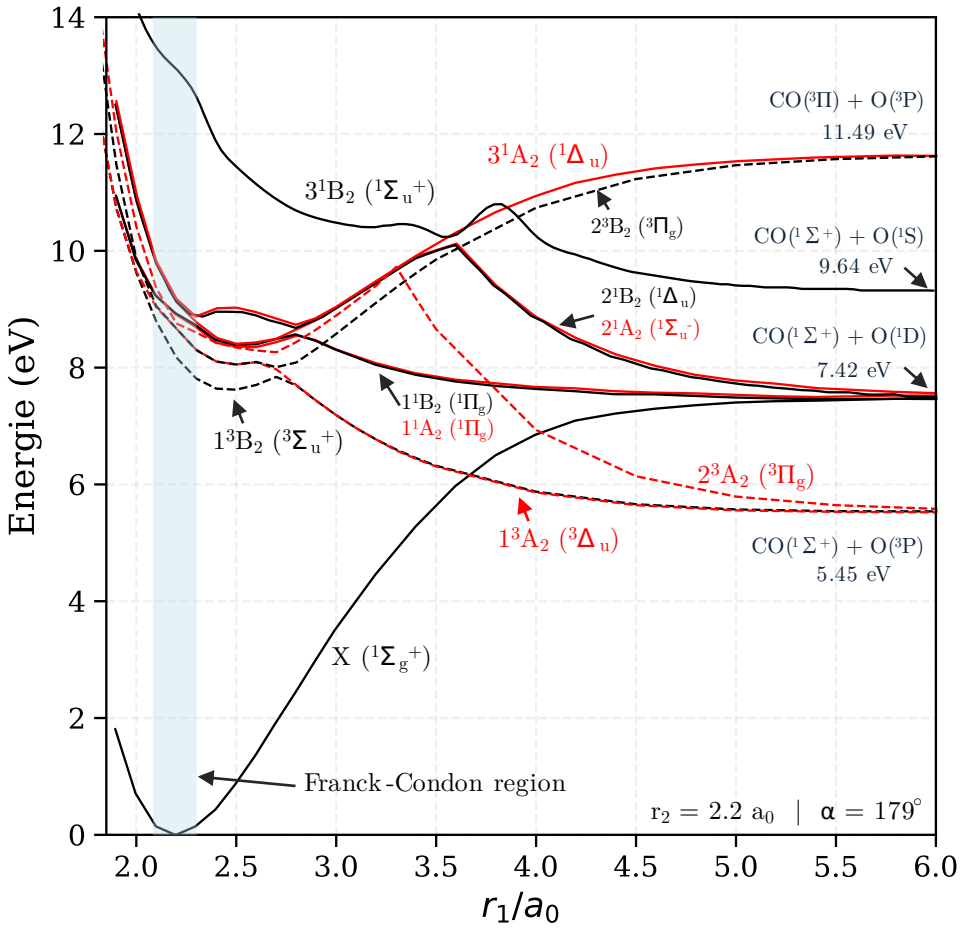

Figure 2-8. First electronic states of CO_2 calculated by Grebenshchikov (singlet states except 3^1B_2), Lu *et al.* 2015 (3^1B_2), and Schmidt *et al.* 2013 (triplet states), for a bond angle $\alpha = 179°$, and the second O-CO distance $r_2 = 2.2$ a_0.

However, the electronic states of CO_2 are scattered with conical intersections and avoided crossings[3], which are as many shortcuts towards interaction with repulsive states and therefore dissociation. These interactions have been studied from the 80s and more recently (Grebenshchikov 2013; Grebenshchikov and Borrelli 2012; Knowles, Rosmus, and Werner 1988; Lu et al. 2015; Spielfiedel et al. 1991, 1992; Watanabe et al. 2013; Wright et al. 2017, Spielfiedel et al. 1993, Chen et al. 2010). Grebenshchikov and Borrelli (Grebenshchikov and Borrelli 2012) demonstrated that the first five singlets meet in a fivefold intersection and that this intersection forms a seam passing through the FC region. Moreover, at linearity, he identified a sevenfold intersection involving higher electronic states (Grebenshchikov 2013). These intersections allow the molecule to transition from one electronic state to another. In particular, a CO_2 molecule in a bound state can find a way to a predissociative state, like a marble rolling into a gutter. The triplet states have been less studied, as they are not subject to photo-dissociation studies, but their PES are also shaped by intersections and avoided crossings. As with the singlet states, Spielfiedel *et al.* (Spielfiedel et al. 1991, 1992) spotted a conical intersection in the FC region between the triplet states, allowing dissociation through the lowest asymptote. Overall, these measurements depict a cluster of porous states. Starting from the Franck-Condon region, it is only a matter of time before a given electronic state transitions to a predissociative state.

To clarify, let us take the example of the 3^1A_2 state. After a vertical excitation, it has 9 eV energy, which is not enough to dissociate via its asymptote at 11.64 eV. Nevertheless, while vibrating along the r_1 coordinate, the molecule crosses the conical intersection seam twice, at 2.3 and 2.7 a_0. Each time, it has a non-zero probability of crossing to the 1^1A_2 state, which would lead to dissociation (here toward $CO(X) + O(^1D)$). This crossing and dissociation will eventually occur, unless the 3^1A_2 state is first de-excited by some other process.

Electronic state dynamics

The real question is: are the transitions through conical intersections or avoided crossing faster than the electronic state de-excitation? Let us take the example of an atmospheric pressure plasma at $T_g \sim 1000$ K. Apart from pre-dissociation, collisional quenching would be the fastest de-excitation process in this scenario. The characteristic time between two heavy-heavy collisions can be estimated as in (Vincenti and Kruger 1965):

[3] Due to the Hermitian nature of the energy operator, the potential energy of two electronic states, described by hypersurfaces of dimension N, can only meet on a manifold of dimension N-2. This property result in the formation of avoided crossing (the two potential energy surfaces approach each other and then move away from each other), and conical intersections (the two potential energy surfaces meet and then move away from each other). These phenomena allow the molecule to transition from an electronic state to another.

$$\tau_{coll} \sim \left(10^{10} \cdot \sqrt{\frac{300}{T[K]}} \cdot P[atm]\right)^{-1} \qquad \text{Eq. 2-5}$$

Thus, in the surrounding gas at atmospheric pressure and 1000 K, $\tau_{coll} \sim 0.2$ ns, which is a lower bound of the characteristic time of quenching.

On the other hand, CO_2 dissociation after conical intersection crossings has been confirmed in photo-dissociation experiments (Lu et al. 2015; Song et al. 2014; Wright et al. 2017) (Chen et al. 2010). Lu *et al.* measured O(^{1}S) and O(^{1}D) formation following CO_2 excitation to 4^1A' at 12 eV. Their measurements of total kinetic energy release spectra suggest that (i) O(^{1}S) arises from the 4^1A' asymptote, whereas (ii) O(^{1}D) is produced via the 3^1A' asymptote, following the transition between 4^1A' and 3^1A' through their conical intersection. For both products, they measure that dissociation happens in less than a rotational period (10 – 100 ps, (Herzberg 1966)). Thanks to the emergence of femtosecond and attosecond lasers, it is now possible to probe the electronic dynamics in molecular systems. Wright *et al.* performed time-resolved measurements of the dissociation dynamics consecutive to $^1\Pi_g(1^1B_2$ & $1^1A_2)$ photo-excitation. They substantiate the existence of two dissociation channels: a direct one occurring in less than 20 fs, and an indirect one, proceeding via a conical intersection and whose lifetime is about 200 fs. In both cases, pre-dissociation is much faster than our quenching time estimate.

Summary

To provide a definitive conclusion on the pre-dissociation of the CO_2 electronic states after a vertical excitation, one would need to probe the dissociation dynamics of every state, which is obviously a very complex task. However, the picture drawn by these studies fully supports the original idea that all CO_2 electronic states pre-dissociate after a vertical excitation from the ground state. The CO_2 PES abounds with conical intersections and avoided crossings. These intersections allow the molecule to jump from higher bound states to lower pre-dissociative states. These jumps are fast: the first measurements in CO_2 indicate they take place in about 200 fs. In a different molecule, CS_2, similar measurements indicate the same order of magnitude (Spesyvtsev et al. 2015). We anticipate that, regardless of the electronic state, they will remain faster than the collisional quenching. In addition to this argument, we have found no evidence of any metastable states in the literature. Last but not least, the doubt instilled by the measurement of photo-dissociation quantum yields lower than one was dispelled by (T. G. Slanger and Black 1978; Slanger, Sharpless, and Black 1977). They explained the lower quantum yields measured in former studies by various reasons (including the omission of the CO($^1\Sigma^+$) + O(^{1}D) dissociation channel between 108 and 116 nm (Koyano, Wauchop, and Welge 1975), and the difficulty to account for the sharp variation of the absorption cross section of CO_2 at 130.2-130.6 nm and 147 nm), and

showed with their own measurements that the quantum yield is one above 8.3 eV (below 150 nm). Therefore, in the following, we will consider with strong confidence that all excited CO_2 states pre-dissociate after a vertical excitation from the ground state, so *a fortiori* following an electron-impact excitation.

Table 2-3. Properties of the first electronic states of CO_2: geometry in D_∞ and C_{2v}[4]; vertical excitation energy E_{vert} (eV); minimum adiabatic energy E_{min} (eV); most likely dissociation asymptote, after a vertical excitation from the ground state. Data from (Grebenshchikov 2013; Johan A Schmidt et al. 2013; Watanabe et al. 2013)

D_∞	C_{2v}	C_s	E_v	E_{min}	Effective dissociation asymptote
$^1\Sigma_g^+$	1^1A_1	$1^1A'$	0	0	/
$^3\Sigma_u^+$	1^3B_2	$1^3A'$	8.2 – 8.4	5.5	$CO(^1\Sigma^+) + O(^3P)$
$^3\Delta_u$	1^3A_2	$1^3A''$	8.7 – 8.8	5.3	$CO(^1\Sigma^+) + O(^3P)$
$^3\Pi_g$	2^3B_2	$2^3A'$	8.6 – 8.7	7.6 – 7.7	$CO(^1\Sigma^+) + O(^3P)$
	2^3A_2	$2^3A''$	8.6 – 8.8	8	$CO(^1\Sigma^+) + O(^3P)$
$^1\Pi_g$	1^1B_2	$2^1A'$	8.9 – 9	5.4 – 5.5	$CO(^1\Sigma^+) + O(^1D)$
	1^1A_2	$1^1A''$	8.9 – 9	5.4 – 5.5	$CO(^1\Sigma^+) + O(^1D)$
$^1\Sigma_u^-$	2^1A_2	$2^1A''$	8.8 – 9.2	8 – 8.1	$CO(^1\Sigma^+) + O(^1D)$
$^1\Delta_u$	2^1B_2	$3^1A'$	9.2	8.7	$CO(^1\Sigma^+) + O(^1D)$
	3^1A_2	$3^1A''$	9.2	8.7	$CO(^1\Sigma^+) + O(^1D)$
$^1\Sigma_u^+$	3^1B_2	$4^1A'$	11.1	/	$CO(^1\Sigma^+) + O(^1S)$

2.3.1.2 Pure electronic dissociation

We saw in the previous section that 1^3B_2 is the electronic state with the lowest vertical energy, 8.3 eV (Table 2-3), and that it predissociates after a vertical excitation. If we consider an energy source that only excites this transition, we get an upper bound for the EE of the pure electronic pathway: $\eta = 2.9/8.3 = 35\%$ (using the definition of the energy efficiency presented in Sec. 2.1).

Let us consider a system composed of CO_2 molecules subjected to an electric field. The electrons are not mono-kinetic and exciting the 1^3B_2 state is just one of the many ways they lose their energy. They can exchange kinetic energy via elastic collisions, excite vibrational

[4] CO_2 electronic states are entangled in multiple conical intersections and avoided crossings (Grebenshchikov and Borrelli 2012; Knowles et al. 1988; Spielfiedel et al. 1991), making the assignment and ordering of the state in linear geometry a subject of controversy (Watanabe et al. 2013). Here we take Watanabe's side, but ultimately, the assignment in D_∞ does not matter in our analysis since the potential energy surfaces are computed using C_{2v} or C_s geometry.

states or other electronic states of the molecule, or ionize it[5]. To estimate the fraction of the energy going to electronic excitation, we compute the electron energy distribution function (EEDF) in pure CO_2 using BOLOS (Luque 2014) – a Python implementation of the BOLSIG+ (Hagelaar and Pitchford 2005) algorithm – and cross-section data from IST-Lisbon (Grofulović, Luís L Alves, and Guerra 2016; IST-Lisbon). In the IST-Lisbon database, based on the work of (Hake and Phelps 1967), the CO_2 electronic states are modeled by two groups of states at 7 and 10.5 eV. Several EEDFs calculated at different E/N values are reported in Figure 2-9. The figure shows that the fraction of the EEDF above the 7 and 10.5 eV energy thresholds increases with E/N.

Thus, from the EEDF, we obtain the electron energy loss fractions, i.e. to which energy mode of the CO_2 molecule the colliding electron will lose its energy. In Figure 2-10 and Figure 2-11, we report the electron energy loss fraction as a function of the reduced electric field and the electron temperature (the latter corresponds to the case where the electron energy follows a Maxwellian distribution). Above 100 Td (calculated EEDF) or 2 eV (Maxwellian EEDF), electronic state excitation dominates.

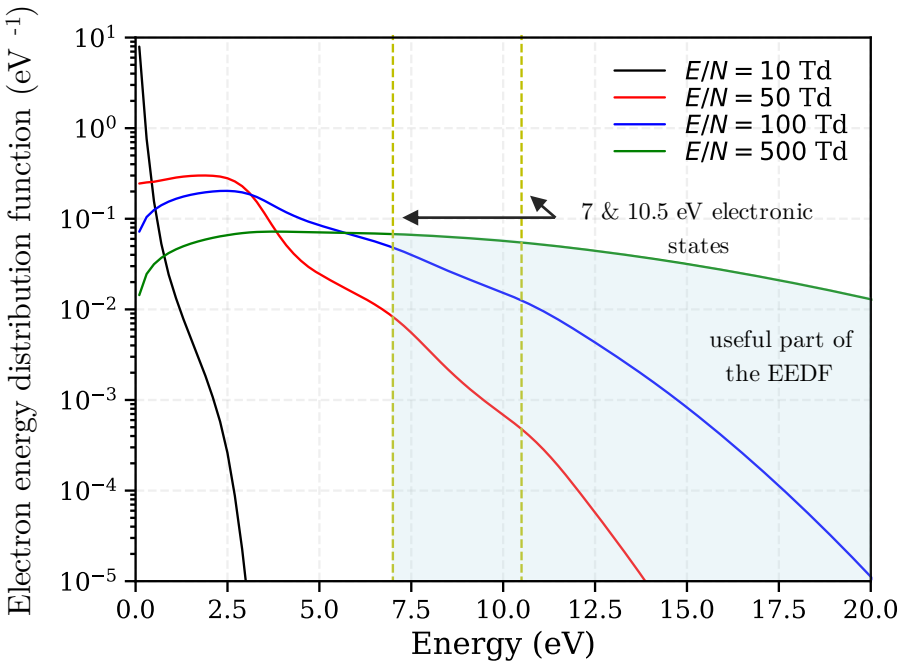

Figure 2-9. Electron energy distribution function in pure CO_2 vs reduced electric field. Calculated using BOLOS (Luque 2014) with cross-sections from IST-Lisbon database (Grofulović, Alves, and Guerra 2016; IST-Lisbon).

[5] Moreover, once the plasma is no longer pure CO_2, the electrons can lose their energy to species other than CO_2.

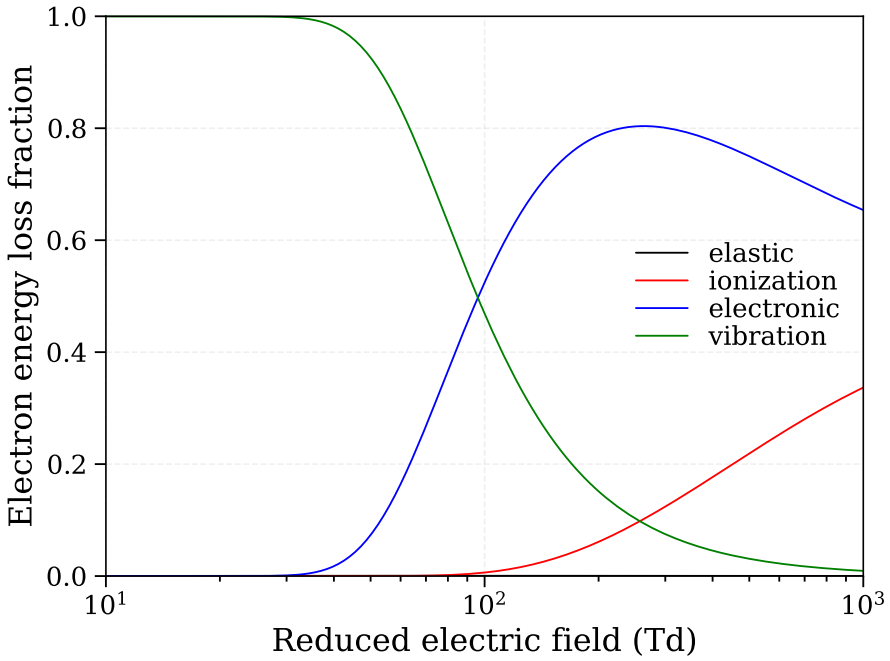

Figure 2-10. Electron energy loss fraction in pure CO_2 vs reduced electric field. Up to 50 Td, the energy mostly goes to the vibration. Above 100 Td, the electronic state excitation dominates, while the ionization grows significantly. Calculated using BOLOS (Luque 2014) with cross-sections from IST-Lisbon database (Grofulović, Alves, and Guerra 2016; IST-Lisbon).

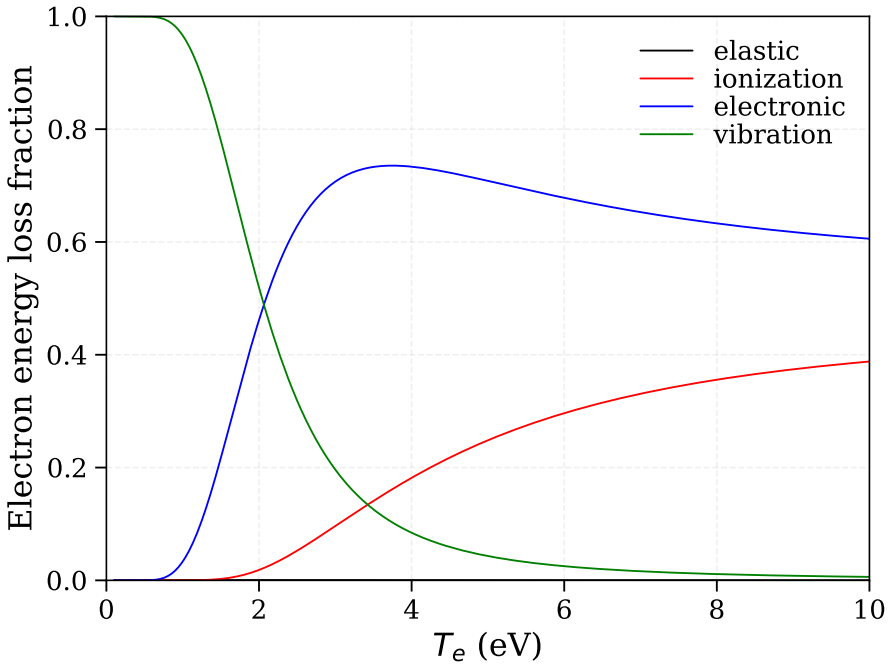

Figure 2-11. Electron energy loss fraction vs T_e. Up to 1 eV, the energy mostly goes to the vibration. Above 2 eV, the electronic state excitation dominates, while the ionization grows significantly.

We now calculate the energy efficiency of "pure" electronic dissociation, i.e. assuming the released heat and O atoms are lost (i.e. not reused). As defined in Sec. 2.1.1, the energy

efficiency is $\eta = \Delta_r H^\circ / E_{CO}$ with $\Delta_r H^\circ = 2.93$ eV, and E_{CO} The energy cost to produce one CO molecule.

We showed in Sec. 2.3.1.1 that all CO_2 electronic states pre-dissociate after electron-impact excitation. Hence, the dissociation rate equals the excitation rate. The energy cost to produce one CO molecule by electron-impact dissociation is the power lost by the electrons in inelastic and elastic processes divided by the rate of electron-impact dissociation. In pure CO_2 we obtain:

$$E_{CO} = \frac{\left(\sum_i E_{th,i} \cdot k_i + \frac{2m_e}{m_{CO2}} \cdot \int \varepsilon \cdot \sigma_{elast}(\varepsilon) \cdot f(\varepsilon) \sqrt{\frac{2\varepsilon}{m_e}} d\varepsilon\right) \cdot n_e n_{CO_2}}{k_{elec} \cdot n_e n_{CO_2}} \qquad \text{Eq. 2-6}$$

where $E_{th,i}$ and k_i are the energy threshold and rate constant for the inelastic process i, m_e and m_{CO2} are the electron and CO_2 masses, σ_{elast} is the elastic collision cross-section, $f(\varepsilon)$ the EEDF, n_e, n_{CO2} the number densities of electrons and CO_2, and k_{elec} is the rate of excitation toward the 7 and 10.5 eV electronic states. We use BOLOS and the cross-section from the IST-Lisbon database (Grofulović, Luís L Alves, and Guerra 2016; IST-Lisbon) to compute the EEDF in pure CO_2 (as in Figure 2-9), and the rate constants k_i. We plot in Figure 2-12 the energy efficiency of the pure electronic dissociation. The EE reaches a maximum value of 25% at 200 Td.

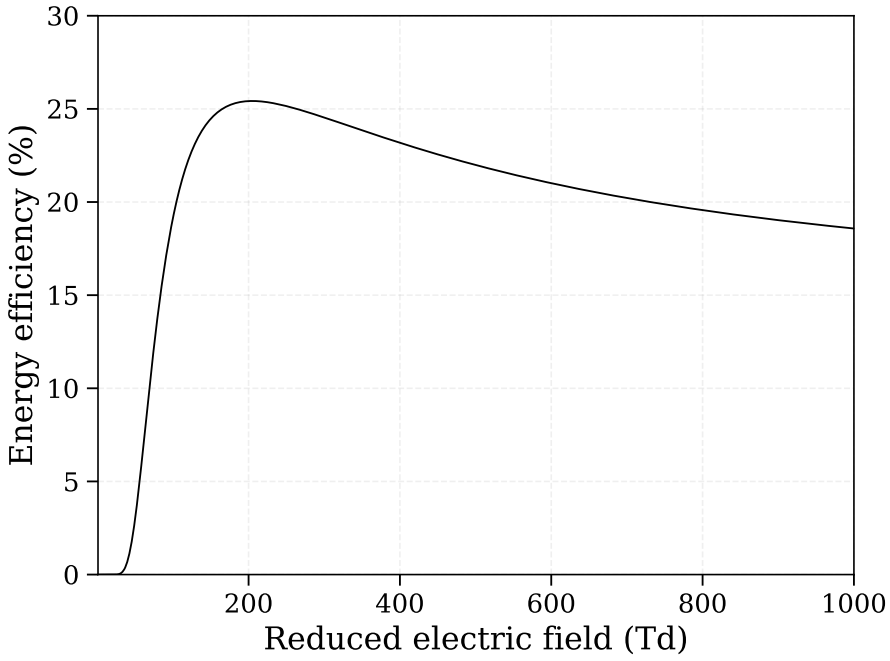

Figure 2-12. Energy efficiency of CO production via the pure electronic mechanism (i.e. via electron-impact excitation of CO_2 to the 7 and 10.5 eV electronic states, followed by predissociation). Cross-section data are from IST-Lisbon.

2.3.1.3 Mixed electronic-vibrational pathway

Electronic excitation can also happen from a vibrationally excited state:

$$CO_2(v) + e^- + x\ eV \ \rightarrow\ CO_2(1^3B_2) + e^- \qquad \text{Reac. 16}$$

This process can be beneficial in two ways:

(i) The energy stored in the molecule vibration lowers the dissociation barrier accordingly. This effect is taken into account by the Fridman-Macheret α-model (Fridman 2008). Thus, electrons with less than 8 eV energy can still excite $CO_2(1^3B_2)$, i.e., a larger part of the EEDF is used. Considering this effect allows improvements compared to Figure 2-12. However, as the total energy needed to excite $CO_2(1^3B_2)$ does not change (it is the sum of the energy required to excite CO_2 vibrationnally plus the energy required to dissociate the excited vibrational level), the EE is still capped by the mono-kinetic case ($\eta \leq 35\%$).

(ii) The vibrational excitation shifts the Franck-Condon region to the right of the potential energy curves. As can be seen in Figure 2-8, the vertical energy of $CO_2(1^3B_2)$ slightly decreases with increasing O-CO distance. Therefore, the energy barrier reduction is larger than the input vibrational energy. This could theoretically improve the energy efficiency. However, the improvement is marginal at moderate vibrational excitation. At high vibrational excitation, the improvement could be significant, up to the EE of vibrational dissociation, which we will study in Sec. 2.3.2. Also, a shifted Franck-Condon region could lead to a potential energy well, thus preventing dissociation (see Figure 2-8 $r_1 = 2.4\ a_0$, and the PES of Schmidt et al. 2013). Usually, the shift of the Franck-Condon region is not taken into account in the models. Anyway, it is unlikely that it would help beat the mono-kinetic case EE significantly.

2.3.1.4 Summary of the electronic pathway

To summarize, we have shown that the EE of "pure electronic dissociation", which names the dissociation following the electron-impact excitation of CO_2(X) to CO_2 electronic states, is capped at 25%. This maximum is reached for a reduced electric field of 200 Td. "Mixed electronic-vibrational dissociation" refers to the electron-impact excitation of CO_2(v*) to dissociative CO_2 electronic states. This mechanism could in principle allow to reach higher EE. The new upper limit for the EE would be the upper limit for pure vibrational dissociation (53%, as we will see in the following section).

2.3.2 Pure vibrational dissociation

As explained in Sec. 2.1.2, the vibrational excitation of CO_2(X) up to 5.5 eV can lead to dissociation into CO and O. Since 5.5 eV is also the standard enthalpy of reaction CO_2 + e^-/M → CO + O + e^-/M, it is the minimal energy cost of CO production in step 1 (the

discharge stage). The upper bound for the EE of the pure vibrational pathway (and of step 1) is then: $\eta = 2.9/5.5 = 53\%$. Actually, several factors hinder the EE.

2.3.2.1 Energy efficiency limitations

Let us consider a system composed of CO_2 molecules subjected to an electric field. Here we present some of the limitations for the EE of the pure vibrational pathway.

Electron energy loss fraction

First, as in the electronic case, only a fraction of the energy of the electrons goes to vibrational excitation. According to Figure 2-10, vibrational excitation dominates at low reduced electric field: near 100% of the electrons energy goes to the vibration for $E/N \leq$ 50 Td. When the reduced electric field exceeds 100 Td, vibration excitation is overcome by electronic excitation. In the case of a Maxwellian distribution, Figure 2-11 shows identical behavior as a function of the electron temperature: below 1 eV, the energy fraction loss to vibration is close to 100%, and it is overcome by electronic excitation above 2 eV.

Vibrational-Translational (VT) relaxation

Second, the energy will not stay in the vibrational modes forever. Part of the vibrational energy ends up in gas heating: this is vibrational-translational (VT) transfer, the central loss mechanism in the pure vibrational pathway.

To achieve the ideal 53% EE promised by the pure vibrational pathway, dissociation processes must be much faster than VT. There are basically two ways of climbing the vibrational ladder up to the dissociation limit: either by electron-impact excitation (e-V) (Reac. 1) or by vibrational-vibrational (VV) pumping. In Sec. 2.3.2.2, 2.3.2.3, and 2.3.2.4, we will compare the speed of these two reactions with VT reactions.

2.3.2.2 Characteristic time of VT relaxation

CO_2 has 3 vibrational modes: symmetric stretch, asymmetric stretch, and bending. In this thesis, we will refer to these modes with the quantum number v_1 for the symmetric stretch, v_2 for the bending, and v_3 for the asymmetric stretch. A given vibrational state of CO_2 is written $CO_2(v_1\ v_2\ v_3)$.

We want to estimate the characteristic time of VT relaxation. The symmetric stretch and bending modes are known to relax much faster with the translation than the asymmetric stretch modes (Dubuet, Pannier, and Laux 2022; Klarenaar et al. 2017; Ana Sofia Morillo-Candas, Guerra, and Guaitella 2020; Pannier 2019). VT nonequilibrium is easier to achieve for the asymetric stretch mode.

Thus, we consider the rate of relaxation of the first excited state of the asymmetric stretch mode $CO_2(001)$. Most CO_2 plasma kinetic models use the rates of (BLAUER and NICKERSON 1974), following the approach of (Kozák et al. 2014). Kozak *et al.* considers three relaxation reactions for $CO_2(001)$, namely toward $CO_2(010)$, $CO_2(020)$, and $CO_2(030)$. Weighting the rates of these reactions with their heat release (0.21, 0.13, and 0.04 eV, respectively), we find that $CO_2(001) + M \rightarrow CO_2(020) + M$ is the reaction that contributes the most to heating. The rate constant of this reaction given in (Blauer and Nickerson 1974) is:

$$CO_2(001) + M \rightarrow CO_2(020) + M$$
$$k_{VT} = 8.57 \cdot 10^{-1} \exp\left(-404 \cdot T_g^{-\frac{1}{3}} + 1096 \cdot T_g^{-\frac{2}{3}}\right) \qquad \text{Reac. 17}$$

We use this reaction to estimate the characteristic time of energy depletion by VT relaxation, τ_{VTD}. This time will be compared with the characteristic times of vibrational-vibrational and electron-vibrational excitation up to the dissociation limit. With $E_a^{diss} = 5.5\ eV$, the energy barrier for vibrational dissociation, the time needed by a CO_2 molecule to lose 5.5 eV via VT is calculated as:

$$\tau_{VTD} = (k_{VT} \cdot n_{tot})^{-1} \cdot \frac{E_a^{diss}}{(w_3 - 2w_2)} \qquad \text{Eq. 2-7}$$

with n_{tot} the total number density of the gas, w_2 and w_3 the bending and asymmetric stretch energy quanta in the harmonic approximation (w_2 = 667.47 cm^{-1} = 0.08 eV, w_3 = 2349.16 cm^{-1} = 0.29 eV). The energy lost to the translation is the difference between the vibrational energies of the reactants and the products, i.e. $w_3 - 2w_2$. τ_{VTD} is plotted against temperature and at atmospheric pressure in Figure 2-14. It is above 10 ms at 300 K, approximately 40 µs at 1000 K, and below 1 µs above 2000 K. Note that this is a lower bound of the energy relaxation time by VT transfer since we only considered relaxation to $CO_2(020)$. It is sufficient to draw conclusions from the comparisons presented in Figure 2-14.

2.3.2.3 Vibrational-vibrational dissociation (VVD) pathway

To estimate the characteristic time of dissociation via VV collisions, we compute the diffusion along the vibrational energy ladder by simulating the Brownian motion along this axis. We follow the journey of a $CO_2(v)$ molecule on the vibrational ladder. To simplify, we only consider the asymmetric stretch mode. At each VV collision, the molecule has a chance to go up or down. We make the simple assumption that these events are equiprobable. If the molecule begins at (or falls to) $v = 0$, it can only go up. When it reaches $v = 21$, dissociation ends the journey. Using a simple algorithm, we can simulate this journey and estimate the average number of collisions necessary to go from a given vibrational level to dissociation.

To deduce the characteristic time of dissociation, we estimate the VV rate constant by considering only the VV transfer of the asymmetric mode, which is known to be the fastest one. The fundamental process and its usual rate (in cm^3/s) (BLAUER and NICKERSON 1974) are:

$$CO_2(0,0,0) + CO_2(0,0,1) \rightarrow CO_2(0,0,1) + CO_2(0,0,0)$$
$$k_{VV} = 1.32 \cdot 10^{-10} \left(\frac{T_g}{300}\right)^{0.5} \cdot \frac{250}{T_g} \qquad \text{Reac. 18}$$

As in (Kozák et al. 2014), the rate constant for higher vibrational levels is scaled using the Schwartz, Slawsky, and Herzfeld (SSH) model. Hence, we get the rates $k_{VV}(v)$ for the reactions:

$$CO_2(0,0,v) + CO_2(0,0,1) \rightarrow CO_2(0,0,v+1) + CO_2(0,0,0) \qquad \text{Reac. 19}$$

Some of these rates are reported in Figure 2-13.

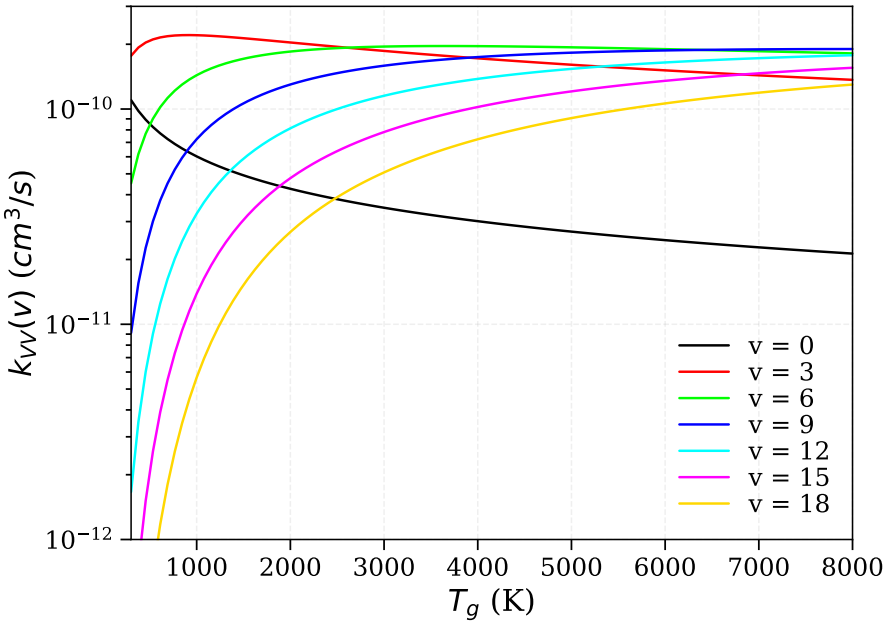

Figure 2-13. Rate constants of VV exchange along the asymmetric stretch mode $CO_2(0,0,v) + CO_2(0,0,1) \rightarrow CO_2(0,0,v+1) + CO_2(0,0,0)$ (Reac. 19). Original data from Blauer 1974, scaled with SSH model.

Thus, depending on its height on the ladder, a molecule will take more or less time to climb a step. Theoretically, k_{VV} also depends on the excitation level of the collider: $k_{vv}(v_{target}, v_{collider})$. In the vibrational temperature range investigated here (below 5000 K), the population quickly decreases with the vibrational quantum number v. Hence, in our order of magnitude calculation, we take the same rate for all colliders, i.e., we assume they all are in $v = 1$. Looking at the rates for:

$$CO_2(0,0,v) + CO_2(0,0,2) \rightarrow CO_2(0,0,v+1) + CO_2(0,0,1) \qquad \text{Reac. 20}$$

$$CO_2(0,0,v) + CO_2(0,0,3) \rightarrow CO_2(0,0,v+1) + CO_2(0,0,2) \qquad \text{Reac. 21}$$

we estimate that the error induced by this assumption is less than 50%.

Finally, the characteristic time of one VV exchange along the asymmetric stretch mode, τ_{VV}, is:

$$\tau_{VV}(v, T_v, T_g, P) = \left(k_{VV}(v, T_g) \cdot n_{v\geq 1}(T_v, T_g, P)\right)^{-1} \qquad \text{Eq. 2-8}$$

where $k_{VV}(v)$ is the v-dependent VV exchange rate constant (of Figure 2-13) and $n_{v\geq 1}$ is the number density of the states with at least one vibrational quantum. τ_{VV} depends on the vibrational distribution function (VDF) $f(v, T_v)$ – that we assumed to be Boltzmann for this order of magnitude calculation – and the total density n_{tot} (calculated from T_g and P):

$$n_{v\geq 1} = n_{tot} \cdot (1 - f(v = 0, T_v)) \qquad \text{Eq. 2-9}$$

Finally, the characteristic time of dissociation following VV transfer is:

$$\tau_{VVD} = \left\langle \sum_{coll}^{n_{coll}} \tau_{VV}(v_{coll}) \right\rangle \qquad \text{Eq. 2-10}$$

n_{coll} being the number of collisions resulting in dissociation. Because each journey is different, τ_{VVD} is an average of many of them. We run our script for T_g in the [300, 5000] K range, and T_v in the [2000, 10000] K range. At each temperature point, τ_{VVD} is averaged over 500 runs. On average, it takes 400-500 VV collisions to go from v=0 to dissociation.

The resulting τ_{VVD} at atmospheric pressure are plotted along with τ_{VTD} in Figure 2-14. For $T_g \leq 1000\ K$, VV transfer is much faster than VT transfer: VV build-up can occur with negligible gas heating, and nonequilibrium conditions may be achieved. At $T_g \approx 1500\ K$, $\tau_{VTD} \approx 5\ \mu s$, and $\tau_{VVD} \approx 1 - 2\ \mu s$ for T_v between 5000 and 10,000 K. VT transfer is on the order of VV transfer, thus a significant amount of energy goes to gas heating. For $T_g \geq 2000\ K$, τ_{VTD} decreases below 1 µs and VT is faster than VV transfer. At lower pressure, τ_{VVD} and τ_{VTD} will be higher (for example, 100 times higher at 0.01 bar), but their ratio will stay the same (they are both proportional to the total density).

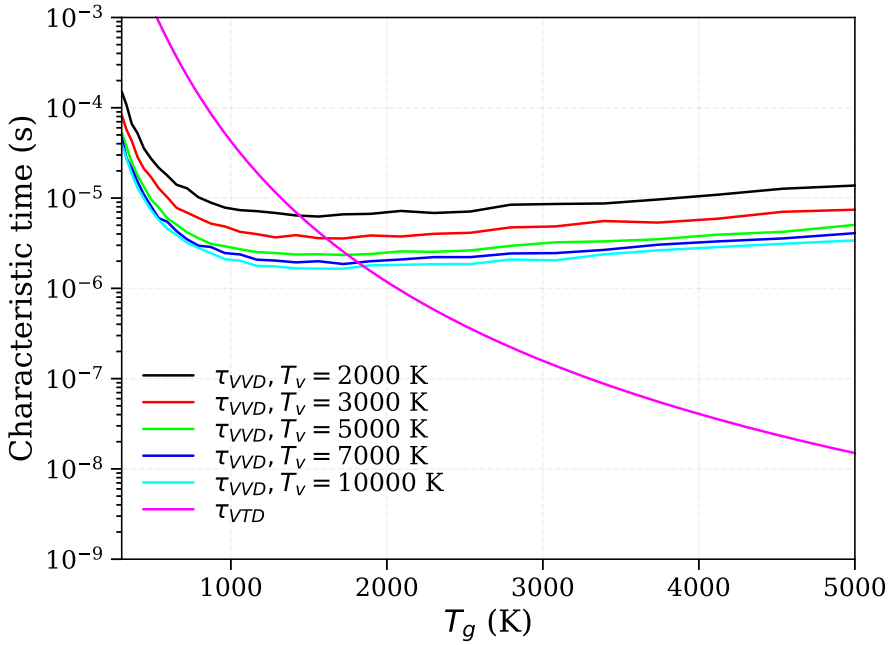

Figure 2-14. Comparison of VV dissociation and VT energy-depletion characteristic times in CO_2 at P_{atm} and their evolution with the gas temperature.

2.3.2.4 Electron-induced vibrational dissociation (eVD)

Electron-impact excitation of the vibrational modes of CO_2 is essential in two ways: (i) it fosters vibrational build-up to the dissociation limit through repeated electron-impact excitations; (ii) it can produce the high vibrational temperatures that are necessary for VV build-up , as shown in the previous subsection.

We define τ_{eVD} as the characteristic time for electron-impact excitation of a vibrational level multiplied by the number of steps needed to reach the dissociation asymptote. (i) is achieved for $\tau_{eVD} \ll \tau_{VTD}$. (ii) imposes than $\tau_{eVD} \leq \tau_{VVD}$. Indeed, if $\tau_{eVD} > \tau_{VVD}$, VV-dissociation drains the vibrational levels faster than eV-excitation fills them, lowering T_v. A lower T_v implies a slower VV-dissociation (Figure 2-14) (τ_{VVD} is monotonic with T_v), thus leading to $\tau_{eVD} = \tau_{VVD}$. To achieve efficient CO_2 dissociation via the vibrational modes, one dissociation mechanism or the other must be quicker than VT losses, while $\tau_{eVD} \leq \tau_{VVD}$ is verified. Thus, the necessary and sufficient condition is:

$$\tau_{eVD} \ll \tau_{VTD} \qquad \text{Eq. 2-11}$$

or equivalently in terms of collision frequency:

$$\nu_{eVD} \gg \nu_{VTD} \qquad \text{Eq. 2-12}$$

To compute τ_{eVD}, we start from the IST-Lisbon database (Grofulović, Luís L. Alves, and Guerra 2016) for CO_2 and weigh each vibrational cross-section by E_a^{diss}/E_{vcs}^{th}, E_{vcs}^{th} being the threshold energy of cross-section *vcs* (*vcs* stands for vibrational cross-section). For

example, for the single quantum jump along the asymmetric stretch mode, $E_a^{diss}/E_{vcs}^{th} = 5.5/w_3 = 19$: it takes 19 excitation iterations to dissociate via this channel[6]. Hence, τ_{eVD} is expressed as:

$$\tau_{eVD} = \left(n_e \cdot \sum_{vcs} k_{eV,vcs} \cdot \frac{E_{vcs}^{th}}{E_a^{diss}} \right)^{-1} \qquad \text{Eq. 2-13}$$

where $k_{eV,vcs}$ is the rate constant for the electron-impact excitation obtained with the vcs cross-section, n_e the electron density, and $E_a^{diss} = 5.5\ eV$ is the energy barrier for vibrational dissociation (defined earlier). Finally, combining with Eq. 2-7, we obtain the ratio of the VT and eV characteristic times:

$$\frac{\tau_{VTD}}{\tau_{eVD}} = \frac{\sum_{vcs} k_{eV,vcs} \cdot E_{vcs}^{th}}{k_{VT} \cdot (w_3 - 2w_2)} \cdot \alpha_i \qquad \text{Eq. 2-14}$$

where α_i is the ionization degree of the plasma. The ratio evolution with gas temperature and ionization degree is mapped in Figure 2-16 and Figure 2-17 for $E/N = 30$ Td and $E/N = 100$ Td, respectively.

At $E/N = 30$ Td, the electron energy loss to vibration is 100% (see Figure 2-10), so no energy is lost to other modes. Figure 2-16 shows that, as the gas temperature increases, the electron density must be higher to sustain efficient dissociation. At 300 K, $\tau_{eVD} \ll \tau_{VTD}$ is satisfied for $\alpha_i \geq 2 \cdot 10^{-7}$, at 1000 K for $\alpha_i \geq 3 \cdot 10^{-5}$, and at 2000 K for $\alpha_i \geq 10^{-3}$.

At $E/N = 100$ Td, the electron energy loss to vibration is 50% (Figure 2-10), but as can bee seen in Figure 2-15, the rate constant of vibrational exciation reaches its maximum. Thus, according to Figure 2-17, $\tau_{eVD} \ll \tau_{VTD}$ is satisfied for $\alpha_i \geq 1 \cdot 10^{-7}$ at 300 K, for $\alpha_i \geq 2 \cdot 10^{-5}$ at 1000 K, and for $\alpha_i \geq 5 \cdot 10^{-4}$ at 2000 K.

Fridman (Fridman 2008) also put forward an ionization degree threshold to be surpassed to activate vibrational dissociation: $\alpha_i \geq 3 \cdot 10^{-7}$. According to our own analysis, this threshold is adequate for ambient temperature plasma. At temperature above 1000 K, a high ionization degree must be sustained to make the vibrational dissociation much faster than the VT losses. We will see in Sec. 2.4 that these conditions are challenging to achieve in practice.

[6] For this ponderation, we used the vibrational energies of the harmonic oscillator. With the anharmonic oscillator energies, the dissociation occurs for $v_3 \geq 21$. This makes little difference for our order of magnitude calculation.

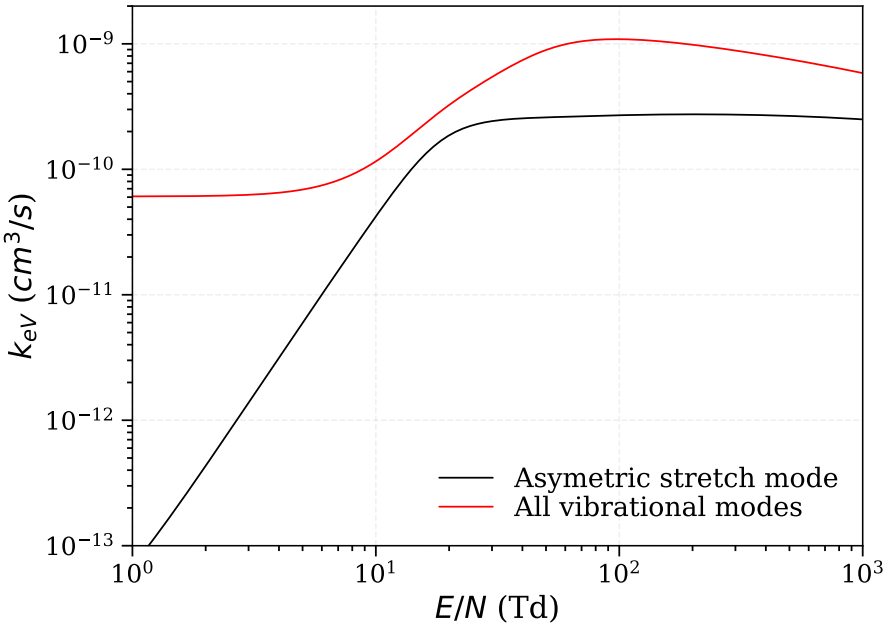

Figure 2-15. Rate constant of electron-impact excitation of the vibrational modes as a function of the reduced electric field. The rate constants are weighted by E_{th}/E_a^{diss}, E_{th}^{vcs} being the energy threshold for the mode *vcs*. In red we plot the rate constant for the grouping of all vibrational mode: $\sum_{vcs} k_{eV,vcs} \cdot E_{th}/E_a^{diss}$.

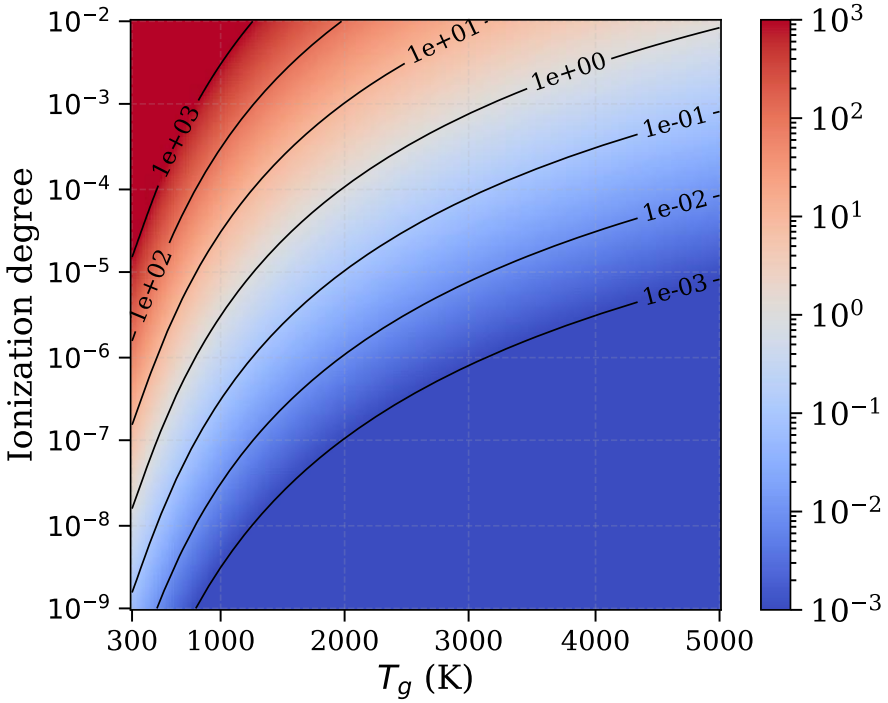

Figure 2-16. Ratio of the VTD and eVD characteristic times as a function of temperature and ionization degree, at E/N = 30 Td.

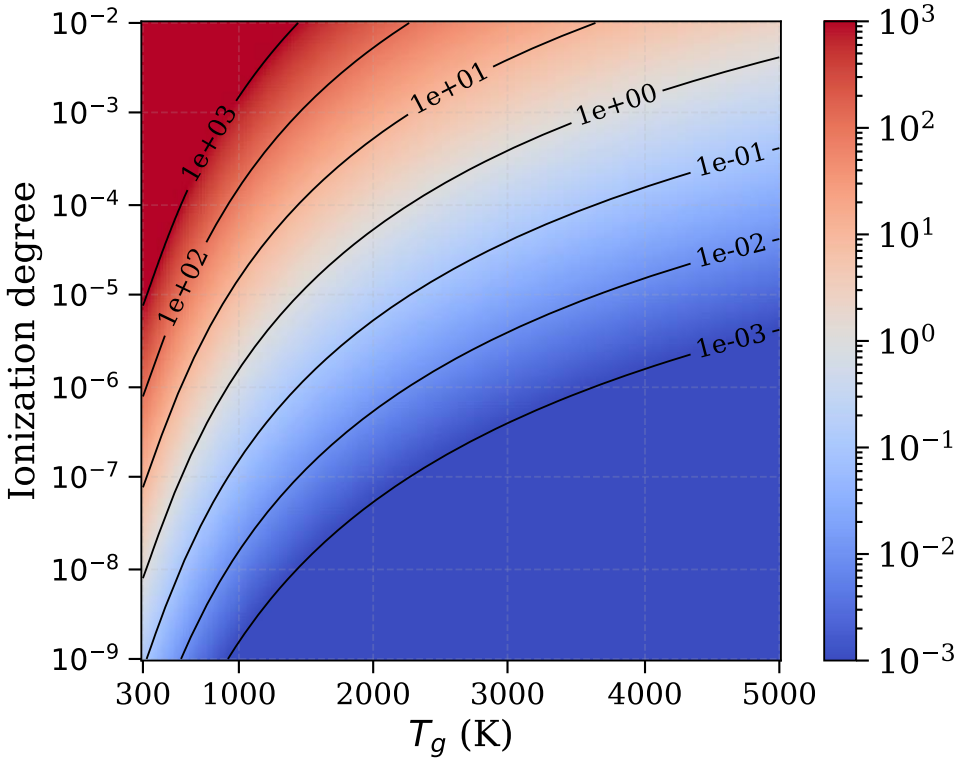

Figure 2-17. Ratio of the VTD and eVD characteristic times as a function of temperature and ionization degree, at E/N = 100 Td.

2.3.2.5 Summary of the vibrational pathway

To summarize, the EE limit of 53% for the pure vibrational dissociation mechanism can only be achieved if VT transfer can be limited. We showed that this is only possible at low gas temperature and high ionization degree (see Figure 2-16 and Figure 2-17).

2.3.3 Thermodynamic equilibrium approach

We continue our study of the discharge stage (step 1 in Figure 2-7) by determining the EE of CO dissociation by a thermal process at various pressures.

We compute the LTE mole fractions using Cantera, a Gibbs's energy minimization code (Goodwin, Moffat, and Speth 2017)). The thermodynamic data are taken from NASA-CEA (McBride, Zehe, and Gordon 2002). Results are shown in Figure 2-18 for 3 different pressures. CO begins to appear around 1500 K at 0.01 bar and 2000 K at 1 bar. Full CO_2 dissociation is achieved at about 3500 K at 0.01 bar and 4500 K at 1 bar. Beyond 5000 K, CO starts to dissociate into C and O.

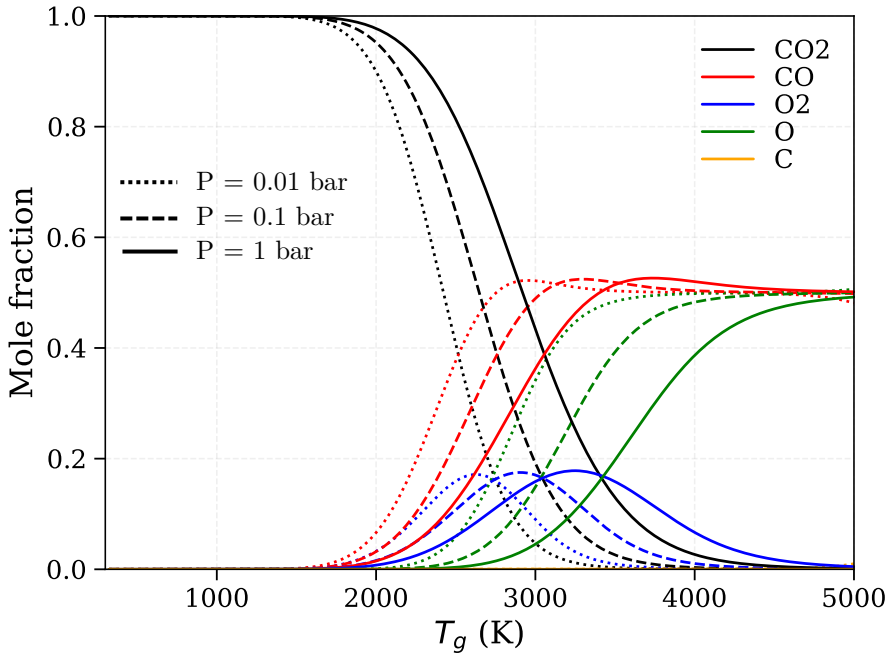

Figure 2-18. Main species mole fractions in a CO_2 gas at thermodynamic equilibrium and a pressure of 1 bar (solid line); 0.1 bar (dashes) ; 0.01 bar (dots).

The energy cost of CO production at a given temperature T is given by the enthalpy difference between the mixture at LTE and T and CO_2 in standard conditions:

$$E_{cost} = h(P,T) - h(P,T_0) \qquad \text{Eq. 2-15}$$

where $h[J/kg]$ is the specific enthalpy, P the pressure, and T_0 the ambient temperature. The amount of CO produced in the heating process times $\Delta_r H°$ (the standard enthalpy of reaction for the global dissociation reaction) is the useful energy. Its ratio to the energy cost yields the EE η_{LTE}:

$$\eta_{LTE}(P,T) = \frac{\frac{y_{CO}}{M_{CO}} \cdot N_a \cdot \Delta_r H°}{E_{cost}} \qquad \text{Eq. 2-16}$$

with $y_{CO}(P,T)$ the CO mass fraction in a gas in LTE at (P, T), $M_{CO}[kg/mol]$ the CO molar mass, and N_a the Avogadro number.

The resulting EE map is shown in Figure 2-19. The EE can exceed 50% below 0.1 bar and at $T_g = 2600 - 3000\ K$. At atmospheric pressure, a maximum EE of 48% is reached at $T_g = 3300\ K$. At 10 bar, the maximum EE is 45%, and is reached at $T_g = 3800\ K$. At 100 bar, it is 42%, reached at $T_g = 4400\ K$. In the following, we will refer to these EEs as the "EE thermodynamic limit".

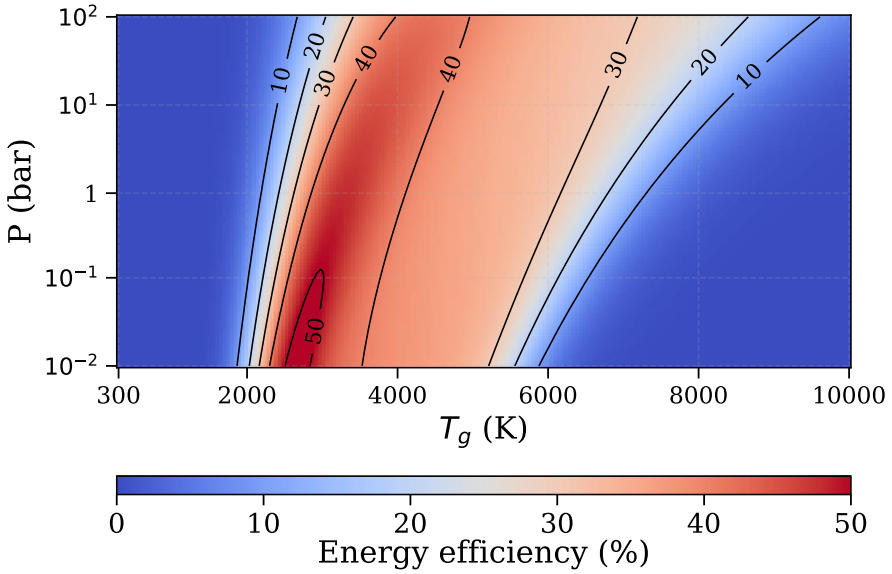

Figure 2-19. EE map of conversion of CO_2 in LTE.

2.3.4 Quenching scenarios

In the last three sections (2.3.1, 2.3.2, and 2.3.3), we studied illustrative cases of the discharge stage (step 1), assuming that the products are frozen. We have pointed out that the EE of the electronic and vibrational pathways alone is capped at 35% and 53%, respectively, while the EE of an LTE heating is between 42% at 100 bar and 52% at 0.01 bar. In any case, the EE cannot exceed 53%, and a thermodynamic process can be almost as close to this limit as the pure vibrational pathway.

However, once CO and O are formed, several reactions can occur. Moreover, the desired product is not highly energetic CO, but CO at room temperature. The mixture must cool down, which also has impact on the kinetics. In the worst-case scenario (in terms of CO production at the end of the whole process), CO and O recombine to CO_2 after collision with a third body (Reac. 6: CO + O + M → CO_2 + M). Otherwise, the O atom can recombine with another O atom and form O_2 (Reac. 22: O + O + M → O_2 + M). In the best-case scenario, the O atom is recycled in dissociating another CO_2 molecule (Reac. 7: CO_2 + O → CO + O_2). The hypothetical scenario where every O atom ends up in an O_2 molecule, leaving the CO density intact, is called **absolute quenching** (AQ). This is the scenario that we implicitly assumed in the previous sections. The scenario where every O atom produces an additional CO is called **super-ideal quenching** (SIQ) (Fridman 2008). In Section 2.3.5, we will evaluate the feasibility of recycling the O atoms in additional CO, which is the major step of the SIQ scenario. In the next subsection, we evaluate the cooling rate needed to achieve AQ.

Freezing temperature of CO

According to thermodynamics mole fractions (Figure 2-18), for a pressure of 0.01 bar, CO begins to overcome CO_2 for $T > 2500$ K. At atmospheric pressure, this occurs for $T > 3000$ K. Thus, below these temperatures, CO will spontaneously recombine to CO_2. Hopefully, in the presence of O_2, CO recombination to CO_2 is kinetically frozen below a certain threshold. Using the kinetics model of GRI-mech (Smith et al. 1999), we calculate the time needed to recombine 1% of a CO + ½ O_2 mixture as a function of the temperature. At 0.01 bar, we obtain that this time is longer than 1 hour for $T_g < 1000$ K. At 1 bar, it is longer than 1 hour for $T_g < 800$ K. Thus, for a pressure between 0.01 and 1 bar, a mixture of CO and O_2 will be considered frozen below 800 K.

On the other hand, let us point out that even at 300 K, a mixture of O atoms and CO is not frozen. Computing the kinetics of an adiabatic system composed of 50% CO, and 50% O, at 1 bar and an initial temperature of 300 K, shows fast O-O and O-CO 3-body recombination. These reactions are highly exothermic and heat the gas up to 3600 K at a heating rate of about 10^7 – 10^8 K/s. As a consequence, even if it was obtained in a cold plasma, a mixture of CO and O has to be cooled down, just as a thermal plasma.

Absolute Quenching (AQ)

To prevent recombination and achieve the **absolute quenching** scenario, the products must be quenched as quickly as possible from 3000 K to 800 K (2500 K to 1000 K at 0.01 bar).

We evaluate the cooling rate needed to achieve AQ at atmospheric pressure. We assume that a plasma process fully converts CO_2 into CO and O at pressure P and gas temperature T. Non-thermal plasmas can convert CO_2 at low temperatures, so T can take different values. We use the rates from GRI-Mech (Smith et al. 1999) to simulate the kinetics at different cooling rates and initial temperatures. The simulation stops at $t = 3600$ s, which is the threshold beyond which the gas is considered frozen.

In Figure 2-20 and Figure 2-21, we report the fraction of CO amount remaining after the cooling phase over the CO amount that was initially produced, for $P = 0.01$ bar and $P = 1$ bar. The main conclusions are: (i) lower cooling rates are needed for low temperature; (ii) whatever the plasma temperature, preservation of more than 95% of the CO produced requires cooling rates above 10^5 K/s = 0.1 K/µs at 0.01 bar, and 10^9 K/s = 1000 K/µs at 1 bar.

These cooling rates are challenging to achieve in practice, in particular because the recombination kinetics is highly exothermic (for example, O + O + M → O_2 + M releases 5.2 eV of energy).

As a comparison, let us estimate the cooling time in an industrial shell and tube heat exchanger at 1 bar. The heat transfer coefficient h is considered to be about 1000 W/m^2/K, which is an upper value for heat transfer. The radius of the tube is $r = 1\ cm$. The cooling rate of a cylindrical system filled with hot CO_2 at a few thousand kelvins is $dT/dt \sim 2h/(\rho c_p r)\ \cdot \Delta T$ where ρ and c_p are the mass density and mass enthalpy of the CO_2 mixture, and ΔT is the temperature gap with the cooling fluid. For CO_2 at 3000 K and a coolant at 300 K, we obtain $dT/dt \sim 10^6\ K/s$. This is much lower than the 10^9 K/s needed to prevent CO losses. The quenching of the products is one of the key issues to consider when evaluating plasma technology.

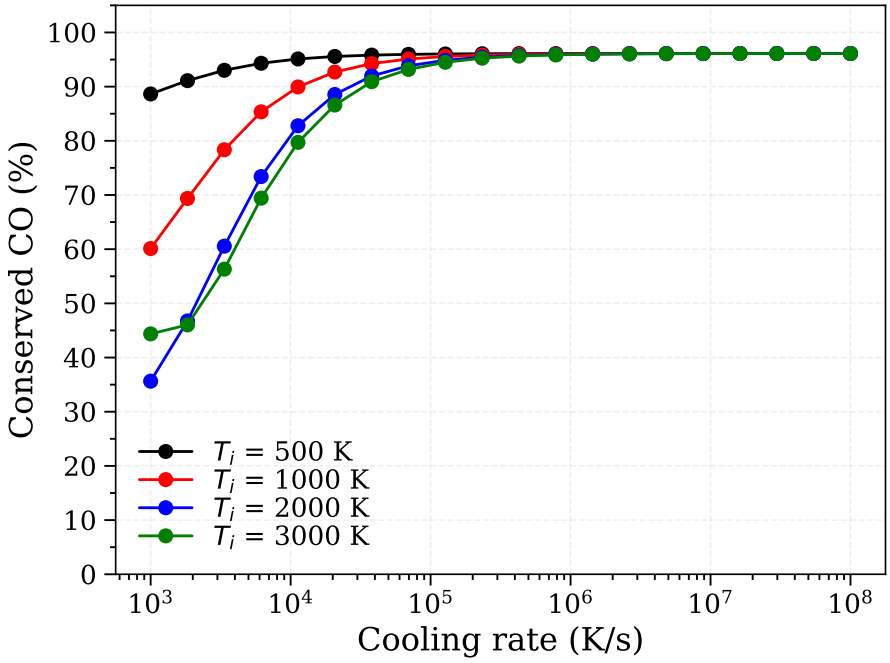

Figure 2-20. Fraction of remaining CO after the cooling of a O-CO mixture at T_i as a function of the cooling rate, at $P = 0.01$ bar. Whatever the plasma temperature, more than 95% of the CO is preverved for cooling rates above 10^5 K/s.

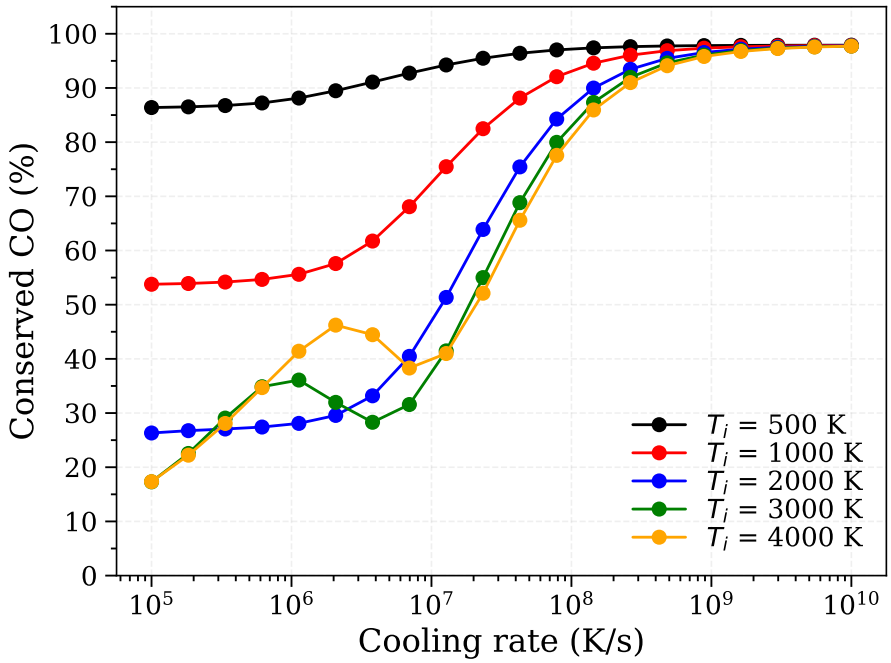

Figure 2-21. Fraction of remaining CO after the cooling of a O-CO mixture at T_i as a function of the cooling rate, at $P = 1$ bar. Whatever the plasma temperature, more than 95% of the CO is preverved for cooling rates above 10^9 K/s.

2.3.5 Oxygen recycling

The oxygen atoms, considered lost in sections 2.3.1, 2.3.2, and 2.3.3, can actually react with CO_2 to form additional CO (Reac. 7). We define "O recycling" as the utilization of the chemical energy of the remaining O atoms by an overproduction of CO via the O-CO_2 association reaction. Since O-CO_2 association has a low reaction enthalpy, this overproduction decreases the overall energy cost for CO production, i.e. increases the energy efficiency.

If every O atom produces a CO molecule and no CO molecule is lost, we are in the super-ideal quenching (SIQ) scenario. In Sec. 2.3.5.1, we estimate the increase in EE enabled by the SIQ. In Sec. 2.3.5.2, we compare the rate of the O-CO_2 association reaction with other O-consuming reactions. Then, in Sec. 2.3.5.3 and 2.3.5.4, we use simple kinetic models to assess the feasibility of O recycling at thermal equilibrium and its potential enhancement by vibrational excitation. In Sec. 2.3.5.5, we discuss the potential enhancement of O recycling by electronic excitation. In Sec. 2.3.5.6, we summarize and discuss the limitations of our calculations.

2.3.5.1 Energy efficiency enhancement in the super-ideal quenching (SIQ) scenario

Here, we estimate the upper bound of the EE of the pure electronic pathway, pure vibrational pathways, and LTE heating, followed by SIQ.

Pure electronic and pure vibrational pathways followed by SIQ

To illustrate the potential gains offered by SIQ, we consider monokinetic processes, where all the energy is channeled in the desired mechanism.

We consider the system formed by an electron and two CO_2 molecules. For the pure electronic pathway, 8.3 eV is transferred to the electron. The electron collides with CO_2, exciting it to $CO_2(1^3B_2)$ (Reac. 3: $CO_2 + e^- + 8.3\ eV \rightarrow CO_2(1^3B_2) + e^-$). The predissociation of $CO_2(1^3B_2)$ releases 2.8 eV (Reac. 4: $CO_2(1^3B_2) \rightarrow CO + O + 2.8\ eV$). Let us imagine that the O atom collides with the second CO_2 molecule and uses the 2.8 eV to overcome the activation barrier of O-CO_2 association (Reac. 7: $CO_2 + O \rightarrow CO + O_2$). An additional CO molecule is produced. The EE of CO production is $\eta = 2 \cdot \Delta_r H°/8.3 = 71\%$.

We can imagine a similar scenario for the pure vibrational pathway. If the vibrational dissociation occurs at 5.5 eV, no energy is left to overcome the activation barrier of the O-CO_2 association. Depending on the height of this barrier (poorly know, as mentioned in Sec. 2.1.2), an additional energy between 0.5 and 2.4 eV has to be added to the system. Eventually, the EE of CO production is between $\eta = 2 \cdot \Delta_r H_0/(5.5 + 0.5) = 98\%$ and $\eta = 2 \cdot \Delta_r H_0/(5.5 + 2.4) = 74\%$.

LTE heating followed by SIQ

We consider now the case of CO_2 conversion at LTE. We can update the map of Figure 2-19 assuming SIQ of the products. We calculate the energy efficiency following the approach of (Wolf, Peeters, et al. 2020). The useful enthalpy is the sum of CO and O formation enthalpy. Hence, the EE is the ratio of CO and O formation enthalpy over the total enthalpy of the gas:

$$\eta = \frac{y_{CO}(T_g) \cdot h^f_{CO} + y_O(T_g) \cdot h^f_O}{h(T_g) - h(T_0)} \qquad \text{Eq. 2-17}$$

where y_{CO} and y_O are the CO and O mass fractions, h^f_{CO} and h^f_O the CO and O formation specific enthalpies, and h the total specific enthalpy of the gas. The resulting EE evolution with gas temperature and pressure is mapped in Figure 2-22.

This map suggest thats a process at thermal equilibrium could also overcome 70% EE: this is the “newly defined thermal limit” (Van De Steeg et al. 2021). Such a process would take

place in two stages: (i) a heating phase, where the gas is in LTE, and (ii) a recycling phase, where the gas is in thermal equilibrium but chemical nonequilibrium.

Summary

To summarize, an EE of 53% cannot be exceeded in our discharge stage (step 1), and O recycling in the quenching stage is the only way to overcome this limit. No matter the dissociation pathway in the discharge stage, O recycling could allow to reach EEs above 70%. Therefore, we should focus on finding the conditions that would allow this recycling.

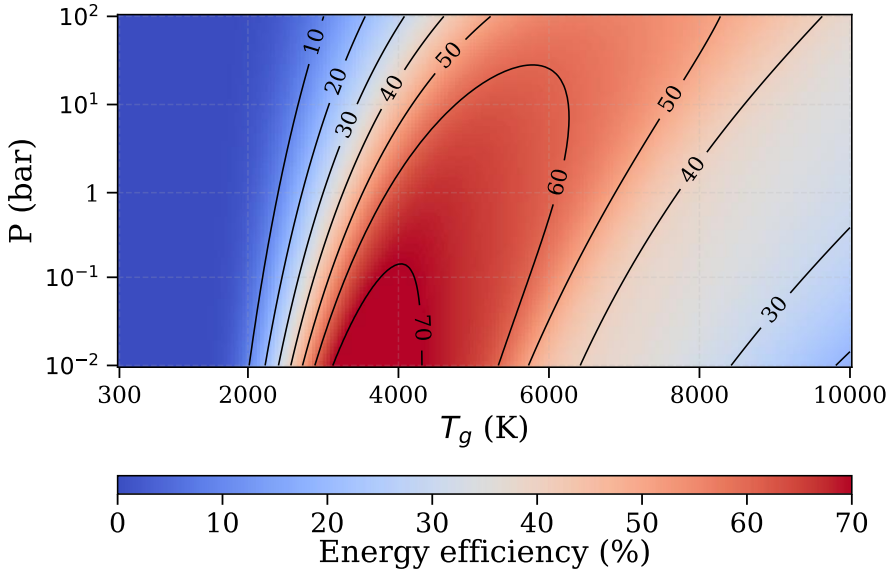

Figure 2-22. EE map of a process at thermodynamic equilibrium, followed by super-ideal quenching.

2.3.5.2 Competition with other O-consuming mechanisms

The O atoms can participate in other reactions than O-CO_2 association, in particular O-O recombination and O-CO recombination:

$$O + O + M \rightarrow O_2 + M \qquad \text{Reac. 22}$$

$$CO + O + M \rightarrow CO_2 + M \qquad \text{Reac. 6}$$

The latter reaction consumes not only O but also CO: it must be avoided to maximise EE.

O atoms are also involved in other reactions, such as recombination to CO (C + O + M → CO + M), neutral exchange (CO + O → C + O_2), electron-impact reactions (O + e^- → O^+ + e^-; O + O + e^- → O_2 + e^-), or charge exchange reactions (such as O + CO_2^+ → O^+ + CO_2). In the conditions investigated in this Chapter (i.e., in cold and warm plasmas, where $T_g \leq 5000\ K$, and conversion degree higher than 10%), these reactions are not expected to deplete the O population signficantly.

Rate constants comparison

We compare in Figure 2-23 the rate constant of O-CO_2 association with those of the 2 detrimental reactions – Reac. 22 and Reac. 6. To allow the comparison, the recombination rate constants are multiplied by the total density of the gas at atmospheric pressure. Different sources are used for each reaction: (Park et al. 1994; Warnatz 1984) for O-CO_2 association, (Tsang and Hampson 1986; Warnatz 1984) and the reverse rates of (Ibragimova et al. 2000; Park et al. 1994) for O-CO recombination, and (Butylkin et al. 1981; Kozàk and Bogaerts 2014; Park et al. 1994; Smith et al. 1999) for O-O recombination. As can be seen in the figure, the O-O recombination rate constants vary considerably between authors. Moreover, they are often deduced from dissociation experiments from the ground state, which may lead to neglecting the recombination toward excited states if the ground and excited states do not stay in partial equilibrium during the dissociation process. As a result, the recombination may be underestimated (Grimaldi 2023). Consequently, we generally use the highest rate reported in the literature, namely that of (Park et al. 1994). At atmospheric pressure and below 2700 K, the 3-body recombination processes dominate. Around 2700 K, O-CO_2 association surpasses O-CO recombination, making the net impact of O atoms positive. Above 3000 K, the O-O recombination rate constant is finally overcome.

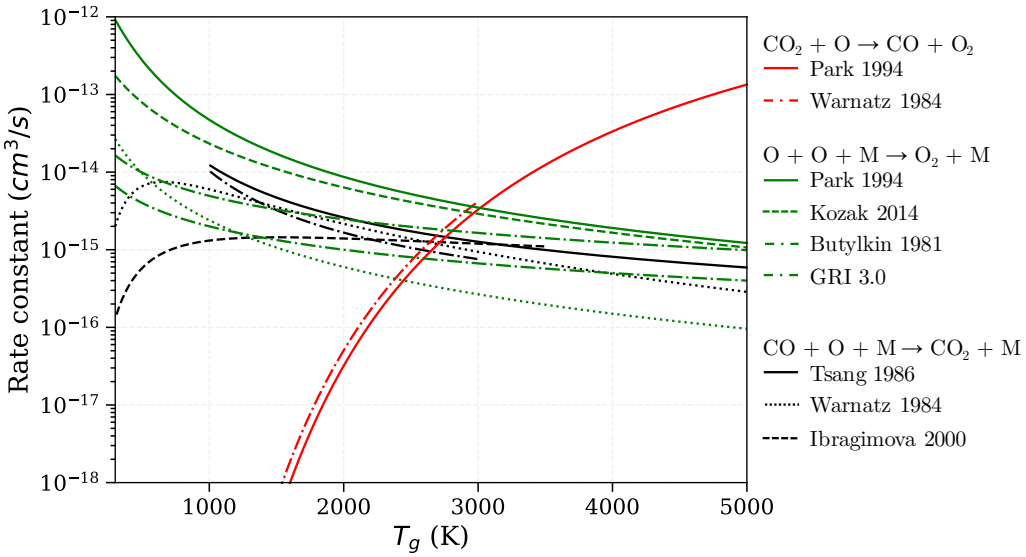

Figure 2-23. Rate constants of O-consuming reactions from different sources. The 3-body rate constants are multiplied by the total number density at P_{atm} and T_g.

The gas temperature is not the only factor determining the utilization of O atoms. The abundance of the colliders in the plasma also plays a role. We map in Figure 2-24 the net CO production rate resulting from the competition between O-CO_2 association and O-CO recombination, as a function of the temperature T_g and conversion degree ϕ. Note that O-O recombination is not considered here as it has a neutral impact on CO production.

Assuming that the O atoms produced by dissociation of CO_2 stay in their atomic form, the conversion degree yields the mole fractions of CO_2 and CO. The perfect gas law yields the total density, which is then multiplied by the mole fractions to obtain the species densities. Using the rate constants of O-CO_2 association and O-CO recombination of (Park et al. 1994), we obtain the rates of O-CO_2 association and O-CO recombination. Their difference yields the net production rate of CO shown in Figure 2-24.

At conversion degree $\phi = 50\%$, the O-CO_2 association overcomes O-CO recombination for $T_g \geq 2700\ K$, as was shown in Figure 2-23. At low conversion degrees (where the plasma is mostly composed of CO_2) the O-CO_2 association dominates for $T_g \geq 2000\ K$. On the other hand, if the plasma is already fully dissociated, O-CO recombination will dominate whatever T_g and form back CO_2. We begin to sense here that a high conversion degree and a high energy efficiency are not compatible unless the products can be separated. In an ideal world, the CO molecules would be extracted from the plasma as soon as they are produced, while the O atoms would stay there and react with fresh CO_2. Chemical nonequilibrium is needed to achieve SIQ.

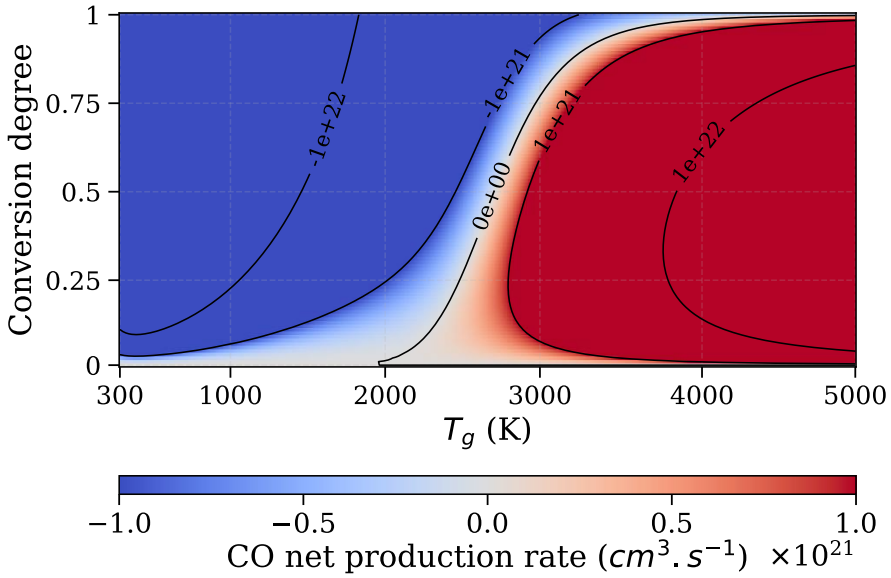

Figure 2-24. Net production rate of CO taking into account O-CO_2 association and O-CO recombination reactions, vs gas temperature and conversion degree. Densities taken at P_{atm}. Rate constants from Park *et al.*

Having O-CO_2 association faster than O-CO recombination is insufficient to significantly increase the EE. To do so, O-CO_2 association must also be faster than O-O recombination. We map the ratio of O-CO_2 association over O-O recombination rates R_{O-CO2}/R_{O-O} as a function of the gas temperature and conversion degree ϕ at atmospheric pressure (Figure 2-25). Even at 1% conversion, where the O density is 100 times lower than the CO_2 density, the gas temperature must be at least 2100 K for O-CO_2 association to surpass O-O

recombination, and 2500 K to be 10 times higher. This map again shows how separating the products or renouncing high conversions would increase the O-CO_2 association.

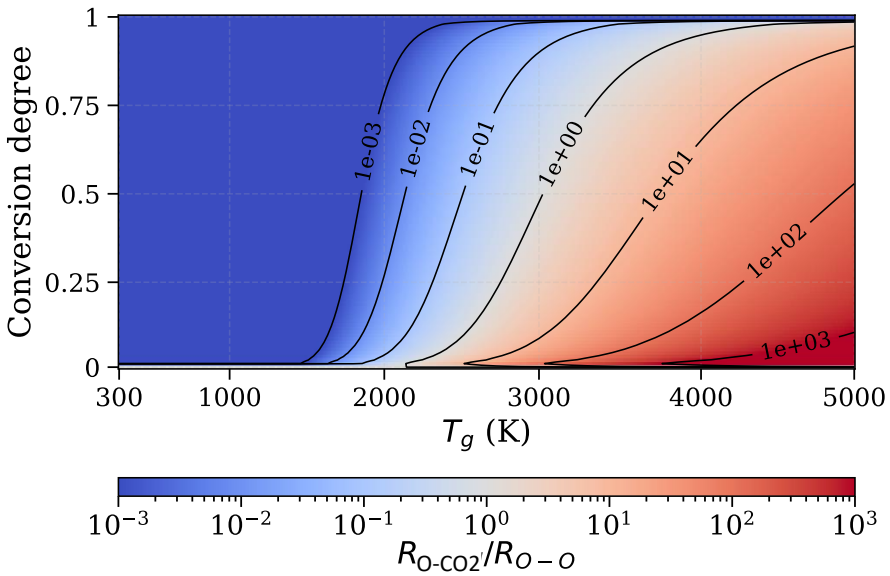

Figure 2-25. O-CO_2 association over O-O recombination rates vs gas temperature and conversion degree. Densities taken at P_{atm}. Rate constants from Park *et al.*

To summarize the balance between O-CO_2 association, O-CO and O-O recombinations, we plot in Figure 2-26 and Figure 2-27 the quantity β_{CO} defined as:

$$\beta_{CO} = \frac{R_{O-CO2} - R_{O-CO}}{R_{O-CO2} + R_{O-CO} + R_{O-O}} \qquad \text{Eq. 2-18}$$

where R_{O-CO2}, R_{O-CO}, and R_{O-O} are the rates of O-CO_2 association, O-CO recombination, and O-O recombination. If the O-CO recombination dominates, β_{CO} is negative, i.e., the O atoms lower the conversion. If O-O recombination dominates, β_{CO} is around zero, i.e., the O atoms have a neutral impact on the conversion. If β_{CO} is positive, the O atoms enhance the conversion.

Figure 2-26 shows three maps of β_{CO} vs (T_g, ϕ) at $P = 10^{-2}, 10^{-1}, 1\ bar$. Below 0.1 bar, as long as the conversion stays below 95%, $\beta_{CO} > -20\%$. The same happens at atmospheric pressure, provided that the conversion stays below 80%. With our assumptions (no O_2 content), O-O recombination to O_2 is much faster than O-CO recombination to CO_2, thus preserving the amount of CO produced.

Nevertheless, the fast O-O recombination imposes going to high temperatures to promote O-CO_2 association. At (1 bar, 50% conversion, 3000 K), only 30% of the O atoms would end up in O-CO_2 association. Going to lower conversion significantly increases this amount: (1 bar, 10% conversion, 3000 K) would allow 80% O-CO_2 association.

Figure 2-27 also shows the influence of the pressure: as recombination is a 3-body process, lowering the pressure favors O-CO_2 association. At $\phi = 50\%$, $P = 10^{-2}$ bar, 50% O-CO_2 association would be achieved at 2200 K, compared with 3200 K at atmospheric pressure.

It has to be kept in mind that β_{CO} is computed assuming equal O and CO densities (we assumed that the O produced is fully atomic). In reality, as O recombines to O_2, the O density decreases, and the O-CO_2 association and O-CO recombination (which are proportional to n_O) increase relatively to O-O recombination (which is proportional to n_O^2). That is, the recycling phase could be more (or less) favorable than what we estimate in Figure 2-26 and Figure 2-27. Moreover, β_{CO} does not consider the energy cost of heating the gas. It provides an understanding of the conditions promoting O-CO_2 association, but we need to calculate the energy cost to know if this is actually O recycling.

Overall, Figure 2-23, Figure 2-24, Figure 2-25, Figure 2-26, and Figure 2-27 point out that: (i) the O-CO_2 association is only favorable at high temperatures. (ii) These temperatures can be reduced at low conversion degrees. Nevertheless, (i) maintaining high temperatures and (ii) artificially creating an environment rich in O and CO_2 have an energy cost. Can O-CO_2 association allow to beat the thermodynamic limit, despite its energy cost? We need to simulate the kinetics to get to the bottom of it.

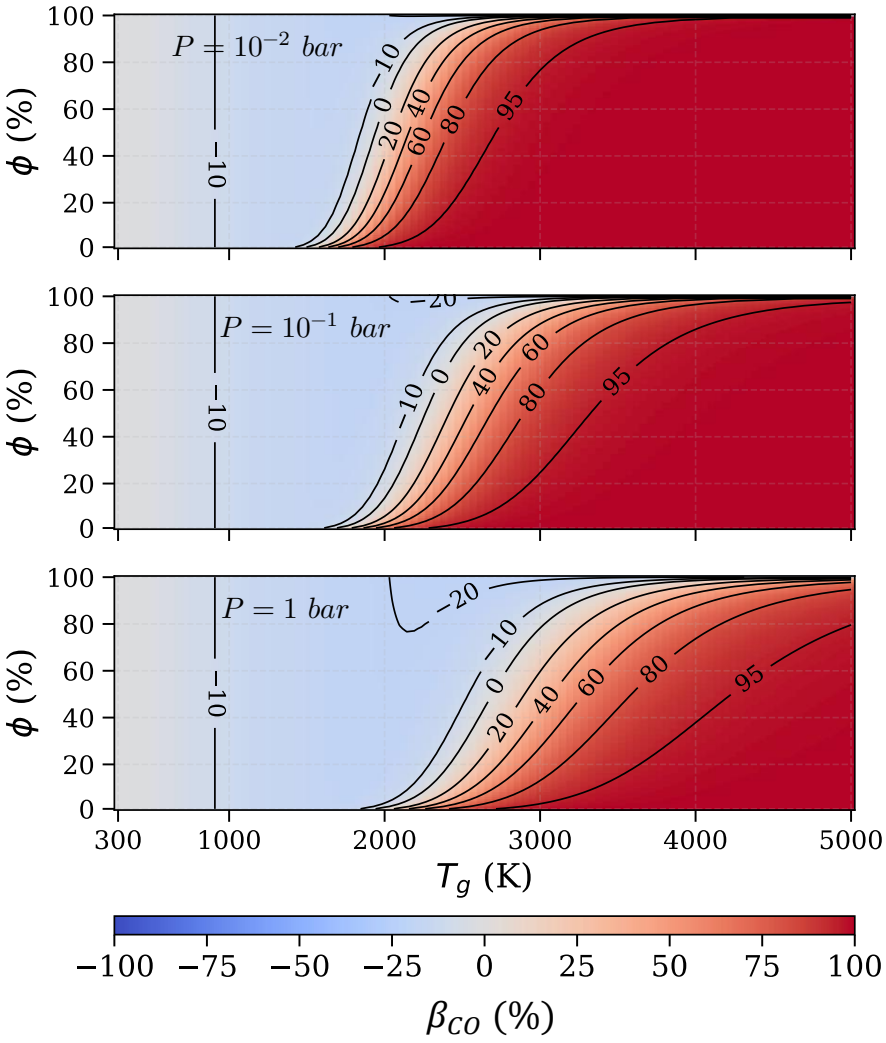

Figure 2-26. Net fraction of O atoms reacting in O-CO_2 association (Reac. 7) mapped vs T_g & Φ (conversion degree), at 10^{-2}, 10^{-1}, and 1 bar. This fraction results from the competition between O-CO_2 association (positive impact, dominant in the blue regions), O-CO recombination (negative impact, dominant in the red regions), and O-O recombination (neutral impact). Rate constants from Park *et al.*

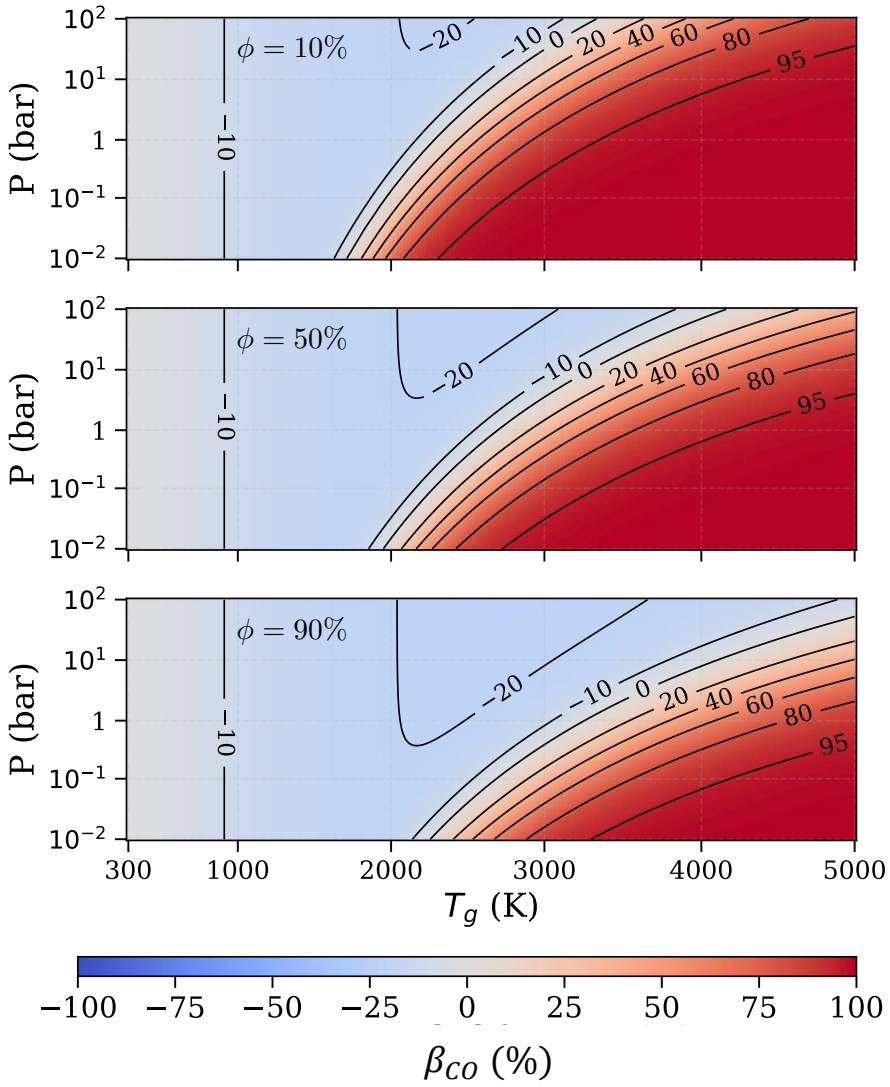

Figure 2-27. Net fraction of O atoms reacting in O-CO_2 association (Reac. 7) mapped vs T_g & P, at several conversion degrees (up 10%, middle 50%, bottom 90%). Rate constants from Park *et al.*

2.3.5.3 Kinetic modeling of the recycling phase

O recycling is the essential step needed to overcome the 50% EE thermodynamic limit. We want to evaluate its feasibility from a kinetic point of view. We will use a basic kinetic model, with favorable assumptions, in order to assess an upper bound of the EE achievable in a plasma process at thermal equilibrium. We will refer to this model as “Model 1”.

We model the plasma process as a discharge stage – where the energy is deposited – and a quenching stage. By definition of our stages, O recycling happens in the quenching stage, when no more energy is deposited. The quenching stage has two purposes: recycling the O and kinetically freezing the CO molecules. Therefore, we further decompose our plasma process by splitting the quenching stage in a “recycling phase” and a “cooling phase”.

In most plasma discharges, this quenching phase begins with a dilution of the hot products with the surrounding gas. This is the case for MW, GA and NRP spark discharges, which are the discharges with the best EE performance. The O atoms and CO molecules produced in the core are brought into contact with surrounding CO_2, and heat transfer from the core of the discharge can lead to high temperatures in the diluted mixture. The O atoms can recombine to O_2 and CO_2 or can produce additional CO. This is the "recycling phase" whose kinetics we will to simulate.

In Model 1, we will focus on a recycling phase at thermal equilibrium, following a conversion at LTE. We will vary the different parameters of the simulation, including the dilution ratio or the initial temperature of the plasma (these parameters will be defined in the next subsection). By covering a vast parameter space, we include all the possible plasma configurations (as long as the plasma stays in thermal equilibrium).

Model description

We consider a system initially composed of pure CO_2 at ambient temperature and a given pressure. We model a plama process at thermal equilibrium in 3 phases: heating, dilution, and recycling phases.

In the heating phase (phase 1), the system is heated to T_1 while keeping LTE (phase 1). Then, in the dilution phase, a given amount of CO_2 at a temperature T_2 is added to the system (phase 2). We define the dilution ratio as the CO_2 amount added in phase 2 over the O amount remaining at the end of phase 1:

$$\alpha_{dilu} = N_{CO2}^{(2)} / N_O^{(1)} \qquad \text{Eq. 2-19}$$

Homogenization of the species densities and the temperature is assumed to be infinitely rapid.

In a plasma process, the diluting gas is either at ambient temperature or it can also be heated by the discharge. For example, in the NRP-spark discharges studied in the following chapters, previous pulses have heated the gas surrounding the discharge around 600 K. Logically, we should have $T_2 < T_1$.

At the beginning of the recycling phase (phase 3, whose kinetics we are going to simulate), the system is a mixture of CO_2 and its dissociation products at temperature $T_3(t = 0\ ns)$. $T_3(t = 0\ ns)$ is a function of T_1, T_2, and of the dilution ratio α_{dilu}.

The energy cost of the process is the sum of the energy cost of phases 1 and 2:

$$E_{cost} = m_0\big(h(T_1) - h(T_0)\big) + m_2(h(T_2) - h(T_0)) \qquad \text{Eq. 2-20}$$

where m_0 is the initial mass, m_2 is the diluant mass, and h is the specific enthalpy of the mixture in LTE.

We simulate the densities and temperature evolution in phase 3 using a kinetic model and the Cantera code (Goodwin et al. 2017). The kinetic evolution is obtained after solving the master equation:

$$\frac{dN_i}{dt} = \sum_j \nu_{ij} R_j(t) \qquad \text{Eq. 2-21}$$

where N_i is the number density of the specie i, ν_{ij} is the stochiometric coefficient of specie i in reaction j, and R_j is the rate of reaction j.

The three relevant reactions to simulate a recycling phase below 5000 K are (i) CO_2 heavy-impact dissociation and its reverse, O-CO recombination (Reac. 5 & Reac. 6), (ii) O-CO_2 association (Reac. 7) and its reverse, and (iii) O_2 heavy-impact dissociation and its reverse, O-O recombination (Reac. 22). Due to the differences in the rate constants proposed by the various authors (see Figure 2-23, and the discussion by (Van De Steeg et al. 2021)) we use the rates from 3 different kinetic mechanisms to simulate the recycling phase: (Park et al. 1994), GRI-MECH (Smith et al. 1999), and (Kozàk and Bogaerts 2014).

We recall the definition of the energy efficiency: $\eta = \Delta_r H_0 \cdot N_{CO}^{tot}/E_{cost}$, where N_{CO}^{tot} is the number of CO molecules produced in the whole process: $N_{CO}^{tot} = N_{CO}^{(1)} + N_{CO}^{(2)} + N_{CO}^{(3)}$. No energy is deposited in the recycling phase, so the EE is maximal at the peak of CO amount in the recycling phase. Since we are interested in the upper bound of the EE, we assume that an additional cooling stage would provide the cooling rate necessary to froze the CO molecules at this peak. Thus, in the following, we only report the EE value obtained at the peak amount of CO.

The modelling steps used in Model 1 are summarized in Figure 2-28 and Table 2-6.

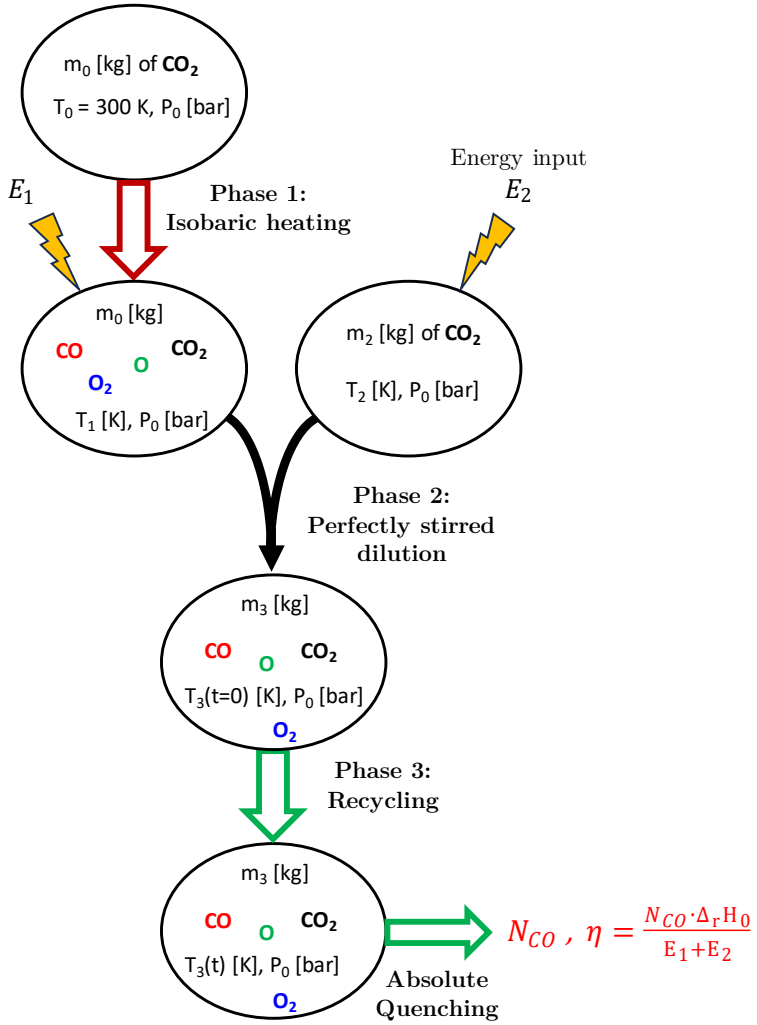

Figure 2-28. Diagram of the modeling steps of Model 1.

Results

We run the simulations for $P = 10^{-2}, 10^{-1}, 1\ bar$, $T_1 = 2000 - 5000$, $T_2 = 300 - 3000\ K$, and the dilution ratio $\alpha_{dilu} = 10^{-2} - 10^{2}$. The parameter domain is summarized in Table 2-4. If the heating temperature T_1 is too low, (i) few O atoms are produced in the heating phase, and (ii) the even lower T_3 leads to little recombination or freezes the composition. Thus, phase 3 reduces or does not improve the EE: it is not a recycling phase. For $\alpha_{dilu} = 1$, the critical T_1 needed to avoid this counterproductive effect is about 2700 K at 0.01 bar, 3000 K at 0.1 bar, and 3300 K at 1 bar. Subsequently, we name this threshold T_1^{recyc}.

When $T_1 \geq T_1^{recyc}$, the quantity of O atoms and T_3 are high enough at the beginning of the recycling phase to produce additional CO molecules. First, we show numerically that, $\forall\ (P, \alpha_{dilu}, T_1, T_2),\ T_1 \geq T_1^{recyc}$, the maximal CO amount is obtained when the simulation reaches equilibrium. In other words, no concave evolution of the CO amount is observed on the parameter domain studied.

Table 2-4. Parameter domain scanned in the calculations, using Model 1.

Parameter	Min value	Max value	Number of points	Scale of the grid
$\boldsymbol{P}$ **(bar)**	0.01	1	3	log
$\boldsymbol{\alpha_{dilu}}$	0.01	100	30	log
$\boldsymbol{T_1}$ **(K)**	2000	5000	50	linear
$\boldsymbol{T_2}$ **(K)**	300	3000	30	linear

We plot in Figure 2-29 an example of the temporal evolution of the temperature, the species amount, and the reaction rates during the recycling phase. In this example, $\alpha_{dilu} = 1$, $P = 1\ bar$, $T_1 = 4000\ K$. The results are presented for two temperatures of the diluting CO_2, $T_2 = 300,\ 2000\ K$, leading to two different initial temperatures of the recycling phase, $T_3(t = 0) = 2500,\ 3100\ K$. The rates used are those of Park. This example illustrates what we have just stated: the maximal CO amount is reached when every net rate is zero, i.e., at equilibrium. The energy has been added by heating the initial system (phase 1) and the diluting gas (phase 2). In phase 3, no more energy is deposited. Thus, the maximal energy efficiency of the recycling phase is reached at the peak of CO amount, that is, at equilibrium. We find this result whatever the kinetic model used (see Figure 2-30 for a model comparison example). Therefore, it would not be beneficial to quench the process before reaching equilibrium.

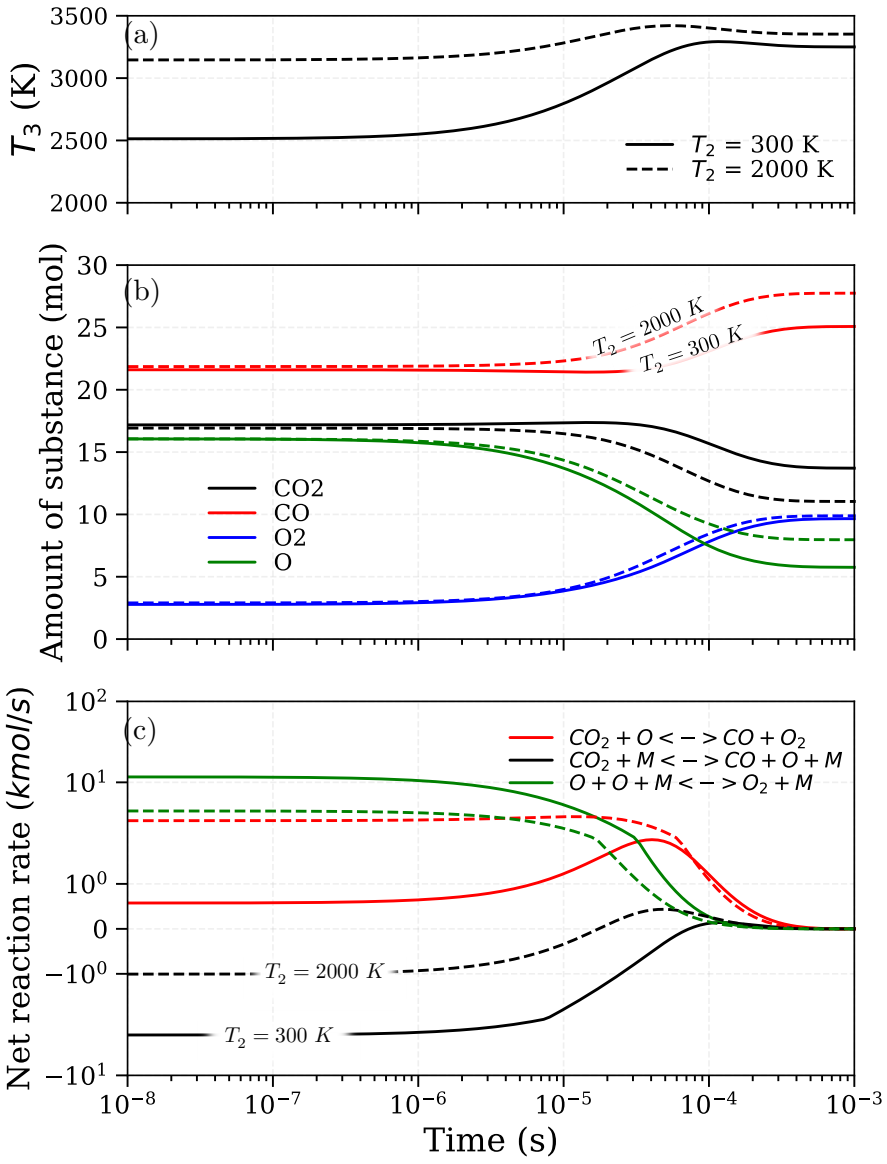

Figure 2-29. Temporal evolution of the gas temperature in the recycling phase T_3 (a), main species amount (b), and net reaction rates (c). Conditions: atmospheric pressure, $\alpha_{dilu} = 1$, heating phase temperature $T_1 = 4000$ K, rate constants from Park 1994. t = 0 ns is the beginning of the recycling phase (phase 3).

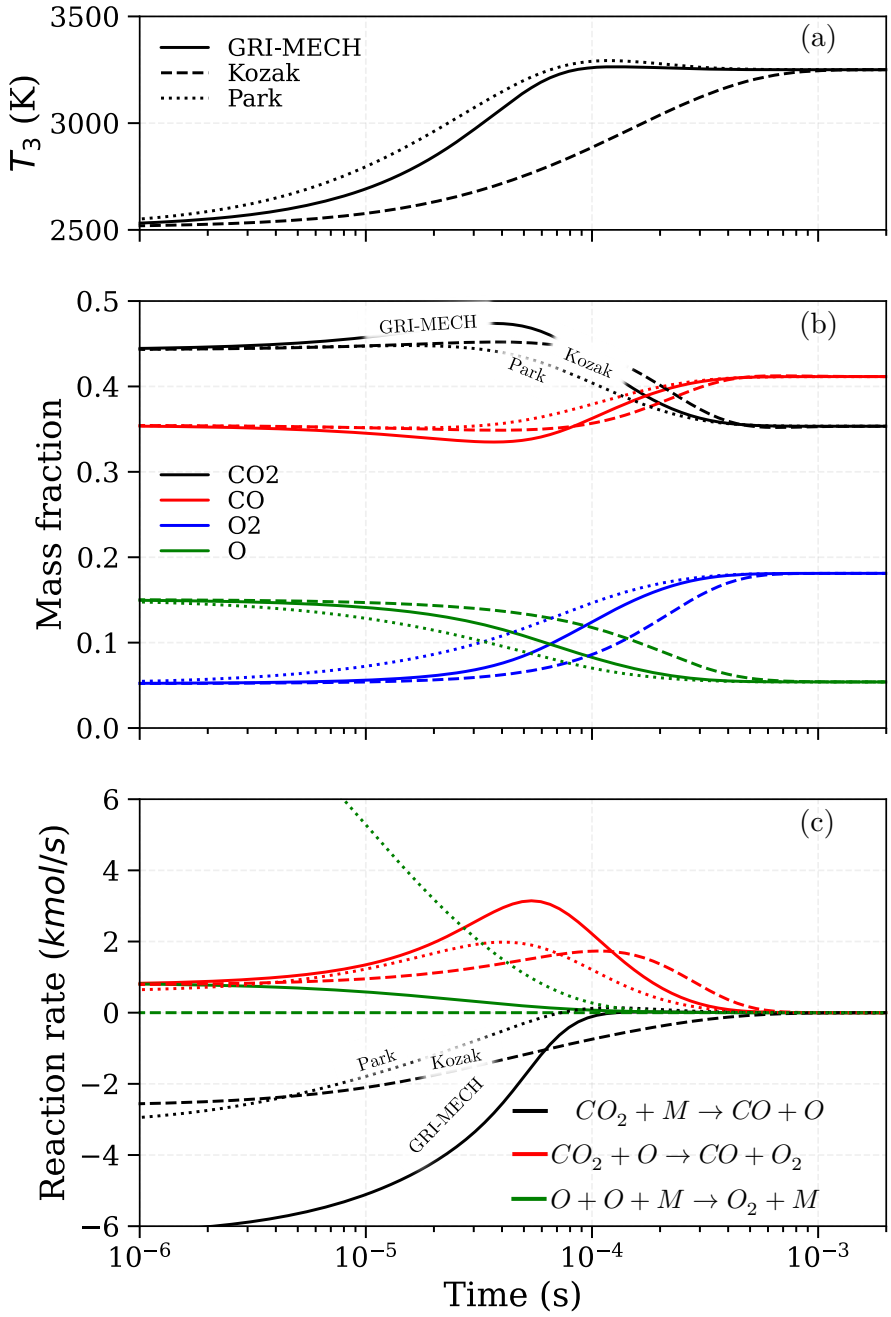

Figure 2-30. Temporal evolution of the gas temperature in the recycling phase T_3 (a), main species amount (b), and net reaction rates (c). Comparison of the three reaction rate sets. Conditions: atmospheric pressure, $\alpha_{dilu} = 1$, heating phase temperature $T_1 = 4000$ K, diluting gas at $T_2 = 300$ K.

To compute the EE, we take the maximal CO amount reached during the recycling phase and divide it by the energy cost of phases 1 & 2. As stated above, for $T_1 \leq T_1^{recyc}$ this maximum is the initial amount – no recycling phase –, whereas for $T_1 \geq T_1^{recyc}$ it is the final amount. We map the EE evolution with T_1, T_2 at $P = 10^{-2}, 10^{-1}, 1$ *bar*, $\alpha_{dilu} = 1$ in Figure 2-31. We observe no improvement in the maximal EE compared to the EE thermodynamic limit (52% at 0.01 bar, 50% at 0.1 bar, 48% at 1 bar). Nevertheless, the EE thermodynamic

limit is reached over a wide temperature range. Indeed, when T_1 is above the optimal temperature for an LTE process, the extra heat and chemical energy are reused in the recycling phase.

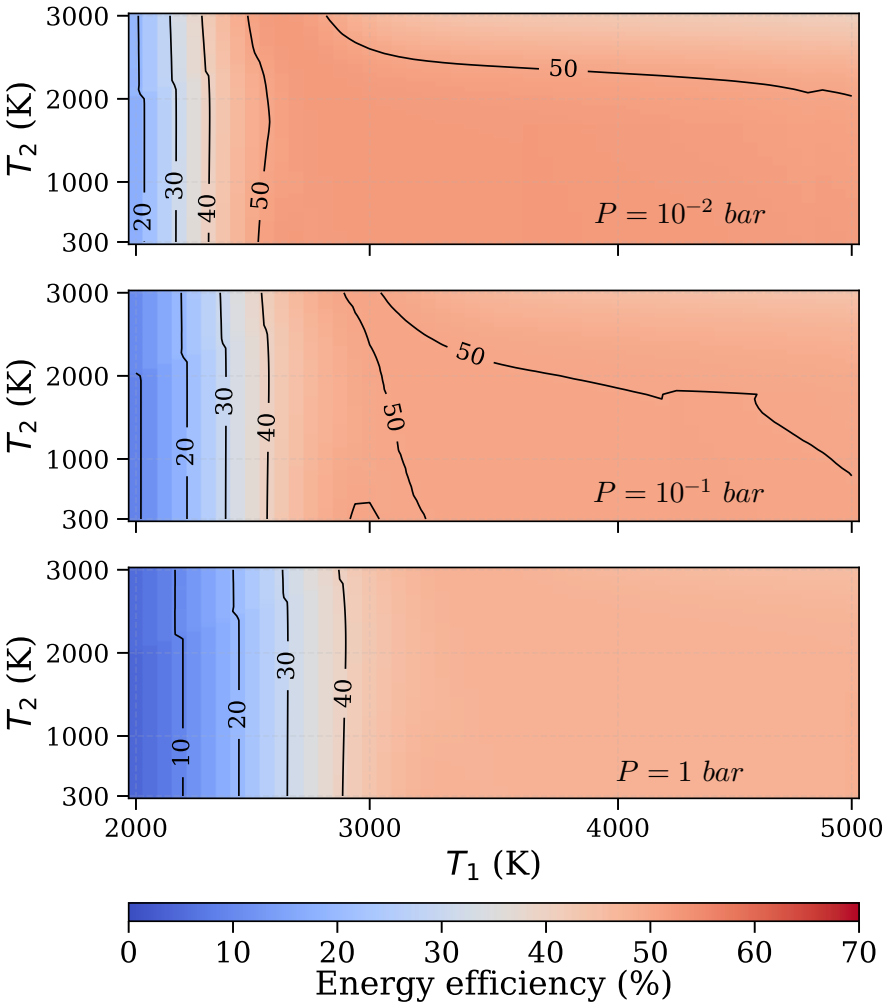

Figure 2-31. Energy efficiency resulting from the recycling model as a function of T_1, and T_2, at 10^{-2}, 10^{-1}, 1 bar, and α_{dilu}=1. The maximum EE after the recycling phase at each pressure does not exceed the EE thermodynamic limit.

Varying the dilution ratio is not the solution either. Figure 2-34 presents the EE maps at 1 bar for three different dilution ratios: 0.1, 1, 10. The maximum EE is still the thermodynamic limit – 48% at 1 bar – but the temperature combination to reach it varies as a function of the dilution ratio. At $\alpha_{dilu} = 10$, we observe that the dilution can either freeze the CO amount – at low T_2 –, induce O-CO recombination – at intermediate T_2 –, or allow some recycling – at high T_2. At $\alpha_{dilu} = 0.1$, the dilution has a small impact, and the EE evolution as a function of the temperature follows the usual trend of LTE conversion: the EE reaches a maximum and then decreases as more energy is spent on dissociating O_2.

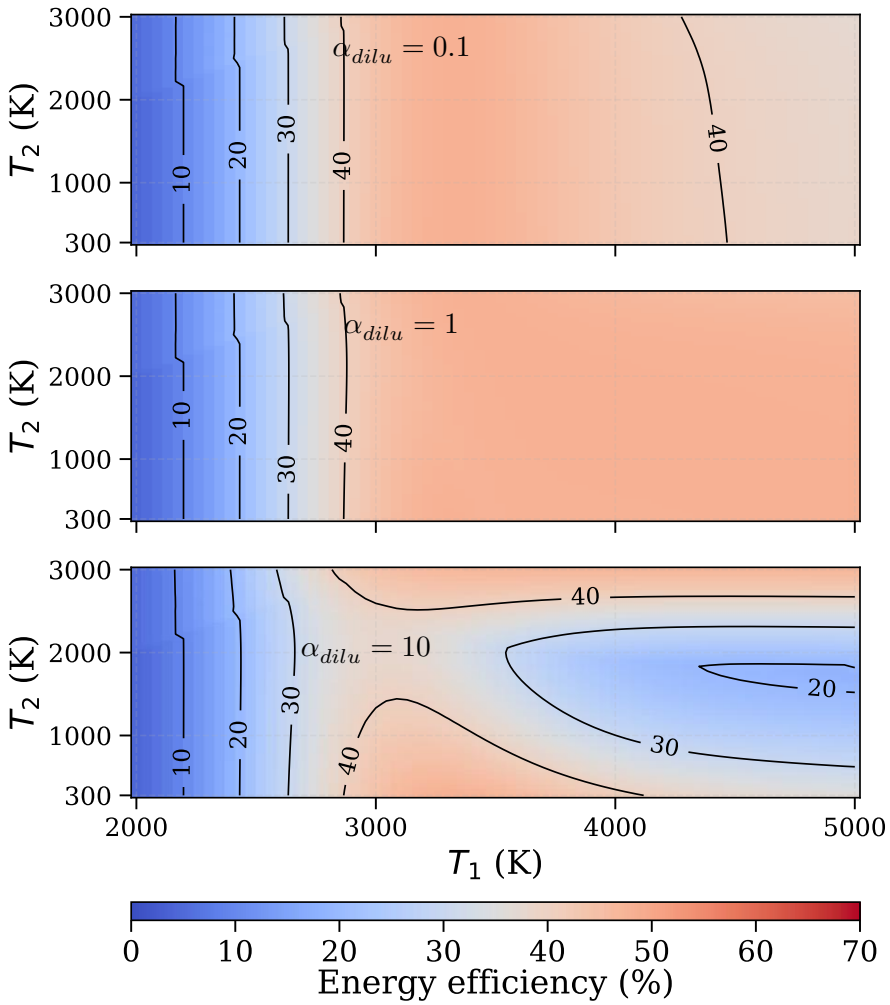

Figure 2-32. Energy efficiency resulting from the recycling model as a function of T_1, and T_2, at 1 bar, $\alpha_{dilu} = 0.1$, 1, 10. The maximum EE after the recycling phase at each dilution ratio does not exceed the EE thermodynamic limit.

Kinetic analysis

To understand qualitatively what prevents the EE from topping the SIQ maximum presented in Figure 2-22, we analyze the results reported in Figure 2-29. In that case, the initial conversion is about 56%. For $T_2 = 300\ K$, we get $T_3(t = 0) = 2500\ K$. Looking at Figure 2-26, we see that, at atmospheric pressure, these conversion and temperature imply a negative net recycled fraction – i.e. recombination is faster than the O-CO_2 association. Then, the net recycled fraction crosses 10% at 2750 K and increases to 50% at 3000 K.

Consistently, Figure 2-29 shows that O-CO_2 association is initially overcome by O-CO recombination. The CO amount hardly decreases because the O-CO and (mostly) O-O recombination reactions heat the gas (about 5 eV is released in both recombination reactions), making the temperature exceed 2750 K at $t = 10\ \mu s$. The conditions are then favorable for O-CO_2 association: the CO density starts increasing.

As the conversion gets higher, the inverse reactions establish steady state. Ultimately, the equilibrium composition at the final high temperature contains a significant amount of O. The EE is limited to 47.8%.

In the case $T_2 = 2000\ K$, the initial temperature is already 3100 K and therefore the conditions are favorable for O recycling. But the high temperature leads to a high remaining O content. The EE is 47.9%.

The other sets of reaction rates yield a slightly different behavior, but the final result is the same. We go back to the previous example ($\alpha_{dilu} = 1,\ P = 1\ bar,\ T_1 = 4000\ K,\quad T_2 = 300\ K$), and display the results of the three models in Figure 2-30. We already described in the previous paragraph what happens with Park's rates. With Kozak's rates, O-O recombination is much slower. O-CO recombination dominates initially, slightly decreasing the CO density. The temperature increases due to recombination reactions and activates O-CO_2 association. Thus, the CO amount increases again to reach its equilibrium value. The GRI-MECH mechanism shows the same behavior despite the faster O-CO recombination at the beginning, and leads to the same result.

Conclusion of Model 1

Our results show that a thermal process without product separation cannot reach the 70% EE mentioned by Van de Steeg *et al.*. We have simulated the impact of dilution on the recycling phase, creating chemical nonequilibrium, and showed that the EE remains capped by the thermodynamic limit (around 50%). There is no "new thermal limit" but only one thermodynamic limit.

First, lowering the recombination and increasing the dissociation by diluting the gas is a dead end, as O-CO_2 association requires high temperatures. The high temperature and low conversion needed to promote O-CO_2 association over O-CO and O-O 3-body recombinations cannot be achieved simultaneously at a low energy cost. Second, when the high temperature conditions needed for fast O-CO_2 association are met, the O atoms become stable in the mixture. Reverse reactions equilibrate the process and stop the system evolution at the LTE concentration of O. Finally, O-CO_2 association is not fast enough to beat thermodynamic equilibrium limits: in the transient recycling phase, the CO amount never exceeds its LTE value.

On the positive side, adding a dilution and recycling phase gives thermal processes room for maneuver. Once the heating temperature is high enough ($T_1 \geq T_1^{recyc}$), there is a wide range of diluent temperatures and diluent ratios (T_2, α_{dilu}) that make it possible to reach the EE thermodynamic limit. Any overshoot of the heating temperature can be rectified by adjusting the diluent amount and temperature.

Now, what could be done to make O recycling work and to overcome the EE thermodynamic limit? (i) Having a constant CO extraction would prevent back reactions reforming CO_2 or O. This would be for sure beneficial, but separating gaseous products at several thousand degrees seems inaccessible. (ii) Accelerating the O-CO_2 association could be a more viable option. By easing the crossing of activation barriers, vibrational excitation offers the stimulating virtue required. In the next section, we assess its impact on O-CO_2 association and O recycling.

2.3.5.4 Vibrationally-enhanced oxygen recycling

O-CO_2 association accelerated by vibrational excitation

The vibrational excitation of CO_2 enhances O-CO_2 association:

$$CO_2(v) + O \rightarrow CO + O_2 \qquad \text{Reac. 23}$$

The rate of this reaction can be calculated according to the Fridman-Macheret α-model (Fridman 2008):

$$k_f(v) = k_0 \cdot \exp\left(-\frac{E_a - \alpha E_v}{T} \cdot \theta(E_a - \alpha E_v)\right) \qquad \text{Eq. 2-22}$$

where $k_f(v)$ is the vibrational specific O-CO_2 association rate constant, k_0 is a pre-exponential factor, E_a the activation energy of the reaction, E_v the energy of the vibrational state, and θ the Heaviside function. According to (Fridman 2008), the α coefficient can be calculated from the activation energy of the forward and backward reactions:

$$\alpha \approx \frac{E_a^f}{E_a^f + E_a^b} \qquad \text{Eq. 2-23}$$

where E_a^f and E_a^b are the forward and backward activation energies. In the commonly used rate constant, the activation energy is 26500 K, i.e. 2.28 eV (Warnatz 1984). Knowing that the reaction enthalpy is 0.35 eV we get $\alpha \approx 0.54$ for the O-CO_2 association.

Now that we have an estimation of the vibrational specific rate constants, we can compute an averaged rate constant over the VDF:

$$k_f^{noneq}(T_g, T_v) = \sum_v f(v) \cdot k_f(v^*) \qquad \text{Eq. 2-24}$$

where $f(v)$ is the VDF. We make the assumption that the VDF is Boltzmann.

Finally, we compute the pre-exponential factor k_0 of the vibrational specific rate constant from the Arrhenius coefficients of the thermal equilibrium rate constant. To do so, we take $T_g = T_v$ in Eq. 2-24, and equal it to the thermal equilibrium rate constant, $k_f(T_g) = A \cdot T_g^b \cdot \exp(-E_a/T_g)$, which yields:

$$k_0(T_g) = \frac{A \cdot T_g^b \cdot Z_v(T_g)}{\sum_0^{v_{th}-1} g_v \exp\left(-(1-\alpha)\frac{E_v}{T_g}\right) + \sum_{v_{th}}^{v_{diss}} g_v \exp\left(-\frac{E_v - E_a}{T_g}\right)} \qquad \text{Eq. 2-25}$$

where A, b are the Arrhenius coefficients of the thermal rate constant, Z_v the vibrational partition function, g_v the degeneracy of state v, v_{th} the first level where $\theta(E_a - \alpha E_v) = 0$, and v_{diss} the first level where CO_2 pre-dissociates. We use the coefficients A, b, E_a of the O-CO_2 association rate constant from (Warnatz 1984). The vibrational energy and partition function are computed using the harmonic oscillator model and considering only the asymmetric stretch mode. In so doing, we assume that the symmetric and bending modes are in equilibrium with the translation, which is a common scenario in plasma discharges (Dubuet et al. 2022; Klarenaar et al. 2017; Ana Sofia Morillo-Candas et al. 2020; Pannier 2019).

We compare the O-CO_2 association nonequilibrium rate constant to the competing mechanisms in Figure 2-33. As expected, vibrational overpopulation speeds up O-CO_2 association. Thus, compared to the recombination reactions, O-CO_2 association becomes favorable at lower T_g. According to the Fridman-Macheret α-model, the O-CO and O-O 3-body recombinations are not accelerated by vibrational excitation because they are highly endothermic, with no energy barrier (which implies $\alpha = 0$).

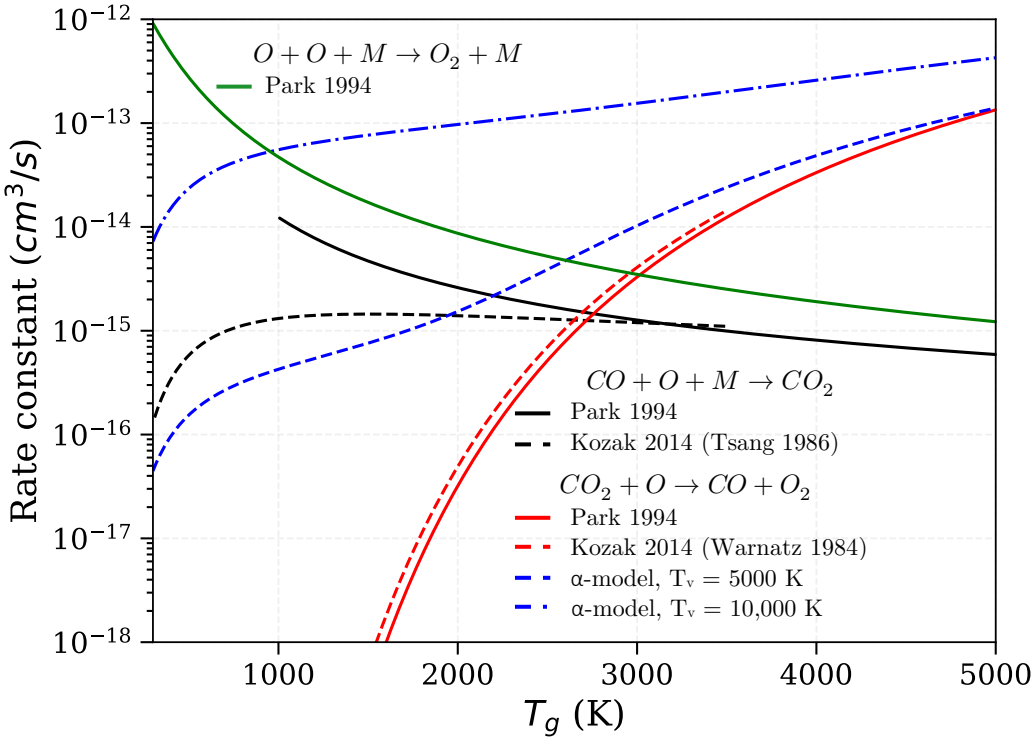

Figure 2-33. Rate constants of O-consuming reactions compared to vibrationally enhanced O-CO_2 association. The 3-body rate constants are multiplied by the total number density at P_{atm} and T_g.

On the other hand, the previous references (Klarenaar et al. 2017; Ana Sofia Morillo-Candas et al. 2020; Pannier 2019) showed that in usual nonequilibrium discharges such as glow, radio frequency (RF), and NRP discharges, the vibrational temperature of CO is close to the asymmetric vibrational temperature of CO_2 and follows the same trend. Just as the vibrational excitation of CO_2 accelerates the O-CO_2 association, the vibrational excitation of CO accelerates the backward reaction. Similarly, we compute the vibrationally-enhanced backward rate constant using the α-model. This time, $\alpha \approx 0.46$. Again, we assume that the VDF of CO is Boltzmann, and we use the harmonic oscillator model to compute the CO vibrational energies. Figure 2-34 shows the rate constants of O-CO_2 association and its backward reaction, both at thermal equilibrium and with a nonequilibrium T_v. The enhanced vibrational distribution accelerates both reactions.

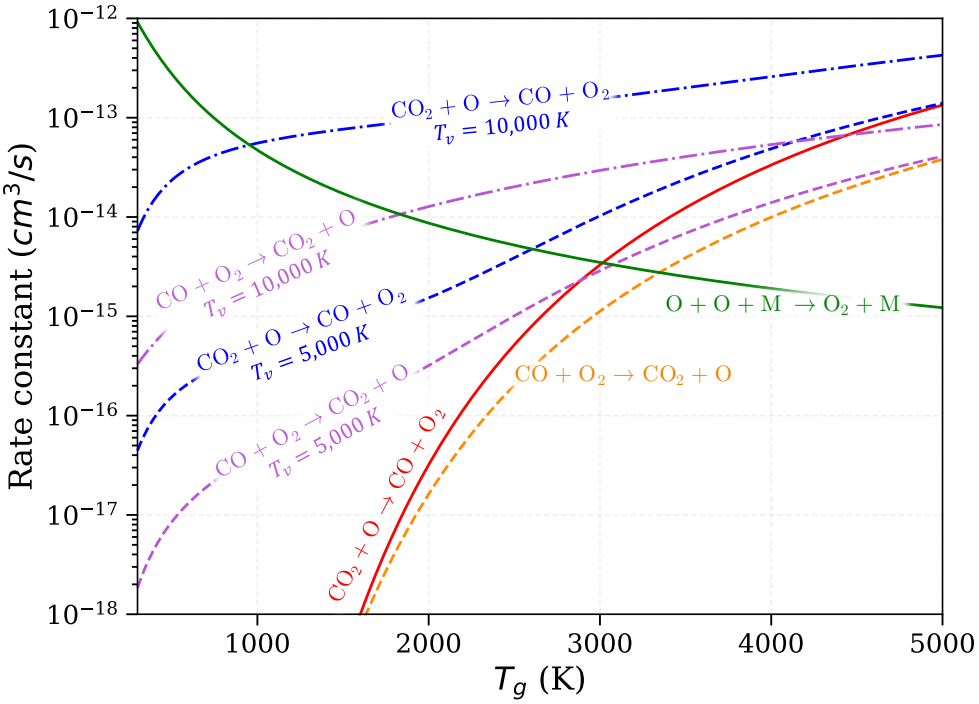

Figure 2-34. Rate constants of the O-CO_2 association and its backward reaction at thermal equilibrium and with $T_v = 5000, 10000\ K$. The nonequilibrium rate constants are computed using the Fridman-Macheret α-model. An increase in the vibrational temperature accelerates both the forward and backward reactions.

In the following of this section, we will generalize Model 1 to nonequilibrium conversion and simulate the kinetics of vibrational-enhanced O-CO_2 association using two models, Model 2 & Model 3. We will use the nonequilibrium rates we just calculated for O-CO_2 association and its reverse, and compute an additional energy cost for vibrational excitation assuming that VT transfer is negligible. The models allow to set new upper bounds for the EE as a function of the pressure, as well as the conditions necessary to achieving it. However, we will show in Sec. 2.3.5.6 that these conditions are not achievable in practice. Therefore,

readers in a hurry can skip directly to Sec. 2.3.5.5, which examines electronically-enhanced O recycling. The results of Models 2 & 3 are summarized and discussed in Sec. 2.3.5.6.

Impact on the kinetics – Model 2

We return to our LTE heating plus recycling phase model. We aim to estimate an upper bound of the EE enhancement due to vibrational excitation. To do so, we impose a constant elevated vibrational temperature during the recycling phase.

We fit with Arrhenius forms the nonequilibrium rates of the O-CO_2 association (forward and reverse) at vibrational temperatures between 5000 and 15,000 K and implement them in our kinetic model. We consider that the vibrational temperatures of CO and of the CO_2 asymmetric mode are equal.

Note that we do not consider the acceleration induced by vibration excitation on the CO_2 + M → CO + O + M reaction. This reaction is in competition with O-CO_2 association for the use of vibrational energy. Yet, it is much less favorable from an EE point of view: CO_2 + M → CO + O + M produces a CO molecule at a 5.5 eV cost, whereas O + CO_2 → O_2 + CO produces a CO molecule at a 0.35 eV cost[7]. Consequently, to compute an upper bound of the EE, we neglect the vibrational enhancement of the CO_2 + M dissociation. This new model – LTE heating plus vibrationally-enhanced recycling – will be referred to as "Model 2". The main characteristic of Model 2 are summarized in Table 2-6.

First, we examine the impact of the O-CO_2 acceleration on the kinetics. We plot in Figure 2-35 one of the examples of Figure 2-29 ($P = 1\ bar$, $T_1 = 4000\ K$, $T_2 = 300\ K$, $\alpha_{dilu} = 1$) and the result of a simulation using the same conditions except for the nonequilibrium vibrational temperature, $T_v = 10{,}000\ K$. As expected, in the nonequilibrium case, O-CO_2 association is now much faster than the other reactions. We get the concave shape of the CO amount we called for. In this example, the CO amount is maximal at about 20 µs, as is the EE (assuming that all O atoms end up in O_2, i.e. AQ). Additionally, the CO density reaches a steady-state value that is slightly above the equilibrium value. This is because vibrational excitation accelerates O-CO_2 association more than its backward reaction.

[7] Here, the energy cost is the reaction enthalpy, as in the equation energy of the kinetic model.

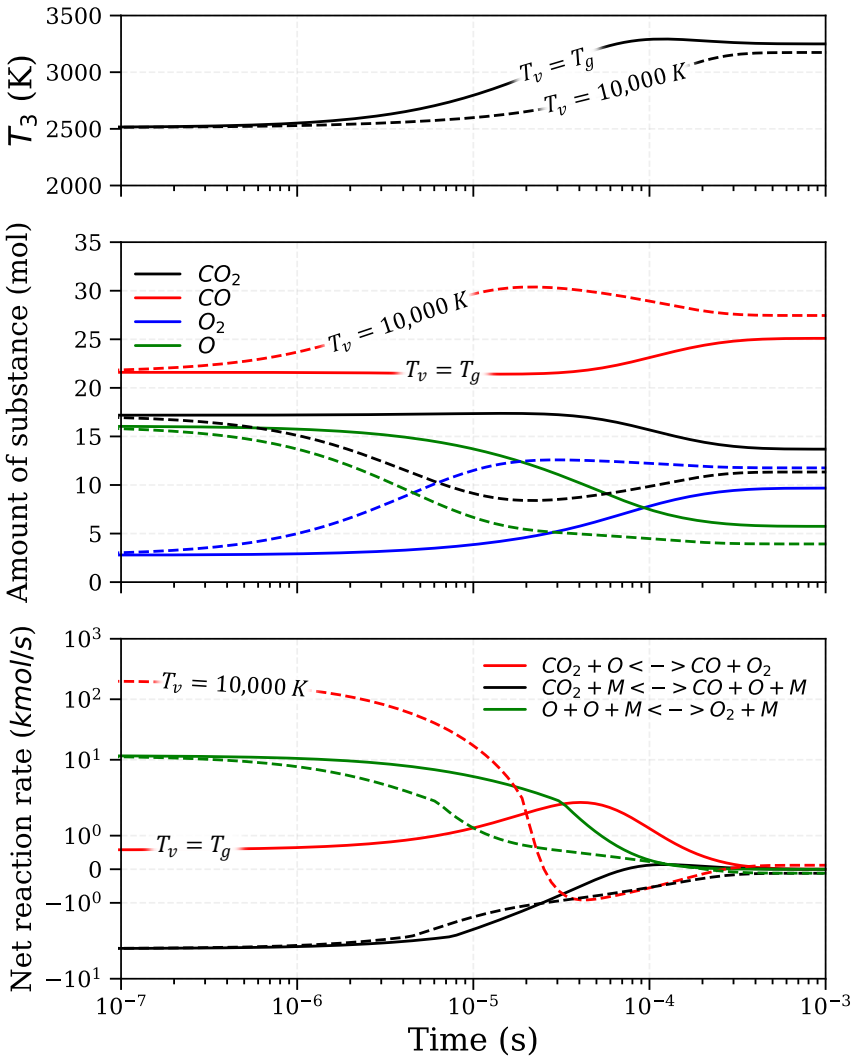

Figure 2-35. Temporal evolution of the gas temperature in the recycling phase T_3 (upper graph), main species amount (middle graph), and net reaction rates (bottom graph). Comparison of the thermal recycling phase with the vibrationally enhanced recycling phase at $T_v = 10,000$ K. Conditions: atmospheric pressure, $T_1 = 4000$ K, $T_2 = 300$ K, $\alpha_{dilu} = 1$. t = 0 is the beginning of the recycling phase (phase 3).

Energy cost of vibrational excitation

Increasing the vibrational excitation has an energy cost. Keeping in mind that we want an upper bound of the EE, we seek to estimate a lower bound of the energy cost of vibrational excitation. To do so, we assume that only the asymmetric stretch mode of CO_2 and the vibration of CO have to be excited and that there is no VT nor vibrational inter-mode transfer (VV'). The energy in the asymmetric stretch mode is:

$$E_{v3}(T_v) = \left(\sum_{v_3} \omega_3 \left(v_3 + \frac{1}{2} \right) \cdot f(v_3, T_v) \right) \cdot \frac{N_a}{M_{CO_2}} \cdot y_{CO_2} m \qquad \text{Eq. 2-26}$$

where $\omega_3 = 2349\ cm^{-1}$ is the vibrational constant of the asymmetric mode, $f(v_3, T_v)$ is the Boltzmann VDF of the asymmetric stretch mode, N_a the Avogadro number, M_{CO_2} the molar mass of CO_2, y_{CO_2} the mass fraction of CO_2 at the beginning of phase 3, and m the total mass of the gas during phase 3. The energy in CO vibration is:

$$E_{vCO}(T_v) = \left(\sum_{v_{CO}} \omega_{CO} \left(v_{CO} + \frac{1}{2} \right) \cdot f_{CO}(v_{CO}, T_v) \right) \cdot \frac{N_a}{M_{CO}} \cdot y_{CO} m \qquad \text{Eq. 2-27}$$

where $\omega_{CO} = 2170\ cm^{-1}$. The energy cost to overpopulate the vibration is:

$$E_v^{cost}(T_v, T_g) = E_{v3}(T_v) + E_{vCO}(T_v) - E_{v3}(T_g) - E_{vCO}(T_g) \qquad \text{Eq. 2-28}$$

In our calculations, depending on the conditions, it represents 10 – 20% of the overall energy cost.

Let us emphasize that this energy cost is computed using the initial quantity of the recycling phase $y_{CO2}(t = 0\ s)$, $y_{CO}(t = 0\ s)$, $T_3(t = 0\ s)$, and the vibrational temperature T_v. This vibrational temperature is kept constant during the simulation without accounting for an additional energy cost. This is an approximation: each CO molecule produced via the O-CO_2 association reaction should cost 0.35 eV. Thus, maintaining the vibrational temperature constant would require a constant energy addition. In the current model, this energy is drawn from the gas temperature instead of adding a new energy cost (in our model, the energy equation involves only the gas temperature). In all cases, this energy cost represents less than 2% of the total energy cost, making our approximation perfectly reasonable.

Table 2-5. Parameter domain scanned in the calculations using Model 2 & 3.

Parameter	Min value	Max value	Number of points	Scale
$\boldsymbol{P}$ **(bar)**	0.01	1	3	log
$\boldsymbol{\alpha_{dilu}}$	0.1	10	16	log
$\boldsymbol{T_v}$ **(K)**	5000	15000	16	linear
$\boldsymbol{T_1}$ **(K)**	2000	5000	20	linear
$\boldsymbol{T_2}$ **(K)**	300	3000	20	linear

Upper bound of the energy efficiency

To determine the EE of the vibrationally-enhanced process, we run the simulations for $T_1 \in [2000;\ 5000]\ K$, $T_2 \in [300;\ 3000]\ K$, $P = 10^{-2}; 10^{-1};\ 1\ bar$, $\alpha_{dilu} \in [0.1; 10]$, and $T_v \in [5000; 15000]\ K$. The parameter domain studied is reported in Table 2-5.

At $P = 1\ bar$, a maximal EE of 52% is reached. The optimal conditions are $T_1 = 4100\ K$, $T_2 = 300\ K$, $\alpha_{dilu} = 1.7$, $T_v = 9000\ K$. The initial temperature of the recycling phase

(resulting from T_1, T_2, and α_{dilu}) is $T_3(t = 0\ s) = 1900\ K$. The optimal EE is 4 points above the thermodynamic limit (48%). Moreover, the conversion degree reaches 65%[8].

At $P = 10^{-1}\ bar$, a maximal EE of 58% is reached. The optimal conditions are $T_1 = 3700\ K$, $T_2 = 300\ K$, $\alpha_{dilu} = 1.9$, $T_v = 8000\ K$, and $T_3(t = 0\ s) = 1700\ K$. The optimal EE is 8 points above the thermodynamic limit (50%). The conversion degree reaches 64%.

At $P = 10^{-2}\ bar$, a maximal EE of 64% is reached. The optimal conditions are $T_1 =$ 3,300 K, $T_2 = 300\ K$, $\alpha_{dilu} = 1.9$, $T_v = 6000\ K$, and $T_3(t = 0) = 1400\ K$. This optimal EE is 12 points above the thermodynamic limit (52%). Again, the conversion degree reaches 64%.

We report the evolution of the maximal EE as a function of the vibrational temperature in Figure 2-36. To clarify, at a given P and T_v, the maximal EE is obtained by varying all the other parameters (T_1, T_2 and α_{dilu}). *A priori,* these other parameters differ at each point of the curve. At each pressure, we observe that the EE curve has a maximum for a different vibrational temperature: about 6000 K at 10^{-2} bar, 8000 K at 10^{-1} bar, and 9000 K at 1 bar. A higher vibrational temperature results in a higher CO production but also a higher energy cost.

The maximal EE as a function of the heating temperature (T_1) is reported in Figure 2-37. A high O content is needed for the recycling phase: at the three pressures studied, the composition at the end of the heating phase at the optimal T_1 is about 50% CO and 40% O. A higher conversion results in a higher energy cost, so the optimal T_1 value results from the balance between the conversion at the end of the heating phase and the energy cost.

[8] Keep in mind that these EE and conversion are computed at the peak of CO. Obtaining this EE requires absolute quenching of the products, and achieving it without lowering the conversion degree imposes to use non-diluting cooling processes.

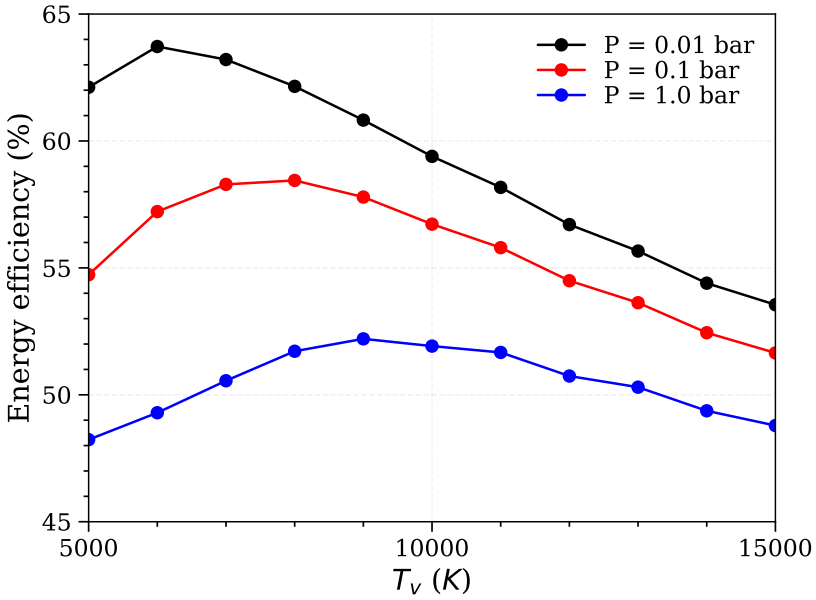

Figure 2-36. Maximal EE obtained with LTE heating followed by vibrational-enhanced recycling as a function of the vibrational temperature (T_v). Conditions: $T_1 \in [2000; 5000]$ K, $T_2 \in [300; 3000]$ K, $P = 10^{-2}; 10^{-1}; 1$ bar, $\alpha_{dilu} \in [0.1; 10]$. Nonequilibrium vibrational temperatures are beneficial to the recycling and thus the EE.

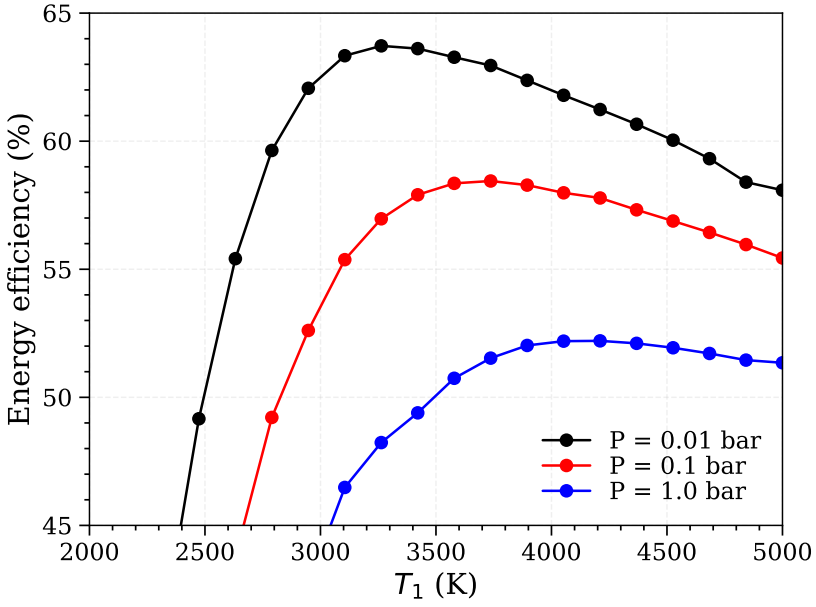

Figure 2-37. Maximal EE obtained with an LTE heating followed by vibrational-enhanced recycling as a function of the heating phase temperature (T_1).

At every pressure, the optimal T_2 is 300 K. When $T_2 = 300$ K, adding more dilution gas does not cost more energy in our model. The dilution ratio impacts CO production in two ways: (i) it increases the CO_2 density, favoring O-CO_2 association over O-O and O-CO recombination, and (ii) it lowers the temperature of the mixture. The optimal dilution ratio

allows to reach a favorable temperature to O-CO_2 association while enriching the mixture in CO_2. The maximal EE as a function of the dilution ratio is reported in Figure 2-38.

Finally, Figure 2-39 shows a map of the EE as a function of T_v and T_1 at the three pressures investigated. It shows the highest EE can be reached over a wide domain of the temperature parameters.

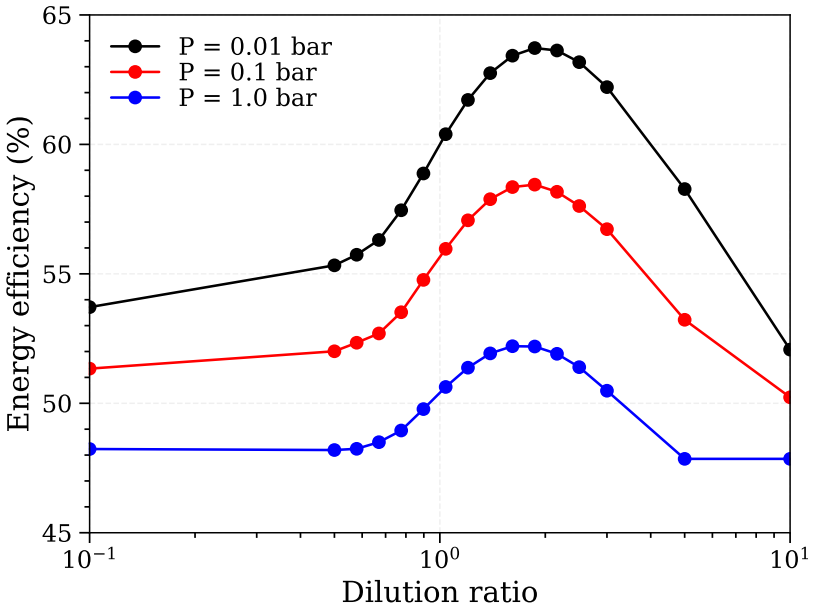

Figure 2-38. Maximal EE obtained with an LTE heating followed by vibrational-enhanced recycling, as a function of the dilution ratio. Contrary to the thermal case, the optimal dilution ratio is around 1.7.

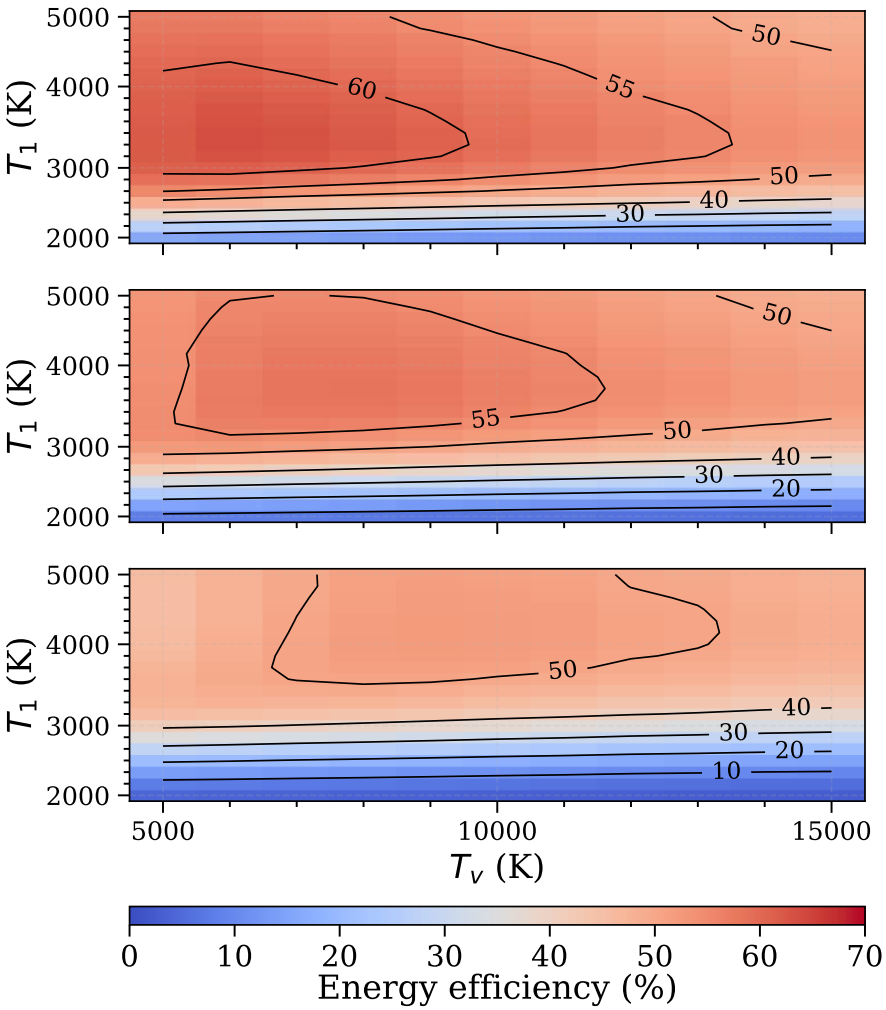

Figure 2-39. EE maps of an LTE heating followed by vibrational-enhanced recycling as a function of the vibrational temperature (T_v) and the heating phase temperature (T_1) at 10^{-2}, 10^{-1}, and 1 bar. Conditions: $T_2 = 300\ K$, $\alpha_{dilu} = 1.4$.

Extension to nonequilibrium conversion

As a reminder, Model 2 includes (i) an isobaric heating phase at LTE, followed by (ii) a perfectly stirred dilution, and (iii) a nonequilibrium recycling phase. It applies, for example, to CO_2 conversion in MW discharges[9]. To extend the applicability of this model, we replace the first phase with an ideal nonequilibrium conversion phase, i.e., we assume that CO_2 is fully converted to CO and O during phase 1. Indeed, many plasma processes can be schematically reduced to a nonequilibrium conversion phase (in the core), followed by a

[9] In a MW discharge, above a certain pressure, most of the energy is deposited in a reduced area (often called "the core"). In the core, the high temperatures make thermal chemistry dominant. The energy and reactive species in the core diffuse to the surroundings and mix with colder CO_2, which is exactly what we aim to model.

dilution (mixing with the surrounding gas), leading to recycling or recombination. This last recombination model will be referred to as Model 3.

Now, in the first phase, the CO_2 is fully converted to CO and O. The gas temperature during this phase – T_1 – is a free parameter that later determines the temperature of the recycling phase. The energy cost of this phase is simply the enthalpy difference between the fully converted gas at T_1 and the initial CO_2 at ambient temperature. As we aim to calculate a majorant of the EE, this phase's course is deliberately ideal.

Then, as in the previous section, a given amount of CO_2 in equilibrium at T_2 is added in a quantity governed by the α_{dilu} parameter. We assume that the reactor is instantly stirred. Finally, the recycling phase can begin. At $t = 0$ – the beginning of the recycling phase – the temperature T_3 is a function of T_1, T_2, and α_{dilu}.

Table 2-6. Summary of the three O recycling models presented in this section.

		Model 1	Model 2	Model 3
Phase 1: heating		LTE, at $T_1 \in [300; 5000]$ K	LTE, at $T_1 \in [300; 5000]$ K	Arbitrary conversion $\phi \in [0; 1]$ at $T_1 \in [300; 5000]$ K
Phase 2: recycling	Dilution	$\alpha_{dilu} \in [10^{-2}; 10^2]$ $T_2 \in [300; 3000]$ K	$\alpha_{dilu} \in [10^{-2}; 10^2]$ $T_2 \in [300; 3000]$ K	$\alpha_{dilu} \in [10^{-2}; 10^2]$ $T_2 \in [300; 3000]$ K
	Thermal model	$T_v = T_g = T_3$	$T_v \neq T_g$ $T_v \in [5000; 15000]$ K	$T_v \neq T_g$ $T_v \in [5000; 15000]$ K
	Kinetic model	$CO_2 + M \leftrightarrow CO + O + M$ $CO_2 + O \leftrightarrow CO + O_2$ $O_2 + M \leftrightarrow O + O + M$	$CO_2 + M \leftrightarrow CO + O + M$ $CO_2 + O \leftrightarrow CO + O_2$ (*) $O_2 + M \leftrightarrow O + O + M$	$CO_2 + M \leftrightarrow CO + O + M$ $CO_2 + O \leftrightarrow CO + O_2$ (*) $O_2 + M \leftrightarrow O + O + M$
	Energy cost (**)	$m_1(h_1 - h_0)$ $+ m_2(h_2 - h_0)$	$m_1(h_1 - h_0)$ $+ m_2(h_2 - h_0)$ $+E_{v3} + E_{vCO}$	$m_1(h_1 - h_0)$ $+ m_2(h_2 - h_0)$ $+E_{v3} + E_{vCO}$

(*) Nonequilibrium rates obtained using the α-model for each vibrational-specific rates, which are then averaged assuming a Boltzmann VDF.

(**) m_1, m_2 are the initial system mass (before dilution), and the mass added during the dilution. h_0, h_1, h_2 are the mass enthalpy of reference, of the gas at the end of phase 1, and of the dilutant. E_{v3} and E_{vCO} are the energies contained in the CO_2 asymmetric stretch mode and of CO stretch mode.

The calculations are conducted over the same parameter domain as Model 2 (cf Table 2-5). The simulations yield upper bounds for the EE achievable in a nonequilibrium plasma process at 0.01, 0.1, and 1 bar. The results are slightly better than in Model 2. At 0.01 bar, the EE maximum attained in the simulations is 71% (+19 points compared to the thermodynamic limit). This maximum is attained at $T_v = 8000$ K, $\alpha_{dilu} = 1.3$, and $T_1 = T_2 = 300$ K. At 0.1 bar, an EE of 64% (+14 points compared to the thermodynamic limit)

is reached at $T_v = 9000\ K$, $\alpha_{dilu} = 1.1$, and $T_1 = T_2 = 300\ K$. At 1 bar, an EE of 57% (+9 points) is reached at $T_v = 11000$, $\alpha_{dilu} = 1$, and $T_1 = T_2 = 300$ K.

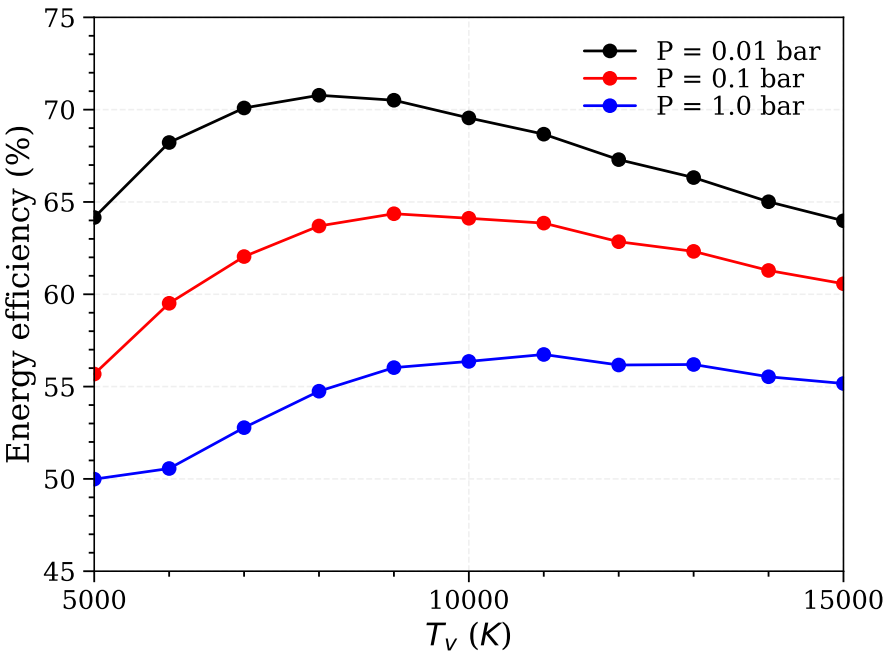

Figure 2-40. Maximal EE obtained in Model 3 as a function of T_v.

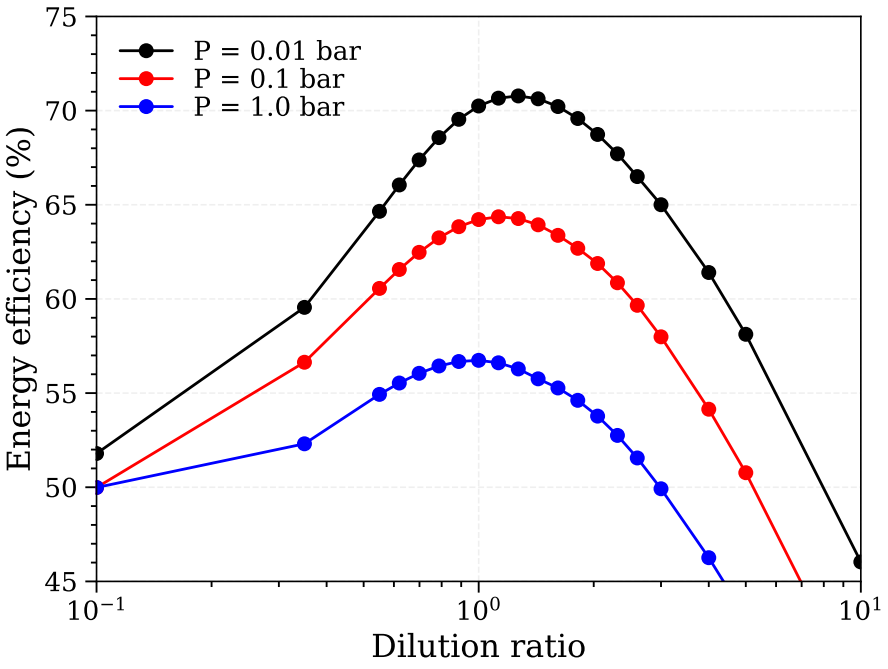

Figure 2-41. Maximal EE obtained in Model 3 as a function of α_{dilu}.

The influence of the vibrational temperature and the dilution ratio on the EE are shown in Figure 2-42 and Figure 2-43. We observe similar trends as Model 2. The EE evolves smoothly

with T_v: the maximal EE is obtained within ± 5% for T_v between 6000 and 11,000 K at 0.01 bar, 5500 and 14,000 K at 0.1 bar, and 7500 K and above 15,000 K at 1 bar.

We find that whatever the pressure, the optimal EE is obtained for $T_1 = T_2 = 300\ K$. Nevertheless, it does not mean that O-CO_2 association can happen at 300 K. This is illustrated in Figure 2-42, representing the temperature, main species amount, and net rates yields by the simulation of Model 3 at $T_1 = T_2 = 300\ K$, $T_v = 10{,}000\ K$, $P = 1\ bar$, $\alpha_{dilu} = 1$. In these conditions, O-CO_2 association overcome O-CO recombination for $t > 30\ ns$ (the instant when the blue line in the bottom graph of Figure 2-42 crosses 0): CO production is enabled by the temperature exceeding 700 K. On this figure, O-CO_2 association is the most favorable (compared to the competing reactions) when T_g $(= T_3)$ is between 1200 and 1500 K.

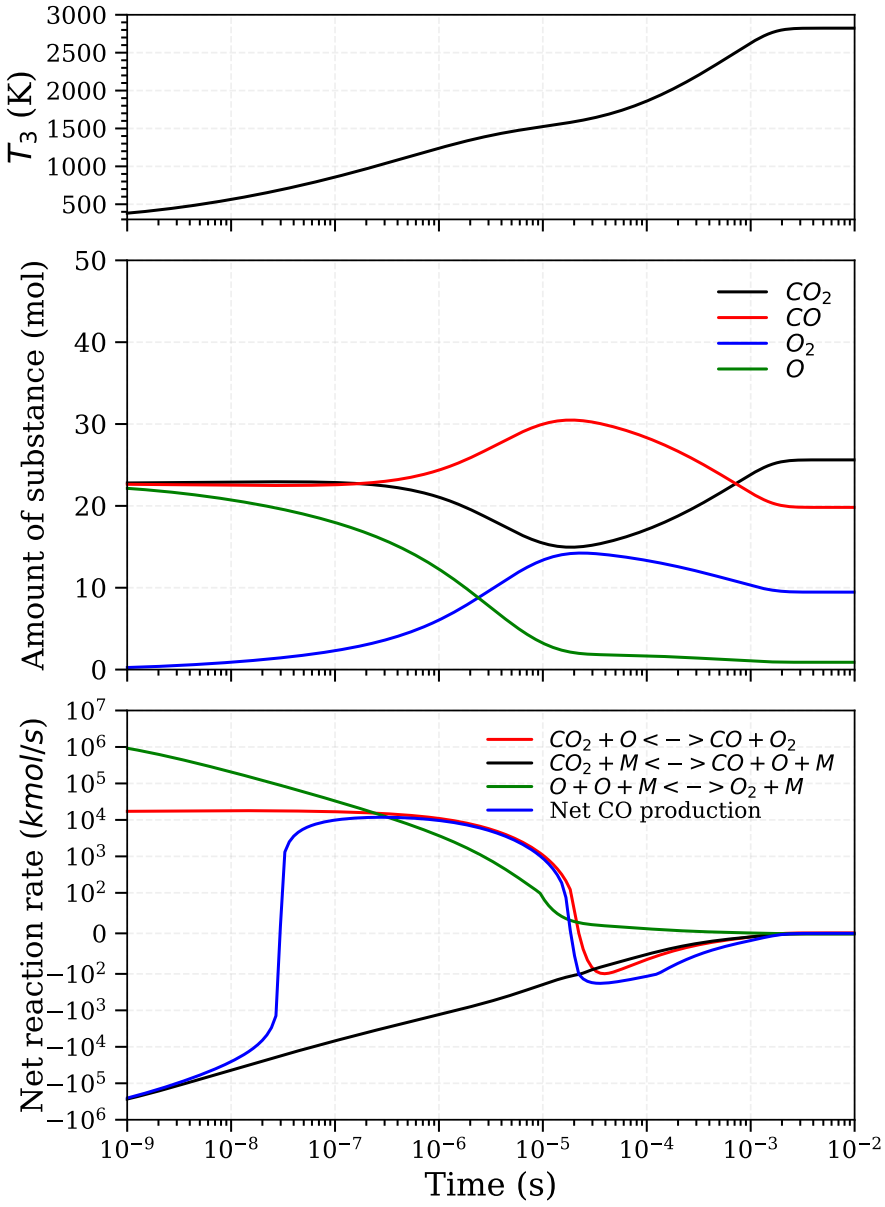

Figure 2-42. Temporal evolution of the gas temperature in the recycling phase T_3 (upper graph), main species amount (middle graph), and net reaction rates (bottom graph) resulting from Model 3, at $P = 1$ bar, $\alpha_{dilu} = 1$, $T_v = 10,000$ K, $T_1 = T_2 = 300$ K.

To study the influence of the gas temperature on O recycling, we launch new simulations of Model 3 on the same parameter domain, but imposing a constant temperature in the recycling phase (T_3). For each T_3, we report in Figure 2-43 the maximal EE obtained (by scanning the rest of the parameter space). The optimal temperature for O recycling (which results from the balance between the high rate constant for O-CO_2 association and the energy cost) is 700 K at 0.01 bar, and the EE stays within ± 5% from its maximum value

(70% here[10]) for T_g in 500 – 1500 K. At 0.1 bar, the optimal gas temperature is 1000 K and the EE stays within ± 5% from its maximum value (62% here) for T_g in 600 – 1700 K. At 1 bar, the optimal gas temperature is 1300 K and the EE stays within ± 5% from its maximum value (54% here) for T_g in 900 – 2000 K.

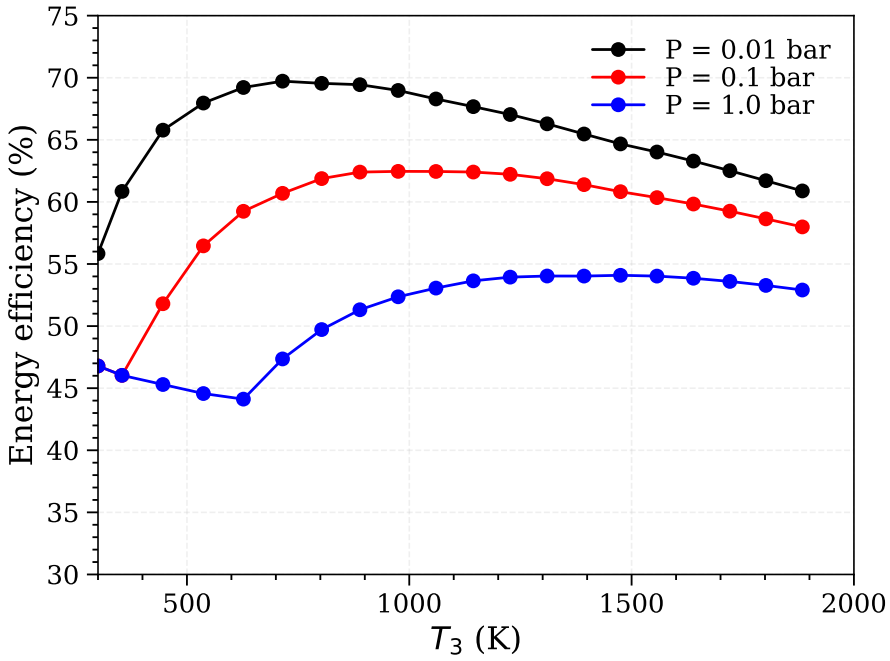

Figure 2-43. Maximal EE obtained in Model 3 as a function of the temperature in the recycling phase.

To conclude, within our assumptions, vibrational excitation allows significant improvements in EE at low pressure but has a moderate effect at high pressure (1 bar). This is due to the higher vibrational excitation needed to overcome the 3-body recombination reactions at high pressure. The higher vibrational excitation needed means a higher energy cost, hence a lower EE. We show that O-CO_2 association needs moderate gas temperatures and high vibrational temperatures to improve the EE. For example, at 1 bar, T_g needs to be between 900 and 2000 K, and T_v between 7500 and 15,000 K to observe an EE of up to 57%. We emphasize that, whatever the pressure between 0.01 and 1 bar, no O recycling occurs at ambient temperature where the O-CO_2 association is too slow. Given the vast parameter domain covered in our simulations, the upper bounds of the EE at 0.01, 0.1, and 1 bar apply to most cold and warm plasma discharges encountered in the literature. These upper bounds and the temperature conditions they require are summarized in Table 2-7, Section 2.3.5.6.

[10] Note that the maximal EEs obtained when imposing a constant T_g are slightly lower than the one obtained when T_g is free (i.e., only governed by the energy conservation equation).

Duration of O recycling

To actually reach the EE computed in the previous subsection, the optimal vibrational and gas temperature conditions must be maintained for a given time, which depends on the pressure, dilution ratio, and temperature conditions. In Sec. 2.3.5.6, this time will be compared to the VT characteristic time to assess the validity of our energy cost calculation.

In Figure 2-44 and Figure 2-45 we report the time when the peak of CO is obtained in the recycling phase, as a function of the vibrational and gas temperatures in the simulations. Figure 2-44 is obtained at 1 bar, whereas Figure 2-45 at 0.01 bar. To achieve 57% EE at 1 bar, $(T_g, T_v) \approx (1300, 11000)\ K$ must be maintained for a few tens of µs. To achieve 70% EE at 0.01 bar, $(T_g, T_v) \approx (700, 8000)\ K$ must be maintained for a few tens of ms.

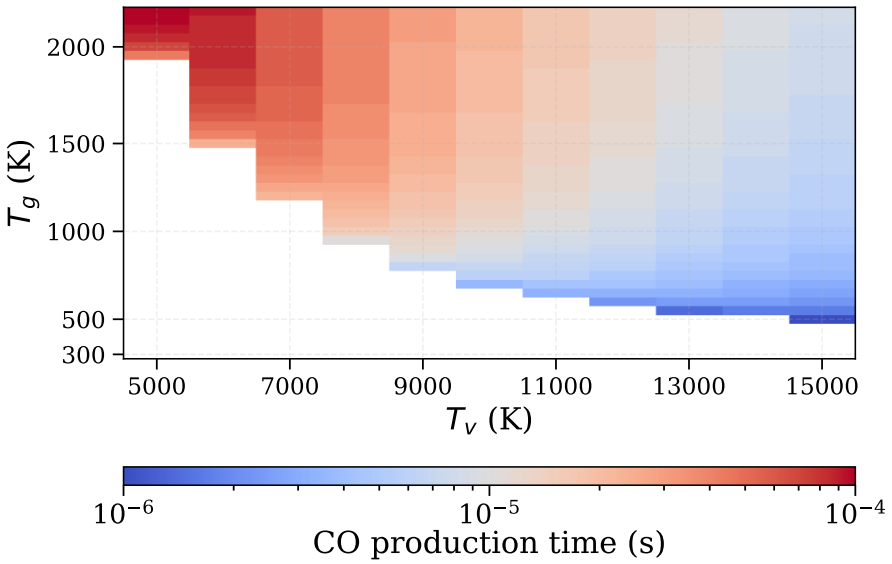

Figure 2-44. Map of the O recycling duration as a function of the vibrational and gas temperatures, maintained constant in the recycling phase. The white area indicates no CO production in the recycling phase. $P = 1\ bar$, $\alpha_{dilu} = 1$, Model 3.

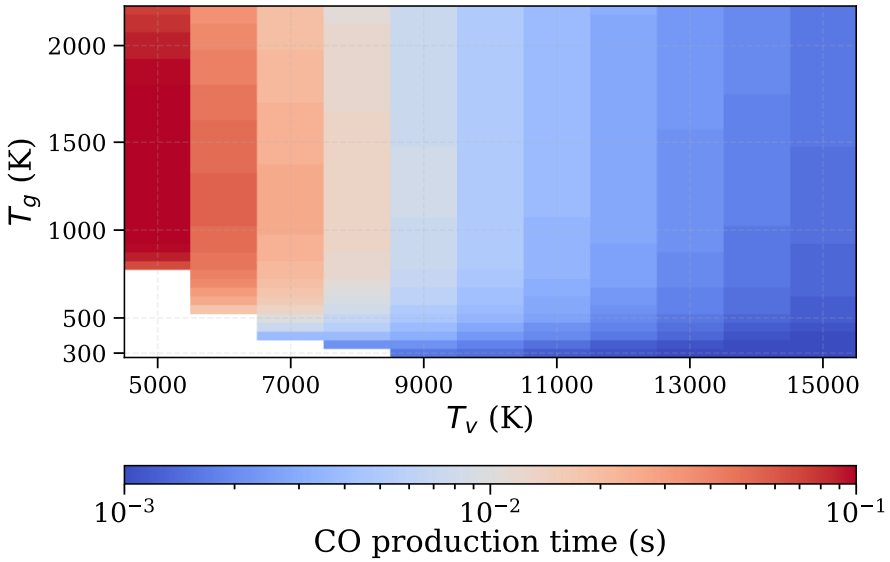

Figure 2-45. Map of the O recycling duration as a function of the vibrational and gas temperatures, maintained constant in the recycling phase. $P = 0.01$ *bar*, $\alpha_{dilu} = 1$, Model 3

2.3.5.5 Electronically enhanced oxygen recycling

We showed that O-CO_2 association is not fast enough at thermal equilibrium to improve the EE above the thermodynamic limit. Vibrational excitation allows the required acceleration. Within the assumptions used in the previous sections ((i) asymmetric stretch mode of CO_2 and CO vibration in equilibrium at T_v, other vibrational modes, rotation, and translation at T_g, and (ii) VT and VV' transfer neglected), there exist VT conditions in which the additional CO produced by the O-CO_2 association is not compensated by the additional energy cost of vibrational excitation, making the EE overcome the thermodynamic limit. Can the same enhancement be achieved by nonequilibrium electronic excitation? One or the other reactant of the O-CO_2 association reaction can be in an electronic excited state. Does it accelerate the O-CO_2 association reaction, and is it favorable from an EE point of view?

As we showed in Sec. 2.3.1, the electronic states of CO_2 dissociate faster than the typical collision time (the latter being about 1-10 ps in a plasma at atmospheric pressure and a few thousand kelvin) after a vertical excitation. In usual cold and warm plasmas, a significant CO_2* excitation can only be achieved by electron-impact vertical excitation. Thus, O-CO_2* cannot happen significantly, because CO_2* instantly dissociates. Furthermore, the vertical excitation of CO_2 electronic states costs more than 8.3 eV: if it produces one CO molecule (by predissociation or by a hypothetic reaction with an O), the EE is still lower than 35%.

The reaction $CO_2 + O(^1D) \rightarrow CO + O_2$ has been studied by (Sedlacek et al. 1989). They showed that 99.8% of the time, the collision between CO_2 and $O(^1D)$ does not result in CO production, but simply in $O(^1D)$ quenching. The energy of $O(^1D)$ – 1.97 eV – goes to gas

heating. Thus, the excitation of O to O(^{1}D) is not an efficient way to favor O-CO_2 association.

Slanger *et al.* (T G Slanger and Black 1978a) studied the products resulting from the interaction between O(^{1}S) and CO_2. They did not observe any CO production from the reaction CO_2 + O(^{1}S) → CO + O_2, i.e. the branching ratio of this reaction is 0. The interaction of CO_2 and O(^{1}S) only results in the quenching of O(^{1}S) to O(^{1}D) and O(^{3}P), and heat. Therefore, the excitation of O to O(^{1}S) does not promote O-CO_2 association and is not beneficial for the EE.

Finally, the other electronic states of O are above 9 eV, thus, even with a branching ratio of unity for the reaction CO_2 + O* → CO + O_2, they would not allow to exceed an EE of 50%.

To conclude, none of the electronic states of CO_2 and O could allow the production of CO with an EE over 50%.

2.3.5.6 Summary and fatal limitations

Summary

We summarize the results from our thermal O recycling model (Model 1) and vibrationally-enhanced O recycling models (Model 2 & 3) in Table 2-7. We add the theoretical EE obtained in an LTE process followed by absolute quenching (the thermodynamic limit, defined in Sec. 2.3.3), and SIQ (Figure 2-22). Overall, in this section, we showed that:

1. Under thermal equilibrium, none of the chemical trajectories overshoot the EE thermodynamic limit: a thermal process followed by AQ cannot overcome the EE thermodynamic limit (Sec. 2.3.5.3, Model 1). The high gas temperature needed to promote the O-CO_2 association over O-O and O-CO recombination leads to a high remaining O content (because of the reverse reactions), i.e. the energy is not fully converted to CO (in accordance to the LTE).
2. Under favorable assumptions, vibrational excitation accelerates the O-CO_2 association over the competing reactions at a reduced energy cost, and thus allows, to overcome the EE thermodynamic limit (Sec. 2.3.5.4, Models 2 & 3). The lower the pressure, the more the limit is exceeded.
3. Even with a high T_v, the recycling requires a relatively high T_g (see Table 2-7).
4. To overcome the thermodynamic limit, the optimal T_v, T_g conditions must be maintained for a few tens of ms at 0.01 bar, and for a few tens of µs at 1 bar (Figure 2-44 and Figure 2-45).

5. The electronic excitation of the plasma is not favorable to O recycling, i.e., it does not accelerate O-CO_2 association at a cost lower than 5.5 eV. Consequently, in a nonequilibrium (and catalyst-free) plasma, the only way to overcome the EE thermodynamic limit is the vibrationally-enhanced O-CO_2 association, we just studied.

Table 2-7. Summary of the energy efficiencies obtained in our O recycling models (thermal recycling and vibrationally-enhanced recycling), compared to the thermodynamic limit and the theoretical case of LTE conversion followed by SIQ.

Pressure (bar)		**0.01**	**0.1**	**1**
Thermodynamic limit (LTE + AQ)	*EE*	52%	50%	48%
	Conditions	T_g = 2,700 K	T_g = 3,000 K	T_g = 3,300 K
LTE + SIQ	*EE*	74%	71%	67%
	Conditions	T_g = 3,300 K	T_g = 3,700 K	T_g = 4,200 K
Thermal recycling (Model 1)	*EE*	52%	50%	48%
	Conditions	$T_1 \geq$ 2,700	$T_1 \geq$ 3,000	$T_1 \geq$ 3,300
Model 2 LTE conversion, followed by vibrational-enhanced recycling.	*EE*	64%	58%	52%
	Conditions (*)	$T_g \approx$ 1,500 – 1,800 K $T_v \approx$ 4,000 – 9,000 K	$T_g \approx$ 1,700 – 2,100 K $T_v \approx$ 5,000 – 11,500 K	$T_g \approx$ 1,900 – 2,500 K $T_v \approx$ 6,000 – 14,000 K
Model 3 Arbitrary nonequilibrium conversion, followed by vibrational-enhanced recycling.	*EE*	71%	64%	57%
	Conditions (*)	$T_g \approx$ 500 – 1,500 K $T_v \approx$ 6,000 – 11,000 K	$T_g \approx$ 600 – 1,700 K $T_v \approx$ 6,500 – 14,000 K	$T_g \approx$ 900 – 2,000 K $T_v \approx$ 7,500 – 15,000 K

(*) For Model 2 & 3, we give the range of conditions allowing to reach the EE maximum ±5%.

Limitations

By estimating the feasibility of O recycling, we aimed to calculate an upper bound of the EE a plasma process can achieve. Thus, some of our assumptions are very favorable.

First, we assumed absolute quenching (AQ) at the peak of CO amount. In a real system, the cooling is rarely fast enough to completely prevent CO recombination to CO_2. We estimated in Sec. 2.3.4 the cooling rate needed to achieve AQ.

Second, in the nonequilibrium models – Model 2 & 3 – we assumed that only the asymmetric stretch mode of CO_2 and the vibrational mode of CO are at T_v. In reality, VV' and VT transfers leak a fraction of the vibrational energy to other modes.

Third, in Model 2 & 3, we assumed that only the O-CO_2 association reaction (and its reverse) is impacted by vibrational excitation. This is motivated by the fact that only this reaction can lead the EE above 53%. Actually, in the recycling phase, CO_2 + M ↔ CO + O + M (reaction enthalpy of 5.5 eV), and O_2 + M ↔ O + O + M (reaction enthalpy of 5.2 eV) compete with CO_2 + O ↔ CO + O_2 (reaction enthalpy of 0.35 eV), depleting the vibrational enery and reducing the EE.

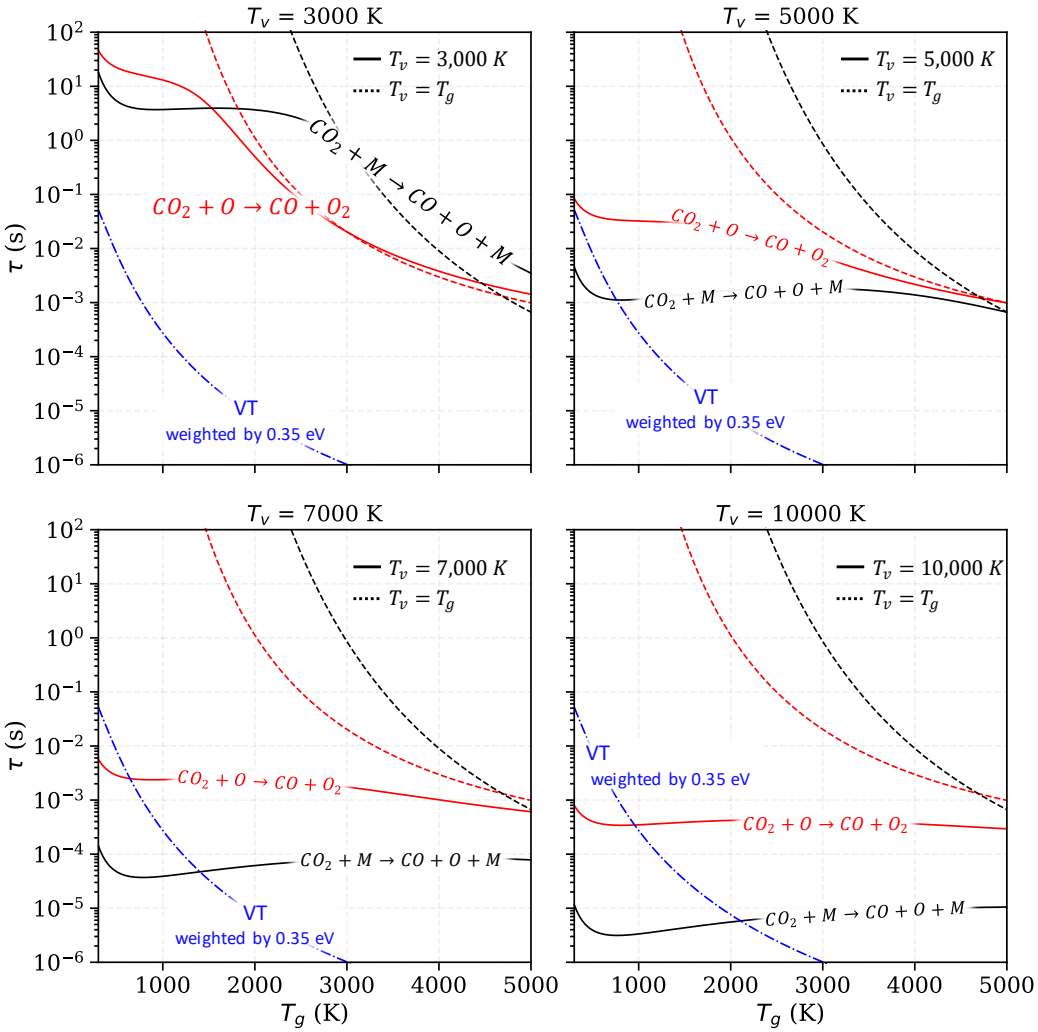

Figure 2-46. Characteristic time of O-CO_2 association (red), heavy-particle impact dissociation of CO_2 (black), and VT transfer weighted by 0.35 eV (blue dash dot), calculated at 0.01 bar. The solid lines represent rate constants in VT nonequilbrium, and the dotted lines represent the rate constants at thermal equilibrium.

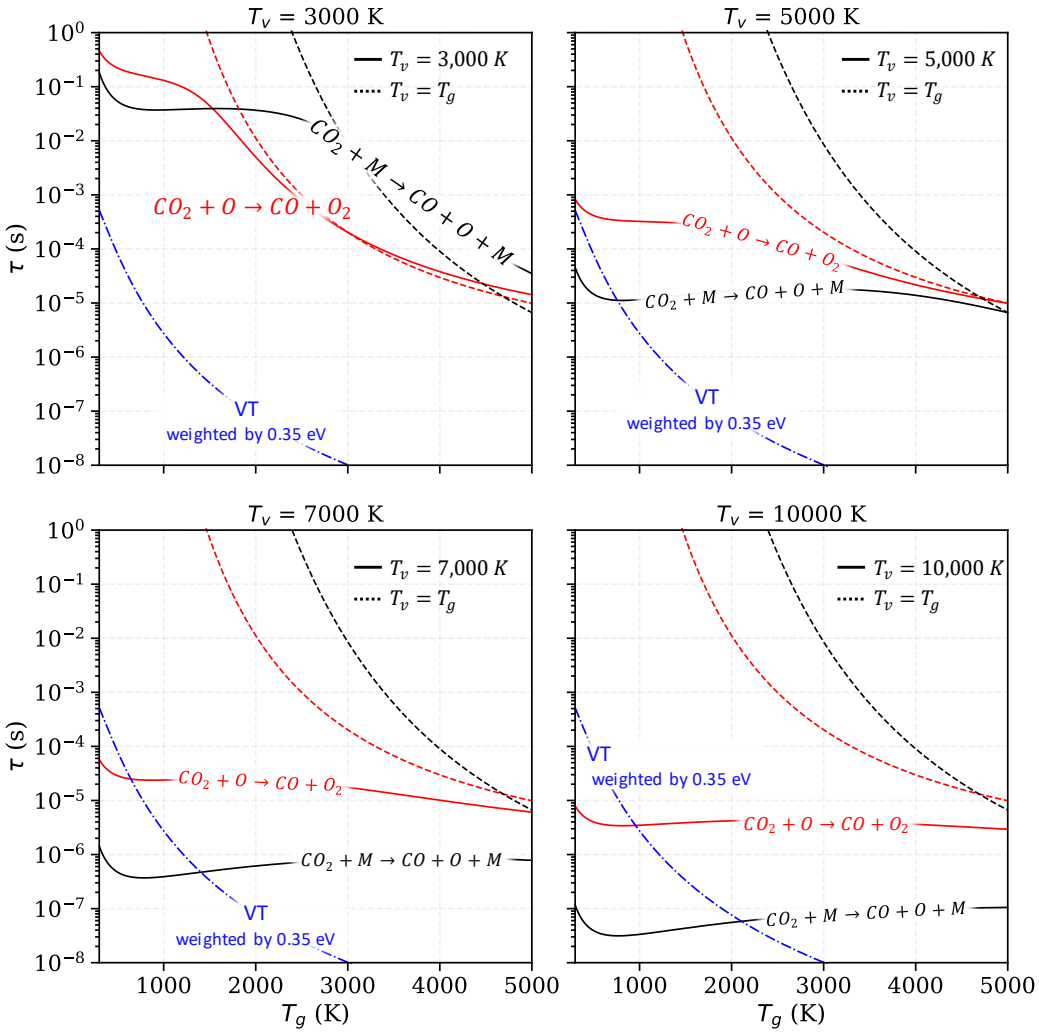

Figure 2-47. Characteristic time of O-CO_2 association (red), heavy-particle impact dissociation of CO_2 and O_2 (black and green), and VT transfer weighted by 0.35 eV (blue dash dot), calculated at 1 bar. The solid lines represent the rate constants in VT nonequilbrium, and the dotted lines represent the rate constants at thermal equilibrium.

In Sec. 2.3.2.2, we have calculated the characteristic time of VT transfer weighted by the O-CO bond energy (5.5 eV), according to Eq. 2-7. Here, we do the same calculation, but we weight the characteristic time by 0.35 eV, which is the reaction enthalpy of O-CO_2 association. We obtain the characteristic time needed for the vibrational states to loose 0.35 eV to the translation. The characteristic times calculated at 0.01 and 1 bar are reported in Figure 2-46 and Figure 2-47.

In these figures, we add the characteristic times of the vibrationally-enhanced O-CO_2 association, and vibrationally-enhanced dissociation of CO_2 by heavy-particle impact (which models the vibrational dissociation pathway). To obtain the characteristic time, we assume for each reaction that it is the only one contributing to CO production, and we integrate the equation between $n_{CO} = 0$ and $n_{CO} = n_{tot}/2$. We assume that $n_O = n_{CO2} = n_{tot}/2$,

which is the most favorable configuration for O-CO_2 association. For O-CO_2 association, we have:

$$\frac{dn_{CO}}{dt} = k_{O-CO2}(T_g, T_v) \cdot n_O n_{CO2} \sim k_{O-CO2}(T_g, T_v) \cdot \frac{n_{tot}^2}{4} \qquad \text{Eq. 2-29}$$

where $k_{O-CO2}(T_g, T_v)$ is the nonequilibrium rate constant of O-CO_2 association and is calculated using the Fridman-Macheret α-model, as in Sec. 2.3.5.4. After integration between $n_{CO} = 0$ and $n_{CO} = n_{tot}/2$ we obtain:

$$\tau_{O-CO2} \sim 2 \cdot (k_{O-CO2}(T_g, T_v) \cdot n_{tot})^{-1} \qquad \text{Eq. 2-30}$$

For heavy-particle impact dissociation of CO_2, we have:

$$\frac{dn_{CO}}{dt} = k_{h-CO2}(T_g, T_v) \cdot n_{CO2} n_{tot} \sim k_{h-CO2}(T_g, T_v) \cdot \frac{n_{tot}^2}{2} \qquad \text{Eq. 2-31}$$

where $k_{h-CO2}(T_g, T_v)$ is the nonequilibrium rate constant. It is calculated using the Fridman-Macheret α-model with $\alpha = 1$. As in Sec. 2.3.5.4, the rates of the vibrational specific dissociation are averaged over a Boltzmann distribution. The base rate constant is the equilibrium rate constant from (Park et al. 1994). After integration we obtain:

$$\tau_{h-CO2} \sim (k_{h-CO2}(T_g, T_v) \cdot n_{tot})^{-1} \qquad \text{Eq. 2-32}$$

According to Model 3, at 0.01 bar, the optimal (T_g, T_v) promoting O recycling are (700, 8000) K and should be maintained for more than 10 ms (Figure 2-45). According to Figure 2-46, at 700 K and 0.01 bar, the VT characteristic time is about 1 ms. At 1 bar, the optimal (T_g, T_v) promoting O recycling are (1300, 11000) K and should be maintained for more than 10 µs (Figure 2-44). However, at 1300 K and 1 bar, the VT characteristic time is about 1 µs. Therefore, in both cases, the VT transfer is about 10 times faster than the O-CO_2 association. Consequently, (i) maintaining the desired VT temperatures long enough to allow for vibrationally-enhanced O recycling would be extremely challenging in a practical system. (ii) Even if attained, it would require much more energy than accounted for in Models 2 & 3. In the current models, the vibrational energy cost represents 10-20% of the total energy cost. We expect that the additional energy cost due to VT transfer would be at least 10 times more, i.e. 100-200% of the total, dividing the EE by 2-3 and making it fall far below the thermodynamic limit.

Figure 2-46 and Figure 2-47 also show that in the VT conditions favorable for O recycling, vibrationally-enhanced heavy-particle impact dissociation of CO_2 is about 100 times faster than O-CO_2 association. At 0.01 bar, T_g = 700 K and $T_v \approx$ 8,000 K, $\tau_{h-CO2} \approx$ 30 µs. At 1 bar, T_g = 1,300 K and $T_v \sim$ 10,000 K, $\tau_{diss} \approx$ 40 ns. Vibrational excitation promote the reaction CO_2 + M → CO + O + M much more than CO_2 + O → CO + O_2. Thus, O-CO_2

association should stay marginal, and the EE no higher than 53% (which correspond to 5.5 eV / CO produced, ie the reaction enthalpy of $CO_2 + M \rightarrow CO + O + M$).

Conclusion on O recycling

Overvall, Models 2 & 3 and our comparison of the characteristic times of VT transfer, vibrationally-enhanced heavy-particle impact dissociation of CO_2, and vibrationally-enhanced O-CO_2 association show that:

1. VT transfer is faster than vibrationally-enhanced O-CO_2 association. Exciting the vibration to accelerate O-CO_2 association over the competing reactions costs too much energy to increase the EE above 53%.
2. Vibrational excitation favours heavy-particle impact dissociation of CO_2 (whose minimum energy cost is 5.5 eV) over O-CO_2 association, making the latter reaction marginal in the total CO production.

Therefore, we conclude that vibrational excitation does not allow O recycling. Since thermal or electronically-enhanced O recycling do not occur neither, we can definitely close this path. Consequently, the EE of a catalyst-free plasma process cannot exceed 53%.

2.3.6 Comparison of the optimal dissociation pathways

In Table 2-8, we summarize the EE upper bounds we set in Sec. 2.3. Let us go back to the goals we set for this part. (i) The maximum value of EE that can be achieved in a plasma discharge without the help of a catalyst is 52-53% at 0.01 bar and 48-53% at 1 bar. (ii) The low ends of these ranges can be achieved by a thermal process followed by fast quenching of the products. This was observed experimentally in (Bongers et al. 2017; den Harder et al. 2016; van Rooij, Van Den Bekerom, et al. 2015). The high end of these ranges could be achieved via the vibrational dissociation, at high ionization degree and low gas temperature (2.3.2.5), but these conditions are challenging to meet in practice. The advantage of converting CO_2 at low temperature is that it would ease the quenching phase (see Sec. 2.3.4).

Let us speculate on the feasability of efficient vibrational dissociation at low temperature (300 – 1000 K). Since the EE stays lower than 53% in the pure vibrational pathway, 47% of the input energy ends up in gas heating and non-desired products, mainly O atoms. Since the O atoms recombines to O_2 and CO_2 at low temperature, the energy lost is ultimately in the form of heat. An EE of 53% means that each CO molecule costs 5.5 eV to be produced. Since 2.9 eV are usefull, 2.6 eV is released when the O atoms recombine (which is all the faster the lower temperature). Thus, either the heat must be extracted quickly – and in this case, no savings are made on the cooling system compared to a thermal plasma – or the power density must stay low. In the latter case, in addition to reduce the conversion, it

would come at the expense of the high ionization and vibrational temperature needed to dissociate efficiently, as shown in the NRP glow discharge (Pannier 2019) for example. As stated in our review of the literature, during the last decade, low temperature plasmas such as glow, or GA discharges demonstrate low EE (typically lower than 10%).

Table 2-8. Summary of the EE of each dissociation pathways, of the thermodynamic calculations, and kinetics simulations.

Pathway	**EE in the ideal quenching scenario**		
Pure vibrational dissociation	53%		
Pure electronic dissociation	25%		
Thermodynamic calculation			
	P = 0.01 bar	P = 0.1 bar	P = 1 bar
Thermodynamic limit (LTE + AQ)	52%	50%	48%
Kinetic simulation			
Thermal recycling (2.3.5.3)	52%	50%	48%

2.4 Analysis of CO_2 plasmalysis in warm plasmas

As we saw in the previous parts, the EE hinges upon two pivotal stages: efficient conversion in the discharge stage and preservation of the products in the subsequent cooling stage. While both vibrational and thermal mechanisms yield the same EE, the cooling stage emerges as the differentiating factor. This cooling stage must be extremely fast at high plasma temperature (for example, 1000 K/µs is required to preserve 95% of the CO produced in a thermal plasma at 1 bar), but slower if the temperature of the plasma is lower (for example, 50 K/µs to preserve 95% of the CO produced in a non-thermal plasma at 500 K). Consequently, optimal EE demands the discharge stage to achieve maximal EE at the lowest temperature possible. Herein lies the potential advantage of non-equilibrium electronic and vibrational dissociation pathways. However, the experiments from the literature show that cold plasmas are limited to low EEs (typically, below 10%). Going through high temperatures and a fast cooling is then indispensable, but warm plasmas, where the temperature is maintained below 3,000 K could be more favorable to the EE than hot plasmas, provided that electronic and vibrational pathways contribute efficiently to the dissociation. We summarize our typologie of plasmalysis processes in Table 2-9.

In the following section, we further analyse some MW, GA, and NRP discharges experiments, which achieve among the best EE results. We focus on the CO production mechanism, in particular on the contribution of nonequilibrium vibrational dissociation, and on the EE achieved.

Table 2-9. Types of plasmalysis processes. ϕ_q is defined as the ratio of CO preserved during the cooling of the plasma. In the quenching stage, the cooling rates are given at $P = 1$ bar.

Plasma type	Discharge stage		Quenching stage		Practical examples
	T_g	Dissociation pathway	$\phi_q > 67\%$	$\phi_q > 95\%$	
Cold plasma	< 1000 K	- Electronic dissociation ($\eta <$ 25%) - Vibrational dissociation ($\eta <$ 53%)	$\frac{dT}{dt} \sim$ 0.1 K/µs for $T_0 =$ 500 K	$\frac{dT}{dt} \sim$ 20 K/µs for $T_0 =$ 500 K	- DBD: $\eta \sim 5-10\%$ - glow DC: $\eta \sim 1\%$ - NRP glow: $\eta \sim 5\%$
Warm plasma	1000 – 3000 K	- Electronic dissociation ($\eta <$ 25%) - Vibrational dissociation ($\eta <$ 53%) - Thermal dissociation ($\eta <$ 48%)	$\frac{dT}{dt} \sim$ 30 K/µs for $T_0 =$ 2,000 K	$\frac{dT}{dt} \sim$ 500 K/µs for $T_0 =$ 2,000 K	- GA: $\eta \sim 20-40\%$ - NRP spark: $\eta \sim 20-50\%$
Hot plasma	> 3000 K	- Thermal dissociation ($\eta <$ 48%)	$\frac{dT}{dt} \sim$ 40 K/µs for $T_0 >$ 3,000 K	$\frac{dT}{dt} \sim$ 1000 K/µs for $T_0 >$ 3,000 K	- MW: $\eta \sim 30-50\%$ - GA - NRP sparks

2.4.1 MW discharges

VT equilibrium

We go back to the experiments presented in Sec. 2.2.2, and reassess the VT nonequilibrium based on the ionization degree criterion established in Sec. 2.3.2.4, Figure 2-16 and Figure 2-17.

In the experiments of (Van Rooij et al. 2015), we estimate that the ionization degree is $\alpha_i < 10^{-7}$, while the gas temperature is above 2,000 K. According to Figure 2-17, under these conditions[11], the electron-impact excitation of the vibration is much slower than VT transfer ($\tau_{VTD}/\tau_{eVD} \sim 10^{-3}$), thus, does not allow to reach VT nonequilibrium.

[11] Figure 2-16 is computed using $E/N = 30$ Td, which is the reduced electric field where the rate of electron-impact excitation of the vibrational states plateaus. If E/N is lower, the rate is lower. If it is higher, is stays approximately the same, but a higher part of the energy goes to electronic excitation. Thus, Figure 2-16 gives an upper bound of the τ_{VTD}/τ_{eVD} ratio.

In (den Harder et al. 2016), the ionization degree is $\alpha_i < 10^{-4}$, while the gas temperature is between 3,000 and 5,000 K. Under these conditions, the electron-impact excitation of the vibration is again much slower than the VT transfer ($\tau_{VTD}/\tau_{eVD} \sim 10^{-1}$).

In both (Spencer and Gallimore 2013) and (Sun et al. 2017), $\alpha_i \sim 10^{-4}$ is reached but the gas temperature is 6000 K, so this high ionization degree is still less than the threshold needed to maintain VT nonequilibrium ($\tau_{VTD}/\tau_{eVD} \leq 10^{-1}$) . Also, there is no point in maintaining VT nonequilibrium at such high temperatures, as CO_2 is already fully converted by thermal chemistry.

In these examples, CO production is dominated by thermal processes. They illustrate the fact that achieving a high degree of ionization while maintaining a low gas temperature is challenging, and consequently, so is VT nonequilibrium.

Energy efficiency limit

In MW discharges, the thermal-ionization instability leads to different discharge modes characterized by the radial extent of the plasma. These modes were studied in particular by (Wolf, Righart, et al. 2020). The best EE results in MW discharges have been reported for pressure in excess of 100 mbar (see for instance, (Bongers et al. 2017; Van Rooij et al. 2015)), which corresponds to the low confinement and high confinement modes (Wolf, Righart, et al. 2020). In these regimes, the MW energy is deposited in a confined region – the core – surrounded by a colder CO_2 shell. The hot mixture from the core is diluted in the cold CO_2 from the shell (van den Bekerom et al. 2019).

Thus, these MW conversion experiments are analogous to the situation modeled in Model 1 (Sec. 2.3.5.3). The specificity of the discharge lies in the particular conversion temperature (T_1), dilution ratio (α_{dilu}), diluent temperature (T_2), and the spatial and temporal evolution of these parameters. As the values of these parameters are included in the range we explored with Model 1 (Sec. 2.3.5.3), the EE majorant we predict applies to this discharge. According to this model, as long as the gas stays in thermal equilibrium in a MW discharge, the EE cannot cross the thermodynamic limit. This is consistent with the EE results reported over the past decade.

The case of pulsed MW

In (Soldatov et al. 2022), a MW pulse of 2.5 µs allows to reach VT nonequilibrium with $T_g \sim$ 3000-4000 K, and $T_v \sim$ 7000-8000 K. However, VT transfer leads the gas temperature to thermalize with T_v in about 2 µs. According to Model 3, these T_g, T_v conditions should be maintained for more than 10 µs to promote O recycling. Coherently, Soldatov et al. report an EE below 30%.

2.4.2 Gliding arc discharges

VT equilibrium

In the GA discharge simulation of (Heijkers and Bogaerts 2017), the ionization degree is $\alpha_i \sim 10^{-6}$ and the gas temperature $T_g \sim 3{,}000$ K. Thus, according to Figure 2-17, $\tau_{VTD}/\tau_{eVD} \leq 10^{-2}$, i.e. the VT transfer is much faster than the electron-impact excitation of the vibration.

In another study (Wang et al. 2017), the same group presented a 2D model of their GA discharge. They obtained similar gas temperatures (about 2500 K in the arc) but did not report the vibrational temperature. The ionization degree was $\alpha_i \sim 10^{-6} - 10^{-5}$, so $\tau_{VTD}/\tau_{eVD} \leq 10^{-1}$. We can predict that $T_v \approx T_g$ in their experiment and model.

In this latter study, Wang et al. predicted that 97% of the CO is produced by collisions with an O atom or another heavy species. As in Heijkers et al.'s study, the dissociation may occur from CO_2 vibrationally excited states, but if the vibration and translation are in equilibrium, all of this is just the fine description of a thermal dissociation mechanism.

Energy efficiency

Like MW discharges, GA discharges can be schematically modeled as a heated core which is then diluted in the surrounding gas. The specificity of the discharge lies in the particular T_1, α_{dilu}, T_2, and the spatial and temporal evolution of these parameters. As the values of these parameters are included in the range we explored with Model 1 (Sec. 2.3.5.3), the EE majorant we predict applies to this discharge. So, it is not surprising that the reported EE measurements in GA discharges are less than 50%.

2.4.3 NRP discharges

As mentioned in Chapter 1 and Sec. 2.2.4, NRP discharges have several advantages that make them a promising candidate for efficient CO_2 conversion. They can reach high ionization degree, VT nonequilibrium, and a wide range of temperatures. They generate shock waves and fast hydrodynamics that could provide favorable quenching trajectories for the products. As mentioned previously, the low-temperature path has been closed by (Pannier 2019), who showed that the glow regime does not exceed an EE of 5%. The warm and hot paths taken in the NRP-spark regime are promising for CO production.

CO_2 conversion in the NRP-spark regime has been studied over the past decade in several teams. However, in the careful examination of the experimental and numerical results of the literature, we spotlight 2 key issues, likely to upset the current understanding of the CO production mechanism in NRP-sparks. Resolving these issues will be the aim of the following Chapters.

A high electron density

In recent work, Ceppelli *et al.* (M. Ceppelli et al. 2021) measured the electron density, the electron temperature, and the gas temperature with nanosecond temporal resolution in an NRP discharge. Using OES, they measured electron densities of about 10^{18} cm^{-3}, electron temperatures of 2–3 eV, and gas temperatures from 500 to 2000 K. During the voltage pulse, the ionization degree is more than 10%, and the gas temperature about 1,000 K.

These OES measurements have not been compared with modeling results yet, but Heijkers's *et al.* simulated similar conditions (see the case $SEI = 0.7\ eV \cdot molec^{-1}$ in (Heijkers et al. 2019b)). In these simulations, the gas and electron temperature are in qualitative agreement with the measurements of (M. Ceppelli et al. 2021), but the simulated peak electron density ($n_e \sim 10^{17}\ cm^{-3}$) is 10 times lower than in the experiment ($n_e \sim 10^{18}\ cm^{-3}$). In relatively close conditions ($SEI = 0.3\ eV \cdot molec^{-1}$), Pannier's simulation of an NRP discharge (Pannier 2019) predicted an electron density peaking at 10^{16} cm^{-3}, i.e., a factor of 100 lower than Ceppelli *et al.*'s measurement.

In light of the work of (Minesi et al. 2020, 2021), the very high electron density measured by Ceppelli *et al.* questions the nonequilibrium nature of the NRP spark. An electron density of 10^{18} cm^{-3} could trigger the thermalization of the plasma at the electron temperature. Moreover, Ceppelli *et al.* performed their measurements at midgap, whereas Pannier (Pannier 2019) observed that the plasma was inhomogeneous with the existence of a hot kernel near the electrodes: therefore, the near-electrode electron density might be higher than 10^{18} cm^{-3} in (M. Ceppelli et al. 2021). The CO production pathway in a thermal spark would be completely different from the non-thermal pathway described by the current models (Heijkers et al. 2019; Pannier 2019). The hydrodynamics of the post-discharge would be also impacted, resulting in a different cooling trajectory.

A low conversion degree

The same group carried out CET-LIF measurements to measure the temporal evolution of CO_2 conversion in the plasma (Montesano et al. 2023). They were able to measure the conversion as soon as 40 ns and 80 ns. The next points are a few µs later. At 40 ns, the measured CO_2 conversion is below 8%, whereas it reaches 40% at 3 µs. Montesano *et al.* attributed this delayed dissociation to the role of metastable electronic states.

The low conversion degree of 8% at 40 ns is surprising. Indeed, the 0D-kinetic models of Pannier and Heijkers *et al.* show that most of the electron energy goes to the electronic states of CO_2, because of the high reduced electric field reached in NRP-spark discharges (typically, it peaks at 100 – 500 Td). Furthermore, our study of CO_2 electronic states (Sec. 2.3.1) shows that electron-impact excitation of CO_2 electronic states leads to predissociation in less than one picosecond. Thus, the low conversion at 40 ns indicates a low excitation of

CO_2 electronic states at these early times, contrary to the predictions of the models. CO being produced at the µs time scale suggests a thermal mechanism (possibly enhanced by vibrational nonequilibrium).

These conversion measurements were performed using the collisional energy transfer LIF (CET-LIF) diagnostic (L. M. Martini et al. 2018). A possible limit is that Montesano *et al.* did not account for the quenching of OH* by O colliders, whereas the OES measurements (M. Ceppelli et al. 2021) suggest that a significant amount of O is present in the mixture.

Next steps

Overall, the kinetics of CO production in NRP discharges is the subject of controversy. The recent electron density and conversion measurements (M. Ceppelli et al. 2021; Montesano et al. 2023) cast doubts on the understanding gained with the recent kinetic models (Heijkers et al. 2019; Pannier 2019).

In the following chapter, we will first attempt to reproduce the EE measurements of (Montesano et al. 2020), the best EE results obtained in NRP discharges. Then, among the many open topics, we will focus on the question of the spark thermalization. We will use optical emission spectroscopy (OES) to provide additional electron and excited species measurements. These measurements should allow us to settle the nonequilibrium nature of the NRP-sparks in CO_2, which is a first essential step towards elucidating the CO production mechanism.

2.5 Conclusions

In this chapter, we first reviewed the literature on CO_2 plasmalysis (Sec. 2.2). We highlighted the gap between the energy efficiencies (EE) achieved in the 1980s and today. In the 1980s, the over 80% EEs was attributed to the high nonequibrium excitation of CO_2 vibration while the gas temperature was maintained below 1,000 K. However, the best EE results in the last decade are below 50%, and have been obtained in plasmas near thermal equilibrium, with T_g exceeding 3,000 K during the process. The low temperature discharge have shown low energy efficiencies, typically 5-10%. These discrepancies between the EE results then and now call into question the vibrational dissociation pathway, which is the commonly accepted route to high efficiencies.

Thus, we aimed to reassess the maximum EE of a plasma process, and the kinetic pathway to achieving it (Sec. 2.3). We schematized plasmalysis processes in two stages: first, a "discharge stage", where energy is added to the system, leading to the production of CO, O_2, and radicals; second, a "quenching stage", where these products react under the effects of the residual heat and excitation of vibrational and electronic modes.

We reviewed the EE of some emblematic pathways of the discharge phase, summarized in Table 2-8. We recalled that the vibrational and thermal dissociation pathways have similar upper bounds for the EE, near 50%. We emphasized that the quenching stage is the differentiating stage. First, in order to prevent the recombination of the CO molecules (Absolute Quenching), the products must be cooled down at tremendous rate. For example, preserving 95% of the CO produced in a thermal plasma at 1 bar requires a cooling rate of 1000 K/µs (Sec. 2.3.4). Second, an EE of 53% cannot be overcome without "O recycling", i.e. the use of the chemical energy of the O atoms to produce CO at a reduced energy cost via the O-CO_2 association reaction. To achieve O recycling, O-CO_2 association must be selectively favored over O + CO + M and O + O + M reactions at a reduced energy cost.

To understand which conditions promote O recycling, we used simple kinetic models – Model 1 to 3 – based on the 2-steps decomposition of a plasma process. The originality of the Models lies in the modelisation of the diffusion and convection of the products in the surrounding gas as an instantaneous dilution controlled by a variable parameter. By varying the parameters of the discharge and quenching stages (pressure, conversion degree, and temperature in the first stage, dilution and temperature in the second stage), we simulated representative conditions of most plasma discharges.

Using Model 1, we showed that whatever the initial chemical nonequilibrium and temperature, O recycling (in the sense of this work) is impossible at *thermal equilibrium* because of the competing recombination reactions (Sec 2.3.5.3). In a plasma in thermal equilibrium, the EE is capped by the thermodynamic limit.

Then, we study the vibrational and electronic enhancement of O-CO_2 association. First, we show that vibrational excitation does accelerate O-CO_2 association. However, Models 2 & 3 (2.3.5.4) and our comparison of the characteristic times of VT transfer, vibrationally-enhanced heavy-particle impact dissociation of CO_2, and vibrationally-enhanced O-CO_2 association (2.3.5.6) show that:

1. VT transfer is faster than vibrationally-enhanced O-CO_2 association. Therefore, exciting the vibration to accelerate O-CO_2 association over the competing reactions costs too much energy to allow the EE to exceed 53%.
2. Vibrational excitation favours heavy-particle impact dissociation of CO_2 over O-CO_2 association, making the latter reaction marginal in the total CO production.

Furthermore, exciting O and CO_2 electronic states require a lot of energy, and they do not promote O-CO_2 association (2.3.5.5). We conclude that whatever the electronic, vibrational, and translational temperature conditions, and whatever the gas composition, O recycling cannot occur in a CO_2 plasma. Consequently, the EE of a (catalyst-free) plasma process cannot exceed 53%.

Even if it does not allow to overcome an EE of 53%, nonequilibrium conversion (via the electronic or vibrational pathways) can be favorable to the EE, since it allows to produce CO at a lower temperature than in a thermal process, and thus, limits CO recombination in the cooling phase (Sec. 2.3.4). Warm plasmas are not expected to exceed the EE of hot plasmas, which has already reached 50% (Bongers et al. 2017; Van Rooij, Van den Bekerom, et al. 2015), but they could be easier to operate at iso-EE. Thus, based on the criterium established in Sec. 2.3.2.4 for efficient vibrational dissociation, we analyze some MW and GA experiments of the literature, showing that nonequilibrium vibrational dissociation is marginal in these discharges. NRP discharges in the spark regime are also a promising candidate to approach the 53% EE limit. They can achieve vibrational and electronic nonequilibrium allowing CO_2 to be converted below 3,000 K, offer a wide temperature range, and generate powerful hydrodynamic effects that could rapidly quench the products.

However, the current models cannot explain the recent electron density ($n_e \sim 10^{18}$ cm^{-3} in the experiments vs $n_e \sim 10^{17}$ cm^{-3} in the models) and conversion measurements, which casts doubt on the current understanding of the CO production pathway. In particular, electron density above 10^{18} cm^{-3} could trigger the thermalization of the plasma, radically changing the CO production mechanism, and the cooling trajectory.

In the following chapter, we will first try to reproduce the EE measurements of (Montesano et al. 2020), the best EE results obtained in NRP discharges. Then, we will focus on the question of the spark thermalization. We will use optical emission spectroscopy (OES) to provide additional electron and excited species measurements. These measurements should allow us to settle the nonequilibrium nature of the NRP-sparks in CO_2, which is a first essential step towards elucidating the CO production mechanism in these discharges.

Take-away messages of Chapter 2

- Achieving high energy efficiencies (EE) strongly relies on the quenching stage, where (i) the products must be cooled down at high rates, and (ii) the radicals react to new products.
- To exceed an EE of 53%, O recycling is necessary, i.e. the plasma conditions must selectively favor O-CO_2 association over O + CO + M and O + O + M recombination reactions in the quenching stage, so that the chemical energy in the O atoms is reused to produce CO at a reduce energy cost.
- For a plasma in thermal equilibrium, for any temperature or composition from 300-5000 K and 0-100% CO_2 conversion, O recycling is impossible.
- Vibrational and electronic excitation does not promote O recycling either, because the additional energy input needed to accelerate O-CO_2 association is too high. Consequently, the EE of a (catalyst-free) plasma process cannot exceed 53%.
- The review of the literature of the last decade on CO_2 plasmalysis shows that low-temperature plasmas achieve low EE (typically less than 10%), and that the best EE performances of about 50% are achieved in MW, GA, and NRP discharges, with peak temperatures of several thousand K.
- Nevertheless, nonequilibrium conversion via the electronic or vibrational pathway could allow warm plasmas to produce CO efficiently in the discharge stage at temperatures below 3,000 K, and thus, ease the quenching stage.
- NRP discharges can foster electronic nonequilibrium allowing CO_2 to be converted at gas temperatures below 3,000 K, and generate powerful hydrodynamic effects that could rapidly quench the products. Understanding the CO production mechanism in NRP discharges motivates the experimental and numerical investigations conducted in this thesis.

Chapter 3

CO_2 conversion by NRP sparks: spotlight on two parallel CO production mechanisms

In this Chapter, we experimentally study the conversion of CO_2 by NRP discharges at atmospheric pressure. We use ns-imaging and quantitative OES to characterize the NRP discharge in CO_2 with time and space resolution. After presenting the experimental setup (section 3.1), we carry out an efficiency study of CO_2 dissociation (section 3.2). This parametric study allows us to choose a reference case, which is thoroughly studied thereafter. We describe the spatial behavior of the plasma (section 3.3) and measure the evolution of the electron density, electron temperature, and gas temperature (section 3.4). These measurements allow us to draw a realistic picture of the physical conditions at play and assess the degree of equilibrium in the spark. Finally, we put these results into perspective in the discussion (section 3.5) to reconsider the relative contribution of non-thermal and thermal sparks to the production of CO.

3.1 Experimental setup

The experimental setup is presented Figure 3-1. The reactor is a 50 mm stainless steel cube. 2.5 slpm of pure CO_2 (Air Liquide AlphaGaz 99.9%) are injected with a Bronkhorst mass flow controller. The operating pressure is 1 atm for all experiments presented in this Chapter. A fraction of the output gas is sent to a gas analyzer (Madur MaMos) to measure

the CO_2 (NDIR[12]), CO (NDIR), and O_2 (paramagnetic[13]) densities in the post-discharge. The relative uncertainty on the species measurements is below 5%.

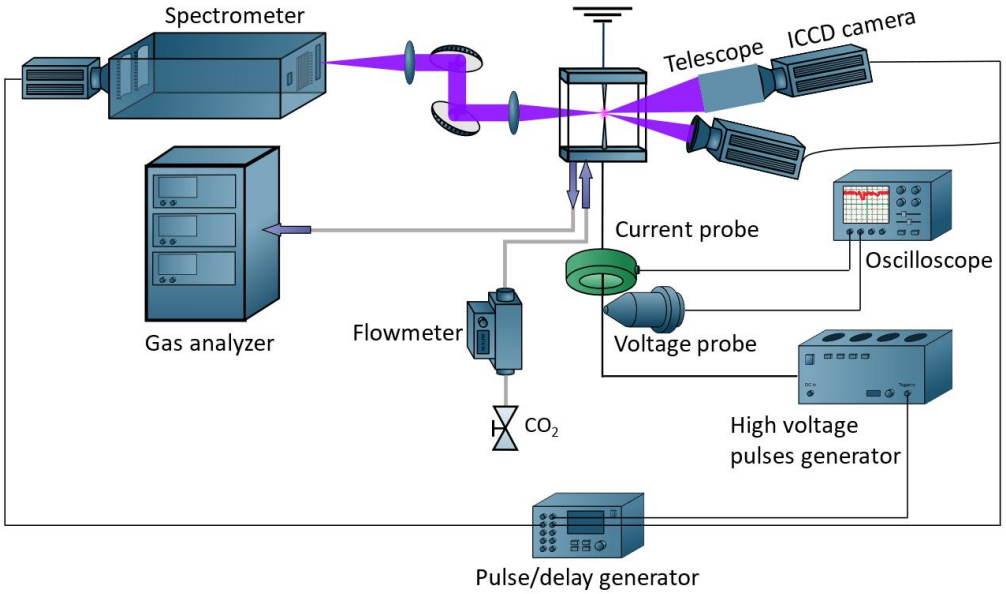

Figure 3-1. Schematic of the experimental setup. The emission from the plasma is illustrated in purple.

The plasma is generated between two tungsten electrodes with a diameter of 2 mm and a tip of about 500 µm in diameter. The interelectrode gap is varied between 1.3 and 4.2 mm. A high-voltage pulse generator (FID Technology 10-30NM10) produces the nanosecond pulses and is connected to the anode through a 6 m long RG11 coaxial cable with 75 Ω impedance. The pulses have a Full-Width-at-Half-Maximum (FWHM) of 15 ns. The peak incident voltage is varied from 3 to 8 kV, and the repetition frequency from 3 to 50 kHz. The voltage and current waveforms are measured in the middle of the coaxial cable between the pulser and the electrodes (i.e. 3 m from the electrodes) by a voltage probe (LeCroy PPE 20 kV, 150 MHz) and a current transformer (Pearson 6585, 200 MHz). The voltage *v(t)* and current *i(t)* are recorded with an oscilloscope (LeCroy Wavepro 7100A, 1 GHz), and multiplied and integrated to determine the instantaneous energy E*(t)*. Figure 3-2 shows a representative example of a voltage, current, and energy measurements. The differences between the line and load impedances create multiple reflections. The second forward pulses – created by reflection of the first pulses and measured in Figure 3-2 at about 70 ns – carry about 0.1-1 mJ, i.e. one tenth of the incident pulses energy. Hereafter, we will refer to it as

[12] Non-dispersive infrared absorption spectroscopy.

[13] Uses the paramagnetic property of O_2. O_2 molecules are set in motion by a strong magnetic field. The measurements of the resulting force yields the O_2 density.

"the reflected pulse." Eventually, E(t) converges to the cumulated energy E deposited by the pulse and its subsequent reflections. E ranges between 2 to 9 mJ per pulse.

Emission spectra are measured with a 50-cm focal length spectrometer (Acton SpectraPro 2500i) equipped with an ICCD camera (Princeton Instruments PIMAX, 1024×256 pixels). The 600 groove.mm^{-1} grating is blazed at 300 nm. The spectrometer entrance slit width is 20 µm. The instrumental broadening profile, measured with a He-Ne laser, has a gaussian shape with a FWHM of 0.2 nm at 632 nm. The response of the spectrometer and of the optical train is calibrated in absolute intensity using an integrating sphere (OPTEEMA, OL455). We use two mirrors to image the plasma orthogonal to the slit. The orthogonal configuration ensures that we capture all pulses, even if they spatially fluctuate on the transverse axis. The probed region of the discharge can be changed by adjusting the mirrors. We consecutively focus the spectrometer at three different positions: cathode (100 µm from the electrode tip), midgap, and anode (100 µm from the electrode tip).

The plasma is imaged with an ICCD camera (PIMAX:512RB) and a long-distance microscope (Questar QM100). The spatial resolution is 3.5 µm/pixel with the long-distance microscope and 15 µm/pixel with the ICCD camera alone. The optical and electrical measurements are synchronized with a pulse/delay generator (BNC model 575), assuming that the emission peak of the spark is simultaneous with the current peak, as is the case for nanosecond discharges in air (Rusterholtz et al. 2013). The time-resolved measurements are obtained in phase-locked mode, by varying the delay of the ICCD cameras with the pulse/delay generator.

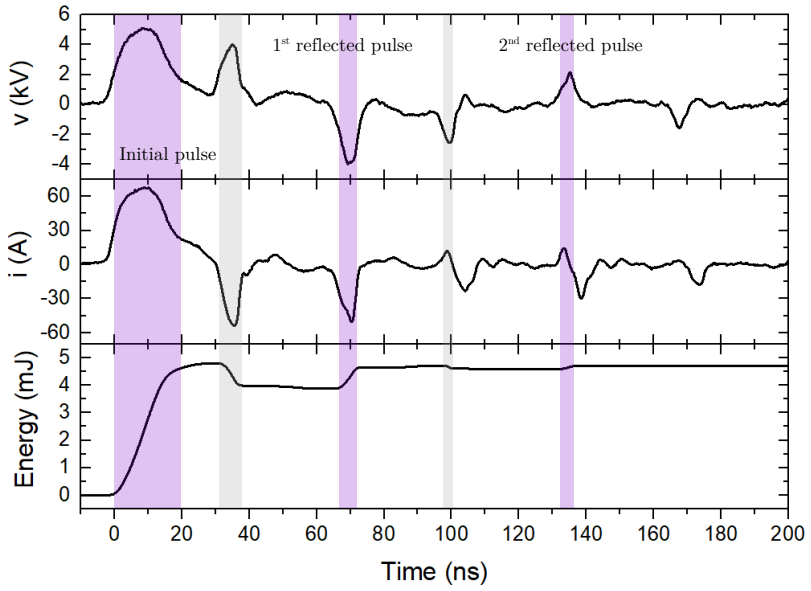

Figure 3-2. Voltage, current, and cumulated energy waveforms in the first 200 ns after the start of the pulse, measured in the middle of the 6-m long coaxial cable (i.e. 3 m away from the

electrodes). The purple areas indicate the pulses traveling toward the electrodes, whereas the grey areas indicate the pulses returning toward the generator.

3.2 Energy efficiency study

In this section, we investigate the Energy Efficiency (EE) of NRP discharges in CO_2 as a function of the electric field and of the Specific Energy Input (SEI). This work extends Pannier's measurements (Pannier 2019) to higher SEI, and to conditions close to those of (Montesano et al. 2020). The experimental parameters are summarized in Table 3-1. In the present experiments, the pulse frequency is varied from 2 to 50 kHz and the incident pulse peak voltage from 3 to 8 kV (and therefore approximately 6 to 16 kV at the electrodes). Experiments were also performed with bursts of 4 to 30 pulses, with an in-the-burst frequency of 50 kHz.

Table 3-1. Experimental conditions used in Montesano et al. (Montesano et al. 2020) and in the present work.

	Montesano 2020	**This work (section 3.2)**	**This work (sections 3.3, 3.4, and 3.5)**
Peak voltage at the electrodes (~twice the incident voltage)	6 – 8 kV	6 – 16 kV	10.6 kV
Inter-electrode distance	5 mm	3 mm	3 mm
Electrode configuration	Tube-tube	Pin-pin and pin-tube	Pin-pin
Flow rate	0.1 slpm	2.5 slpm	2.5 slpm
Energy / pulse	4 – 5 mJ	2 – 9 mJ	4.7 mJ
Frequency in the continuous mode	0.9 – 2.7 kHz	3 – 50 kHz	10 kHz
Frequency in the burst	10 – 95 kHz	50 kHz	/
SEI	0.6 – 1.8 eV/molecule	0.1 – 1.5 eV/molecule	0.3 eV/molecule
Residence time in tube–tube configuration	~ 2 ms	~ 1 ms	/
First reflection	~ 90 ns	~ 70 ns	~ 70 ns
Secondary pulse	~ 400 ns		

Figure 3-3 shows that the energy efficiency does not vary much with the electric field: in the range of electric fields investigated (20 to 80 kV/cm), the EE stays constant at about 30%. On the other hand, Figure 3-4 shows that the EE has a stronger dependence on the SEI: it first increases with the SEI, then plateaus for SEI between 0.2 and 1 eV/molecule, and finally decreases when the SEI is above 1 eV/molecule. Additionally, the EE does not

increase with the 50 kHz burst. The maximum EE we obtain is 36% at 0.5 eV/molecule, way below the 58% measured by Montesano *et al.*

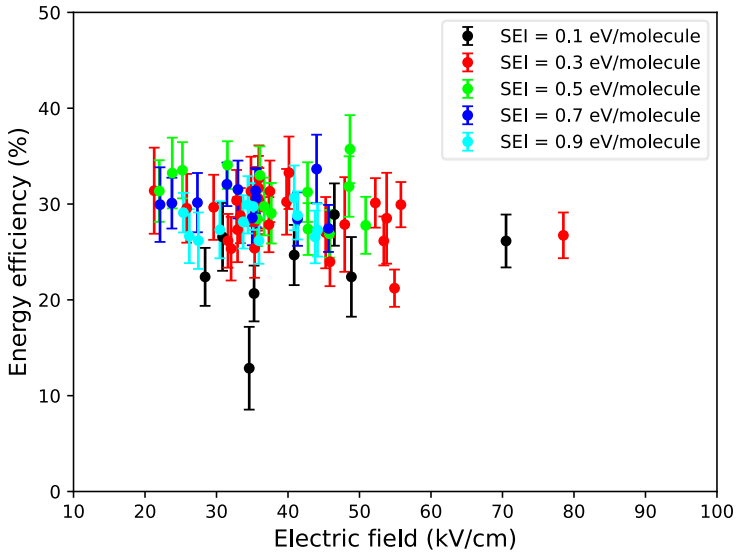

Figure 3-3. Energy efficiency of CO production vs. peak electric field applied between the electrodes. The colors indicate the SEI. At a constant electric field, different SEI are reached by varying the pulse repetition frequency.

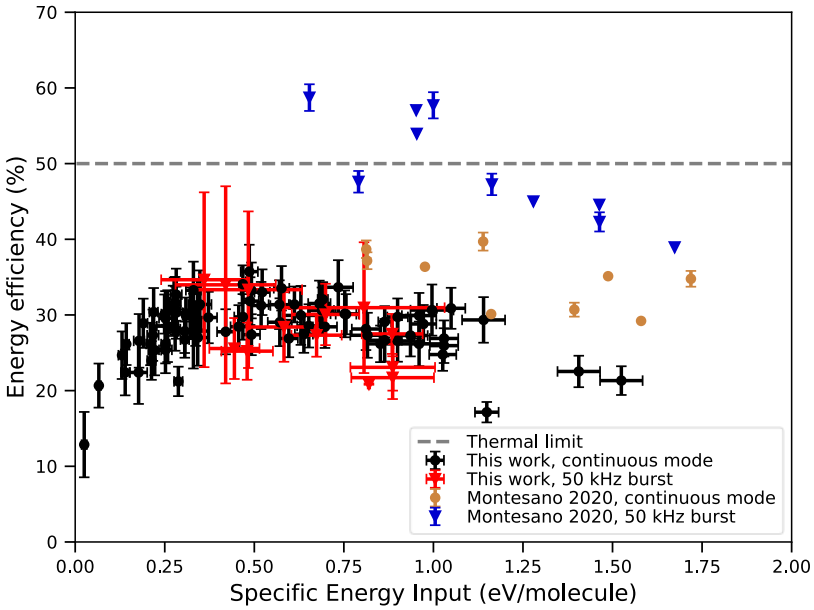

Figure 3-4. Energy efficiency of CO production vs. SEI. Comparison of our measurements with those of Montesano et al. 2020. The different SEI values are achieved by varying the pulse repetition frequency and the electric field in the continuous mode, the number of pulses in a burst and the electric field in the burst mode.

The differences between this work and the measurements of Montesano *et al.* may be explained by the different geometries used in the two experiments. The sharpness of the electrodes impacts the local electric field near the electrode tips. The gas injection through Montesano *et al.*'s tubular electrodes, as well as the electrode size, impacts the hydrodynamics and the gas temperature. Also, the electrical setups may induce significant variations: the timing of the generator retriggering and the different reflections caused by impedance mismatch are specific to the setup. For instance, Montesano *et al.* have power reflections every 40 ns approximately, whereas they occur every 70 ns in our case. There is also a difference in the flow residence times, which can be estimated as $\tau_{res} = (e\pi r^2)/q$ where e is the inter-electrode gap, r the tube radius, and q the input CO_2 volumetric flow rate. The residence time in Montesano *et al.*'s experiment – about 2 ms – is twice as long as ours. All these differences could explain the significantly higher energy efficiencies obtained by Montesano *et al.*. New experiments reproducing their exact geometry and conditions should be carried out.

On the other hand, the EE downward trend after 1 eV/molecule is observed in both experiments. The same trend is observed in microwave (MW) discharges (Bongers et al. 2017; Rusanov et al. 1981). It may indicate common features in the conversion mechanism.

Our objective in the rest of this Chapter is to study the thermochemical conditions behind the EE achieved in NRP discharges. We will focus on a reference case close to Pannier's (Pannier 2019): V = 5.3 kV, E = 4.7 mJ, f = 10 kHz, d = 3 mm, q_{CO2} = 2.5 slpm, in pin-pin configuration. With about 0.3 eV/molecule SEI, this reference case is on the energy efficiency plateau. Moreover, the electrode erosion is minimal in this case (more than 50 hours of operation without replacement).

3.3 Plasma imaging

3.3.1 Spatial distribution of optical emission

To understand the early spatial structure of the discharge, we acquire 500 single-shot ICCD images of the discharge under our reference conditions (defined at the end of the previous section) at different times within the first 180 ns. The camera gate width is 4 ns. Based on the analysis of this set of images, the pulses can be classified into six types – from a to f – illustrated in Figure 3-5. As a symmetrical behavior at the two electrodes is observed, the six types can be further reduced into 4 categories: a/b, c, d/e, and f. A localized emission near the cathode or the anode characterizes a/b-types pulses. Type c emission appears at both electrodes. Types d/e are characterized by a longer filament starting from one of the electrodes and filling about half of the gap. Type f emission fills the whole inter-electrode gap and is characterized by a bright filament surrounded by a fainter region. We will show

in section 3.4.1 that the bright emission measured in this typology comes from the most ionized zone of the plasma.

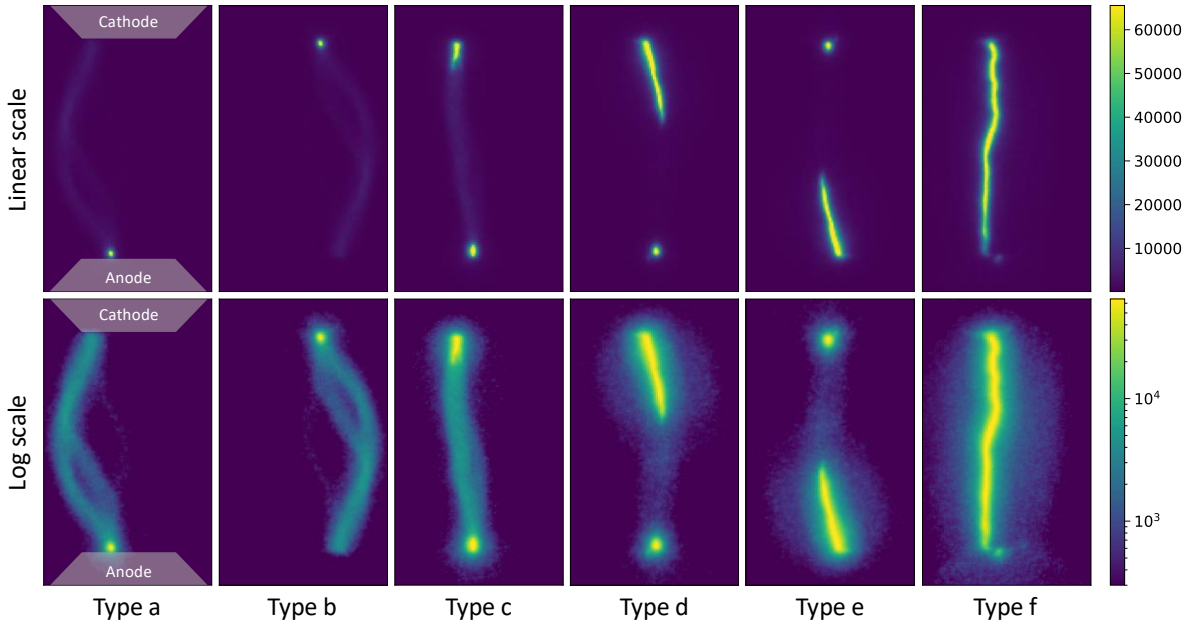

Figure 3-5. Single-shot visible emission imaged with a 4 ns gate width. Each image illustrates a pulse type. In type a/b pulses, the emission stays close to the cathode or the anode. In type c, there is intense emission at the cathode and the anode. Types d/e are characterized by a longer filament growing from the cathode or the anode. Type-f emission fills the whole 3 mm inter-electrode gap. All images are on the same intensity scale.

The temporal evolution of the pulse typology is presented in Figure 3-6. The upper graph shows the probability of bright emission occurrence at the anode, cathode, and midgap versus time, and the lower graph is the probability of occurrence of the six pulse types as a function of time. Initially, the emission is localized at the cathode (or the anode). By the end of the pulse, the emission appears occasionally at midgap. At that time, most pulses are of type a/b and d/e. There is always intense emission at the cathode or the anode, whereas midgap filaments do not occur at each pulse. In some cases, the role of the cathode and anode are reversed: the emission starts at the anode and develops from there. This symmetric role of the electrodes is consistent with the hydrodynamic regimes in the post-discharge identified by Pannier (Pannier 2019), which can be “anode-directed” or “cathode-directed”. At $t = 50$ ns, the filament frequently reaches the middle of the gap. After the reflected pulse arrives ($t \geq 70$ ns), the discharges are mostly of type f, i.e. with a filament filling the whole inter-electrode gap.

Around the bright emission region, a fainter emission region is distinguished. This faint emission appears clearly in the bottom images of Figure 3-5, plotted in log scale. We will show that the faint regions present very different conditions from the bright regions.

Simultaneously with the ICCD measurements, the energy deposited by each pulse into the plasma is recorded with a synchronized oscilloscope. These synchronized measurements show that the total energy is approximately the same, whatever the pulse type.

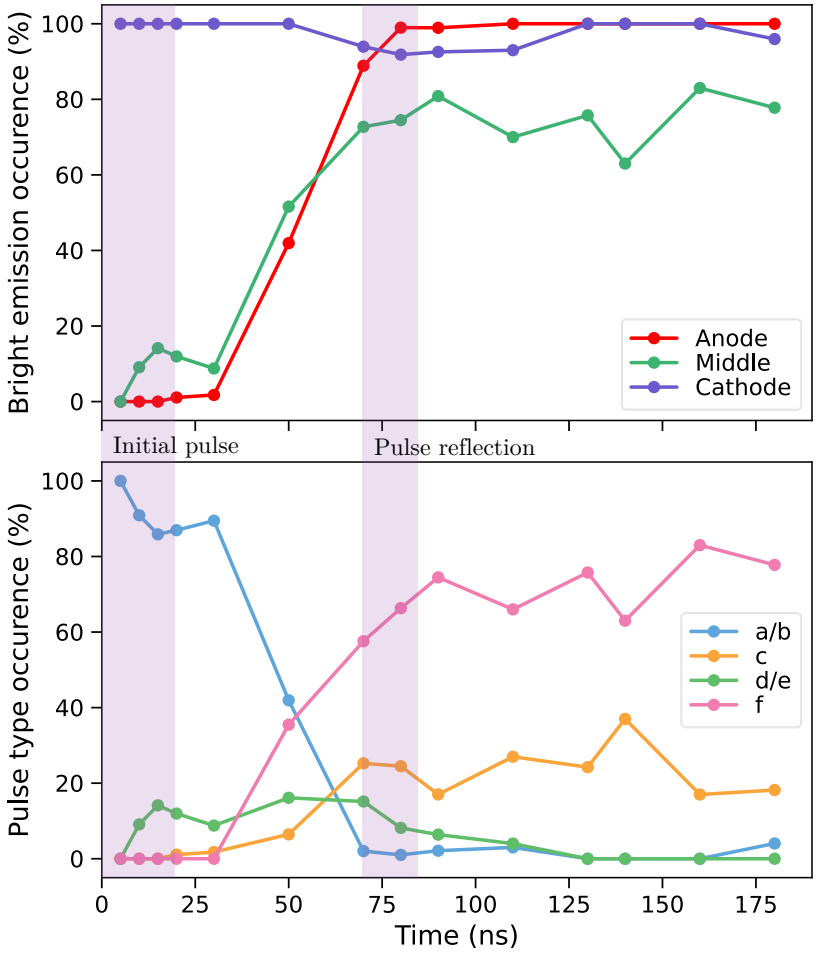

Figure 3-6. Top graph: probability of the bright emission occurrence at the anode, cathode, and midgap versus time. Bottom graph: probability of pulse-type occurrence versus time. Initially, the bright emission is localized at the cathode. By the end of the pulse, the bright emission also appears at the anode. When the reflected pulse arrives (at about 70 ns), a bright filament fills the whole inter-electrode gap.

3.3.2 Plasma dimension

To characterize the various types of pulses and to quantify the energy deposited in the plasma, the diameters of the bright and faint regions are needed. The ICCD camera is used to image the visible emission (Figure 3-5). The resolution is about 15 µm/pixel. When the diameter of the plasma is smaller than 80 µm, a telescope is added to the setup, which allows to reach a resolution of 3 µm/pixel and to image objects as small as 15 µm.

Here, the diameter is defined as the FWHM of the radial optical emission profile. We measure 500 pulses in single shot between 5 and 180 ns after the breakdown, with a 4-ns gate width. Illustrative single-shot images of type c and f pulses, taken with the ICCD

camera, and their measured diameters are reported in Figure 3-7. Figure 3-8 shows illustrative single-shot images of the temporal evolution of type-a emission measured with the telescope setup.

In its embryonic stage, the bright region is a small sphere of about 20 µm in diameter. The sphere grows and is distorted over time, developing as a filament toward the center of the gap. Depending on the pulse type, the filament reaches different lengths. The temporal evolution of the bright region diameter is reported in Figure 3-9. The diameter increases after the breakdown until the reflected pulse re-ionizes the gas in a narrower channel. Then, the diameter starts increasing again.

Looking at the emission in log scale (Figure 3-7), we can also estimate the diameter of the faint emission region. It is much larger than the bright region diameter. Figure 3-10 shows the temporal evolution of the faint region diameter in the middle of the gap for the first 30 ns after the pulse. The measured range of diameters (400 – 600 µm) is consistent with literature values for non-thermal NRP-sparks (Pannier 2019; Rusterholtz et al. 2013).

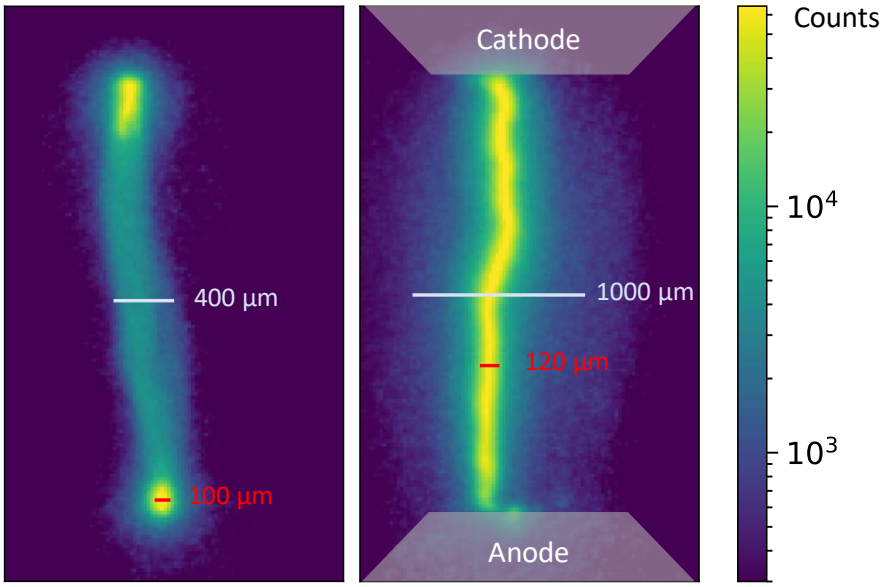

Figure 3-7. Visible emission in log scale of (left) a type-c pulse (at about 15 ns) and (right) a type-f pulse (at about 70 ns), and estimation of the faint and bright region diameters. The diameter is defined as the FWHM of the emission profile. Single-shot, exposure time 4 ns.

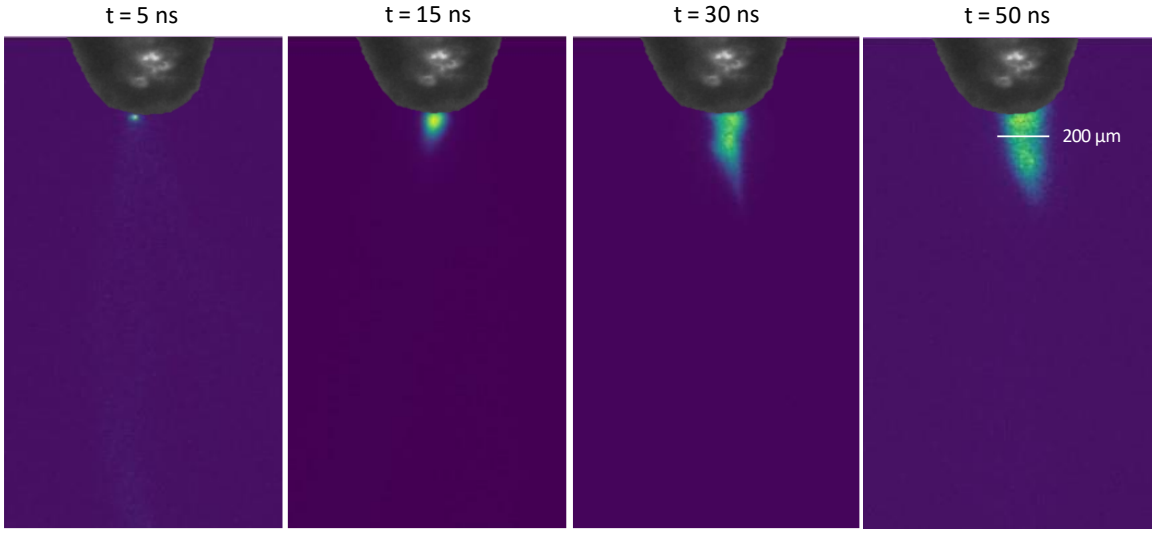

Figure 3-8. Evolution of the visible emission of a type-a pulse in the first 50 ns of the discharge. Single shot, exposure time 4 ns. Images taken with the QUESTAR telescope.

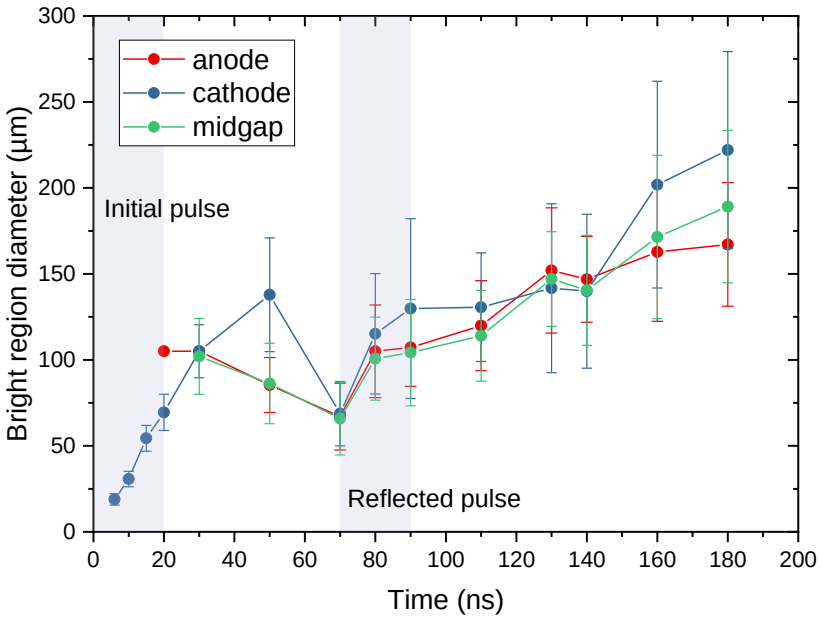

Figure 3-9. Temporal evolution of the bright region (sphere or filament) diameter at the cathode, anode, and middle of gap.

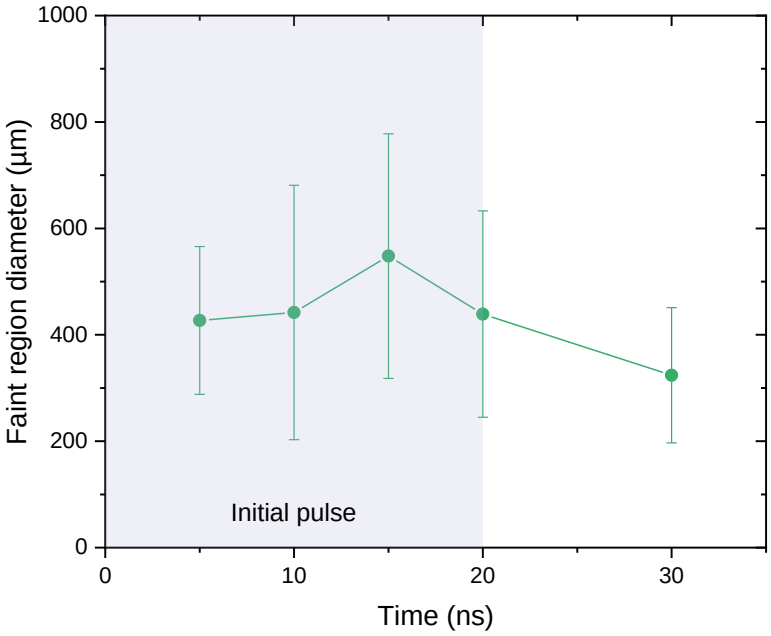

Figure 3-10. Temporal evolution of the faint region diameter in the middle of the gap.

3.4 Optical Emission Spectroscopy measurements

3.4.1 Qualitative analysis of the emission spectra

We record the temporal evolution of the plasma emission spectra between 400 and 800 nm at the anode, cathode, and midgap. To get enough signal, each spectrum is averaged over thousands of pulses. The gate width is 4 ns and the spectra are calibrated in absolute intensity.

Cathode

Figure 3-11 presents the successive spectra measured at the cathode. Except for a small contribution of the C_2 Swan band at 516 nm, the spectra are predominantly composed of atomic lines. From the beginning of the pulse to 70 ns (i.e. before the reflected pulse), most of the emission comes from O* and O^+*, suggesting a significant dissociation of CO_2. We do not observe emission lines of C and C^+, which suggests that there are no carbon products other than CO, CO_2^+, or CO^+. Also, an intense continuum emission attributed to Bremsstrahlung and recombination radiation indicates that the plasma is highly ionized. With the arrival of the reflected pulse at 70 ns, emission lines of C and C^+ appear, indicating that the reflected pulse dissociates CO.

Midgap

At midgap, the observations are very different. As shown in Figure 3-12, except for O lines, the emission at midgap before 70 ns is much less intense than at the cathode. This result was expected from section 3.3.1, where we showed that, before 50 ns, there is no bright emission at midgap (Figure 3-6). At 50 ns, we find the same spectral features as at the cathode, but with lower intensity. After 70 ns, the spectra at midgap and at the electrodes are similar in both spectral content and intensity. This evolution is consistent with Figure 3-6 which shows that at midgap, a filament occurs in 50% of cases at 50 ns, and in 75% of cases after the reflection.

The spectroscopic measurements show that the spectral content of the brightest features is identical, whatever the location. We can thus draw an important conclusion: the bright, spatially narrow emission measured in section 3.3.1 is primarily dominated by atomic lines and continuum radiation. The bright regions correspond to a highly ionized and atomic plasma.

Finally, Figure 3-13 zooms in on the low intensity spectra measured at midgap between 8 and 12 ns. In addition to the O lines mentioned above, the spectrum features molecular emission: C_2 Swan, CO Angström, and $CO_2^+(A^2\Pi_u - X^2\,\Pi_g)$. These bands are typical of CO_2 plasmas and have already been identified in NRP discharges (M. Ceppelli et al. 2021; Pannier 2019), (Pokrovskiy 2021) but also in MW (Britun et al. 2018; Carbone et al. 2020; Qin et al. 2020; Silva et al. 2014b; Soldatov et al. 2021) and DBD (Belov et al. 2016) discharges. Here they are superimposed on the emission of spectrally broad O^+ lines, attributed to the filaments occasionally reaching the middle of the gap (we showed in section 3.3.1, Figure 3-6, that filaments occur about 20% of the time at this position and time). The faint emission evidenced in the log scale images of Figure 3-5 is the same as in Figure 3-13 and is composed of molecular spectral features. Finally, let us emphasize that the lower emission of the faint region does not mean that this region does not contribute to dissociation. Detecting the nascent CO, C_2, and CO_2^+ molecules in excited electronic states attests to the electron-induced reactivity of the discharge.

The bright and faint regions show very different spectra, indicating different physics and CO_2 dissociation mechanisms. In the following, we will investigate the physics at play in each region.

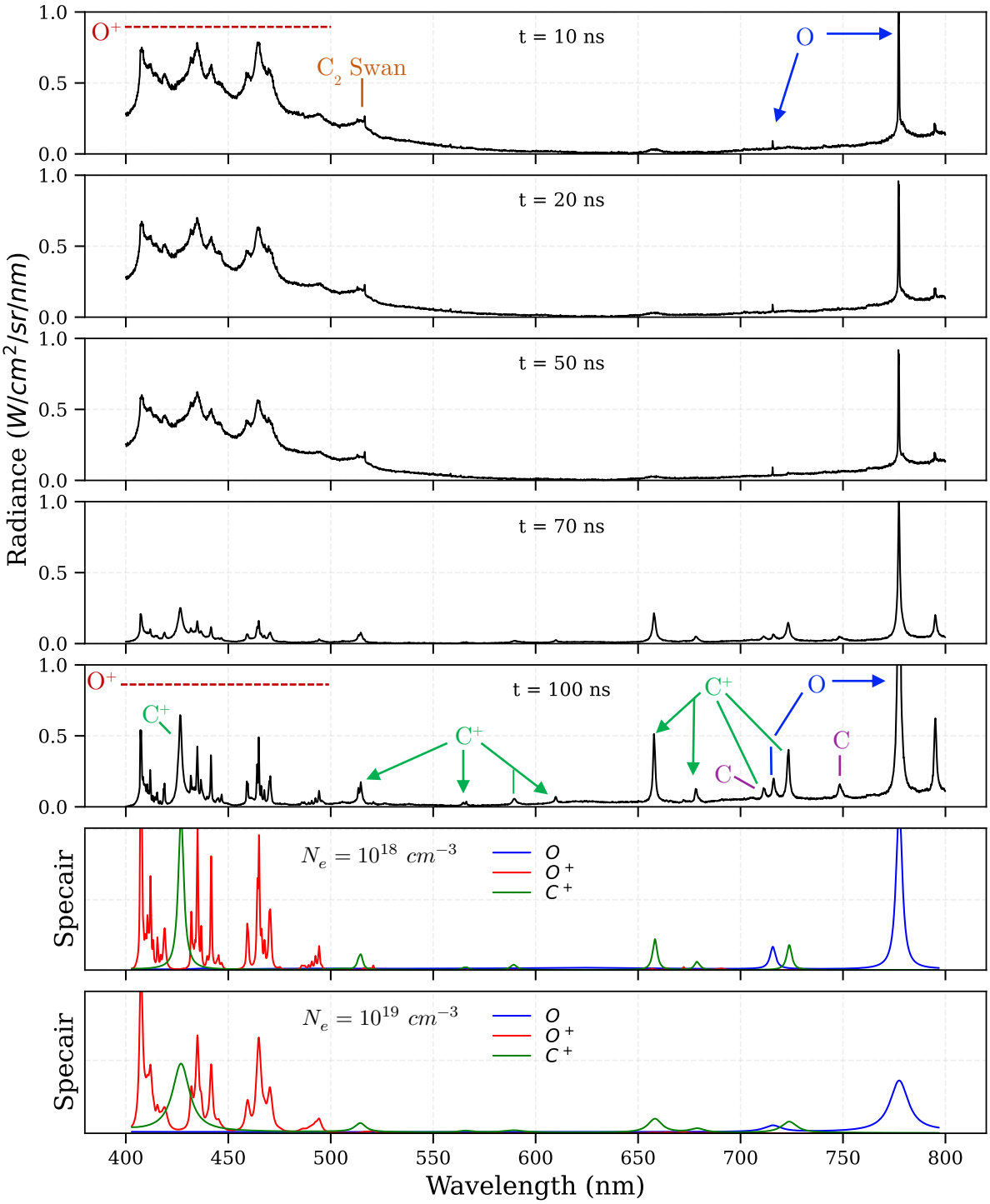

Figure 3-11. Emission spectra recorded at the cathode from t = 10 to t = 100 ns, using a 4 ns gate width. The two bottom plots are theoretical emission spectra of O, O^+ and C^+ calculated with SPECAIR (Laux et al. 2003) at two different n_e (10^{18} and 10^{19} cm^{-3}) to support the line identification (the SPECAIR calculations assume T_e = 30,000 K, $n_O = 5{\cdot}10^{17}$ cm^{-3}, $n_{O+} = 10^{18}$ cm^{-3}, $n_{c+} = 2{\cdot}10^{17}$ cm^{-3}). An intense and spectrally broad emission from O^+ lines, as well as continuum radiation, are observed at early times between 400 and 550 nm. O emits strongly at 777 nm, the emission of C_2 is visible but minor. After the arrival of the reflected pulse at 70 ns, C and C^+ lines arise. The spectra suggest a highly ionized and dissociated plasma.

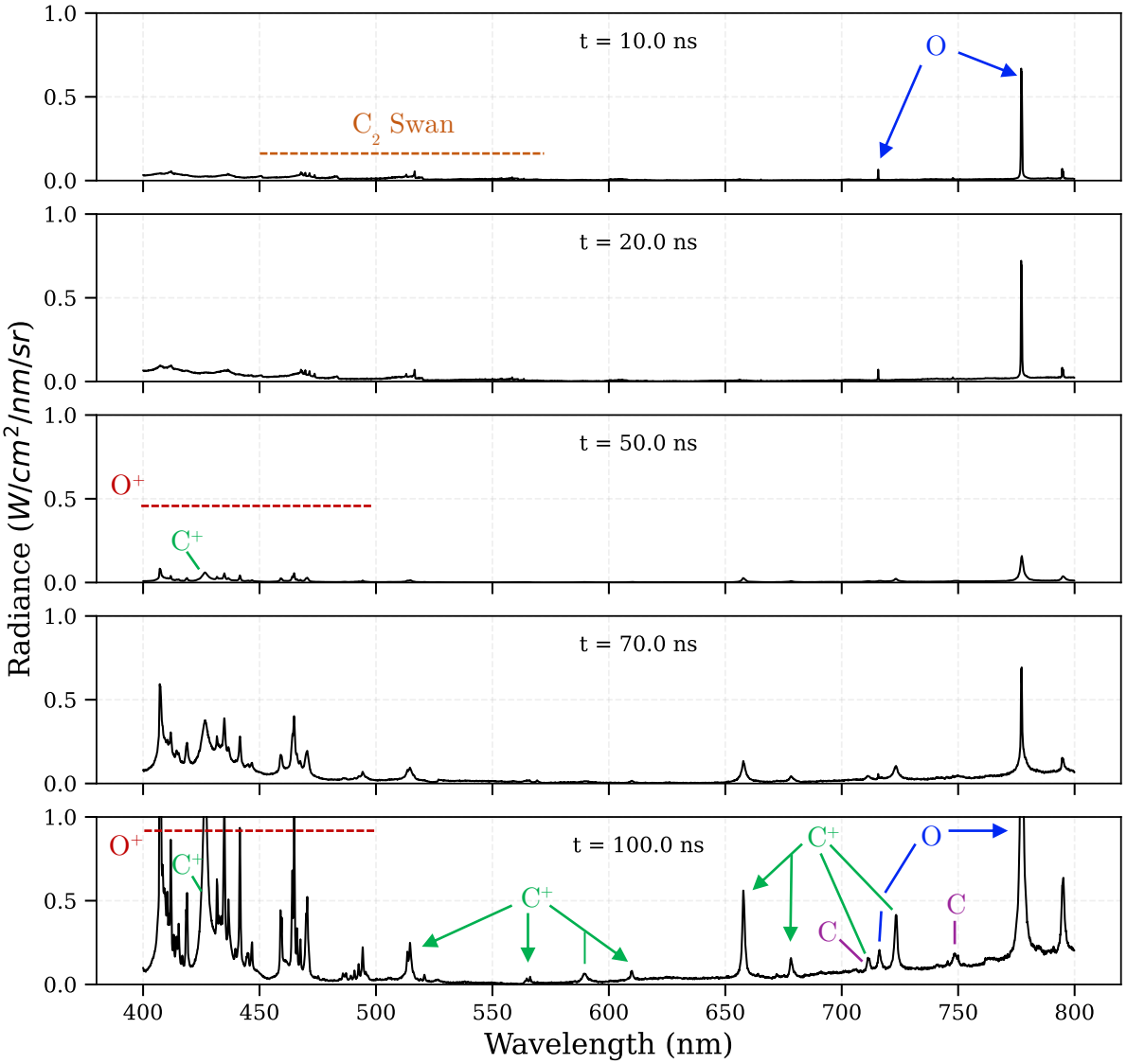

Figure 3-12. Emission spectra recorded at midgap from t = 10 to t = 100 ns, using a 4 ns gate width. Before 70 ns, the emission is negligible compared to the emission near the cathode. With the arrival of the reflected pulse after 70 ns, we observe the same spectral features with about the same radiance as near the cathode. The spectral content of the bright regions is thus identical, whatever the location.

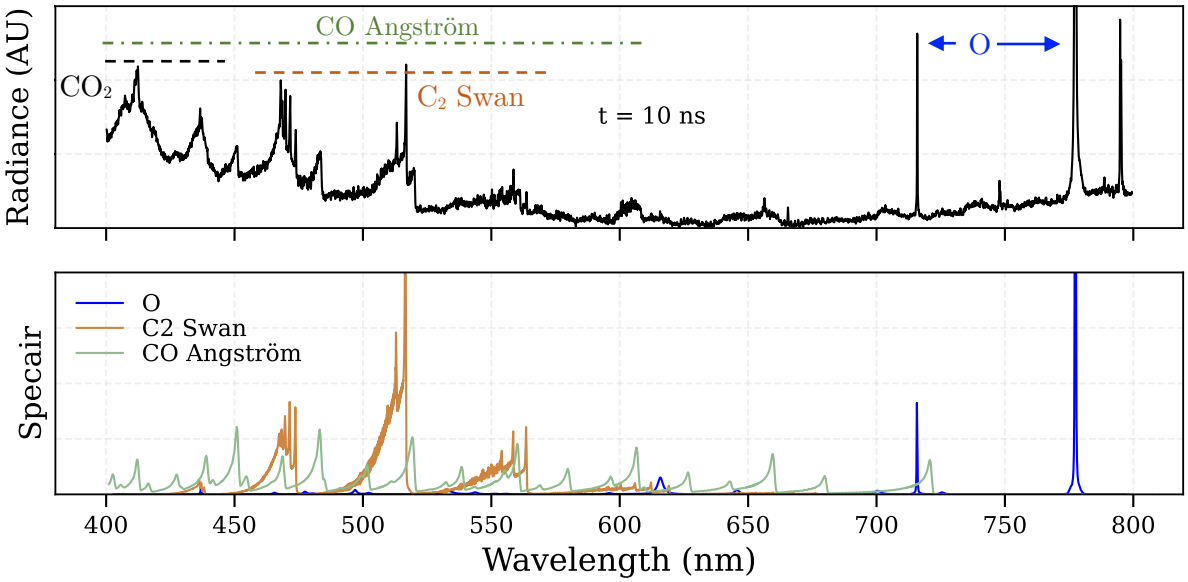

Figure 3-13. Emission spectrum measured at midgap, t = 10 ns (top), and theoretical spectrum calculated with SPECAIR (bottom) to help identify some experimental lines. The molecular bands of C_2 and CO are roughly fitted assuming $T_{rot} = T_{vib} = 2000$ K, and $T_e = 30{,}000$ K. Between 700 and 800 nm, the main features are atomic lines of O.

3.4.2 Gas temperature measurements

We add 3% N_2 to the mixture and measure the emission of the N_2 2nd positive system (SPS) at 337 nm and 380 nm. Since the bright region is dominated by atomic lines, N_2 emission comes predominantly from the faint region. Figure 3-14 shows typical emission spectra of the 337 nm (0,0) band measured at the cathode at several times. The signal-to-noise ratio becomes high enough to fit the spectrum from 5 ns onwards. As the gas gets ionized and N_2 dissociated, the N_2 SPS emission disappears progressively, until it becomes completely overlapped by other lines at 20 ns. For the 380 nm (0,2) band, the signal is sufficient only from 6 to 12 ns.

When $N_2(C)$ is excited by electron-impact – which is the case during the pulse –, the rotational temperature of $N_2(C)$ is representative of the gas temperature within a 10% uncertainty (M. Ceppelli et al. 2021; Maillard et al. 2022; Rusterholtz et al. 2013). The rotational temperature is deduced by fitting the spectra using the line-by-line radiation code SPECAIR (Laux et al. 2003). A fit example can be seen in Figure 3-15.

The time and space evolution of the $N_2(C)$ rotational temperature is presented in Figure 3-16. The average uncertainty from the fits is about 200 K. In similar conditions, Pannier (Fig. 11.23 in (Pannier 2019)) also measured the rotational temperature of the gas, using infrared emission spectroscopy of the CO_2 bandhead at 4.173 µm. He measured an initial

temperature of 1200±100 K. The discrepancy between the measurements of Pannier and this work could be explained by the 5 µs integration time used in (Pannier 2019) compared to 4 ns in this work. Figure 3-16, the point from Pannier at 2 ns is in fact integrated between $t = -5$ µs and $t = 0$ µs.

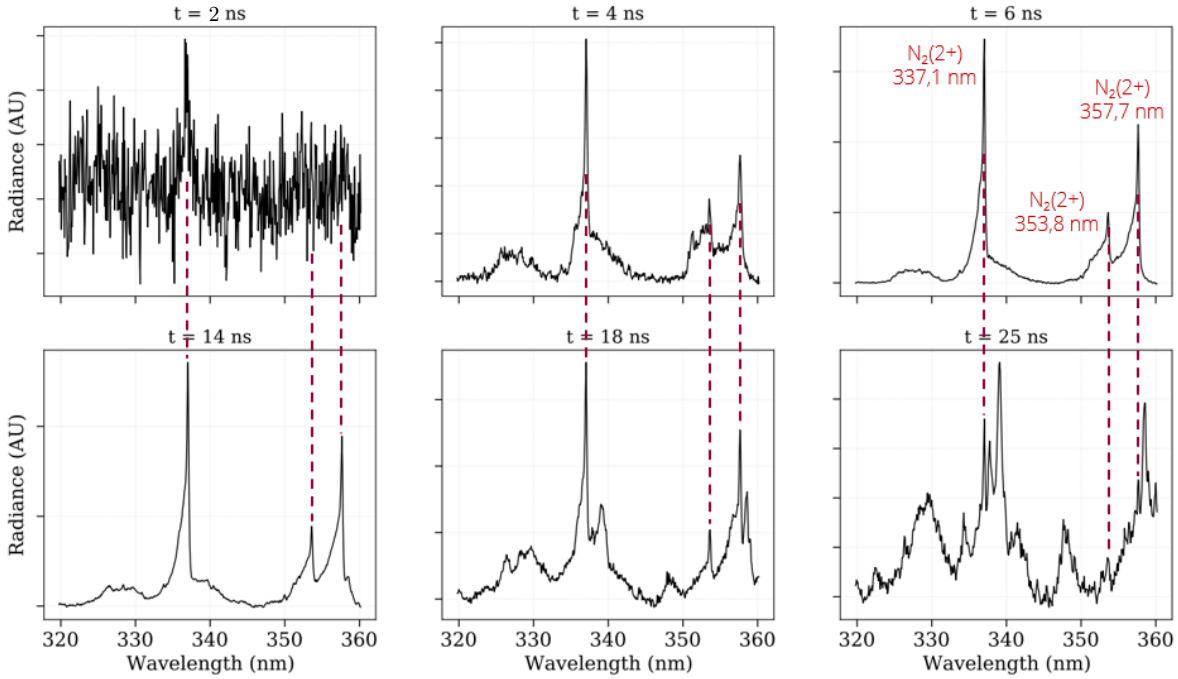

Figure 3-14. Emission spectra in the 320 – 360 nm range of the CO_2 plasma containing 3% N_2.

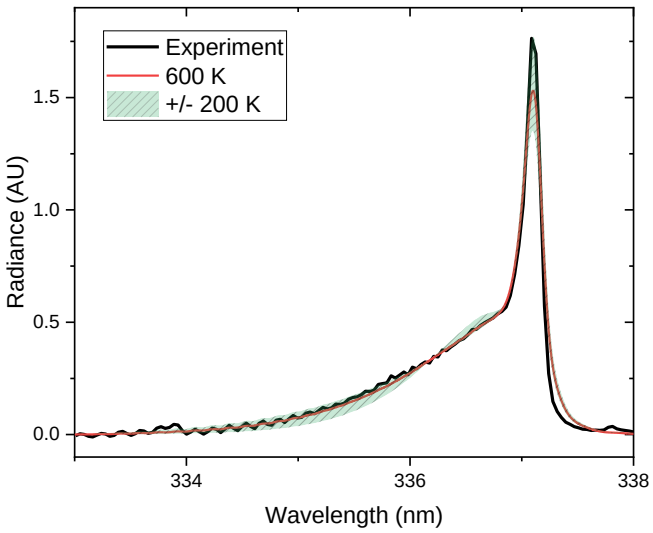

Figure 3-15. N_2 337 nm band emission measured at the cathode at t = 7 ns. T = 630 ± 200 K gives the best fitting result.

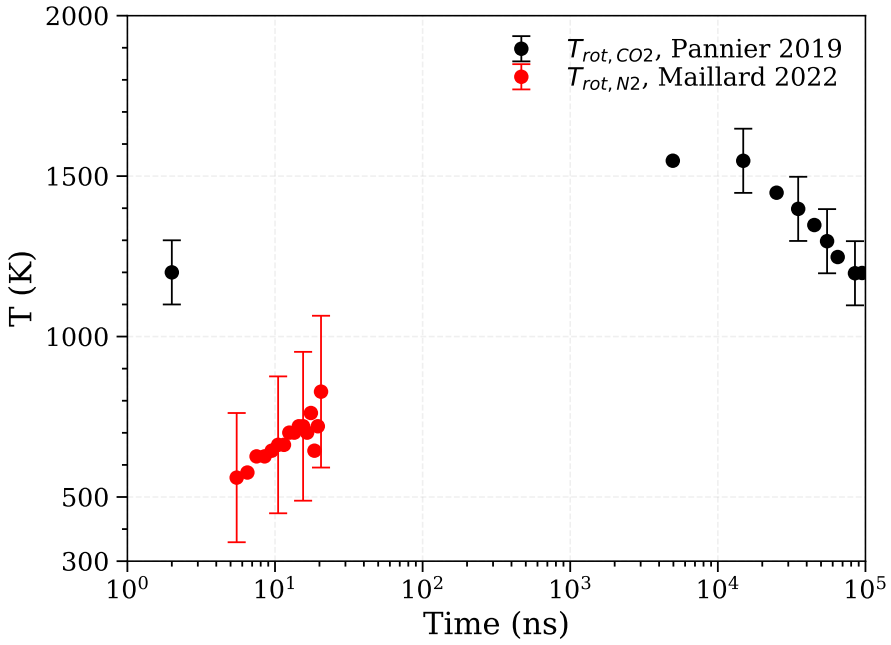

Figure 3-16. Temporal evolution of the gas temperature in the faint region measured via the N_2 SPS emission (red). The black symbols correspond to the rotational temperature of CO_2 measured by (Pannier 2019) using the IR emission of CO_2.

3.4.3 Electron density measurements

The electron density is measured using the Stark broadening of several lines including the O triplet at 777.14, 777.41, and 777.54 nm, O^+ lines from 455 to 475 nm, and C^+ lines at 658 and 678 nm. The measured lines are analyzed by fitting them using SPECAIR (Laux et al. 2003).

In the conditions investigated, the measured FWHM of the O-triplet ranges from 0.4 to 8 nm. For the $O^+(455 - 475)$ and $C^+(658)$ lines, we measure FWHMs of 0.2 to 2 nm and 1 to 5 nm, respectively. Several physical phenomena account for these broadenings: natural, resonant, Doppler, Van der Waals (VdW), Stark, and instrumental broadening. Their values are estimated using Refs. (Minesi et al. 2020; Martin and Wiese 2006) and are reported in Table 3-2. Self-absorption can also broaden the lines, and thus must be considered. All these phenomena are included in the SPECAIR calculations.

3.4.3.1 Spectroscopic observations

O(777)

The temporal evolution of the emission spectrum of the O(777) triplet is reported in Figure 3-17. For $t \leq 10$ ns, at every location, it appears as two narrow lines. The narrowness of these lines is characteristic of the faint region.

Then, between 10 and 25 ns, the lines appear as the sum of narrow component superposed to a broad component. Such double-component spectra were already observed in water vapor (Sainct et al. 2020) and CO_2 (Maillard et al. 2022) plasmas. As we saw in Figure 3-5, the bright regions are always observed together with a faint region surrounding them. Moreover, according to Sec. 3.4.1, the broad component is characteristic of the highly ionized bright region. Therefore, we attribute the broad component to the bright region, while the narrow component originates from the faint region.

After 25 ns, the spectra are characterized by a single broad component. The bright region dominates the emission.

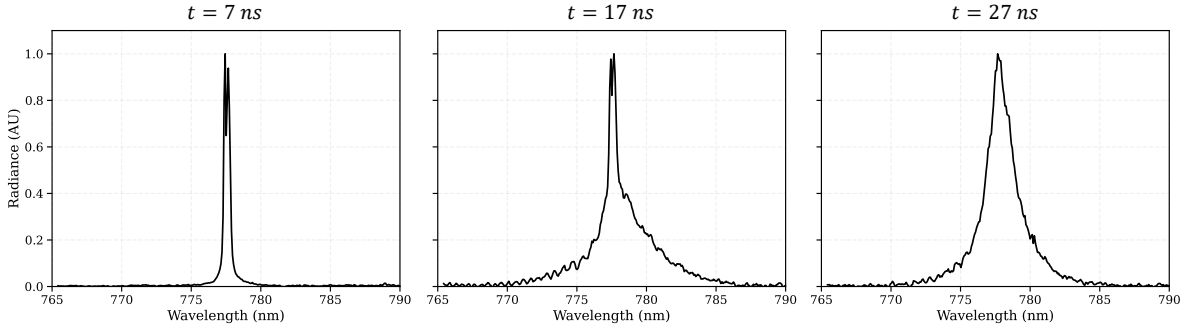

Figure 3-17. Emission spectra of O(777) triplet, measured at the cathode at 7, 17, and 27 ns. Gate width 4 ns. Spectra averaged over 10,000 pulses.

O^+(455-475) & C^+(658)

The emission spectra of these lines, which originate from the bright regions, present only one component per line. Illustrative examples of the measured emission are reported in Figure 3-23.

3.4.3.2 Analysis of the faint region

In this section, we discuss the dominant broadening phenomena in the faint region, and the impact on the measured electron densities. The FWHM of each phenomenon is reported in Table 3-2.

Van der Waals broadening

For $t \leq 10$ ns, the thermodynamic quantities (P, T_g) are expected to be at their initial values. In our experiment, the reactor is at atmospheric pressure but the pressure increases in the plasma during the pulse due to fast gas heating and dissociation. In a non-thermal spark, the pressure relaxes to the ambient value after 1 – 10 µs (Xu et al. 2014) (see Chapter 4, Sec. 4.3.4). Since the pulse repetition frequency is 10 kHz – i.e. a period of 100 µs between 2 pulses –, at the beginning of the pulse, the pressure has already relaxed from the previous pulse, i.e. $P = 1$ bar. We measured an initial temperature of 600±200 K, but Pannier

measured an initial temperature of 1200±200 K (Figure 3-16). This range of temperatures will be used to bracket the VdW broadening widths for the SPECAIR fits.

At $P = 1$ bar and $T_g = 600$ K the total number density is $n_{tot} = 1.2{\cdot}10^{19}$ cm^{-3}. If $T_g = 1200$ K, $n_{tot} = 0.6{\cdot}10^{19}$ cm^{-3}. We calculate the FWHM of the Van der Waals broadening $\Delta\lambda_{VdW}$ of the O(777) triplet using the following approximate formula (Minesi et al. 2020):

$$\Delta\lambda_{VdW}[\text{nm}] = 2 \cdot \sum_{pert} \frac{\gamma_{pert}}{100} \cdot \frac{n_{pert}}{2.7 \cdot 10^{19}\ \text{cm}^{-3}} \cdot \left(\frac{T_{gas}}{273\ \text{K}}\right)^{0.3} \qquad \text{Eq. 3-1}$$

where γ_{pert} is a characteristic coefficient of the transition and the collider, n_{pert} is the number density of the collider, and T_{gas} is the gas temperature. Given a mixture of CO_2, CO, and O (the main species expected in the faint region, as will be seen later), the approximate γ_{pert} for the O(777 nm) triplet is 1.3 (Minesi et al. 2020). Taking $n_{pert} = n_{tot}$, we obtain the following bounds for the VdW FWHM: $\Delta\lambda_{VdW} \approx 0.015$ nm for $T_g = 600$ K, and $\Delta\lambda_{VdW} \approx 0.010$ nm for $T_g = 1200$ K.

For $10 < t < 25$ ns, the fast gas heating increases the temperature to about 800±200 K according to our N_2 SPS measurements (Figure 3-16). Additionally, electron-impact dissociation of CO_2 to CO and O could double the total density (since it occurs faster than the pressure relaxation time, as will be seen in Chapter 4, Sec. 4.3). This time, to estimate the upper bound of the VdW broadening, we use $T_g = 800$ K and $n_{tot} = 2.4{\cdot}10^{19}$ cm^{-3} ($P \approx 3$ bar), which yields $\Delta\lambda_{VdW} \approx 0.03$ nm, and to estimate the lower bound we still use $T_g = 1200$ K and $n_{tot} = 0.6{\cdot}10^{19}$ cm^{-3} ($\Delta\lambda_{VdW} \approx 0.01$ nm).

All the broadening values are summarized in Table 3-2.

Doppler broadening

The Doppler broadening is calculated according to (Griem 1964):

$$\Delta\lambda_{Doppler}[nm] = 7.17 \cdot 10^{-7} \lambda_{ul}[nm] \sqrt{T_{gas}[K]/M[g/mol]} \qquad \text{Eq. 3-2}$$

with $\lambda_{ul} = 777$ nm and $M = 16$ g/mol for the O(777) line. For $600 \leq T_g \leq 1200$ K, we obtain $\Delta\lambda_{Doppler} \approx 0.004$-$0.005$ nm. Thus Doppler broadening is much smaller than VdW broadening.

Self-absorption

Considering the conversion degrees above 60% measured by Pannier (Pannier 2019) for conditions similar as in this work, the O number density may exceed 10^{18} cm^{-3}. The diameter of the faint region is about 400 µm. In these conditions, self-absorption of O(777) may be significant, and we must *a priori* take it into account.

Since the spectra are calibrated in absolute intensity, they contain two independent pieces of information: the width and the integral of the triplet emission. The electron density is related to the width, while the product of the O(^{5}P) density (O(^{5}P) is the upper state of the O(777) transition) and the optical path length is related to the integral. If the plasma is not optically thin, the integral of the emission also depends on the density of O(^{5}S°) (the lower state of the O(777) transition), which determines the self-absorption. The density of O(^{5}S°) is calculated by assuming that O(^{5}S°) and O(^{5}P) follow a Saha-Boltzmann distribution at $T_e \approx$ 20,000 K, the electronic temperature measured in the following section. The Saha-Boltzmann assumption is supported by characteristic time calculations in Sec. 3.4.6.2, showing that these states equilibrate with the free electrons in less than 0.1 ns. Then, we use SPECAIR to fit (i) the product of the O(^{5}P) density times the optical path length and (ii) the electron density.

At $t = 6$ ns, for an optical path length of $d = 400$ µm (the radius of the faint region measured in Figure 3-10), the fit yields $n_{5S^\circ} \approx 2{\cdot}10^{13}$ cm^{-3} and a peak optical thickness of 0.04. At $t =$ 10 ns, $n_{5S^\circ} \approx 2{\cdot}10^{14}$ cm^{-3} and the peak optical thickness is 0.3. At $t = 19$ ns, $n_{5S^\circ} \approx 6{\cdot}10^{14}$ cm^{-3} and the peak optical thickness is 0.9. Thus, self-absorption has a significant effect on the shape and the amplitude of the spectra. It is thus taken into account in all our analyses of the O(777) line.

Stark broadening & fit of the electron density

Based on (Griem 1964), the Stark broadening in SPECAIR is calculated as:

$$\Delta\lambda_{Stark}[A] = n_e[10^{16}\ cm^{-3}] \cdot 2\gamma[A] \cdot \left(\frac{T_e[K]}{10{,}000}\right)^{\alpha} \qquad \text{Eq. 3-3}$$

For O(777 nm), $\gamma_{777} \approx 0.0315\ A$ and $\alpha_{777} \approx 0.471$. We will see in Sec. 3.4.4 that the electron temperature in the faint region is near 20,000 K. The electron density in the faint region is expected to be on the order of 10^{16} – 10^{17} cm^{-3}. Using these values in Eq. 3-4, we get a Stark broadening of 0.01 – 0.1 nm for the O(777) triplet lines (Table 3-2).

Thus, Stark broadening is *a priori* not the dominant broadening mechanism in the faint region. Consequently, the uncertainties on the calculation of the Van der Waals broadening (and to a lesser extent, of the Doppler broadening) could prevent reliable measurement of the electron density. To assess the sensitivity of the n_e density to the VdW broadening, each fit is performed with 2 sets of conditions corresponding to the lower and upper bounds of the VdW and Doppler broadening widths.

For $t \leq 10$ ns, we consider $P = 1$ bar and $T_g = 600$ or 1200 K. The fit performed at $t = 9$ ns, considering $T_g = 1200$ K, is shown in Figure 1-17. The fit yields $n_e \approx 5{\cdot}10^{16}$ cm^{-3}, which is an upper bound on the electron number density because the temperature of 1200 K

corresponds to the smallest VdW width. The lower bound on the electron density is determined for the VdW width obtained at 600 K, and its value is $n_e = 2{\cdot}10^{16}$ cm^{-3}. Although the Stark width is comparable with the VdW width and much smaller than the instrumental width, it is interesting to note that the relative intensity of the two peaks and the dip between them are still sensitive to the electron number density.

For $10 \leq t \leq 25$ ns, the highest VdW broadening width is reached if T_g and n_{tot} reach about 800 K and $2.4{\cdot}10^{19}$ cm^{-3} ($P \approx 3$ bar), corresponding to ischoric heating and full dissociation of CO_2 into CO and O. Figure 3-19 represents a double-component fit performed at the anode at 16 ns. We note that the two components are shifted from each other, as a result of the Stark shift, which depends on the electron number density. At $t = 19$ ns, the fit of the narrow component with $P = 3$ bar, $T_g = 800$ K yields $n_e \approx 6{\cdot}10^{16}$ cm^{-3}, while the fit at $P = 1$ bar, $T_g = 1{,}200$ K yields $n_e \approx 1{\cdot}10^{17}$ cm^{-3}. Overall, in this time range, the uncertainty in the VdW broadening width leads to an uncertainty of less than a factor of about 2 in the measured n_e.

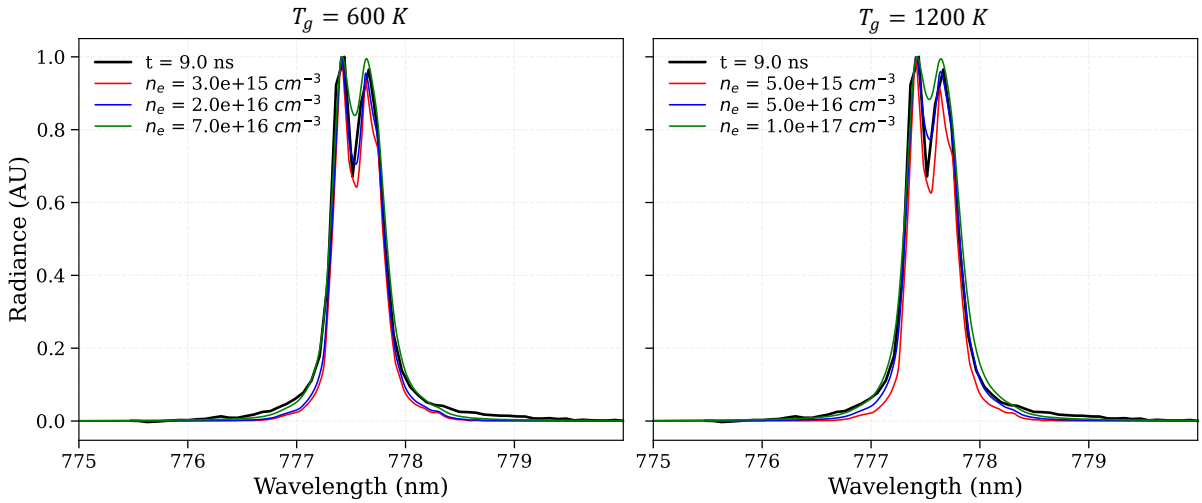

Figure 3-18. O(777) triplet emission from the faint region at time 9 ns, with a gate width of 4 ns. The spectrum is an average over 10,000 pulses, and is normalized in intensity. The SPECAIR fit with $T_g = 600$ K yields the best agreement with the experiment for $n_e = 2 \cdot 10^{16}$ cm^{-3}, whereas for $T_g = 1200$ K, it yields $n_e = 5 \cdot 10^{16}$ cm^{-3}.

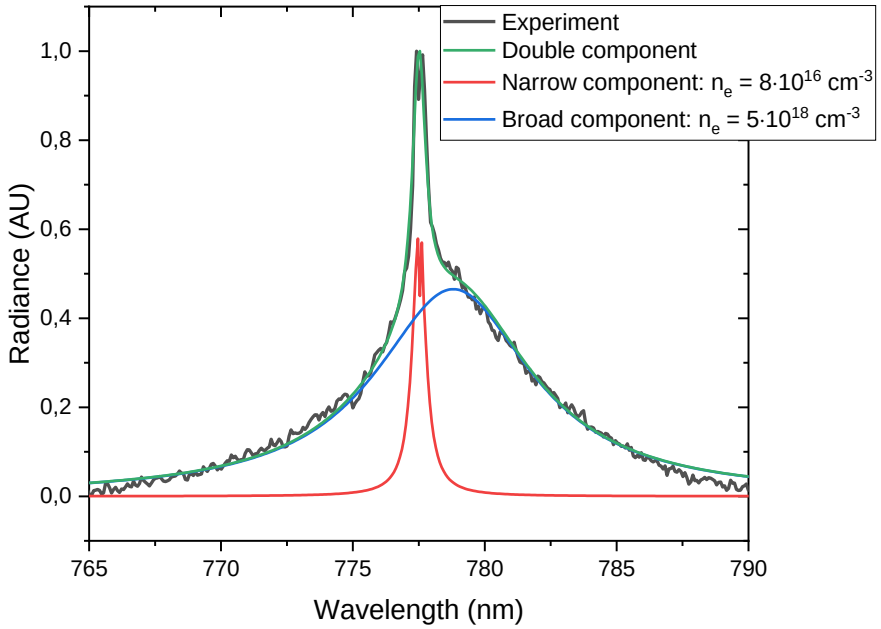

Figure 3-19. O(777) triplet emission from the faint and bright regions (measured at the anode in type a pulse) at time 16 ns, with a gate width of 4 ns. The spectrum is an average over 10,000 pulses and is normalized in intensity. Each component is fitted individually using SPECAIR, which yields $n_e = 8{\cdot}10^{16}$ for the narrow component, and $n_e = 5{\cdot}10^{18}$ cm^{-3} for the broad component.

3.4.3.3 Analysis of the bright regions

In this section, we discuss the dominant broadening phenomena in the bright regions, and their impact on the measured electron density. The FWHM of each phenomenon is reported in Table 3-2.

Van der Waals broadening

We estimate an upper bound of the Van der Waals broadening in the bright region using Eq. 3-1. From the analysis of the spectra of the bright region (showing high ionization and dissociation, cf Sec. 3.4.1), we suspect that it could be a thermal plasma. As will be shown later, the temperature is estimated to reach 30,000 K, the pressure about 50 bar after the first pulse, and about 10-20 bar after the reflection. The VdW broadening would be 0.02 for O(777) (obtained with $\gamma_{pert} = 1.3$). For O^+(470) and C^+(658) we use $\gamma_{pert} = 1$, which yields a VdW broadening of 0.01 nm. Since the total broadening measured for these lines in the bright region is on the order of 1 nm, we conclude that VdW broadening is negligible.

Doppler

We estimate an upper bound of the Doppler broadening using Eq. 4-5 with T_g = 30,000 K. We obtain FWHMs of the order of 0.02 nm, which is negligible compared to the total measured broadening.

Self-absorption

For O(777), we use the same two-parameters fitting procedure as for the faint region, this time using T_e = 30,000 K, and d = 100 µm. Self-absorption is as significant as in the faint region. For example, at t = 27 ns, the fit yields $n_{5S^\circ} \approx 8{\cdot}10^{15}$ cm^{-3} and a peak optical thickness of 0.7.

We estimate an upper bound of the optical thickness for O^+(455 – 475) and C^+(658) lines using SPECAIR. In the case of a thermal plasma at 30,000 K and 20 bar, the optical thickness of these lines is lower than 0.01. Thus, they can be considered optically thin in our experiments.

Stark broadening

In the bright region, we measure that the O(777) and C^+(658) lines are several nm broad. Such widths are much larger than the other broadening widths listed above (instrumental, VdW, Doppler, resonance, natural) and are indicative of Stark broadening at $n_e > 10^{18}$ cm^{-3}. Sample fits of O(777) and C^+(658) emission are reported in Figure 3-20 and Figure 3-23. The coefficients for the Stark broadening of C^+(658) implemented in SPECAIR are γ_{658} = 0.0519 A, and $\alpha_{658} = -0.2508$.

The Stark effect is weaker for the O^+(455 – 470) lines, but we still measure FWHMs between 0.2 and 2 nm. The instrumental broadening can account for a significant part of the FWHM, but as with O(777) in the faint region, the relative peaks and the dip between the peaks are sensitive to n_e. Contrary to the case of the faint region, the VdW width is small compared to the Stark width, so the fits of n_e are not sensitive to the (T_g, P) assumptions. A sample fit for these lines is reported in Figure 3-23. The coefficients for the Stark broadening of $O^+(^2D^\circ - {}^2F)$ implemented in SPECAIR are γ_{470} = 0.01233 A, and $\alpha_{470} = -0.2306$.

Table 3-2. Broadening FWHMs (in nm) for O(777 nm), O^+(470 nm), and C^+(658 nm).

Broadening type	O(777) FWHM [nm]			O^+(470) FWHM [nm]	C^+(658) FWHM [nm]
	$t < 10\ ns$	$10\ ns < t < 25\ ns$	$25\ ns < t$		
Natural (Lorentzian)	$< 10^{-4}$				
Resonant (Lorentzian)	$< 6{\cdot}10^{-4}$	< 0.001	< 0.004	10^{-4}	10^{-5}
Doppler (Gaussian)	0.004 – 0.005	0.004 – 0.005	0.02	0.02	0.02
Van der Waals (Lorentzian)	0.01 – 0.02	0.01 – 0.06	0.02	0.01	0.01
Instrumental (Trapezoidal)	0.2				
Stark at n_e = 10^{16} cm^{-3} and T_e = 20,000 K	0.01			0.002	0.01
Stark at n_e = 10^{17} cm^{-3} and T_e = 20,000 K	0.1			0.02	0.1
Stark at n_e = 10^{18} cm^{-3} and T_e = 30,000 K	1			0.2	1

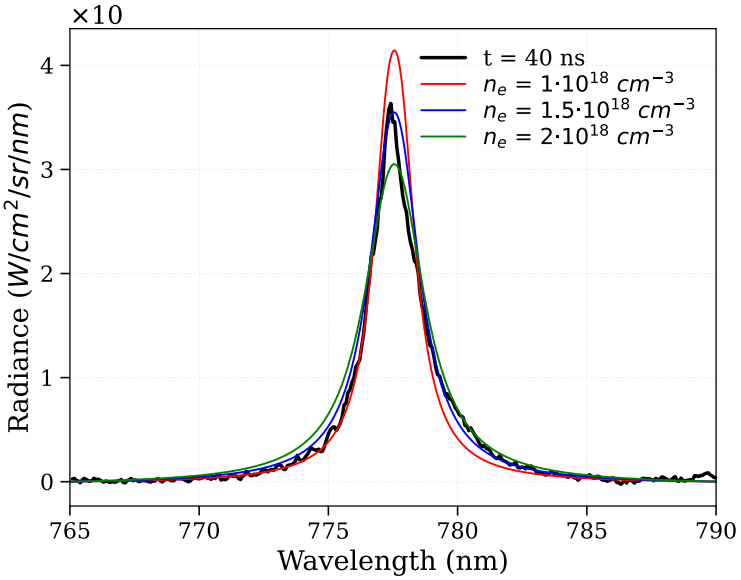

Figure 3-20. O(777) triplet emission measured in the bright region (anode) at time 40 ns, with a gate width of 4 ns. Theoretical spectra are computed using SPECAIR, with $T_e = 30,000\ K$, $d =$ 100 µm. The number densities $n_O = 2.8 \cdot 10^{18}\ cm^{-3}$ and $n_e = 1.5 \cdot 10^{18}\ cm^{-3}$ yield the best agreement with the experiment.

3.4.3.4 Temporal evolution of the electron density

Figure 3-21 shows the temporal evolution of the electron density in the faint and bright regions. The electron density in the faint region is in the range of 10^{16}-10^{17} cm^{-3}, whereas in the bright region it reaches $5{\cdot}10^{18}$ cm^{-3} after 13 ns at the anode and cathode, and $3{\cdot}10^{18}$ cm^{-3} after 28 ns at midgap. At 20 ns, the narrow component disappears, and the emission originates only from the bright region. The electron density in the bright region then decreases to $8{\cdot}10^{17}$ cm^{-3} at 70 ns (at the cathode and midgap). At 70 ns, the reflected pulse ionizes the plasma again to a few times 10^{18} cm^{-3}. Then, the electron density decays to about 2.10^{17} cm^{-3} at 400 ns.

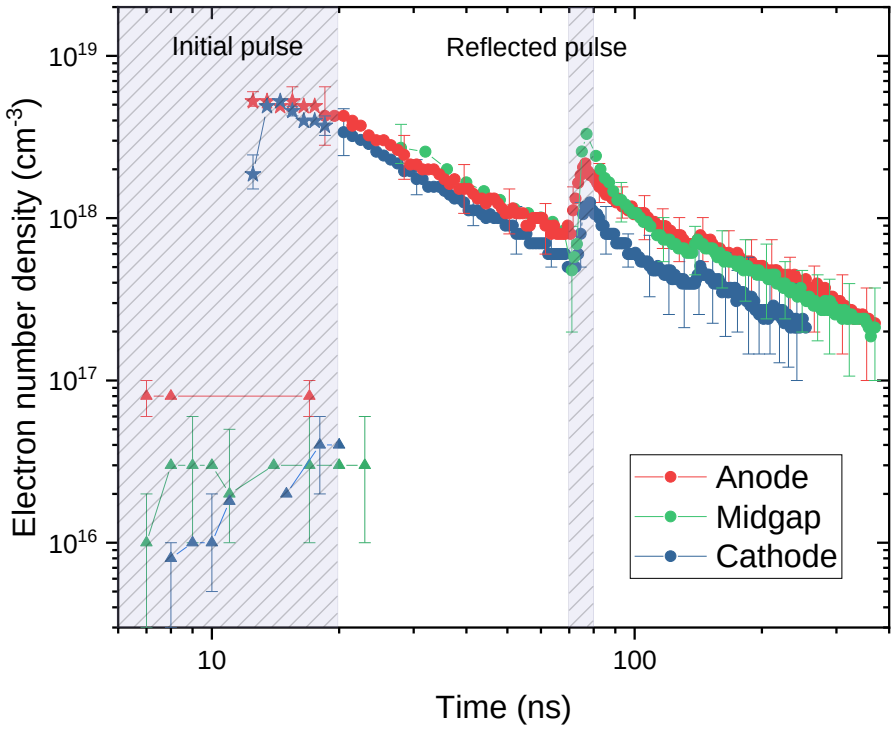

Figure 3-21. Temporal evolution of the electron number density at three locations along the inter-electrode gap. The measurements are made using the O triplet. The signal is integrated over about 10^3-10^5 pulses and using a 4 ns gate width. From 10 to 25 ns, the double-component spectra yield two different electron density values at each location: the star symbols stand for the wide component of the fit, whereas the triangles stand for the narrow one. After 25 ns, the circles stand for the single component spectra. The hatched areas indicate the duration of the pulse and of its first reflection.

We compare the electron densities obtained from O, O^+ and C^+ lines in Figure 3-22. Note that O^+ and C^+ emission only comes from the bright region, thus, in this graph, we only show the electron density measured in this region. Given the uncertainty on the measurements, the three methods give consistent results (within a factor 2). The electron densities deduced from the O(777) triplet are the most accurate because the Stark width of

these lines is known with the highest accuracy. Also, the Stark broadening width is larger for O(777) and C^+(658) than for O^+(455 – 475), making the electron density measurements with O(777) and C^+(658) more reliable than with O^+(455 – 475).

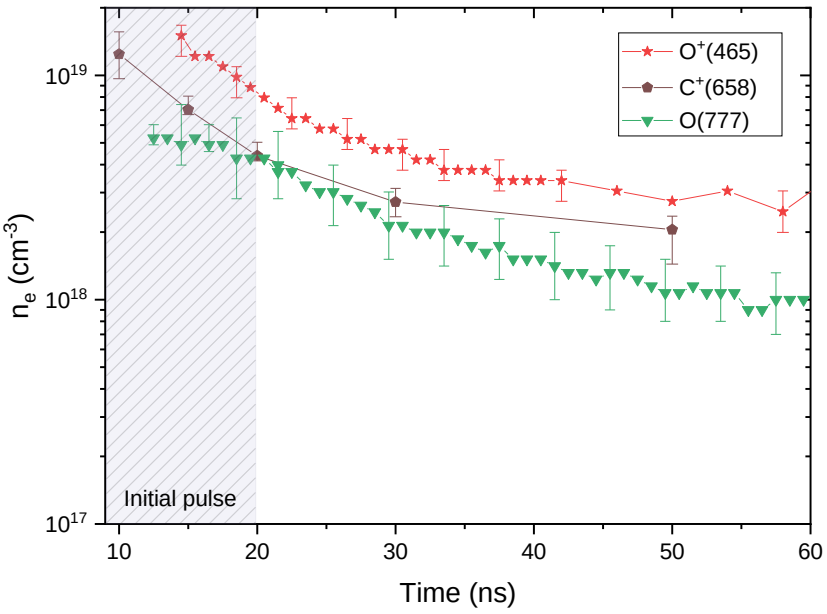

Figure 3-22. Temporal evolution of the electron number density in the bright region (anode), measured from Stark-broadened lines of O(777 nm), O^+(455 – 475 nm), and C^+(658 & 678 nm).

3.4.4 Electronic temperature measurements

Bright regions

We measure the emission lines of O^+ at 459, 465, and 470 nm – corresponding to radiative deexcitation of electronic states at 28.4, 25.7, and 28.9 eV above the ground state of O^+ – and the emission lines of C^+ at 658 and 678-681 nm – corresponding to electronic states at 16.3 and 22.5 eV above the ground state of C^+. According to Sec. 3.4.1, these lines come from the bright regions.

If these high electronic states of O^+ and C^+ follow a Boltzmann distribution, the electronic temperature describing this distribution can be deduced from the relative emission of the measured electronic states. The spectra are fit using SPECAIR (Laux et al. 2003), considering the diameter of the bright region (see Figure 3-9) as the emission length, using a pressure of 50 bars and a gas temperature of 30,000 K. The values of P and T_g are orders of magnitude that will be confirmed by the measurements, but they have a negligible impact on the fits (the Stark effect dominates). The fits yield the densities of electrons (from the Stark width) and of several electronic states, as well as the electronic temperature. A sample

fit is reported in Figure 3-23. The good fit quality supports the relevance of using a Boltzmann distribution for the measured electronic states. We obtain the temperature of the electronic states.

In Sec. 3.4.6.2, we estimate the time of relaxation of these electronic states toward Saha-Boltzmann equilibrium. We obtain less than 1 ps for all O^+ and C^+ states investigated during the whole 20 – 150 ns period, showing that the temperature of these electronic states equals the temperature of the electrons.

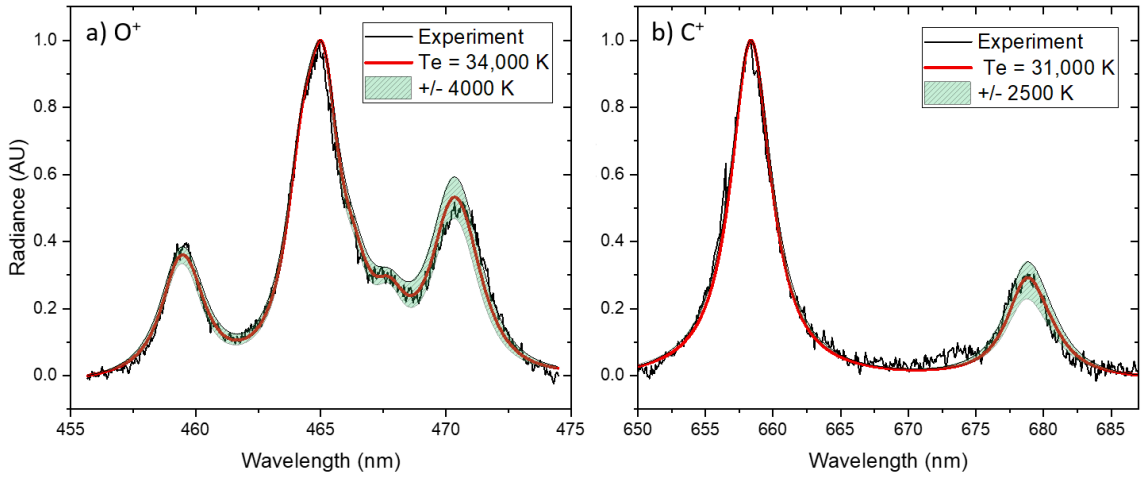

Figure 3-23. Plasma emission spectra in the bright region at the anode integrated from 18 to 22 ns, along with their fits obtained with SPECAIR. The emission is dominated by a) O^+ lines between 455 and 475 nm, and by b) C^+ lines between 650 and 685 nm.

We measure the O^+ and C^+ lines at the anode, midgap, and cathode with a 4 ns gate width up to the disappearance of their signal, i.e., for the first 200 ns. We obtain the electronic temperatures of O^+ and C^+ in the bright region. The comparison of these two temperatures at the anode is reported in Figure 3-24. Given the 5-10% error bars, the two temperatures match quite well, which confirms the Saha-Boltzmann equilibrium.

The temporal evolution of T_e at the anode, midgap, and cathode in the bright regions is plotted in Figure 3-25. The electron temperature reaches about 33,000 K by the end of the pulse, then slowly decreases with bounces due to the reflected pulses at 70 and 140 ns. The homogeneity of the electron temperature in the bright regions echoes the homogeneous spectral features (Sec. 3.4.1) and electron density (Figure 3-21). It suggests that, at a given time, the physical conditions are similar in the bright regions, whatever the pulse type and the location of the region in the interelectrode gap.

Faint region

To estimate T_e in the faint region at midgap before 30 ns, we use the O lines at 716 nm and 777 nm, corresponding to electronic states at 14.5 and 10.7 eV. In Sec. 3.4.6.2, we estimate

that it takes less than 0.1 ns for these states to reach Saha-Boltzmann equilibrium. Thus, their relative density yields the electron temperature. As shown in Figure 3-25, we obtain $T_e \sim$ 20,000 K in the faint region, whereas it is about 30,000 K in the bright region. The electron temperature is much higher than the gas temperature (600 – 800 K) in the faint region, confirming its high degree of nonequilibrium.

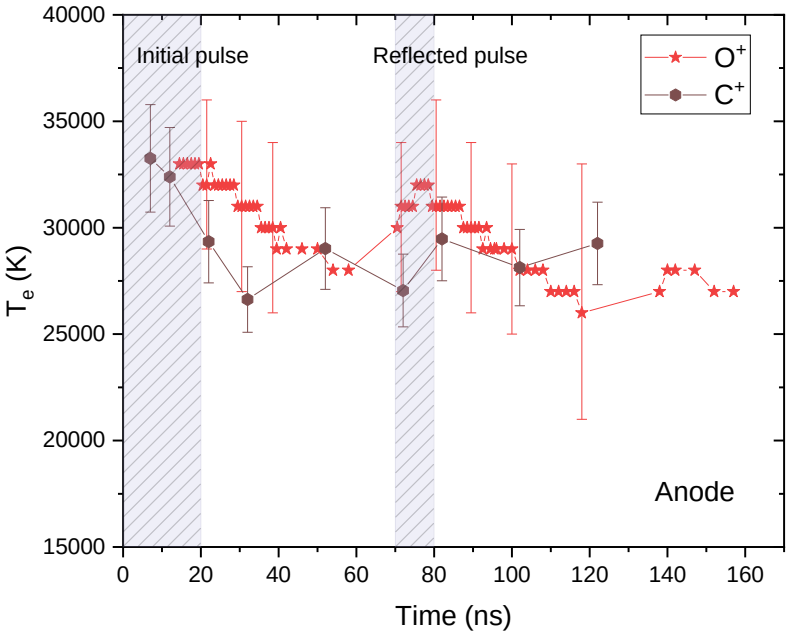

Figure 3-24. Temporal evolution of the electron temperature measured in the bright region (here at the anode) from O^+(455 – 475 nm) and C^+(458 & 478 nm) emission, using a 4 ns gate width.

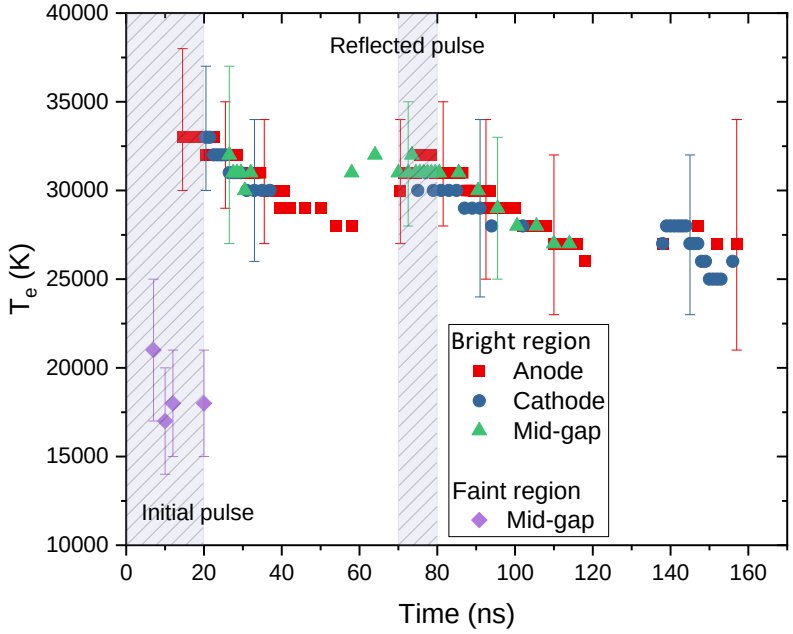

Figure 3-25. Temporal evolution of the electron temperature measured from O^+(455 – 475 nm) in the bright regions, and from O(716) and O(777) in the faint region. The gate width used is 4 ns.

3.4.5 Excited species measurements and assessment of Local Thermodynamic Equilibrium in the bright region

In the *bright region*, we measure the excited state densities of O, O^+, and C^+ using the O 777 nm lines (broad component), the O^+ lines between 459 and 471 nm, and the C^+ lines at 658, 678 – 681, 711 – 713, and 723 nm. These lines are calibrated in absolute intensity, they are measured with a 4 ns gate width, and averaged over 1000 pulses. Since the O^+ and C^+ lines are optically thin, their integrated emission is proportional to the product of the excited state density times the filament diameter. We obtain the excited state densities using the filament diameter measured in Figure 3-9. As mentioned in the previous section, the O(777) triplet is not optically thin in our conditions, so we use a fitting procedure to obtain the product of its excited state density times the plasma diameter.

We present the results of several illustrative cases: at the anode at 20 and 80 ns in Figure 3-26 and Figure 3-27, and at midgap at 80 ns in Figure 3-28. The experimental data are compared to LTE calculations using CANTERA (Goodwin et al. 2017) and the thermodynamic data of NASA-CEA (McBride et al. 2002) supplemented with data for O^{++} and C^{++} taken from Capitelli et al. (Capitelli et al. 2005).

First, we fit the O^+ excited state measurements with a Boltzmann distribution, as shown on the upper graph of each figure (Figure 3-26, Figure 3-27, and Figure 3-28). The slope gives the electronic temperature of O^+, $T_{e,O+}$. Then, assuming that all O^+ electronic states

follow a Boltzmann distribution, we deduce the ground state density of O^+ by extrapolating the distribution, and we infer the total O^+ density. This assumption is motivated by the fast relaxation time of the distribution of O^+ electronic states in our high n_e conditions (see calculation in Appendix A and the bottom graph in Figure 5-1), and by the good alignment of the points on the Boltzmann plot. We then perform LTE calculations at $T_{e,O+}$, and adjust the pressure to match the O^+ density. The resulting pressure is named $P_{LTE,O+}$. Finally, we calculate the LTE composition at $T_{e,O+}$ and $P_{LTE,O+}$, and we obtain the LTE densities of O and C^+. As an illustration, we report in Figure 3-29 the LTE composition of the plasma at 30,000 K and as a function of the pressure.

The LTE distributions of the O and C^+ states are plotted as dotted lines in Figure 3-26, Figure 3-27, and Figure 3-28. At t = 20 ns at the anode (Figure 3-26), neither the C^+ excited states nor O(^{5}P) agree with the LTE calculation at ($T_{e,O+}$ $P_{LTE,O+}$). They are overpopulated by a factor of 20 and 500 respectively. Thus, the bright region is not in LTE at t = 20 ns. We obtain the same result at t = 10, 30, and 50 ns, as well as at the cathode and at midgap.

In contrast, after the reflection, we observe a much better agreement between the excited state measurements and the LTE calculation in the whole interelectrode gap. This is illustrated in Figure 3-27 and Figure 3-28, which show that, at 80 ns, the C^+ excited states fall on the LTE distribution (at the anode and midgap) and that O(^{5}P) is reasonably close to the LTE distribution (within a factor 5 at the anode, and a factor 10 at midgap). Additionally, the measured electron density agree with the LTE simulation: at the anode, $t = 80$ ns, we measured $n_e \sim 3.8{\cdot}10^{18}$ cm^{-3} and the LTE simulation predicts $n_e \sim 2.7{\cdot}10^{18}$ cm^{-3}; at midgap, we measured $n_e \sim 1.3{\cdot}10^{18}$ cm^{-3} and the LTE simulation predicts $n_e \sim 1.5{\cdot}10^{18}$ cm^{-3}. We conclude that the reflected pulse brings the plasma near LTE conditions. Thus, it results that $T_g = T_e$ and $P \approx P_{LTE,O+}$: our measurements yield estimations for the gas temperature and pressure in the filament. At 80 ns, the gas temperature is homogeneous at about 30,000 K. At the anode, $P \approx P_{LTE,O+} = 12$ bar. At midgap, $P \approx P_{LTE,O+} = 21$ bar.

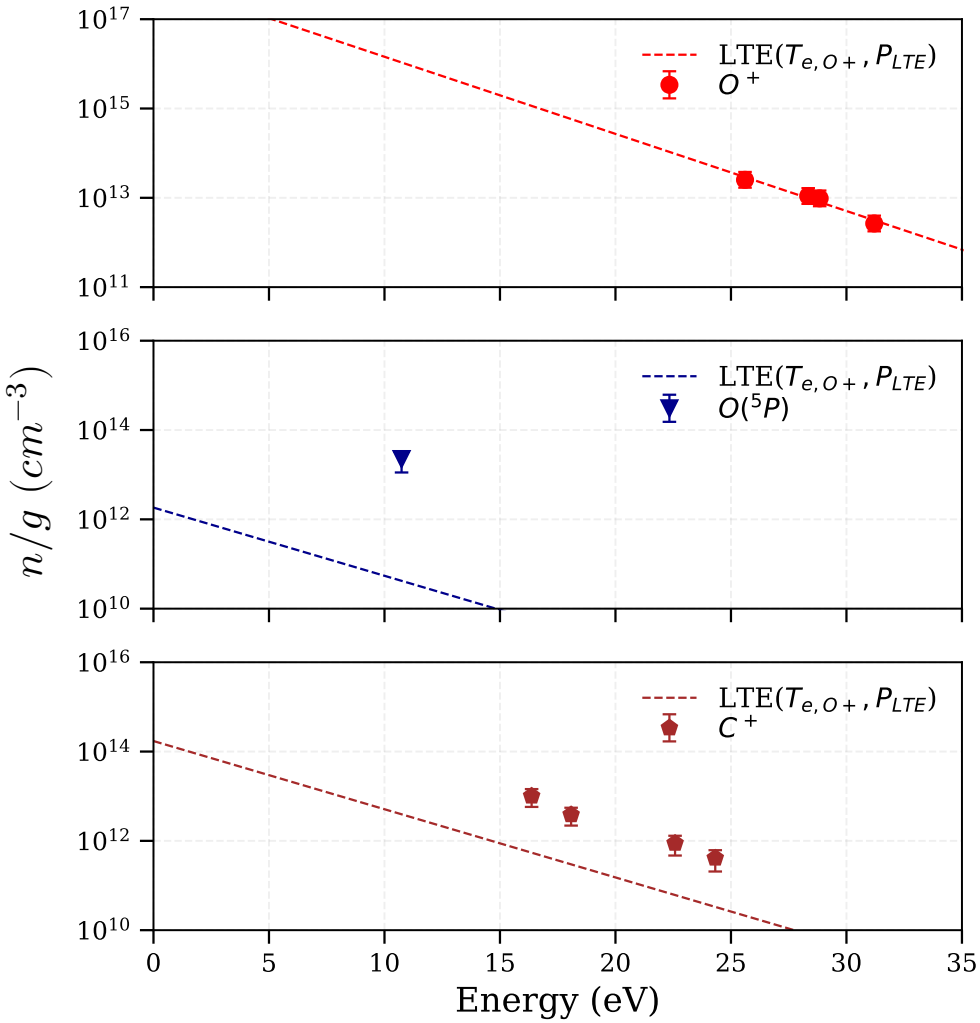

Figure 3-26. Boltzmann plot of O^+ (top), O (center), and C^+ (bottom) excited states measured in the bright region at the anode at t=20 ns. The O^+ excited state densities are deduced from the 459 – 471 nm lines, O(^{5}P) from the 777 nm line, and C^+ excited states from 658 – 724 nm lines. On the top graph, the pressure $P_{LTE,O+}$ is deduced by (i) assuming LTE at $T_{e,O+}$ and (ii) determining the ground state density of O^+ by assuming Boltzmann equilibrium with the O^+ excited state densities. We obtain $T_{e,O+}$ = 32,000 K and $P_{LTE,O+}$ = 2 bar. The O and C^+ excited state densities are then plotted along with the LTE distribution at ($T_{e,O+}$ $P_{LTE,O+}$). We find that O(^{5}P) and C^{+*} are overpopulated by factors of 500 and 20, respectively, compared to the LTE calculation.

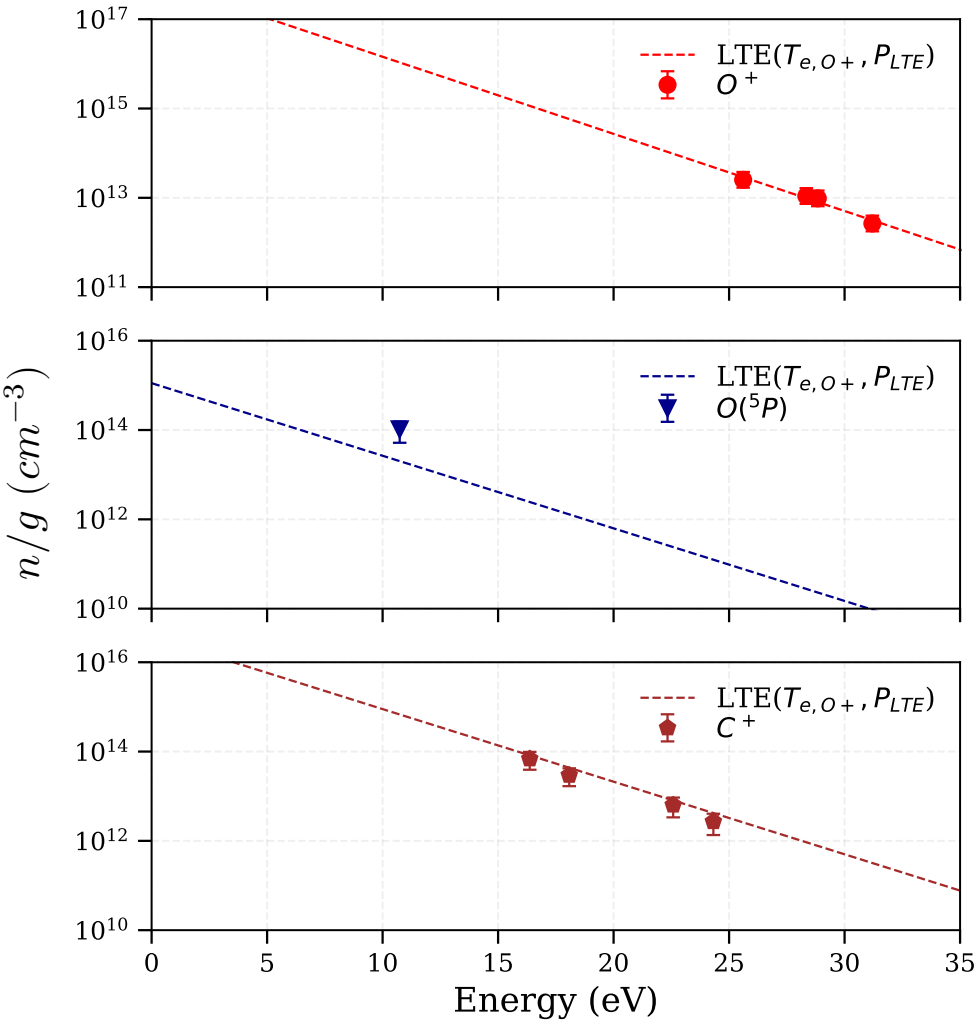

Figure 3-27. Boltzmann plot of O^+ (top), O (center), and C^+ (bottom) excited states measured at the anode at t=80 ns. The O^+ excited state densities are deduced from the 459 – 471 nm lines, $O(^5P)$ from the 777 nm line, and C^+ excited states from 658 – 724 nm lines. On the top graph, the pressure $P_{LTE,O+}$ is deduced by (i) assuming LTE at $T_{e,O+}$ and (ii) matching the O^+ excited state densities. We obtain T_e = 31,000 K and $P_{LTE,O+}$ = 21 bar. The O and C^+ excited state densities are then plotted along with the LTE distribution at (T_e, $P_{LTE,O+}$). The C^+ excited states fall on the LTE distribution and the $O(^5P)$ density agrees within a factor 5.

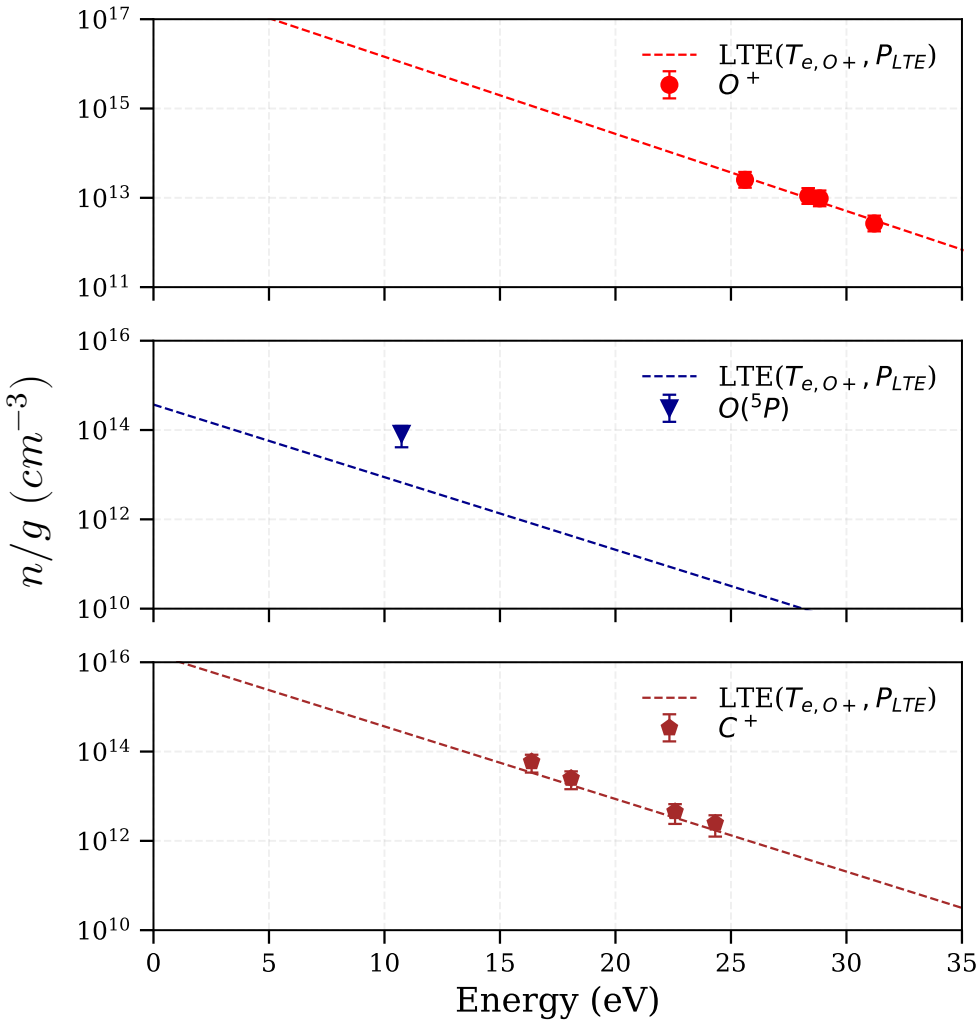

Figure 3-28. Boltzmann plot of O^+ (top), O (center), and C^+ (bottom) excited states measured at midgap at t=80 ns. The O^+ excited state densities are deduced from the 459 – 471 nm lines, $O(^5P)$ from the 777 nm line, and C^+ excited states from 658 – 724 nm lines. On the top graph, the pressure $P_{LTE,O+}$ is deduced by (i) assuming LTE at $T_{e,O+}$ and (ii) matching the O^+ excited state densities. We obtain T_e = 31,000 K and $P_{LTE,O+}$ = 12 bar. The O and C^+ excited state densities are then plotted along with the LTE distribution at (T_e, $P_{LTE,O+}$). The C^+ excited states fall on the LTE distribution and the $O(^5P)$ density agrees within a factor 10.

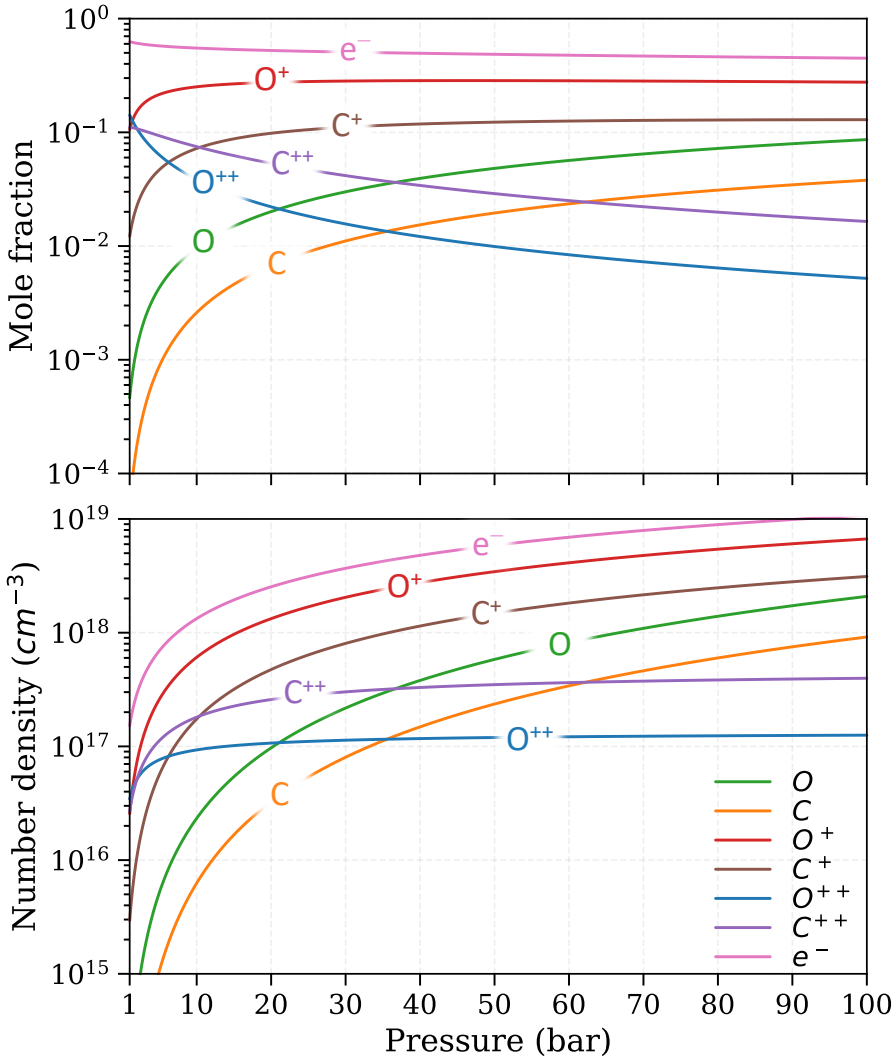

Figure 3-29. LTE mole fractions (top) and number densities (bottom) of the main species at T_g = 30,000 K as a function of pressure. Calculated with CANTERA using data from NASA-CEA (McBride et al. 2002) and Capitelli et al. (Capitelli et al. 2005).

3.4.6 Degree of equilibrium in the bright and faint regions

3.4.6.1 Thermal equilibrium in the bright region before the reflection

Before the reflection, the bright region near the electrodes is not in LTE. Still, it is highly ionized, and electron-ion collisions could establish thermal equilibrium, i.e., $T_g = T_e$. Thermal equilibrium is reached if the characteristic time of thermalization between electrons and heavy species is much shorter than the characteristic time of temperature variation. This condition can be expressed as:

$$\frac{T_e(t+\tau_{ei}) - T_e(t)}{T_e(t)} \ll 1 \qquad \text{Eq. 3-4}$$

which is equivalent to:

$$\tau_{ei} \ll \frac{T_e(t)}{\frac{\partial T_e}{\partial t}(t)} \qquad \text{Eq. 3-5}$$

Using the measurements from Figure 3-25, we estimate $\frac{\partial T_e}{\partial t}(20 \leq t \leq 60\ ns) \approx 150\ K/ns$. Thus, knowing that $T_e \approx 30{,}000\ K$ during this period, we deduce that thermal equilibrium is reached if $\tau_{ei} \ll 200\ ns$.

We estimate the electron-ion thermalization time τ_{ei} as in (Minesi et al. 2021):

$$\tau_{ei} \approx \left(\frac{2m_e}{m_{ion}}\nu_{ei}\right)^{-1} \qquad \text{Eq. 3-6}$$

where m_e and m_{ion} are the electron and ion masses, and ν_{ei} the electron-ion collision frequency. ν_{ei} can be estimated as:

$$\nu_{ei} \approx n_i \sigma_{Coul} v_e \qquad \text{Eq. 3-7}$$

with n_i the ion number density (equal to n_e), σ_{Coul} the Coulomb cross-section, and v_e the mean thermal velocity of electrons, $v_e = \sqrt{8k_bT_e/\pi m_e}$. The Coulomb cross-section is calculated as in (Raizer 1991):

$$\sigma_{Coul} \approx 2.87 \cdot 10^{-14} \frac{\ln(\Lambda)}{T_e[eV]^2}[cm^2] \qquad \text{Eq. 3-8}$$

where $\ln(\Lambda) = 13.57 + 1.5\log(T_e[eV]) - 0.5\log\left(n_e[cm^{-3}]\right)$ is the Coulomb logarithm. Thus, using the values of n_e and T_e measured in the filament (Figure 3-21 and Figure 3-25), and assuming $m_{ion} = m_{CO2+}$ (the heaviest significant ion), we obtain an upper bound of τ_{ei}.

In Figure 3-30, we report the temporal evolution of τ_{ei} and of the characteristic time of T_e variation. At $t = 15$ ns at the electrodes, τ_{ei} is approximately 4 ns. Thus, at $t = 20$ ns, the bright regions at the electrodes are already in thermal equilibrium, $T_g = T_e$. As the

thermalization condition is verified at every location (in the bright regions) up to 50 ns, thermal equilibrium is maintained at least during this period.

As a comparison, $\tau_{ei} \sim 100\ ns$ in the faint region ($T_e \sim 2\ eV$, $n_e \sim 10^{16} - 10^{17}\ cm^{-3}$), which is consistent with the measurement of $T_e \neq T_g$ there.

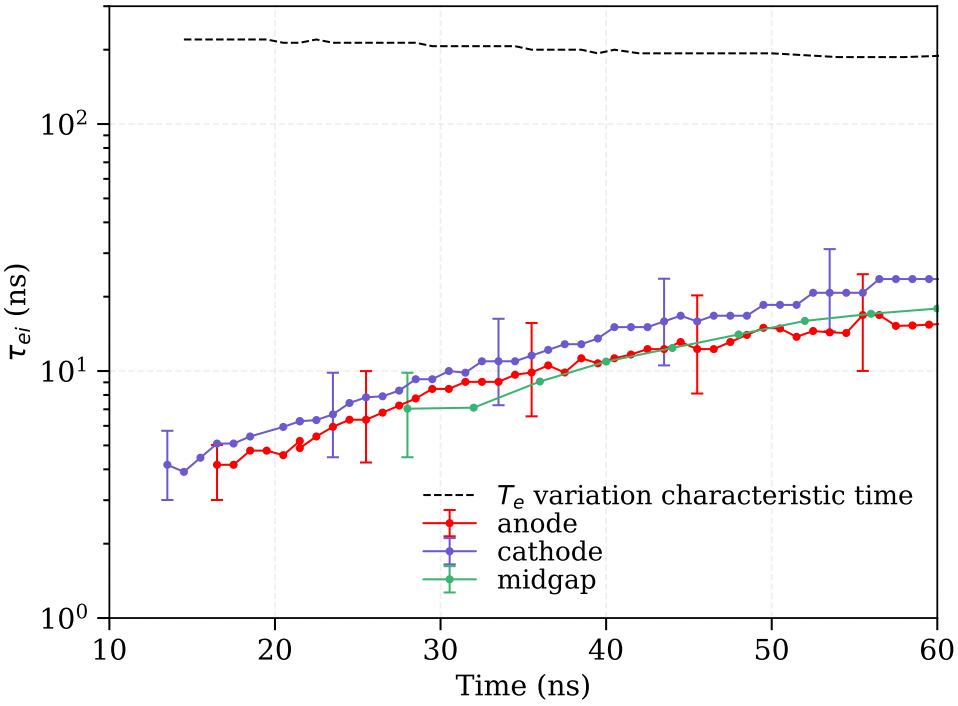

Figure 3-30. Electron-ion thermalization characteristic time (τ_{ei}) compared to the T_e variation characteristic time of about 200 ns. At t < 60 ns, τ_{ei} << 200 ns at every location, suggesting that the bright regions are in thermal equilibrium.

3.4.6.2 Saha-equilibrium in the bright & faint regions

We want to assess the validity of the Saha-Boltzmann assumption used to infer the electron temperature in the bright and faint regions from the measured electronic state distributions. This electron temperature was also used in the electron density measurements to determine the Stark broadening and the self-absorption.

Based on the approach of Cristoforetti *et al.* (Cristoforetti et al. 2010) and Griem (Griem 1963), we estimate the time needed for two electronic states to equilibrate as the characteristic time of collisional excitation from the lower state to the upper state. According to these authors, this time can be estimated as:

$$\tau_{rel} = \frac{6.3 \cdot 10^4}{n_e f_{lu} \langle \bar{g} \rangle} \cdot \Delta E_{ul} \cdot (kT)^{\frac{1}{2}} \cdot e^{\frac{\Delta E_{ul}}{kT}} \cdot \eta_i \qquad \text{Eq. 3-9}$$

with n_e $[cm^{-3}]$ the electron density, f_{lu} the absorption oscillator strength of the transition, $\langle \bar{g} \rangle$ the Gaunt factor, ΔE_{ul} $[eV]$ the transition energy, kT [eV] the electron temperature,

and η_i the ionization fraction of the species i considered (for example, for O: $\eta_O = n_{O^+}/(n_O + n_{O^+})$).

For the **bright regions**, we compute the equilibration time of the $\mathbf{O}^+(2s^22p^2(^3P)3p\ ^4D°)(23.0\text{ eV}) \leftrightarrow \mathbf{O}^+(2s^22p^2(^3P)3s\ ^4P)(25.6\text{ eV})$ transition which emits at 465 nm. These are the lowest electronic states of O^+ involved in our measurements. Using $f_{lu} = 1.2$, $\Delta E_{ul} = 2.6$ eV, and the n_e, T_e measurements from Figure 3-21 and Figure 3-25 in Eq. 4-5, we obtain an equilibration time of 0.5 – 4 ps during the whole 20 – 150 ns period. A similar calculation for $\mathbf{C}^+(2s^23s\ ^2S)(14.4\text{ eV}) \leftrightarrow \mathbf{C}^+(2s^23p\ ^2P°)(16.3\text{ eV})$ using $f_{lu} = 0.7$ and $\Delta E_{ul} = 1.9$ eV results in a relaxation time of 0.5 – 3 ps. Moreover, it is faster for the upper state to equilibrate with higher states, so $\mathbf{O}^+(2s^22p^2(^3P)3p\ ^4D°)(23.0\text{ eV})$ and $\mathbf{C}^+(2s^23s\ ^2S)(14.4\text{ eV})$ also equilibrate with the higher states and the electrons in about 1 ps, which is small compared to the characteristic times of n_e and T_e variation in the bright regions (which are on the order of 10 and 200 ns, respectively, according to Sec. 3.4.5 for T_e and Appendix A for n_e). Therefore, these electronic states are in Saha-Boltzmann equilibrium, and the electronic temperature measured with these states equals the electron temperature.

For the **faint region**, the lowest transition we measure is the triplet at 777 nm: $O(^5S°) \leftrightarrow O(^5P)$, with states at 9.1 and 10.7 eV, respectively. With $f_{lu} = 1$, $\Delta E_{ul} = 1.6$ eV, $n_e = 10^{16}$ cm^{-3} (the lowest n_e measured in the faint region), and $T_e =$ 20,000 K (the electron temperature measured in the faint region), we obtain $\tau_{rel} \approx 0.1$ ns, which is small compared to the characteristic times of n_e and T_e variation in the faint region. Thus, the O electronic states above $O(^5S°)$ (which lies 9.1 eV above the ground state) are in Saha-Boltzmann equilibrium with the electrons. This supports our measurement of T_e in the faint region using these states, as well as our measurement of n_e using the Boltzmann distribution assumption to calculate the self-absorption of O(777).

To summarize:

(i) The bright region produced by the first pulse is in chemical nonequilibrium but in thermal equilibrium. Moreover, the measured electronic states of O^+ and C^+ are in Saha-Boltzmann equilibrium with the electrons. After the reflection, the bright region is close to the LTE.

(ii) The faint region produced by the first pulse is in chemical and thermal nonequilibrium. Nevertheless, the measured electronic states of O are in Saha-Boltzmann equilibrium with the electrons, allowing us to infer the electron temperature from their electronic temperature.

3.5 Discussion

3.5.1 Succession of a non-thermal and thermal spark. Comparison with literature.

Following Ceppelli *et al.* (M. Ceppelli et al. 2021), we decompose the temporal evolution of the discharge into two phases. Phase I, from 0 to 70 ns, is the breakdown phase. The plasma is heterogeneous along the gap. Phase II, after 70 ns, occurs after the reflection arrives.

Phase I:

Near the electrodes the micrometric bright spheres or filaments are highly ionized – up to $n_e = 5 \cdot 10^{18}\ cm^{-3}$ (Figure 3-21) – and their spectra are dominated by atomic lines (O and O^+, see Figure 3-11), revealing significant dissociation of CO_2. However, since we do not see C or C^+ emission, CO_2 is likely to be dissociated only into O (or O^+) and CO (or CO^+). The electron temperature in these bright regions is about 30,000 K (Figure 3-25). The high electron density allows the gas and electron temperatures to equilibrate quickly via electron-ion collisions (Figure 3-30). The plasma in the bright regions is thus in thermal equilibrium, but not in LTE.

In the middle of the gap, for the first 30 ns, the spectrum is dominated by molecular emission – CO Angström, C_2 Swan, and $CO_2^+(A^2\Pi_u - X^2\ \Pi_g)$ – and O lines (Figure 3-13). The ns-images of the discharge show a faint region, with the occasional appearance of a filament. In the faint region, the electron density is about 10^{16} cm^{-3} (Figure 3-21), and the electron temperature about 20,000 K (Figure 3-25). In contrast, we measured a gas temperature around 600-800 K using the rotational temperature of the (0,0) vibrational band of the 2nd positive system of N_2. Thus, the faint region is a nonequilibrium plasma of the non-thermal spark type. Additionally, we observed that the faint region diameter is about 400 – 600 µm, which is consistent with literature values for non-thermal NRP-sparks (Pannier 2019; Rusterholtz et al. 2013).

Initially rare at midgap – less than 20% occurrence before 30 ns (Figure 3-6) – filaments become progressively more frequent – about 50% occurrence at 50 ns – and start to dominate the total emission. After 30 ns, the spectra, electron densities, and electron temperatures in these filaments at midgap are similar to those in the bright spheres near the electrodes. These plasmas are near thermal equibrium, but not in LTE.

Phase II:

In phase II, which starts just after the reflection at 70 ns, more than 80% of the pulses are of type-f, i.e. homogeneous filaments in the inter-electrode gap (Figure 3-6). The electron density, which had decreased to about 10^{18} cm^{-3} by the end of phase I, jumps to about $4 \cdot 10^{18}$ cm^{-3} in the middle of the gap. The spectra at the electrodes and midgap are similar, showing strong C^+ lines in addition to the O and O^+ lines already observed in phase I. We showed that the plasma is near LTE conditions at 30,000 K and 10 – 30 bar (Figure 3-27, Figure 3-28). Thus, the gas is fully dissociated and ionized. The main species are e^-, O^+, C^+, C^{++}, O, O^{++}, C (in descending order of mole fraction between 20 and 30 bar, see Figure 3-29).

Micron-size filaments near full-ionization and thermal equilibrium were already observed for discharges in air. In the 70s, Albrecht and Maly (Albrecht et al. 1977; Maly and Herweg 2008) studied high-voltage pulses to ignite car engines. After about 10 ns, they reported electron densities above 10^{19} cm^{-3}, gas temperatures of about 50,000 K, and LTE in the early stages of the plasma. Later on, filaments were also observed by Parkevich *et al.* (Parkevich et al. 2019), using a 25 kV – 40 ns voltage pulse in a pin-to-plate configuration, by Minesi *et al.* (Minesi et al. 2020), using a 17 kV – 20 ns voltage pulse in a pin-to-pin configuration, and by Shcherbanev *et al.* (Shcherbanev et al. 2019), with a 40 kV – 20 ns voltage pulse in a DBD configuration. Minesi *et al.* (Minesi et al. 2021) then demonstrated that the full ionization proceeds via the ionization of excited electronic states of the atomic species, and that thermalization occurs via electron-ion elastic collisions. They named this new NRP regime the thermal spark. For the first time, our measurements indicate that a thermal spark occurs in CO_2.

Comparison with literature results:

Figure 3-31 shows a comparison of our measurements of electron densities and temperatures with those of Ceppelli *et al.* (M. Ceppelli et al. 2021) and other studies from the same group (Luca Matteo Martini et al. 2018; Montesano et al. 2023).

In phase I (of their type I pulse), Ceppelli *et al.* measured CO Angström and $CO_2^+(A^2\Pi_u - X^2\,\Pi_g)$ bands, as well as O lines. All their measurements were made at midgap. From $t = 15\ ns$, they measured $n_e \sim 10^{18}\ cm^{-3}$, which is similar as the electron density that we obtain in the filament at midgap. They did not report electron density measurements between 0 and 15 ns, whereas our measurements indicate values around $3{\cdot}10^{16}$ cm^{-3} during that period. Using the N_2 2^{nd} positive system (N_2 SPS) as a probe, they measured an initial gas temperature of 400 K, whereas we obtained about 600 K in this work. Overall, their measurements of phase I are consistent with the measurements of the faint region in this work and Ref. (Maillard et al. 2022). Moreover, the faint region corresponds to what Pannier

(Pannier 2019) and Heijkers *et al.* (Heijkers et al. 2019) simulated. The 10^{16} – 10^{17} cm^{-3} electron density we measure agrees with the predictions of both models.

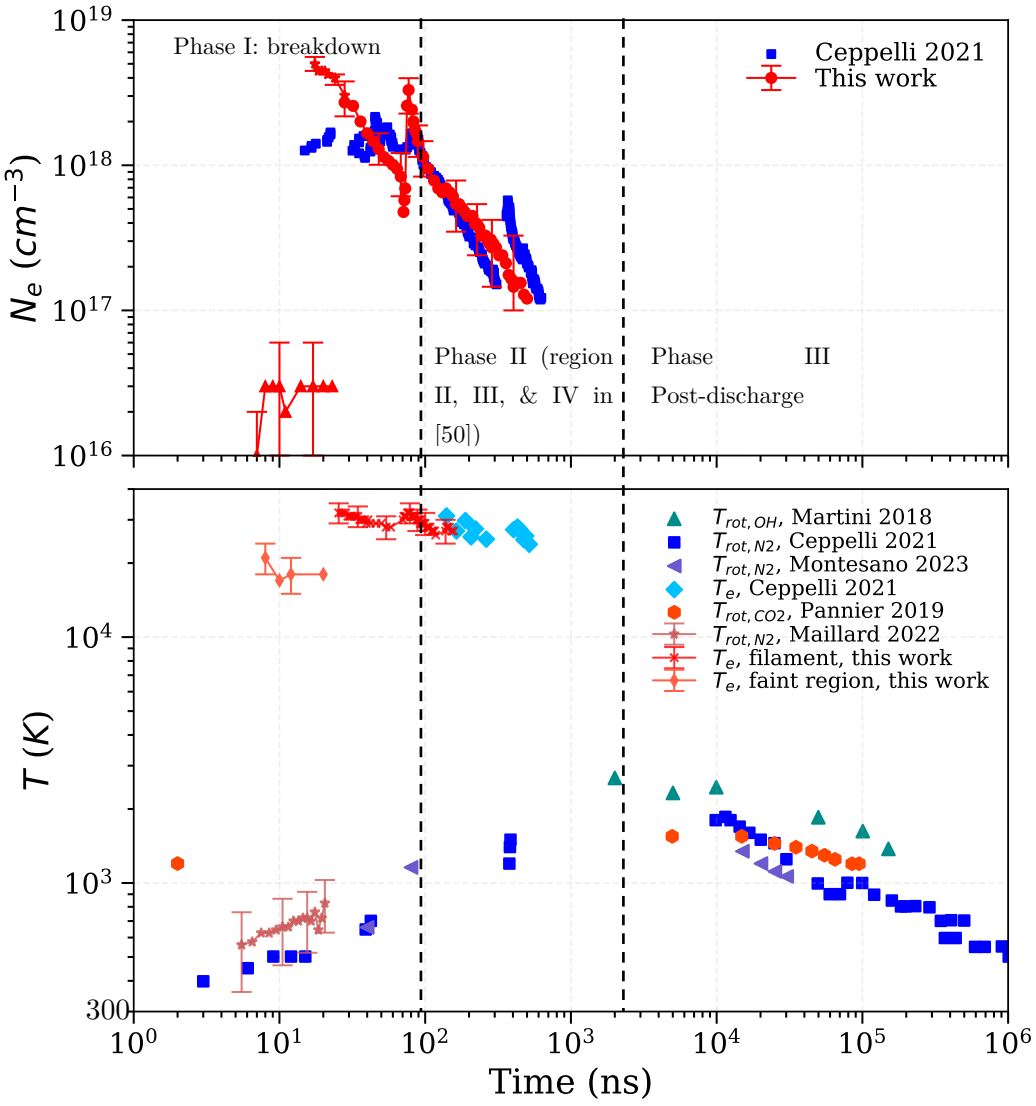

Figure 3-31. Comparison of electron densities (top) and temperatures (bottom) measured at midgap in the Trento experiments and in the present work. In Trento's experiments, the secondary pulse is at 400 ns. In the present work, the reflected pulse is at 70 ns. Hence, the electron temperature increases to high values at earlier times in the present work.

In phase II (region II, III, IV in (M. Ceppelli et al. 2021)), Ceppelli *et al.*, like us, measured a change in the spectral composition at midgap due to a power reflection (or a secondary pulse). Their spectra at midgap are compared to those obtained in the present work in Figure 3-32. They are quasi-identical. The spectral features they did not identify are the same O^+ and C^+ lines we measure. In addition, similar electron densities and temperatures were measured in both experiments (Figure 3-31). Thus, we suggest that the sparks generated by the power reflection and the secondary pulse are also thermal and near LTE in their conditions.

In phase III, the temperature measurements of Martini *et al.* (Luca Matteo Martini et al. 2018) (using OH LIF), Ceppelli *et al.* (M. Ceppelli et al. 2021) (using N_2 SPS OES), and Montesano *et al.* (Montesano et al. 2023) (using N_2 SPS OES) agree with those of Pannier (Pannier 2019) (using CO_2 IR emission) (Figure 3-31). The gas temperature is about 1000 – 2000 K. Recombination during this phase is likely to be important for CO production.

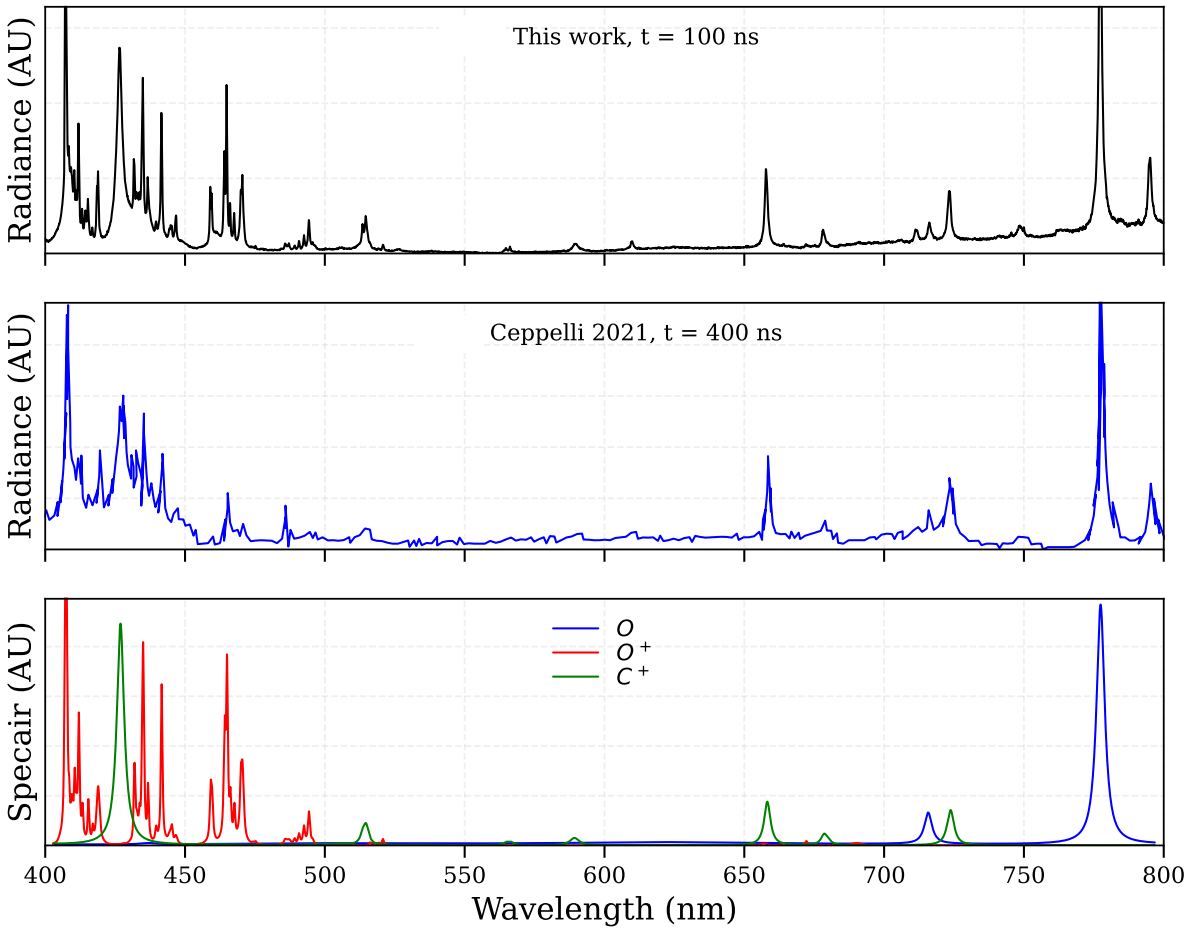

Figure 3-32. Comparison of emission spectra measured after the power reflection at midgap in this work (top) and Ceppelli et al. (bottom). The spectral features are strikingly similar in both experiments: we recognize the same spectral lines – O^+, C^+, and O – which are characteristic of a thermal spark.

3.5.2 Energy deposition scheme

As shown in Figure 3-2, each pulse deposits 4.5 mJ, including 4 mJ during the incident pulse (beginning of phase I), and 0.5 mJ after the reflection at 70 ns (beginning of Phase II). We observed in section 3.3.1 that this energy is about the same for all types of pulses. Thus, part of this energy goes into the bright region, and the other into the faint region. The objective of this section is to estimate the energy deposited by the incident and the reflected pulses in each region.

Energy deposition by the incident pulse in Phase I

Consider first the system formed by the gas within the bright region volume. As we know the bright region diameter and gas temperature (since $T_g = T_e$ in the bright region), we can estimate the energy deposited there. Owing to the fast energy deposition, the discharge can be considered isochoric and therefore the mass of the system is conserved. The energy E_f of the system is then given by:

$$E_f = m \cdot (h_f - h_i) = \rho_f V_f \cdot (h_f - h_i) \qquad \text{Eq. 3-10}$$

where m is the mass of the system, ρ_f and V_f are the density and the volume, and h_f and h_i are the final and initial specific enthalpies. We use the CANTERA code (Goodwin et al. 2017), and the NASA9 coefficients of Capitelli *et al.* to compute the specific enthalpies before and after the pulse. Two limiting cases are considered to calculate h_f: either the composition is frozen (so the filament is only composed of CO_2), or the composition is LTE. Just after the pulse ($t = 20\ ns$), 90% of the pulses are of type a/b (Figure 3-6). In this case, we can approximate the bright region as a sphere (Figure 3-5) to compute its volume. The other pulses (occurring 10% of the time) are type d/e, so their volume can be approximated as a cylinder of height equal to half the interelectrode gap. The diameter of the sphere and of the filament is measured to be about 70 µm at 20 ns. In Table 3-3, we summarize the input parameters of the calculation, and we report the estimated energies in Table 3-4.

Table 3-3. Input parameters and thermophysical quantities in the bright regions.

Parameter	**Initial conditions (t = 0 ns)**	**Final conditions (t = 20 ns)**	
		Frozen	**LTE**
T	600 K	30,000 K	30,000 K
P	1 atm	50 atm	270 atm
ρ	0.88 kg/m^3	0.88 kg/m^3	0.88 kg/m^3
h	-8.6x10^6 J/kg	3.8x10^7 J/kg	1.8x10^8 J/kg
Energy density (relative to initial conditions)	0	40 MJ/m^3	170 MJ/m^3

Table 3-4. Energy deposited into the bright region during type a/b and type d/e pulses

Type of pulse	**Energy $E_f = \rho_f V_f \Delta h$**	
	Frozen composition	**LTE composition**
Type a/b pulse (V_f = 1.8x10^{-13} m^3)	0.007 mJ	0.03 mJ
Type d/e pulse (V_f = 5.8x10^{-12} m^3)	0.24 mJ	0.97 mJ

The low energy values obtained for the small spheres of type a/b pulses are striking: at most 0.03 mJ is needed to reach the thermal spark conditions, which is negligible (less than 1%) compared to the 4 mJ deposited by the incident pulse. In types d/e pulses, between 0.2 mJ and 1 mJ are deposited in the filament. In this case, the filament represents between 6 and 24% of the energy: its role could be significant.

The energy lost by the plasma during the time of pulse energy deposition ($\sim 10\ ns$) is negligible because the characteristic times of cooling by conduction and radiation are much longer than 10 ns (they are estimated to be on the order of 500 ns and 250 ns, respectively, as shown in Sec. 4.3.3). Thus, the remaining energy of the first pulse (i.e. more than 99%) should be deposited in the faint region.

Is the energy deposited in the faint region consistent with the energy density of a non-thermal spark? Pannier (Pannier 2019) simulated a non-thermal spark in our conditions (the electric field profile was 15 ns of FWHM and peaked at 24 kV/cm, and the initial temperature 1,200 K) and found an energy density of 7 MJ/m^3. In our experiment, the faint region is a cylinder with a height equal to the inter-electrode gap distance and a diameter of about 500 µm (Figure 3-10). The volume of this faint region is then $V_{faint} \approx 6 \cdot 10^{-10}\ m^3$. Assuming that all the energy (4 mJ) goes into the faint region, we obtain exactly 7 MJ/m^3. With this verification, we conclude that although the faint region produces much less optical emission than the filament, it is where the vast majority of the pulse energy is deposited.

Energy deposition in Phase II

At the beginning of phase II, about 0.5 mJ are deposited by the reflected pulse (Figure 3-2). This additional energy arrives in an already ionized and hot plasma, creating a type f filament in LTE. The filament is approximated by a cylinder, whose height is the inter-electrode distance (3 mm) and diameter at 80 ns is about 100 µm (Figure 3-9). The filament volume is $V_f \approx 2 \cdot 10^{-11}\ m^3$. As illustrated in Figure 3-33, the energy deposited into the filament just after the reflection can be approximated as the difference between the energy required to bring a filament from 600 K, 1 bar to about 30,000 K, 10-20 bar, and the energy already present in the filament. As a first approximation, the energy already present in the filament volume can be calculated assuming an energy density of 7 MJ/m^3, i.e. assuming that the volume is adiabatic during the first 70 ns. We report the details and the results of the energy estimations in Table 3-5 and Table 3-6.

The filament enthalpy in relation to the initial conditions at 600 K and 1 bar is between 0.16 and 0.32 mJ. The energy pre-existing in the filament volume before the reflection is 0.16 mJ. Thus, during the reflection, the formation of the filament costs between 0 and 0.16 mJ, to be compared with an input energy of 0.5 mJ. Keeping in mind that our

approximations only provide an order of magnitude, we cannot definitely conclude on the fraction of the reflected pulse energy going into the filament.

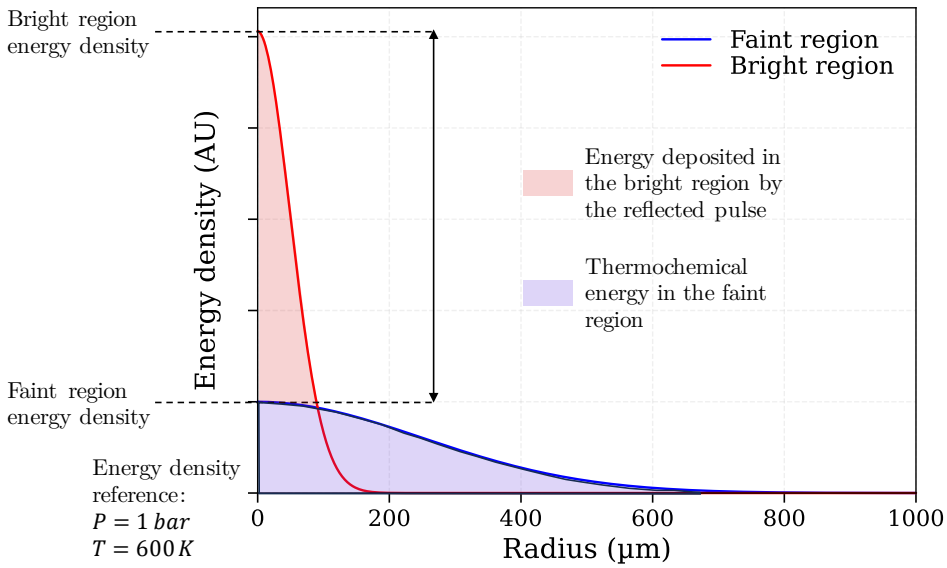

Figure 3-33. Determination of the energy required to bring the filament from the initial conditions in the faint region to a state of LTE at about 30,000 K, 10-20 bar.

Table 3-5. Input parameters and thermophysical quantities

Parameter	**Reference conditions (1 bar, 600 K)**	**Faint region conditions**	**LTE filament conditions (t = 80 ns)**	
P	1 bar		10 bar	20 bar
T	600 K		30,000 K	30,000 K
ρ	0.88 kg/m^3		0.026 kg/m^3	0.055 kg/m^3
h	-8.6·x10^6 J/kg		2.5·10^8 J/kg	2.4·10^8 J/kg
Energy density (relative to reference conditions)	0	7 MJ/m^3	6.9 MJ/m^3	13.4 MJ/m^3
Energy in V_f = 2·10^{-11} m^3	0	0.16 mJ	0.16 mJ	0.32 mJ

Table 3-6. Energy deposited to create the LTE filament: volume × (energy density in LTE filament – energy density in reference conditions – energy density in initial faint region). The volume is $2 \cdot 10^{-11}$ m³.

LTE filament conditions	Energy deposited
10 bar – 30,000 K	0.00 mJ
20 bar – 30,000 K	0.16 mJ

In summary, the estimation of the energy contained in non-thermal and thermal plasmas indicates that in our conditions, contrary to what the overwhelming filament emission would suggest, most of the energy goes to the faint region. Nevertheless, evaluating the true impact of the thermal regions on CO production would require understanding the potential interactions – the heat or reactive species diffusion for instance – between the two regions. Also, different input parameters (peak electric field, frequency, input gas flow, …) or geometry could favor one regime over the other.

3.5.3 Two CO production mechanisms

The faint region measured in Phase I attests of a non-thermal spark, and is consistent to what Pannier (Pannier 2019) and Heijkers *et al.* (Heijkers et al. 2019) simulated (in particular for the electron density agreement, as mentioned in 3.5.1). We already exposed some results of the model of Pannier in Chapter 2. In both models, the EE remains at moderate values of 20 – 30%. In our reference case, we have just shown that very little energy goes to the thermal region, and, according to Chapter 2, the EE of the thermal spark should be lower than 50%. Thus, in the reference case, most CO is produced in the non-thermal spark. The EE measured in the reference case is about 30% (Figure 3-4, SEI = 0.3 eV/molecule), which is then consistent with the EE computed with the non-thermal spark models (Pannier 2019, Heijkers et al. 2019).

In Figure 3-34, we report one of the main results from Pannier's model for conditions similar to our reference case. The CO_2 conversion to CO is plotted as a function of time. The colors account for different CO production channels. As we can see on this graph, about 13% conversion is reached in 20 ns, mostly through the excitation of CO_2 electronic states followed by their predissociation. At longer time scales (1.2 µs), the conversion increases to about 30%, thanks to thermal dissociation and O-CO_2 as-sociation reactions.

Our measurement of $T_e \approx 2$ eV in the faint region suggests a high vibrational excitation: at this electron temperature, about 50% of the electron energy goes to the vibration (Chapter 2, Figure 2-11), and the overall peak of electron-impact vibrational excitation is reached (Chapter 2, Figure 2-15). However, Pannier's model shows that, while the vibrational

temperature reaches about 8,000 K during the pulse, the vibrational excitation channel has a negligible contribution to CO production. The high vibrational excitation relaxes with the translation in about 100 ns, which is too soon to allow significant dissociation.

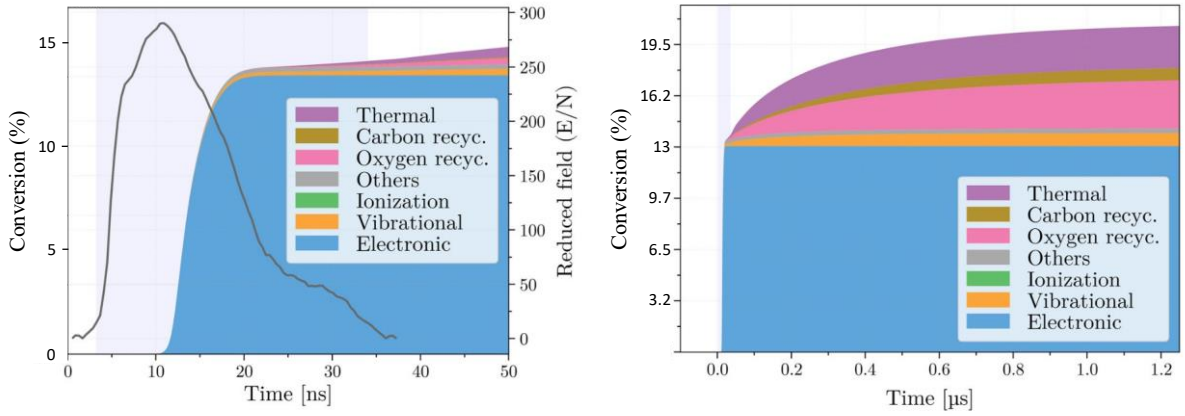

Figure 3-34. CO_2 conversion to CO and reduced electric field (grey line) in a non-thermal spark, from the 0D kinetic model of Pannier (Pannier 2019). The various CO production channels are indicated. The main channel for CO production is via electron-impact electronic excitation of CO_2, and it occurs during the pulse. Vibrational excitation by electron impact has a negligible contribution. At longer time scales, the main channels are oxygen recycling (O-CO2 association) and thermal dissociation. The conversion to CO is about 14% at 50 ns after the pulse, and about 20% after 1.2 µs (reproduced with permission from Pannier (Pannier 2019))

In the thermal filament of Phase II, no model has yet described the kinetics of nanosecond discharges in CO_2. We showed that the LTE calculation performed in section 3.4.5 reasonably estimates the plasma composition after the reflection. At the end of the reflected pulse, the plasma is fully atomic, and the pressure is about 10-20 bar. Following that phase, it is expected that the following events occur. The excited atomic species are ejected at high speed – between 10 and 100 m/s (Castela et al. 2017) – while recombining. Some of them may react with the surrounding CO_2 to produce CO. The Eindhoven group described a similar process (van den Bekerom et al. 2019), (Van De Steeg et al. 2021). Thus, a plausible scenario for the thermal filament is that CO is produced by atomic species recombination (O, O^+, C, and C^+) and by these species reacting with surrounding CO_2. Modeling this CO production mechanism will be the subject of future work.

3.6 Conclusions

First, we conducted a parametric study of the energy efficiency (EE) of CO production by NRP discharges in CO_2, using electric diagnostics, and post-discharge product analysis. We found an EE plateau around 30%, for SEI values between 0.25 and 1 eV/molecule. Using

burst of pulses with in-the-burst frequency of 50 kHz did not allow significant improvement of the EE, contrary to the measurements of (Montesano et al. 2020).

Then, we studied a reference case on the EE plateau: V = 5.3 kV, E = 4.7 mJ, f = 10 kHz, d = 3 mm, q_{CO2} = 2.5 slpm, in pin-pin configuration. We used time-resolved imaging and Optical Emission Spectroscopy. The electronic state distributions of various atomic species (O, O^+, C, C^+) were measured to determine the electron temperature. The electron number density was obtained from Stark-broadened lines of O, O^+ and C^+. The Stark-broadening effects were found to be measurable down to low electron densities of about 10^{16} cm^{-3} thanks to the use of closely spaced triplet lines. These measurements provided a detailed set of spatially and temporally resolved data in the interelectrode gap.

We then compared our measurements to those of the Trento group. The discharges are complex and heterogeneous, making their analysis challenging. Nevertheless, we succeeded in disentangling the various spatio-temporal phenomena and showed that the NRP discharges of the Trento group and this work proceed in two similar phases. Phase I is triggered by the first pulse, while phase II is triggered by a reflection (70 ns after the initial pulse in our experiment, and 70 to 400 ns after the initial pulse in Trento's experiment).

Following the initial pulse (phase I), two cases are observed:

1. For 90% of the pulses (types a/b pulses), a partially ionized gas (ionization degree less than 1%) is formed in a state of nonequilibrium in the gap. The faint emission from this plasma is composed of molecular bands and has a diameter of about 500 µm. More than 99% of the first pulse energy (about 4 mJ) is deposited in the faint region. Near the electrodes, a fully ionized, thermal plasma is produced in micrometric spheres. From 30 to 70 ns, these spheres develop into filaments, gaining ground in the gap. The energy deposited in these spheres during the pulse is less than 1% of the pulse energy.
2. For the remaining 10% of the pulses (types d/e pulses), a longer fully ionized filament reaching the middle of the gap is formed during the pulse, simultaneously with the nonequilibrium faint region. The energy in the filament is on the order of 0.1-1 mJ. The rest of the deposited energy is in the faint region.

Then, after the pulse reflection (or, equivalently, a secondary pulse) reaches the electrodes (phase II), the gas becomes fully ionized and is in a state of LTE at about 30,000 K and 10-20 bar, with all molecules fully dissociated. To our knowledge, this is the first identification of a thermal spark in CO_2. At this time, the plasma has the shape of a filament filling the whole inter-electrode gap and has a diameter of approximately 100 µm.

In our reference case, our energy calculations suggest that most CO is produced in the non-thermal region of phase I. In the general case, however, both non-thermal and thermal spark regimes could contribute to CO_2 dissociation. They underlie completely different CO_2 dissociation mechanisms. Existing 0-D kinetic models (Heijkers et al. 2019; Pannier 2019) correspond to the non-thermal spark conditions of the faint region. According to these models, CO_2 dissociates via its electronic states in about 20 ns. These models are in qualitative agreement with the measurements of this work. In the thermal spark regime, CO_2 is highly dissociated into atomic species (neutral and ionized), and CO is expected to be produced by the recombination of these atomic species rather than by direct CO_2 dissociation. This regime has not been modeled in CO_2. Thus, in the next Chapter, the filament-induced CO production will be modeled, and its efficiency compared with the non-thermal spark pathway.

In short, NRP discharges can produce both non-thermal and thermal sparks. In our conditions, the thermal spark dominates the emission features but does not produce significant conversion of CO_2. The non-thermal spark, in contrast, is more difficult to observe and characterize, but is responsible for most of the production of CO.

Take-away messages of Chapter 3

- We used OES and ns-imaging in NRP discharges in CO_2 to reveal the simultaneous existence of non-thermal and thermal regions in the plasma.
- The non-thermal region is characterized by molecular band emission, gas temperature of 600-800 K, electron temperature of about 20,000 K, and electron density of about 10^{16}-10^{17} cm^{-1}. The diameter of this region is about 400-500 µm.
- The thermal region is characterized by atomic line emission, thermal equilibrium at $T_g \approx T_e \approx$ 30,000 K, and electron density above 10^{18} cm^{-3}. The diameter of this region is about 20-100 µm.
- When a pulse arrives (phase I), it creates most of the time a non-thermal region throughout the interelectrode gap. Additionally, thermal regions in the form of micrometric spheres appear near the electrodes. The size and location of these thermal regions fluctuate from pulse to pulse.
- A fraction of the pulse energy is reflected, bounces off the generator, and goes back to the plasma at t = 70 ns (phase II). This reflected pulse causes the formation of a thermal filament throughout the interelectrode gap. This filament can reach the Local Thermodynamic Equilibrium at about 30,000 K and 10-20 bar.
- In our conditions, most of the pulse energy goes to the non-thermal region, which in turn is responsible for most of the CO production. We measure an energy efficiency of CO production in the non-thermal region of about 30%.

Chapter 4

Modeling of thermal and non-thermal sparks in CO_2

4.1 Introduction

In the previous chapter, we showed the simultaneous presence of a narrow filament near LTE conditions at about 30,000 K (a thermal spark (TS)), and a wider non-equilibrium plasma at lower temperature (a non-thermal spark (NTS)). Modeling studies can help understand the CO production mechanisms induced by the TS and the NTS and to assess their respective energy efficiency (EE). Identifying the optimal dissociation pathway and how to favor it is crucial to guide future experimental investigations.

Modeling efforts of CO_2 conversion in plasma discharges were recently reviewed by (Pietanza et al. 2021). We already detailed in Chapter 2 some of these works, particularly the main models of CO_2 conversion by NRP discharges (Pannier 2019; Heijkers et al. 2019; Pokrovskiy, Popov, and Starikovskaia 2022). The models can be roughly classified into two categories: plasma models primarily focusing on vibrational kinetics at room temperature (Naidis and Babaeva 2022; Pietanza, Colonna, and Capitelli 2023; Fromentin et al. 2023; Biondo et al. 2022; Pietanza, Colonna, and Capitelli 2022; A. F. Silva et al. 2020; T. Silva et al. 2020), and plasma models at $T \sim 1000$ K focusing on CO production, often also including the state-to-state vibrational kinetics (Kozák et al. 2014; Kozák and Bogaerts 2015; Vialetto et al. 2022; Wolf et al. 2020; Heijkers et al. 2019; Heijkers and Bogaerts 2017; Pokrovskiy et al. 2022; Pannier 2019).

In the latter category, the available NRP models focused on the non-thermal spark (NTS) (Heijkers et al. 2019; Pannier 2019; Pokrovskiy et al. 2022). They showed that in the NTS, CO is produced either by electron-impact excitation of CO_2 electronic states, thermal dissociation, O-CO_2 association ($O + CO_2 \rightarrow CO + O_2$), CO_2^+ dissociative recombination ($CO_2^+ + e \rightarrow CO + O$), or vibrational dissociation. However, none of these models predicted the high electron densities and temperatures we measure in the thermal spark (TS) (at most, Pannier obtained $n_e = 10^{16}\ cm^{-3}$ and Heijkers *et al.* $n_e = 8 \cdot 10^{17}\ cm^{-3}$).

On the other hand, in recent work, Minesi *et al* (Minesi et al. 2021) modeled and simulated the kinetics of the transition to a TS in air. They showed that, when a reduced electric field of about 200 Td is maintained during several ns, the ionization of N and O electronic states leads to the full ionization of the air plasma, and that the translational temperature of the heavies and the electrons equilibrate near 30,000 K via elastic electron-ion collisions. Similar mechanisms could be at play in CO_2.

This chapter has two main objectives:

i. Simulate the formation of thermal and non-thermal sparks and understand the transition between the two regimes. The underlying objective is to be able to control this transition and favor one or the other regime.
ii. Study the CO production mechanisms in thermal and non-thermal sparks and estimate the EE achievable in each regime. The underlying objective is to identify how to optimize the EE in these two regimes.

We pursue the first objective using a 0D kinetic model. To guide the modeling, we begin in Section 4.2 by presenting results on the hydrodynamics of spark discharges, and we evaluate in Section 4.3 the characteristic times of the physical phenomena at play. Then, in section 4.4, we present the kinetic model of nanosecond discharges in CO_2 developed in the present thesis. In section 4.5, we present the modeling results, and compare them to our measurements of the non-thermal and thermal sparks described in Chapter 3. In Section 4.6, we analyze the mechanisms of the transition to the thermal spark.

The second objective is addressed in two steps in Section 4.7. First, in Section 4.7.1, we analyze the CO production mechanism in the non-thermal spark regime using the kinetic model developed in Section 4.4. Second, in Section 4.7.2, we examine the case of the thermal spark. In order to account for hydrodynamic effects in a simple way, we add a variable dilution flux. This allows us to discuss qualitatively the potential EE of thermal-spark-induced CO production. Finally, in Section 4.7.3, we conclude on the relative contributions of the thermal and non-thermal mechanism to CO production in our experiments.

4.2 Hydrodynamic effects in sparks

Before describing the kinetics of nanosecond discharges, it is important to recall that these discharges may induce hydrodynamic effects in the form of shock waves and recirculation zones that impact the dynamics of species recombination following the spark. In this section, we present a summary of these effects, and we examine their magnitude for non-thermal and thermal sparks.

4.2.1 Non-thermal spark

The hydrodynamics generated by NTSs have been studied by the EM2C group for the past ten years. The propagation of a shock and the subsequent formation of a recirculation zone and of high-speed jets of hot gases were experimentally evidenced using Schlieren diagnostics (Dumitrache et al. 2019; Stepanyan et al. 2017; Xu et al. 2014), and simulated using 1D, 2D, and 3D models (Castela et al. 2017; Dumitrache et al. 2019; Xu et al. 2014) (Pavan and Guerra-Garcia 2023; Tholin 2012). An illustration of the shock waves and of the toroidal recirculation zone is shown in Figure 4-1, taken from (Castela et al. 2017).

The initial shock wave is due to the sudden increase in pressure caused by fast heating and dissociation inside the discharge volume. This pressure increase occurs during the pulse in about 10 ns. It is faster than the pressure relaxation time τ_P, which causes the shock.

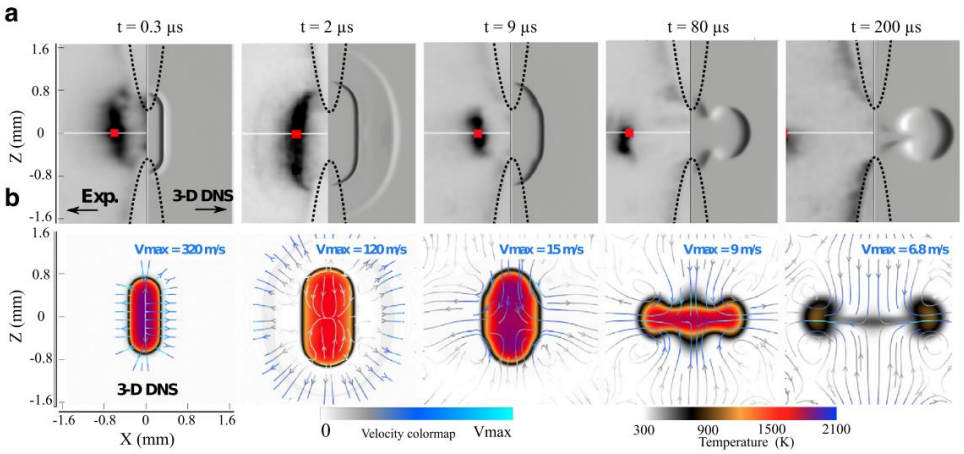

Figure 4-1. Hot kernel topology captured at 5 instants after the plasma discharge in methane-air mixture: (a) Experimental (left side) and computational (right side) Schlieren images. (b) Superposition of the computed gas temperature field and flow streamlines coloured by velocity magnitude. The same color map of velocity magnitude is used in for all images shown here, but the maximum value V max varies and is indicated above each image. Figure reproduced from (Castela et al. 2017)

In NTSs, the pressure in the plasma typically reaches 1 to 5 bars and the temperature 1,000 to 3,000 K. Using a 1D cartesian shock model as in (Roger 2023), the Mach number of the shock in the NTS is estimated to be 1.1 – 1.2 in air in the conditions of (Xu et al. 2014), and potentially up to 1.7 in CO_2 in the conditions of (Pannier 2019) and this work. For example, let us consider CO_2 at atmospheric pressure and 600 K. Let us imagine that it reaches approximately 5 bars and 3000 K under the effect of the nanosecond pulse. According to the cartesian shock model, the heating in the ambient gas crossed by the shock is about 100 K, and the overpressure is approximately 2 bar.

The pressure relaxation time is equal to the radius of the plasma cylinder divided by the expansion speed of the pressurized volume[14]. We estimate an upper value of this expansion speed by considering the latter example. Using the cartesian shock tube model, we estimate the expansion speed to be around 390 m/s. Taking a plasma radius of 200 µm, we obtain $\tau_P \approx 500$ ns.

The expansion of the plasma volume and other hydrodynamic effects begin at this time scale. This point will be further detailed in Sec. 4.3, where we will show that the exchange phenomena (advection, diffusion, radiation) between the plasma and the surrounding region are of the order or greater than 1 µs. Therefore, 0D kinetic simulations assuming constant volume are representative of the evolution of a NTS composition and temperature during the first µs following the pulse.

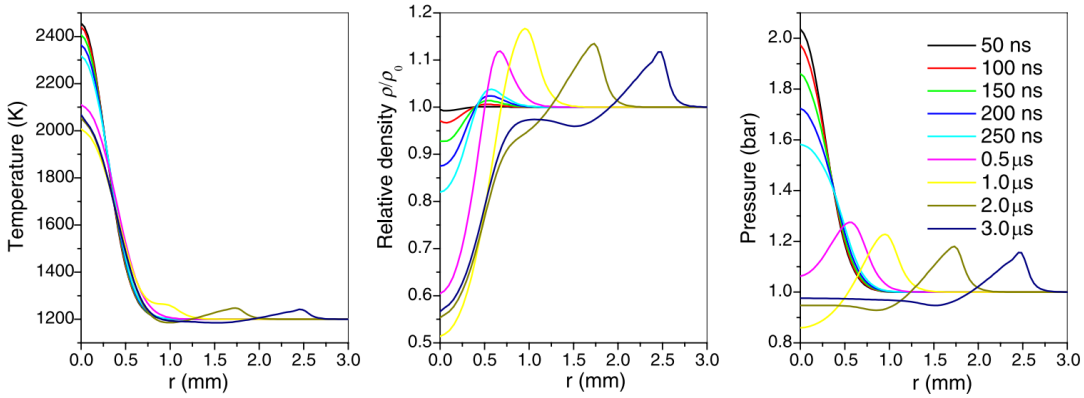

Figure 4-2. Calculated temperature, density, and pressure profiles at different times in a typical non-thermal spark in air. The calculations are performed using a non-reactive 1D axisymmetric model. Figure reproduced from (Xu et al. 2014).

4.2.2 Thermal spark

In the thermal spark, the temperature increase and the dissociation degree are much higher than in the non-thermal spark. The resulting overpressure is several tens of bars. Consequently, the shock generated by a TS is stronger, and the hydrodynamic effects are

[14] Strictly speaking, the pressure relaxation is driven by the slowest process between expansion and sound speed propagation in the pressurized volume. Since the speed of sound in the pressurized volume is usually higher than the expansion speed, we only present the expansion speed. The speed of sound is equal to $c_s = \sqrt{\gamma R T_g / M}$, where γ is the ratio of specific heats, R the perfect gas constant, T_g the gas temperature and M the mean molar mass. For a NTS in CO2, T_g ranges typically between 1,000 and 3,000 K. Assuming that CO2 is fully converted into CO and O during the pulse, we obtain $M = 22\ g/mol$, and $\gamma = 1.40 - 1.44$ (in the 1,000 – 3,000 K temperature range). If CO2 is not converted at all, $M = 44\ g/mol$, and $\gamma = 1.15 - 1.18$. Thus, we obtain $c_s \approx 500 - 1300\ m/s$.

much more significant. This subject is currently being studied in our group, and this section highlights the preliminary results of (Roger 2023).

Insights from a non-reactive fluid simulation

A chemically inert, monospecies, 1D axisymmetric shock representative of a TS in CO_2 was simulated using ANSYS FLUENT 2021 (Roger 2023). This simulation aims to give a qualitative representation of the hydrodynamics triggered by a canonical TS and to determine the temporal range of validity of 0D modeling. Roger used an Eulerian compressible flow solver with an implicit temporal scheme, $dt = 10^{-11}\ s$, $dx = 3 \cdot 10^{-8}\ m$, over a domain extending 1 mm from the center of the plasma.

The calculation starts from the conditions measured at t = 15 ns[15] in Chapter 3, i.e. $T_g = T_e = 33{,}000\ K$ and $n_e \approx 5 \cdot 10^{18}\ cm^{-3}$ (Figure 3-21, Figure 3-25). Assuming that the plasma is fully ionized, and that singly ionized species are dominant, we can estimate the total density, $n_{tot} \approx 2 \cdot n_e = 1.1 \cdot 10^{19}\ cm^{-3}$, and thus the pressure: $P \approx 50\ bar$. Note that this pressure is higher than the 10 – 20 bar estimated in the TS formed by the voltage reflection (cf Chapter 3). This is due to the higher number density before the first pulse than before the reflected pulse. As a first approximation, the evolution of the heat capacity ratio γ during the simulation is obtained from the pressure and temperature evolution, and assuming LTE composition. Initially, $T_g = 33{,}000\ K$ and $P = 50\ bar$: $\gamma \approx 1.7$.

The profiles of temperature, pressure, and total number density are reported at different instants in Figure 4-3. As we can see in this figure, as early as 10 ns after the formation of the high-pressure filament, most of its volume has been subjected to the expansion wave. The Mach number of the shock is about 4, and the expansion velocity is about 4,000 m/s. Taking 50 µm as the filament radius, we obtain a pressure relaxation time of $\tau_P \approx 13\ ns$. The brutal changes of the thermodynamic quantities generated by the shock happen at this time scale. Thus, a TS simulation lasting more than 10 ns after the filament formation should include the effect of the shock on the pressure and temperature and the ensuing flow dynamics.

Figure 4-3 shows that, at $t = 1\ ns$, most of the initial filament volume is still at the initial temperature and pressure. Figure 4-4 represents the temporal evolution of the pressure at different locations. At t = 2 ns, only the filament's edge at r = 50 µm has begun to relax. The central half of the volume (delimited by $r = 35\ \mu m$) is not affected until $t = 4\ ns$. Thus, most of the filament volume will not experience the shock for about 4 ns after its formation. Assuming that the TS formation in CO_2 is as fast as in air, i.e. less than 1 ns, fluid dynamics

[15] $t = 15\ ns$ corresponds to the beginning of the temperature measurements.

should play a marginal role in the formation of the TS. Thus, the TS *formation* can be simulated in a 0-D approximation without considering the hydrodynamic effects.

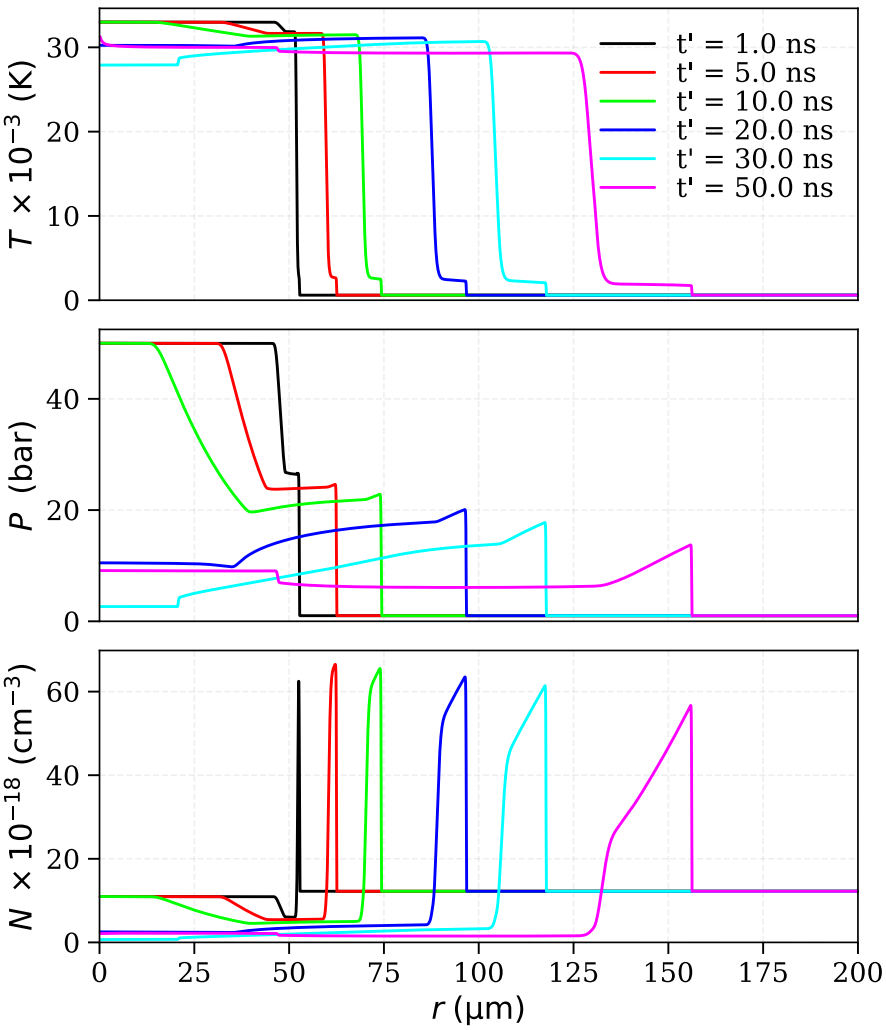

Figure 4-3. Spatiotemporal evolution of the temperature, pressure, and number density obtained from the simulation of an axisymmetric shock using Fluent. We use representative conditions of a TS triggered by NRP discharges in CO_2. Initial conditions in the high-pressure region: $P_1 = 50$ bar, $T_1 = 33{,}000$ K, $r_1 = 50$ µm. The surrounding gas is at P_{atm} and 1000 K.

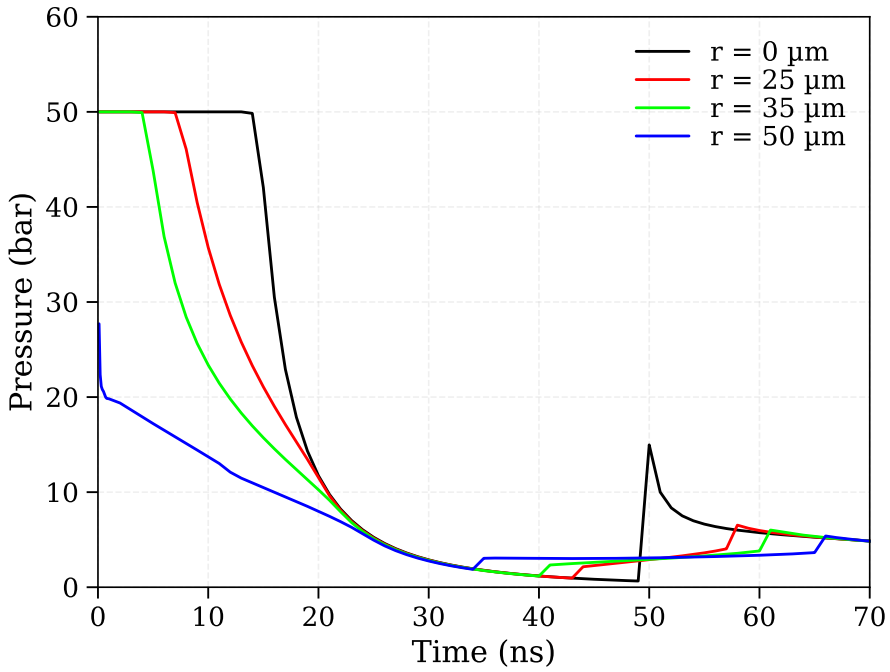

Figure 4-4. Temporal evolution of the pressure at different locations in the filament. Shock simulation with Fluent. Initial conditions in the high-pressure region: P_1 = 50 bar, T_1 = 33,000 K, r_1 = 50 µm. The surrounding gas is at P_{atm} and 1000 K.

Role of hydrodynamics during the early after-glow

We now assess the effect of hydrodynamics on the evolution of the temperature and densities of the main species. Previous work in air (Lo et al. 2017; Minesi et al. 2020) suggested that the decrease of n_e and T_e in the first 100 ns after the pulse is driven by an isentropic expansion. To reach this conclusion, they noted that ln (T_e) is a linear function of ln (n_e). The slope yields an estimate of γ, which they found consistent with the γ of the gas. This reasoning assumes that (i) the plasma is homogeneous at T_e, and (ii) γ is constant. In (Roger 2023), the 1D simulation (i) yields the spatial behavior of the plasma and (ii) shows that γ varies with the thermodynamic conditions and the composition. We use these results to reconstruct the optical emission spectrum emitted along the line of sight, accounting for the non-uniform regions created by the shock, and we compare it to the measurements of Chapter 3.

Two different assumptions are made for the gas composition: (i) either an LTE composition at the pressure and temperature provided by the simulation (i.e., assuming that chemical kinetics are much faster than hydrodynamics), (ii) or a frozen composition, with the mole fractions staying at their initial values (i.e., assuming that the hydrodynamics are much faster than the kinetics).

The line-of-sight measurements of Chapter 3 used to reconstruct the spectra are schematically described in Figure 4-5. Reconstructed spectra are obtained by solving the

radiative transport equation along this non-uniform domain. The reconstructed spectra are shown in Figure 4-6 and Figure 4-7. These spectra are then fitted as in Chapter 3 to obtain the electron density and temperature that would have been measured. Figure 4-6 shows Lorentzian fits of the Stark-broadened O^+(465 nm), C^+(658 nm), and O(777 nm) lines, which yield the electron density that would be measured by OES. Figure 4-8 shows a reconstructed Boltzmann plot of the O^+ electronic states, which can be used to determine the electron temperature.

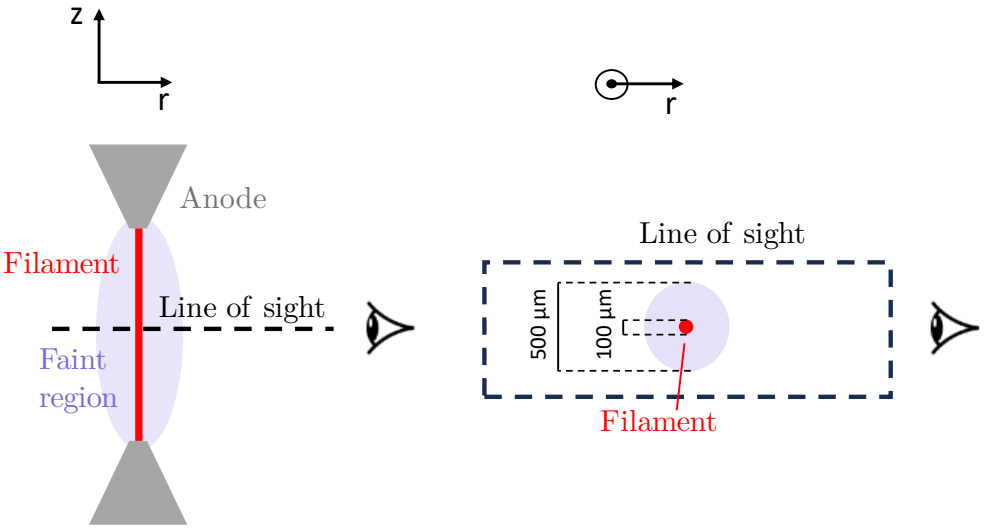

Figure 4-5. Schematic of the line-of-sight OES measurements of Chapter 3.

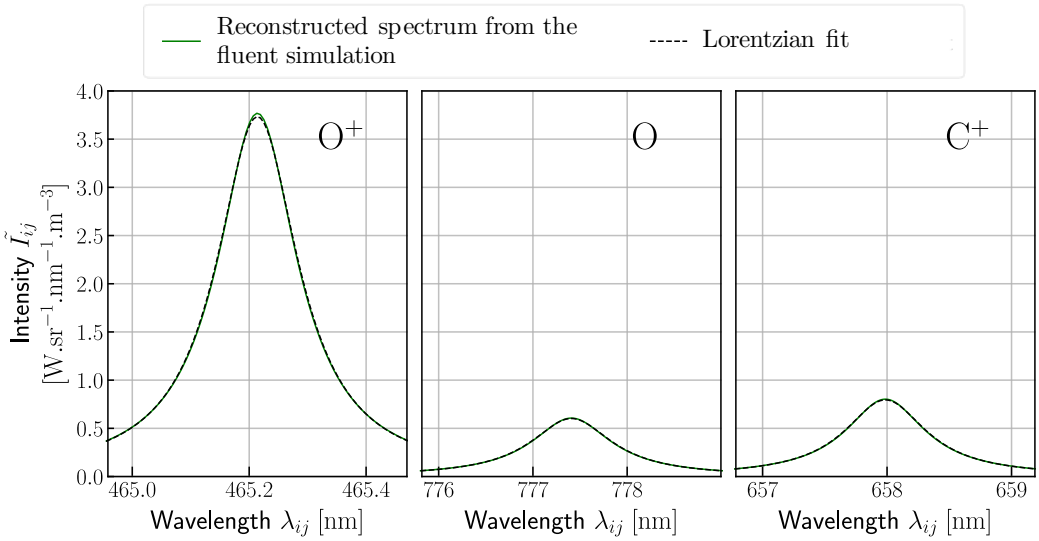

Figure 4-6. Reconstructed spectra of O^+(465 nm), O(777 nm), and C^+(658 nm) at t = 14 ns, fitted with Lorentzian functions.

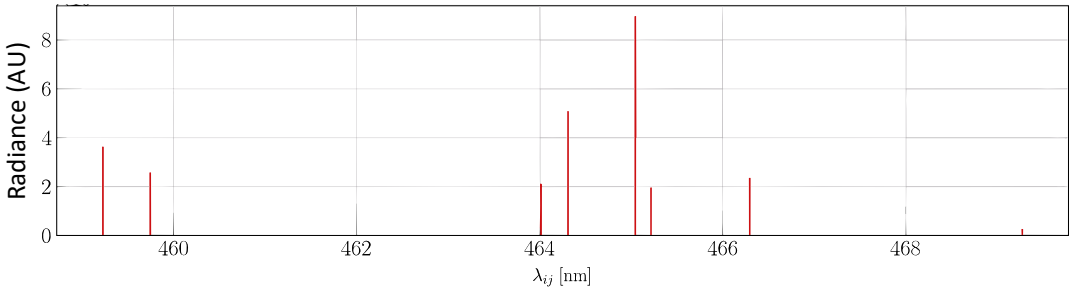

Figure 4-7. O^+ reconstructed spectra between 459 and 470 nm at t = 14 ns.

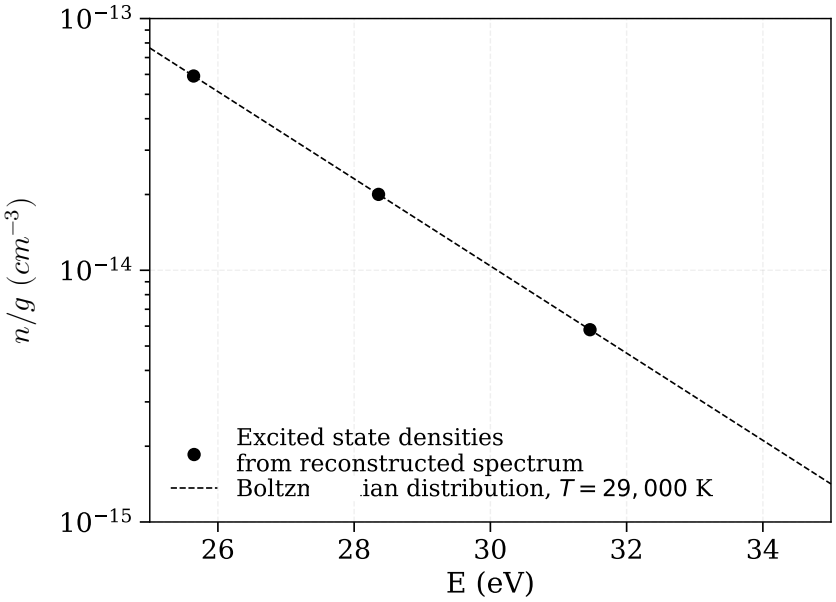

Figure 4-8. Boltzmann distribution of O^+ excited states densities extracted from the reconstructed spectra at t = 14 ns. The resulting temperature is a spatial average of the temperature weighted by the emission intensity.

Figure 4-9 and Figure 4-10 show the temporal evolution of n_e and T_e that would have been measured if the plasma behaved as in the Fluent simulation of (Roger 2023). In both figures, these "reconstructed" n_e and T_e are compared with the OES measurements of Chapter 3. The good agreement suggests that hydrodynamics explain the n_e and T_e decrease after $t = 15\ ns$ and strengthens the conclusions of (Lo et al. 2017; Minesi et al. 2020) on this issue.

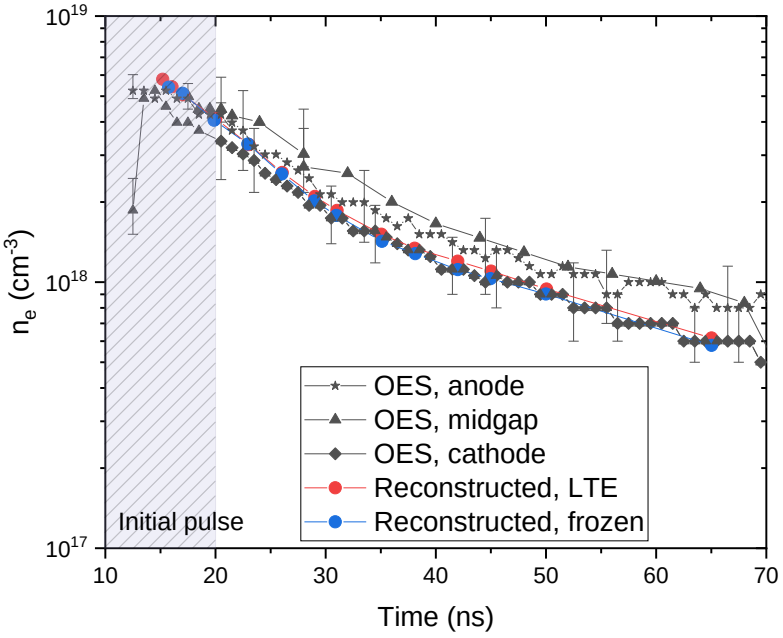

Figure 4-9. Apparent electron densities derived from the line-of-sight spectra reconstructed from the Euler fluid simulation of (Roger 2023) compared with the OES measurements of Chapter 3 (bright region).

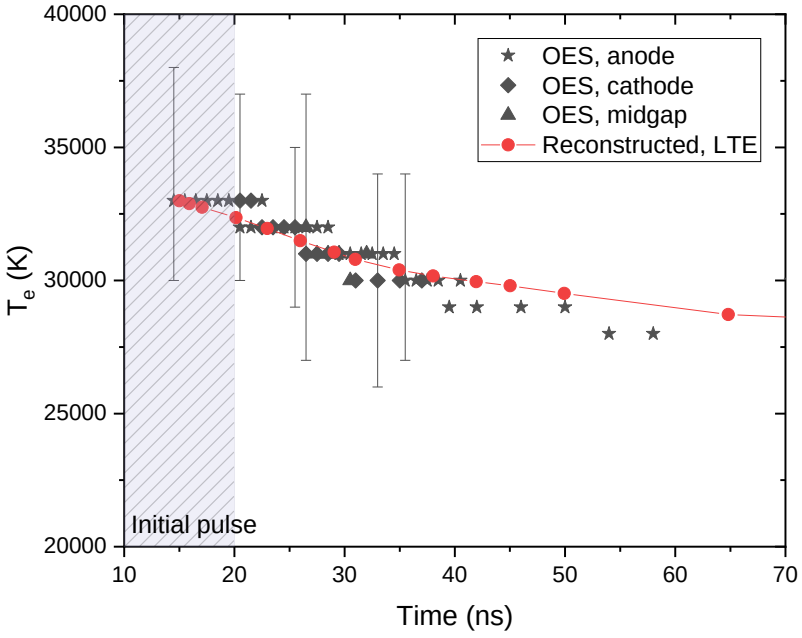

Figure 4-10. Apparent electron temperature derived from the line-of-sight spectra reconstructed from the Euler fluid simulation of (Roger 2023) compared with the OES measurements of Chapter 3 (bright region).

To summarize, non-thermal and thermal sparks generate significant hydrodynamic effects. These effects are particularly pronounced in the thermal spark regime. In this regime, we showed that as early as 15 ns after the beginning of the pulse, the gas expansion is the

primary explanation for the decay of electron densities and temperature. As a result, a 0D kinetic model is adequate up to approximately 10 ns after the beginning of the pulse in the thermal spark regime, and up to about 500 ns in the non-thermal spark regime.

4.3 Characteristic times of the physical phenomena

To better understand the non-thermal and thermal sparks, and to define the validity time span of our 0D modeling, we calculate the characteristic times of the different phenomena at play: advection, diffusion, radiation, pressure relaxation and shock absorption, and finally CO production. The resulting characteristic times are summarized in Table 4-1.

4.3.1 Advection

The shock wave generated by the spark heats and pressurizes the surrounding plasma. After interacting with the shock, the particles are entrained at a high speed (u).

Non-thermal spark

For example, for a spark at 2000 K, 3 bar, surrounded by CO_2 at 600 K, 1 bar, the initial shock velocity is 500 m/s, and the velocity of the gas entrained by the shock is $u \approx 200\ m/s$[16] (Roger 2023). In typical NTSs, $u \approx 200 - 400\ m/s$ (Castela et al. 2017). Thus, the characteristic time of heat and particle advection just after the shock is $\tau_{adv} = r_{NTS}/u \sim 0.5\ - 1\ \mu s$, where $r_{NTS} = 200 - 300\ \mu m$ is the NTS radius.

It should be noted that u rapidly decreases as the shock is absorbed. After 10 µs, the hot gases are ejected at about 10 m/s due to hydrodynamic effects causing flow recirculatin (Dumitrache et al. 2019; Stepanyan et al. 2017).

Thermal spark

For a filament at 30,000 K, 50 bar, surrounded by gas at 2000 K, 3 bar, the initial shock velocity is about 4500 m/s (Roger 2023). In this example, the gas after the shock is

[16] The properties of the shock are estimated using the 1D cartesian shock tube model, solved analytically (Roger 2023).

entrained at $u \approx 3500\ m/s$. Thus, the characteristic time of heat and particle advection following the shock is $\tau_{adv} = r_{TS}/u \sim 10\ ns$, where $r_{TS} = 50\ \mu m$ is the TS radius.

4.3.2 Diffusion

In the core of the plasma, the pressure falls abruptly. The steep temperature and density gradients between the core and the surroundings cause heat and mass diffusion. We estimate the characteristic time of mass and thermal diffusion, $\tau_{diff} = r^2/D_{ij}$ and $\tau_{th} = r^2/\alpha$, where D_{ij} and α are the species and thermal diffusion coefficients, respectively.

Non-thermal spark

In Figure 4-11, we report some relevant diffusion coefficients from (Gupta et al. 1990) at 3 bar and as a function of temperature. In the NTS conditions, i.e. near 3 bar and in the temperature range 1,000 – 5,000 K, the species and thermal diffusion coefficients are between 0.1 and 10 cm^2/s. Thus, using the NTS diameter r_{NTS}, we obtain $\tau_{diff} \sim \tau_{th} \sim 10\ \mu s - 10\ ms$.

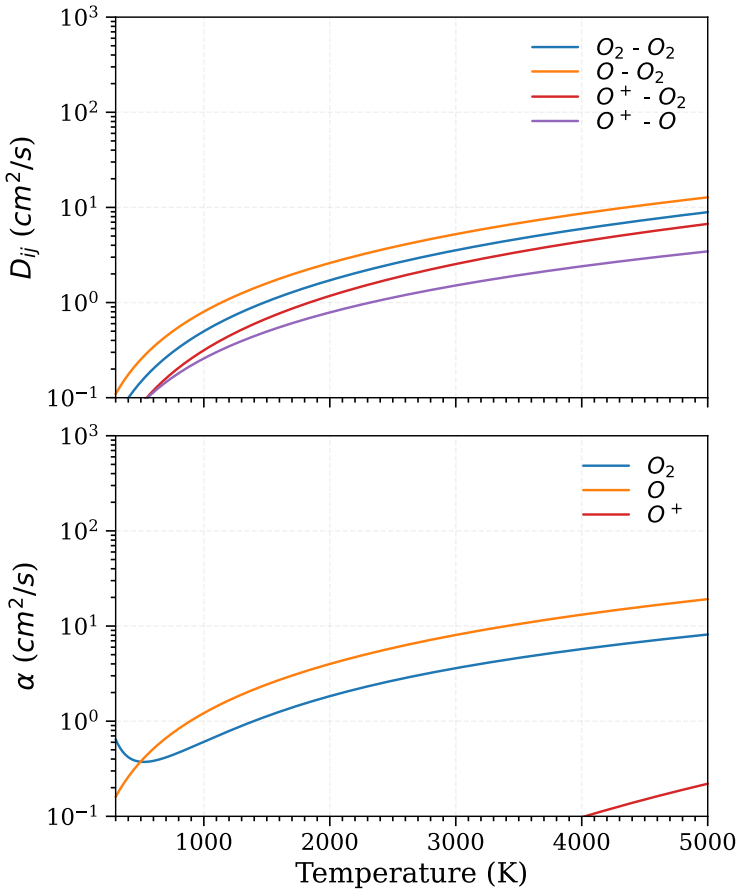

Figure 4-11. Species (D_{ij}) and thermal (α_{ij}) diffusion coefficients as a function of temperature at 3 bar (in typical NTS conditions). Data from Gupta *et al.* 1990.

Thermal spark

Figure 4-12 shows some relevant diffusion coefficients from (Gupta et al. 1990) at 50 bar and as a function of temperature. In TS conditions, i.e. near 50 bar and in the temperature range 20,000 K – 30,000 K, the species and thermal diffusion coefficients are between 1 and 10 cm^2/s. Thus, using the TS diameter r_{TS}, we obtain $\tau_{diff} \sim \tau_{th} \sim 1 - 10$ µs.

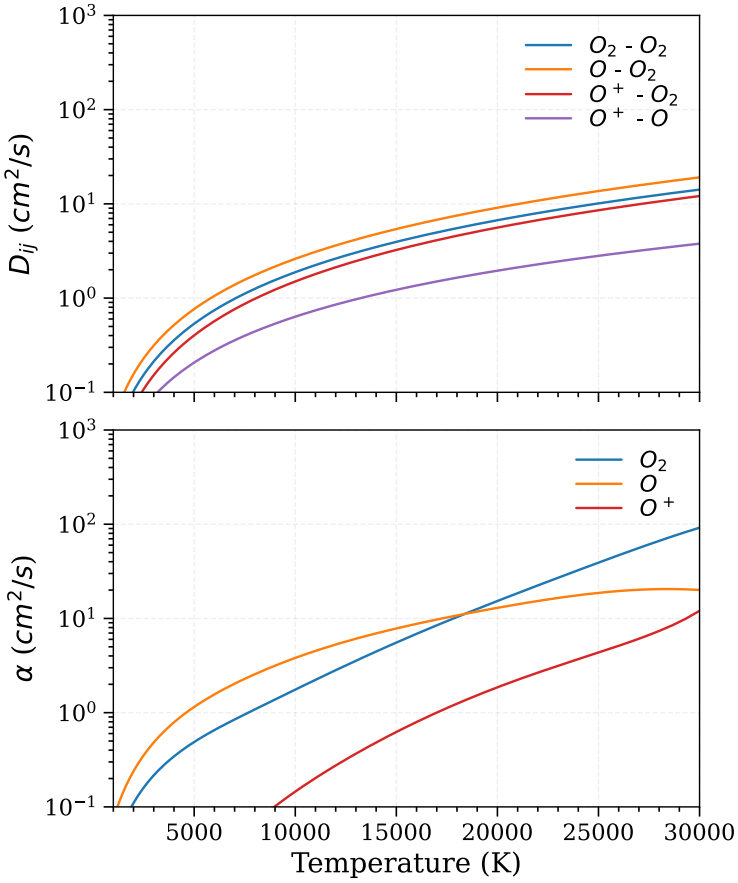

Figure 4-12. Mass (D_{ij}) and thermal (α_{ij}) diffusivity of some relevant species as a function of temperature at 50 bar (in thermal spark typical conditions). Data from Gupta *et al.* 1990.

4.3.3 Radiation

Thermal spark

To estimate the radiative transfer from the filament, we compute its emission spectra in LTE at $T = 30{,}000\ K$, $P = 50\ bar$, using SPECAIR (Laux et al. 2003). SPECAIR models the spectra of O, O^+, and C^+. For O, 843 lines from 70 nm to 4 µm are included; for O^+, 876 lines from 40 nm to 10 µm; for C^+, 233 lines from 50 nm to 2 µm. A calculation using NIST LIBS (Kramida, Olsen, and Ralchenko 2023) shows that the main contributors to the emission are C^+ followed by C^{++} and O^+. C^{++} is not included in SPECAIR, but the C^+ and O^+ lines are sufficient to provide an order of magnitude of the emission. Since we only have

atomic lines, computing the spectrum from 10 to 2,000 nm is enough to get most of the emitted power. We use 100 µm (the approximate filament diameter) for the path length. The spectrum obtained, including self-absorption, is shown in Figure 4-13 .

Integrating the spectral radiance over the wavelength range, we get a radiance of $\phi_{rad} = 7.5 \cdot 10^4\ W/cm^2/sr$. The filament is approximately a cylinder with a diameter of 100 µm and a height of 3 mm (inter-electrode gap distance). As an approximation, we integrate the radiative flux over 2π steradians and the cylinder surface. We obtain a radiative power of about 4000 W. With this level of radiative power, the filament energy of about 1 mJ would be lost by radiation in 250 ns. Thus, the characteristic time of radiative transfer is $\tau_{rad} \sim 250\ ns$.

As a side note to the simulations presented in Sec. 4.7.2, it is interesting to estimate whether or not the radiation emitted by the filament is lost at the walls (which are typically a few centimeters away from the filament). The emission spectrum in Figure 4-13 shows that the energy is predominantly emitted in the Extreme UV range. At these wavelengths, the attenuation coefficient of CO_2 is about 10^3 cm^{-1} at 1 bar (Pancheshnyi 2015). Thus, the characteristic length of absorption into a surrounding gas comprised of CO_2 is 10 µm.

Following photoexcitation, the electronic states of CO_2 predissociate in less than 1 ps (Chapter 2, 2.3.1.1), which results in the production of CO, O, and heat. Since predissociation is much faster than radiative deexcitation, very little energy will be reemitted by the excited CO_2. Consequently, after a few times 10 µm, the radiative flux from the filament is completely absorbed by the gas, and thus does not reach the walls of the reactor.

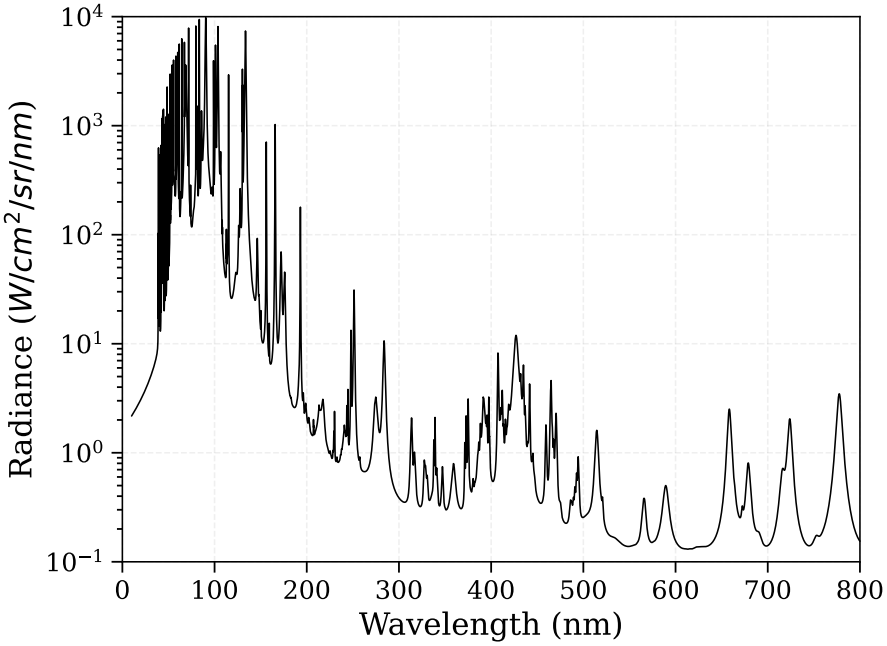

Figure 4-13. Emission spectrum of a CO_2 plasma in LTE at 30,000 K and 50 bar, for a 100 µm pathlength. The spectrum is computed with SPECAIR, including self-absorption over the pathlength. The main emitting species are C^{+}* (233 lines) and O^{+}* (876 lines). The energy is predominantly radiated in the Extreme UV range.

Non-thermal spark

Estimating the radiative power in an NTS is more challenging since it is highly non-equilibrium. Nevertheless, the radiative power of a NTS at $T_g \leq T_v \leq T_e$ is lower than the radiative power of a TS at $T_g = T_v = T_e$. Thus, we use the measurement of T_e in the faint region from Chapter 3 (Figure 3-25), and we consider as an upper bound the emission of a thermal spark at this temperature. The total number density is kept equal to 10^{19} cm^{-3}. This time, the emission pathlength is 500 µm, i.e. the approximate diameter of the faint region.

We find a radiance of $\phi_{rad} = 2.8 \cdot 10^4\ W/cm^2/sr$. By integrating over the faint region surface and 2π steradians, we obtain a radiative power of 8000 W. Considering the energy in the faint region of about 4 mJ, we obtain $\tau_{rad} \approx 500\ ns$ (which is, in reality $\tau_{rad} > 500\ ns$ considering our assumptions).

4.3.4 Pressure relaxation and shock absorption

Pressure relaxation

As mentioned in Section 4.2, the pressure relaxation time is the radius of the cylinder divided by the expansion speed of the pressurized volume. For the typical NTS and TS considered in this section, we obtain $\tau_p \sim 0.5 - 1$ µs and $\tau_P \sim 10$ ns, respectively.

Shock absorption

The heat, mass, and momentum diffusion attenuate the shock. Thus, the shortest time of the three diffusion phenomena is the characteristic time of the shock absorption. It is about 10 µs in the NTS and 1 µs in the TS.

To visualize the impact of the shock on the system, we estimate the distance the shock travels before it attenuates. By multiplying the diffusion time and the initial shock velocity, we obtain an upper bound of the shock absorption length of a few mm in both regimes.

In addition to the diffusion phenomena, the shock is also attenuated by the increase of its surface. This phenomenon was modeled by Whitham (Whitham 1976). In the case of a weak cylindrical shock, he showed that $M(r) - 1 \propto r^{-0.5}$, where M is the mach number and r is the radius of the expanding cylinder. In the case of a strong cylindrical shock, he showed that $M(r) \propto r^{-1/n_{gas}}$, where n_{gas} is a function of the heat capacity ratio: $n_{gas} = 1 + 2/\gamma + \sqrt{2\gamma/(\gamma - 1)}$. For a thermal spark in CO_2 in LTE at 30,000 K and 50 bar, $\gamma \approx 1.6$ and $n_{gas} \approx 4.6$. According to the measurements of Chapter 3, when the optical emission spectra indicate full ionization of the plasma (i.e. around $t = 15$ ns), the radius of the discharge is about 20 µm. Initially, the strong cylindrical shock hypothesis is more appropriate since $M(r) \sim 4$. The Mach is divided by a factor of two when the radius reaches 380 µm. Let us assume that, at this point, the weak cylindrical shock hypothesis applies ($M(r) \sim 2$). Therefore, $M(r) - 1$ is divided by two when the radius reaches $4 \times 380 \approx 1500$ µm. We obtain the same order of magnitude of the distance covered by the shock before its attenuation.

4.3.5 CO production

Non-thermal spark

In the NTS, a previous model (Pannier 2019) predicts that two thirds of CO production occurs via the electron-impact excitation and predissociation of CO_2 electronic states: CO_2 + e− → CO_2* + e− (E7-E10, Table C-1) and CO_2* → CO + O (P1-P4, Table C-4). This dissociation occurs during the voltage pulse, in about 10 ns.

We verify this result by calculating the characteristic time of this reaction: $\tau_{kin} \sim (k_{ee} n_e)^{-1}$, with k_{ee} the average rate constant of electron-impact excitation of CO_2*. (Predissociation is much faster than excitation, so the excitation reaction determines the characteristic time.) k_{ee} is obtained by integrating the electronic excitation cross-section from IST-Lisbon (Grofulović, Luís L Alves, et al. 2016) over a Maxwellian distribution. At $T_e \sim 2-3\ eV$, $k_{ee} \sim 10^{-9}\ cm^3/s$. Thus, using the electron density of 10^{16} – 10^{17} cm^{-3} measured in the NTS (Figure 3-21), we obtain $\tau_{kin} \sim 10-100\ ns$.

Pannier also showed that the remaining third of the CO production occurs through thermal dissociation (N1) (CO_2 + M → CO + O + M) and (N2) (CO_2 + O → CO + O_2). To estimate an upper bound of the characteristic time of CO production by these reactions, we consider their rate constant at 5,000 K, which is about 10^{-13} cm^3/s for both reactions. Since $n_O < n_{tot}$, (N1) is faster than (N2). For (N1) $\tau_{kin} \sim (k \cdot n_{tot})^{-1}$ where k is the rate constant. If the pressure has not relaxed (it takes 0.5 – 1 µs in the NTS), $n_{tot} \sim 10^{19}\ cm^{-3}$, thus we obtain $\tau_{kin} \sim 1\ \mu s$. If the pressure has relaxed to 1 bar, $n_{tot} \sim 10^{18}\ cm^{-3}$ (the number density at $P = 1$ bar, $T_g = 5000$ K), thus $\tau_{kin} \sim 10$ µs.

Thermal spark

In the TS, the CO molecules are expected to be produced by heavy species kinetics, once the temperature has decreased below 5,000 K. We can estimate how fast the temperature decreases to 5,000 K by extrapolating our temperature measurements from Chapter 3. On Figure 3-25, we obtain a mean cooling rate of 100 K/ns (10^{11} K/s !), which would make the temperature fall below 5,000 K in approximately 250 ns.

Then, to estimate how fast CO molecules are produced at this temperature we consider two potentially significant reactions: (i) 3-body recombination of C and O (N5r) (C + O + M → CO + M) and (ii) CO_2 dissociation by heavies impact (N1) (CO_2 + M → CO + O + M). We use the rate constants from (Park et al. 1994).

For (i), we estimate the characteristic time of CO production by assuming that $n_O = n_C = n_{tot}/2$ (n_{tot} is the total number density of the plasma) and by computing the time needed for n_{CO} to equal $n_{tot}/2$. We obtain $\tau_{kin} \sim (k_{N5,r} \cdot n_{tot}^2/2)^{-1}$ where $k_{N5,r}$ is the rate of C + O recombination. For (ii), the characteristic time is about $\tau_{kin} \sim (k_{N1} \cdot n_{tot})^{-1}$ where k_{N1} is the rate constant of the CO + O recombination. We assume a temperature of 5000 K, and $n_{tot} \sim 10^{18}$ cm^{-3} to account for the expansion of the plasma, and we find $4 \cdot 10^{-4}$ s and 10^{-5} s for the characteristic CO production times. We keep the fastest process (N1) (CO_2 + M → CO + O + M. Thus, in the TS, the CO production occurs in $\tau_{kin} \sim 10\ \mu s$.

4.3.6 Summary

Table 4-1 summarizes the characteristic times estimated in the previous subsections, and a cartoon of the physical phenomena following breakdown is shown in Figure 4-14. In both investigated regimes, the spatial non-uniformity of the discharge causes transport phenomena (advection, pressure relaxation), with characteristic times of about 0.5-1 µs in the NTS regime and about 10 ns in the TS regime. Thus, 0D kinetic simulations should be limited to durations less than these characteristic times.

Table 4-1. Characteristic times of the physical phenomena at play in the non-thermal and thermal sparks.

Regime	Non-thermal spark	Thermal spark
Voltage FWHM	$\tau_{pulse} \sim 10\ ns$	
Transition to the thermal spark	$\tau_{TTS} \sim 1\ ns$	
Pressure relaxation	$\tau_P \sim 0.5 - 1$ µs	$\tau_P \sim 10\ ns$
Heat and species advection	$\tau_{adv} \sim 0.5 - 1$ µs	$\tau_{adv} \sim 10\ ns$
Species diffusion	$\tau_{diff} \sim 10$ µs $- 10\ ms$	$\tau_{diff} \sim 1 - 10$ µs
Heat diffusion	$\tau_{th} \sim 10$ µs $- 10\ ms$	$\tau_{th} \sim 1 - 10$ µs
Radiation	$\tau_{rad} > 500\ ns$	$\tau_{rad} \sim 250\ ns$
CO production	$\tau_{kin,elec} \sim 10\ ns$ $\tau_{kin,thermal} \sim 1 - 10$ µs	$\tau_{kin} \sim 10$ µs

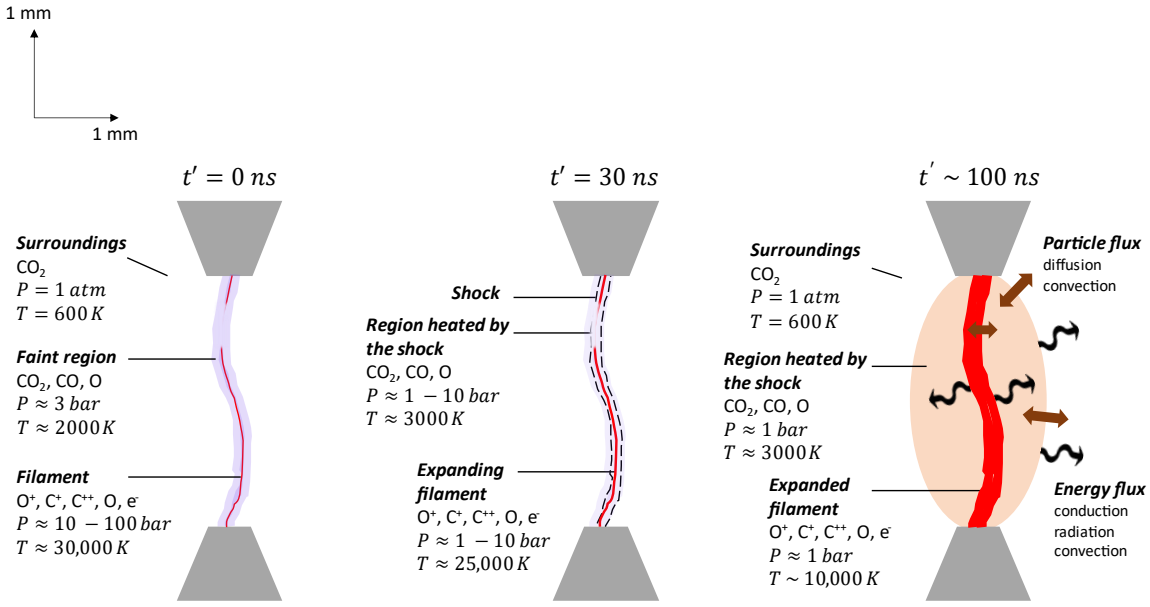

Figure 4-14. Illustrative sketch of the plasma behavior as measured in Chapter 3. When $t' = 0$, the TS has just been established. It is surrounded by a NTS (the faint region) at a temperature on the order of 2000 K and by CO_2 heated from previous pulses. The shock generated by the thermal filament propagates and heats the gas in its path. Finally, after a few hundred ns, the

shock has been absorbed by the gas, and the pressure has relaxed to 1 atm. The energy and reactive species fluxes interact with the surrounding CO_2, leading to CO production.

To add even more complexity, as we showed in Chapter 3, the TS appears as a 100-µm diameter filament surrounded by a 500-µm diameter NTS region, with significant interactions between these two regions. A 2D simulation resolving the kinetics, the shock propagation, the species and energy diffusion and advection, and the Poisson equation for the electric field is required to fully understand the interaction between the hot and cold regions. Such a simulation is beyond the scope of this work.

Nevertheless, a detailed analysis can still be performed to answer the two objectives of this chapter, recalled below:

1) simulate the TS formation. This phenomenon occurs in $\tau_{TTS} \sim 1\ ns$ according to (Minesi et al. 2021), although we will later see that it is about 5-6 ns in our simulations. During this time scale, a 0D model is valid.
2) study the CO formation mechanism (and its EE) in both regimes. In the NTS, the CO formation is expected to occur in two phases: in about 10 ns (Pannier 2019) during the voltage pulse, and in about 1-10 µs in the post-discharge. Since the fastest hydrodynamic effect occurs at the µs time scale, only the first phase can be studied with our 0D model. In the TS, CO is expected to be produced in about 10 µs. The advection, diffusion, and radiation effects must be considered. We will provide a qualitative analysis in section 4.7.2.

4.4 Kinetic model presentation

This section presents the 0D kinetic model developed to simulate the formation of non-thermal and thermal sparks. In the following, we will refer to this model as Model 4.

4.4.1 Model equations

The kinetic model is solved using the ZPlasKin code (Pancheshnyi et al. 2008) coupled with BOLSIG+ (Hagelaar 2015), which solves the electron energy distribution function (EEDF) and computes the rate constants of electron-impact reactions. In this subsection, the model equations and their resolution are described.

Master equation

The kinetic evolution in the early stages of the nanosecond discharge is obtained by solving the master equation:

$$\frac{dn_i}{dt} = \sum_j \nu_{ij} R_j(t) \qquad \text{Eq. 4-1}$$

where n_i is the number density of species i, ν_{ij} is the stoichiometric coefficient of species i in reaction j, and R_j is the rate of reaction j.

Boltzmann equation

The EEDF – and the rate constants of the electron-impact reactions – require the cross-sections of the significant electron-impact processes. Particularly, in the case of highly ionized plasmas, electron-electron and electron-ion collisions must be accounted for. However, ZDPlasKin only considers electron-electron collisions. For electron-ion collisions, we resort to a virtual species, as explained in section 4.4.2.2.

Maxwellian assumption

The resolution of the EEDF is numerically expensive. In a TS in air, (Minesi et al. 2021) showed that, for $n_e = 10^{17}\ cm^{-3}$, only the tail of the EEDF (above 10 eV) departed from the Maxwellian distribution. At $n_e = 10^{18}\ cm^{-3}$, the EEDF was Maxwellian up to 40 eV. More importantly, they performed kinetic simulations first using the EEDF calculated with BOLSIG+, and then using the assumption of a Maxwellian EEDF for $n_e > 10^{17}\ cm^{-3}$. Interestingly, the results of the two simulations were quasi-identical. Thus, in our model, we also use a Maxwellian EEDF for $n_e > 10^{17}\ cm^{-3}$.

Energy equation

The temperature is computed from the energy balance equation at constant volume:

$$\frac{N_{tot}}{\gamma - 1} \cdot \frac{dT_{gas}}{dt} = \sum_j \varepsilon_j \cdot R_j + P_{elast} \cdot N_e \qquad \text{Eq. 4-2}$$

with N_{tot} the total density, γ the heat capacity ratio, R_j the rate of reaction j, ε_j the energy released or consumed in reaction j, and P_{elast} the power transferred from the electrons to the heavy species in elastic collisions.

4.4.2 Species and reactions

The kinetic model developed here includes 26 species and 315 reactions. The species included are summarized in Table 4-2. The reactions, cross-sections, and rate constants are reported in Appendix C.

4.4.2.1 Species

We start with Pannier's mechanism (Pannier 2019) based on (Kozák et al. 2014). To limit the complexity, we remove the species that play a marginal role in Pannier's simulations and that are unlikely to contribute at higher power density: the neutrals O_3, C_2, C_2O, the cation CO_4^+ and all anions (including the atomic anions). A major addition in our model is the incorporation of electron-impact ionization of the excited electronic states of C and O. These processes were found to be essential to model the thermal spark in air according to the work of (Minesi 2020; Minesi et al. 2021).

Vibrational states

Pannier's model was vibrationally specific. Despite a significant VT nonequilibrium during the pulse, he showed that the vibration had a minor impact on dissociation in NRP discharges. Indeed, in his model, vibration and translation equilibrate in a few tens of a ns, and thus vibrational nonequilibrium does not last enough to enable significant dissociation.

Thus, we remove all vibrational species. We assume that the vibrational levels follow a Boltzmann distribution at $T_v = T_g$. To support this approximation, we also performed simulations using the Park model with $T_v \neq T_g$ to account for vibrationally-enhanced dissociation (Park et al. 1994). The results reported in Appendix D show minor differences between the two assumptions, thus confirming the minor role of vibrational excitation in NRP discharges.

Table 4-2. Summary of the species included in this work and other warm plasma models. Compared to Pannier's model, the species not considered in our model are shown in red, and those added in our model are shown in green.

	Kozak 2014	Pannier 2019	Heijkers 2019	This work
Neutrals	O, O_2, O_3, C, CO, CO_2, C_2, C_2O	O, O_2, O_3, C, CO, CO_2, C_2, C_2O	O, O_2, O_3, C, CO, CO_2	O, O_2, C, CO, CO_2
Positive ions	O^+, O_2^+, O_4^+, C^+, CO^+, CO_2^+, CO_4^+, C_2^+, $C_2O_2^+$, $C_2O_3^+$, $C_2O_4^+$	O^+, O_2^+, C^+, CO^+, CO_2^+, CO_4^+	O^+, O_2^+, C^+, CO^+, CO_2^+, CO_4^+, C_2^+	O^+, O_2^+, C^+, CO^+, CO_2^+, O^{2+}, C^{2+}
Negative ions	O^-, O_2^-, O_3^-, O_4^-, CO_3^-, CO_4^-	O^-, O_2^-, O_3^-	O^-, O_2^-, CO_3^-, CO_4^-	
Electronic states	CO_2(7 eV), CO_2(10 eV) CO($A^3\Pi$), CO($A^1\Pi$) CO(sum of triplet states), CO(sum of singlet states) $O_2(a_1+b_1)$, O_2(4.5 eV)	CO_2(7 eV), CO_2(10 eV) CO($A^3\Pi$), CO($A^1\Pi$) CO($A^3\Sigma$), CO($B^3\Sigma$) CO($C^1\Sigma$), CO(13.5eV) $O_2(a_1)$, $O_2(b_1)$, O_2(4.5 eV) O(^{1}D), O(^{1}S), O(^{5}P), O($3p^3$P)	CO_2(7 eV)	CO_2(7 eV), CO_2(10 eV) CO($A^3\Pi$) $O_2(a_1)$, $O_2(b_1)$, O_2(4.5 eV) O(^{1}D), O(^{1}S) C(^{1}D), C(^{1}S), C($^5S_0$)
Vibrational levels	$CO_2(v_1+v_2$:4, v_3:21) O_2: 4 CO: 11	$CO_2(v_1+v_2$:4, v_3:21) O_2: 4 CO: 11	$CO_2(v_1+v_2$:4, v_3:21) O_2: 4 CO: 10	

Electronic states

Minesi *et al.* (Minesi et al. 2021) simulated the transition to a TS in air. They showed that the main ionization reactions involve the electronic states of atomic species, N and O. The inclusion of 8 electronic states of N and 3 electronic states of O was sufficient and the addition of higher states did not influence the kinetics in their conditions. In CO_2 plasma, we expect a similar role for O* and C*. We simulate three cases: (1) without any excited electronic states, (2) with only the excited electronic states of molecular species, and (3) with the excited electronic states of both atoms and molecules; for the atoms, we include the electronic states below 7 eV, i.e. O(^{1}D), O(^{1}S), C(^{1}D), C(^{1}S), and C($^5S_0$) (cf Table 4-2). The latter model is the **nominal Model 4**. Unless specified otherwise, the results presented in this chapter are obtained with this model.

The impact of these electronic states on the ionization mechanism is discussed in section 4.6.1.

4.4.2.2 Electron-impact reactions

As the reduced electric field ranges between 100 and 500 Td in a ns-spark, the electron-heavy collisions mainly generate electronic state excitation (and possibly subsequent dissociation) and ionization. To a lesser extent, vibrational states are also excited. For most of these electron-impact reactions, we use the same data as (Pannier 2019), that is, the cross-sections of the IST-Lisbon database (Grofulović, Luís L Alves, et al. 2016) retrieved from LXCat (Pancheshnyi et al. 2012; Pitchford et al. 2017). The cross-section data and rate coefficients used are listed in Table C-1 and Table C-2.

Electronic-specific collisions

In Pannier's model, the depopulation processes of electronic states were limited to quenching and spontaneous emission for CO*, and predissociation and quenching for CO_2*. Our model's major improvement is the addition of some missing reactions for the electronic states, notably ionization.

First, we add ionization reactions from the excited electronic states of CO_2. Unfortunately, no state-specific cross-sections are available in the literature for the CO_2 electronic states. Therefore, we use the model of (Drawin 1967) to approximate these cross-sections. This model was initially developed to compute excitation and ionization cross-sections of atoms. Nevertheless, it has shown satisfactory predictions for the excitation and ionization cross-sections of N_2, O_2, and NO (Bacri and Medani 1980, 1982; Teulet, Sarrette, and Gomes 1999). The ionization cross-section of level i is written as:

$$\sigma_i^{Drawin} = 4\pi a_0^2 \left(\frac{R_y}{\Delta E_i^{ioniz}}\right)^2 \xi_e \alpha_{iI} \frac{u-1}{u^2} \ln\left(1.25\beta_{iI} u\right) \qquad \text{Eq. 4-3}$$

where ΔE_i^{ioniz} is the ionization energy of level i, ξ_e is the number of equivalent electrons in the outer shell, and $u = \varepsilon/\Delta E_i^{ioniz}$ is the reduced electron energy (with ε the electron energy). α_{iI} and β_{iI} are empirical parameters, close to 1. To simplify, we also take $\xi_e = 1$. For CO_2(7 eV) (attributed to $CO_2(^3\Sigma_u)$ in (Pannier 2019)), we take $\Delta E_i^{ioniz} = 13.8 - 7 = 6.8\ eV$. For CO_2(10 eV), $\Delta E_i^{ioniz} = 3.8\ eV$. For CO($A^3\Pi$), $\Delta E_i^{ioniz} = 13.8 - 6 = 7.8\ eV$.

We report in Figure 4-15 the state-specific ionization cross-sections of CO_2* (and CO*) calculated using the model of (Drawin 1967). The predicted cross-section for ground state ionization agrees within a factor of 2 with the cross-section of the IST-Lisbon database (Grofulović, Luís L Alves, et al. 2016). This level of agreement is indicative of the estimated error on the CO_2* cross sections. For lack of a more accurate electronic-specific cross-section of ionization for CO_2, Drawin's model is used in our simulations.

The cross-sections for elastic collisions of CO_2* are assumed to be the same as that of CO_2(X).

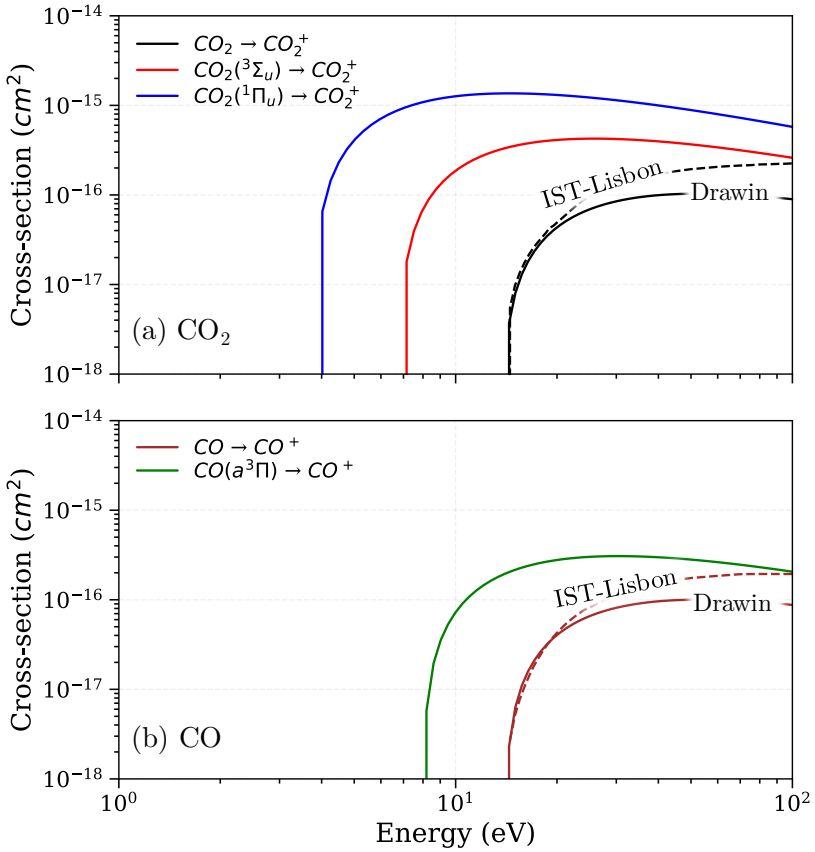

Figure 4-15. Electronic-specific ionization cross-sections of CO_2* (a) and CO* (b) calculated using Drawin's model (Drawin 1967). As a comparison, we add the ionization cross-section of the ground states taken from IST-Lisbon database (Grofulović, Luís L Alves, et al. 2016)**.**

For CO* and O_2*, we add ionization, elastic collisions, inter-state excitation, and direct electron-impact dissociation. For $O_2(a_1)$ and $O_2(b_1)$, we use the cross-sections from (Ionin et al. 2007). Nevertheless, there are no cross-sections available for the grouping O_2(4.5 eV), nor for CO($a^3\Pi$). Thus, for these two states, we proceed in the same way as for CO_2*. For elastic collisions, we use the cross-section of the ground state, and Drawin's model for ionization.

We add the electron-impact ionization and excitation from the O and C electronic states using the cross-sections of (Tayal and Zatsarinny 2016) and (Wang, Zatsarinny, and Bartschat 2013).

Doubly ionized ions

To model the electron-impact ionization of O^+ to O^{++} and of C^+ to C^{++}, we integrate the ionization cross-sections of O^+ and C^+ from (Tawara and Kato 1987) assuming a Maxwellian distribution for the electrons. This assumption is motivated by the high electron density

associated with O^{++} and C^{++} formation, and thus the quick relaxation of the EEDF to its Maxwellian form.

Electron-ion elastic collisions

Due to the high Coulomb cross-section, as soon as the ionization degree exceeds 10^{-3}, electron-ion collisions significantly slow the electrons and lead to Joule heating (Raizer 1991). By default, ZDPlaskin does not allow for these reactions in BOLSIG+. Thus, we implement them using a virtual species representing the average ion. The mass of this virtual species is taken equal to the average of the masses of C^+ and O^+. The momentum transfer cross-section for electron-ion collisions is calculated according to (Lieberman and Lichtenberg 2005):

$$\sigma_m(\varepsilon) = 4\pi b_0^2 \ln\,(2/\theta_{min}) \qquad \text{Eq. 4-4}$$

where $b_0 = e^2/(4\pi\varepsilon_0\varepsilon)$, with e the elementary charge, ε_0 the vacuum permittivity, and ε the energy of the incident electron. θ_{min} is the minimum scattering angle related to the Debye length λ_{De} by $\theta_{min} = b_0/\lambda_{De}$. The Debye length is expressed as $\lambda_{De} = \sqrt{\varepsilon_0 k_B T_e/n_e e^2}$, where T_e and n_e are the electron temperature and number density. Since these collisions are only significant at high n_e, we compute the Debye length with $n_e = 10^{18}$ cm^{-3} and $T_e =$ 30,000 K.

Electron-ion recombination

Electrons and ions can recombine via 3-body reactions with electrons or heavy species as the third body:

$$O^+ + e^- + e^- \rightarrow O + e^- \qquad \text{Reac. 24}$$

$$O^+ + e^- + M \rightarrow O + M \qquad \text{Reac. 25}$$

Electrons also recombine via dissociative recombination reactions such as:

$$CO_2^+ + e^- \rightarrow\ CO + O \qquad \text{Reac. 26}$$

We implemented Reac. 2 using the rate constant from (Biberman, Vorob'ev, and Yakubov 1987). In our high-density conditions ($n_{tot} \sim 10^{19}\ cm^{-3}$), the simulations showed that this reaction is negligible compared to the two other recombination pathways. So, we remove recombination reactions with heavy 3rd bodies from the nominal model.

Also, dissociative recombination reactions usually dominate over 3-body electron recombination. For the sake of simplicity, we remove the 3-body recombination of CO_2^+ and O_2^+ with electrons as a third body. We keep CO^+ 3-body recombination with electrons as a third body as a telltale of 3-body recombination insignificance for molecular ions. For O^+ and C^+, we only consider 3-body recombination with an electron as the third body.

4.4.2.3 Predissociation of CO_2 electronic states

As explained in Chapter 2, the CO_2 electronic states pre-dissociate after an electron-impact excitation. Cossart-Magos *et al.* (Cossart-Magos et al. 1982) measured the predissociation rate of the $^3\Sigma_u^-$ state at 11.2 eV to be greater than $6{\cdot}10^{11}$ s^{-1}. Wright *et al.* (Wright et al. 2017) measured sub-20 fs and 200 fs lifetimes for the predissociation of $CO_2(^1\Pi_g)$ (1^1B_2 and 1^1A_2, at 9.5 eV) via direct and indirect[17] channels. The equivalent rates are $5{\cdot}10^{12}$ - $5{\cdot}10^{13}$ s^{-1}. We use $5{\cdot}10^{13}$ s^{-1} as an estimate for CO_2* predissociation.

4.4.2.4 Quenching of the electronic states

The quenching of the many states introduced must be included in the most accurate way possible, as it may significantly change the role played by the electronic states. For example, instantaneous quenching would induce heating, whereas slow quenching would allow the electronic state to be ionized. Unfortunately, quenching rate constants have been studied for limited combinations of electronic states and colliders. Therefore, we are often forced to make rough approximations. The quenching rates implemented are reported in Table C-4.

For CO_2*, we implement no quenching rate, as predissociation is much faster than quenching (see Chapter 2).

For O_2*, many quenching rates have been measured. We mostly use the review of (Capitelli et al. 2000). Still, we have to make a few assumptions. We did not find a rate for the reaction:

$$O_2(a_1) + CO \rightarrow O_2 + CO \qquad \text{Reac. 27}$$

so we take the same rate as for $O_2(b_1)$, from (Dunlea and Ravishankara 2004) (assumption 1). We did not find rates for C, O^+, and C^+ colliders, whereas these species become the main species (with O) in the TS. To remedy this, we estimate that these rates are the same as for a collision with O (assumption 2). We will use this assumption for every electronic state implemented in the model.

For $CO(A^3\Pi)$, we follow the recommendations of (A. F. Silva et al. 2020). For C, O^+, and C^+ colliders, we still assume the same rate as for O (assumption 2).

For $O(^1D)$ quenching, we mainly use rates from (Capitelli et al. 2000; Sander et al. 2003). As the rate for CO colliders is missing, we take the same rate as for O_2 (assumption 3). For $O(^1S)$, we use rates from (Capitelli et al. 2000; Filseth, Stuhl, and Welge 1970; T G Slanger and Black 1978a) (Slanger and Black 1976). Slanger and Black measured branching ratios

[17] The predissociation of CO_2 electronic states can proceed via the crossing of conical intersection between bound and repulsive states. This dissociation channel is named "indirect" in the work of (Wright et al. 2017). See Chapter 2 for more details.

of O(^{1}S) deexcitation toward O(^{1}D) and O(^{3}P) for different colliders, but not for CO. Thus, we take the same branching ratio for CO as for O_2 (assumption 4). The total removal rates come from Filseth *et al.* (Filseth, Stuhl, and Welge 1970). For C, O^+, and C^+ colliders, we take the same rate as for O (assumption 2).

Finally, we assume that every C* deexcites directly toward the ground state with the same rate as O(^{1}S) (assumption 5). We check *a posteriori* that this assumption has little impact on the simulation results. Indeed, in the conditions investigated in this work, the main C* deexcitation processes are the super-elastic collisions with electrons and the electron-impact ionization.

4.4.2.5 Charge exchange reactions

We start from the charge exchange reactions used in (Kozák et al. 2014; Pannier 2019), to which we add some missing reverse reactions, including ($CO + O_2^+ \rightarrow CO_2^+ + O$), ($CO_2 + O_2^+ \rightarrow CO_2^+ + O_2$), ($C^+ + O_2 \rightarrow C + O_2^+$), and ($CO + O^+ \rightarrow C^+ + O_2$). Although these reverse reactions are negligible at the temperatures usually reached in NTSs, it is necessary to include them in order to retrieve the equilibrium composition with our model up to 30,000 K.

As we expect a significant amount of atomic species O, C, O^+, C^+, we add the following reaction:

$$O^+ + C \leftrightarrow O + C^+ \qquad \text{Reac. (I15)}$$

to allow these ions to equilibrate. Its rate constant is not in UMIST (McElroy et al. 2013), so we use the Langevin reaction rate constant (Haynes, Lide, and Bruno 2016) for the exothermal way of the reaction, and detailed balance for the other way. The charge transfer reactions and rate constants are summarized in Table C-5.

4.4.2.6 Neutral reactions

The O-CO 3-body recombination (reverse of N1) rate constant used in (Kozák et al. 2014; Pannier 2019) comes from (Tsang and Hampson 1986). The CO_2 + M dissociation (N1 forward) rate constant comes from (Eremin et al. 1997). Computing the reverse rate constant of Eremin *et al.* by detailed balance yields a significantly different rate constant than Tsang and Hampson's. This is illustrated in Figure 4-16.

Eremin's rate constant is valid between 2,600 and 4,400 K, whereas Tsang's rate constant is valid between 300 and 3,500 K. As shown in Figure 4-16, when the temperature is lower than 2,000 K, the reverse of Eremin rate constant is much higher than the other literature's rate constants. Given that the forward and reverse rate constants of Eremin have a narrow validity range, we replace them with the rate constants of Park *et al.*

We add the O_2 dissociation by heavy-species impact (N6) (O_2 + M ↔ O + O + M). We replace the rate constant of CO + O_2 → CO_2 + O by the rate constant calculated from its reverse reaction using detailed balance. We also add several missing reverse reactions: CO + CO → CO_2 + C, CO + O → C + O_2.

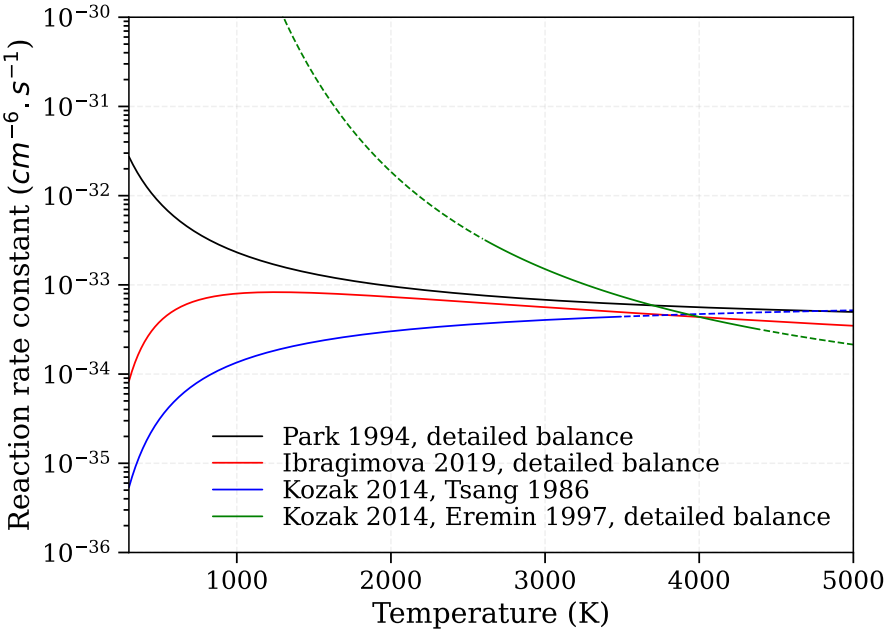

Figure 4-16. Comparison of the O – CO 3-body recombination rate constants from the literature. The validity range is 300 – 40,000 K for Ibragimova, 300 – 3500 K for Tsang 1986, 2,600 – 4,400 K for Kozak, and is not mentioned for Park.

4.4.3 Equilibrium verification of the kinetic mechanism

As a consistency check of our kinetic model, it is important to ensure that it converges toward the equilibrium composition. We run calculations for $T_e = T_g \in [1000;\ 30{,}000\ K]$ and P_{atm}. We report the converged mole fractions in Figure 4-17 as well as the equilibrium composition calculated with the NASA-9 coefficients (McBride et al. 2002a). For doubly and triply ionized ions (O^{++}, C^{++}, O^{+++}, C^{+++}), we add the NASA9 coefficients computed by (Capitelli et al. 2005). Apart from small deviations of the mole fractions of C and O above 10,000 K, the equilibrium mole fractions computed with our model are generally in good agreement with the NASA CEA calculations. This test confirms that the detailed balance relations are correctly implemented in our model.

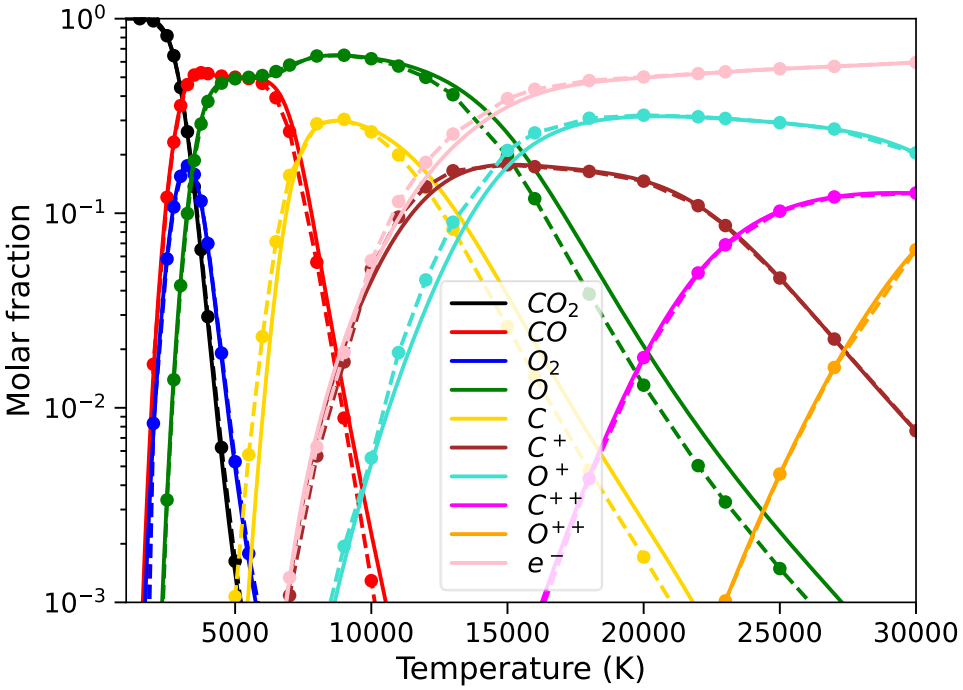

Figure 4-17. Equilibrium mole fractions vs gas temperature, at P_{atm}, CEA-NASA and Capitelli (solid line) vs our simulations (dotted lines).

4.5 Simulations of the non-thermal and thermal sparks and comparisons with experiments

In the experimental chapter, we saw that the application of the high voltage pulse can produce either non-thermal sparks (i.e. the faint region observed in the middle of the gap), or thermal sparks (i.e. the bright region observed most of the time at the electrodes, and in 10% of the cases in the middle of the gap). Our objective in this section is to simulate the formation of these two regimes in our experimental conditions. We run several simulations to account for the different initial temperature conditions that are attributed to turbulence and non-uniformity in the initial flow field. In all simulations, the initial pressure is 1 bar. In all cases, we consider a pulse in the steady state pulsing regime.

4.5.1 NRP discharge model (inputs and assumptions)

This section details the inputs and assumptions we use to simulate non-thermal and thermal sparks. All input parameters are summarized in Table 4-3. Their choice is justified in the following subsections.

Table 4-3. Summary of the initial values for the model parameters in the two nominal cases simulated in this thesis.

Physical parameters	Non-thermal spark	Thermal spark
Cathode fall	500 V	500 V
$\boldsymbol{T_0}$	650 K	1100 K
$\boldsymbol{P}$	1 bar	1 bar
$\boldsymbol{n_{tot}}$	$1.1 \cdot 10^{19}$ cm^{-3}	$6.6 \cdot 10^{18}$ cm^{-3}
$\boldsymbol{n_{e,0}}$	10^{10} cm^{-3}	10^{10} cm^{-3}

Input electric field

In Figure 4-18, we report the input voltage at the electrodes, reconstructed from the difference of incident and reflected voltages measured in Chapter 3. The same input voltage is used for the TS and the NTS because in Chapter 3 we measured no significant differences between the voltage traces in the two regimes. We subtracted an arbitrary 500 V cathode fall from the input voltage, as was done in (Minesi et al. 2021, 2023) in their simulations of a thermal spark in air.

We assume that the electric field is uniform in the 3-mm gap. A justification of this assumption is based on two previous works on NRP spark discharges in air: 1) (David Z Pai, Lacoste, and Laux 2010) measured the emission of several excited states of N_2 and N_2^+ at different locations along the interelectrode gap and found that this emission was uniform over most of the gap (except in small regions near the electrodes, possibly corresponding to the bright spots we observed in the type a-b discharges presented in Chapter 3). They deduced that the electric field was uniform over the inter-electrode gap. 2) In numerical simulations, (Tholin 2012) computed a uniform distribution of the electric field along the gap as long as the initial electron number density remained above a threshold of about 10^{10} cm^{-3}. This preionization level is typical of NRP discharges in the steady-state regime.

Consequently, we assume that the electric field is uniform and approximately equal to the voltage (minus the cathode fall) divided by the 3-mm inter-electrode distance. The resulting profile is shown in Figure 4-18.

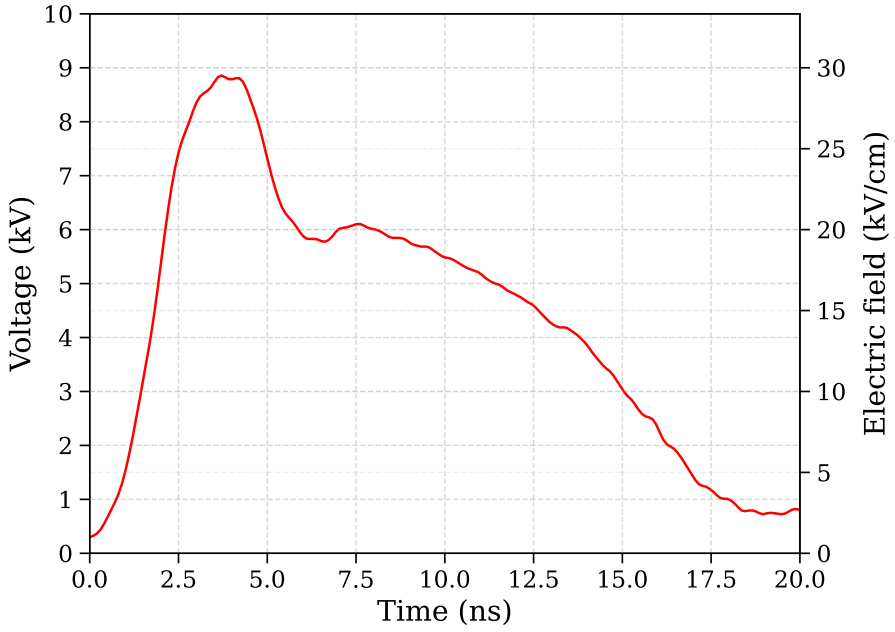

Figure 4-18. Voltage and electric field profiles used in the simulations. The voltage is reconstructed from the difference of the incident and reflected voltages measured in Chapter 3. The electric field is calculated as the voltage (to which we subtract a 500 V cathode fall) divided by the inter-electrode gap distance of 3 mm.

Initial temperature T_0

In Chapter 3 (Figure 3-16), the gas temperature at the beginning of a pulse in the steady state pulsing regime at 10 kHz was measured from the second positive system of N_2 and was found to be around 600±200 K. In earlier work with similar conditions, Pannier observed hot spot regions in which he measured radially resolved temperature profiles using the IR emission of the fundamental ν_3 bandhead of CO_2, showing the non-uniformity of the temperature in the discharge. Then, by averaging over the discharge profile, he measured an initial temperature of 1200±100 K.

The initial temperature in the gap is fluctuant and non-uniform, and may vary between 400 and 1300 K. These temperature variations will directly affect the reduced electric field E/N (since the density N in the discharge is inversely proportional to the initial temperature T of the gas).

We will see in the following that these temperature variations are the main factor controlling the nature (non-thermal or thermal) of the spark produced.

Initial electron density $n_{e,0}$

The initial electron density is a free parameter of the simulation. In Chapter 3, we could not measure the initial electron density in the plasma because of the very small Stark broadening of the O(777) triplet for $n_e \leq 10^{15}\ cm^{-3}$ and because the emitting electronic

state of the 777 nm line is not sufficiently populated at the early stages of the pulse. Pannier (Pannier 2019) suggested that, for 10 kHz pulses, the only self-consistent electron density possible is $n_{e,0} = 10^{10}\ cm^{-3}$: higher initial values lead to a higher peak electron density, but n_e always return to 10^{10} cm^{-3} after 100 µs (the inter-pulse time at 10 kHz). We follow his recommendation.

A justification of this assumption is as follows. In the post-discharge of nanosecond sparks, the fastest electron recombination process is via dissociative recombination (e.g. $CO^+ + e^- \rightarrow C + O$ or $CO_2^+ + e^- \rightarrow CO + O$). If we assume that CO^+ (or CO_2^+) is the dominant ion, then $n_e = n_{CO+}$ or n_{CO2+}. The temporal evolution of the electron number density starting from the electron density $n_e(t_p)$ produced by the pulse is given by the following expression:

$$n_e(t) = \frac{n_e(t_p)}{1 + n_e(t_p) k_{DR} t} \qquad \text{Eq. 4-5}$$

where k_{DR} is the rate constant for dissociative recombination. At time τ corresponding to the end of the interpulse period, the electron density is then:

$$n_e(\tau) = \frac{n_e(t_p)}{1 + n_e(t_p) k_{DR} \tau} \qquad \text{Eq. 4-6}$$

If the electron density produced by the pulse is sufficiently high, i.e. $n_e(t_p) \gg (k_{DR}\tau)^{-1}$, the value of n_e at the end of the interpulse period becomes independent of the electron density produced by the pulse and equal to:

$$n_e(\tau) = \frac{1}{k_{DR}\tau} \qquad \text{Eq. 4-7}$$

In our case, $k_{DR} \approx 10^{-7}$ cm^3/s, and $\tau = 100$ µs (10 kHz discharge). The condition is verified if $n_e(t_p) \gg 10^{11}$cm^{-3}, which is clearly the case in the thermal or the non-thermal spark. Thus we expect the density at the end of the interpulse period, and therefore at the beginning of the next pulse, to be of the order of $(k_{DR}\tau)^{-1} = 10^{11}$ cm^{-3}. This approximate analysis is consistent with the value proposed by Pannier.

The simulations will therefore be conducted assuming the initial electron density of 10^{10} cm^{-3} suggested by Pannier. Additionally, we will perform a sensitivity analysis to assess the impact of $n_{e,0}$ on the simulation results (see Appendix D).

Isochoric assumption

As discussed in Sections 4.2 and 4.3, the pressure relaxation and transport phenomena can be neglected for about 1 µs in the NTS, and 10 ns in the TS. Therefore, the isochoric assumption is valid during the pulse for the NTS discharge. For the TS discharge, we assume

that the plasma is isochore during the transition to the thermal filament since this transition occurs within about 5-6 ns (see 4.5.4).

Heat losses

We saw in section 4.3 that the characteristic time of radiative cooling (the dominant heat loss process) is more than 250 ns in the thermal spark regime, and on the order of microseconds for the non-thermal spark. Thus, as we only simulate the first tens of ns of the discharge, we assume that the system is adiabatic.

4.5.2 Predicted peak electron number density as a function of the initial temperature

Simulations are performed at different initial temperatures in the 600 – 1,300 K interval, using the electric field obtained from the electrical measurements (Figure 4-18), as explained in Section 4.5.1. As shown in Chapter 3, the peak electron density is an indicator of the non-thermal or thermal nature of the spark regime: we obtain a thermal spark for n_e~10^{18} cm^{-3}, and a non-thermal spark for n_e~10^{16}-10^{17} cm^{-3}.

Thus, in Figure 4-19, we plot the peak electron density obtained in the simulations as a function of the initial temperature. This graph shows that the initial temperature in the plasma drives the ionization during the pulse, and thus, the thermalization of the spark. Initial temperatures below 700 K leads to peak n_e below 10^{17} cm^{-3}, which is characteristic of the NTS regime. $T_0 \geq 950$ K leads to peak n_e above 10^{18} cm^{-3}, characteristic of the TS regime. Between 700 and 950 K, n_e is between 10^{17} and 10^{18} cm^{-3} so we cannot settle the nature of the spark for now.

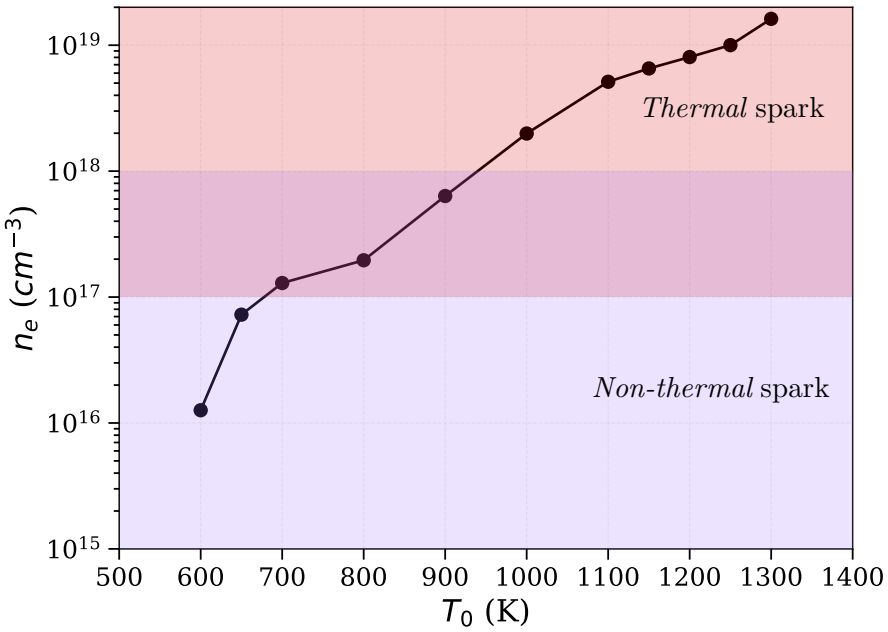

Figure 4-19. Peak electron density obtained in the simulations as a function of the initial temperature. For $T_0 > 900$ K, the model predicts the formation of a thermal spark.

4.5.3 Non-thermal spark

We now consider the simulations of the measured electron density in the faint region (Chapter 3). In that region, an electron density of $n_e \sim 10^{16} - 10^{17}$ cm^{-3} was measured from the Stark broadening of the O(777) triplet. According to Figure 4-19, this corresponds to an initial gas temperature of 600 – 700 K.

Thus, we analyze the simulation results for $T_0 = 600, 650, 700$ K. The cases $T_0 = 600$ and 700 K represent a temperature variation of about ±10% compared to 650 K, and allow to visualize the sensitivity of the results to T_0.

For $T_0 = 600$ K, about 7% CO_2 is converted to CO after 15 ns with an EE of 21%. The gas temperature stays below 1,000 K (during the 20 ns of the simulation). The electron density peaks at 10^{16} cm^{-3} at 14 ns.

For $T_0 = 650$ K, the conversion and EE are 36% and 20%, respectively. The gas temperature reaches 3,000 K at 15 ns, and the electron density peaks at $7 \cdot 10^{16}$ cm^{-3} at 11 ns.

For $T_0 = 700$ K, the conversion and EE are 59% and 18%, respectively. The gas temperature reaches 5,000 K at 15 ns, and the electron density peaks at 10^{17} cm^{-3} at 9 ns.

The evolution of the temperatures and main species densities are reported in Figure 4-20, where the solid line corresponds to the case $T_0 = 650$ K, and the colored swaths indicate the spread of results between the extreme cases at $T_0 = 600$ K and $T_0 = 700$ K. Along with

the simulation results, we report the T_e and n_e measured in the faint region (Chapter 3). T_e was measured from the O(716) and O(777) lines assuming Saha-Boltzmann equilibrium.

The experimental and simulated electron temperatures agree within a factor 2. At t = 20 ns, the predicted electron and gas temperatures equilibrate at about 3000 K. This temperature is higher than the measured temperature of about 800 K, but it is highly sensitive to the initial gas temperature. Indeed, for an initial gas temperature of 600 K, the simulated gas temperature (indicated by the lower border of the gray swath) is much closer to the experimental values.

By construction, the experimental and simulated n_e are comparable, although the measured n_e increases earlier in the pulse. The main dissociation products are CO and O, in accordance with the results of Chapter 3.

The main result is the high sensitivity of the conversion, electron density, and gas temperature to the initial temperature. Between $T_0 = 600$ and $T_0 = 700$ K, the conversion increases by a factor 8, the electron density by a factor 10, and the gas temperature by a factor 5. Thus, the T_0 heterogeneity in the interelectrode gap creates non-thermal sparks with a wide range of electron number densities and CO_2 conversion degrees.

On the other hand, the EE of CO production at 20 ns stays approximately constant at a value of about 20% for T_0 in the range 600-800 K. This behavior will be related in Section 4.7.1 to the CO production mechanism in non-thermal sparks.

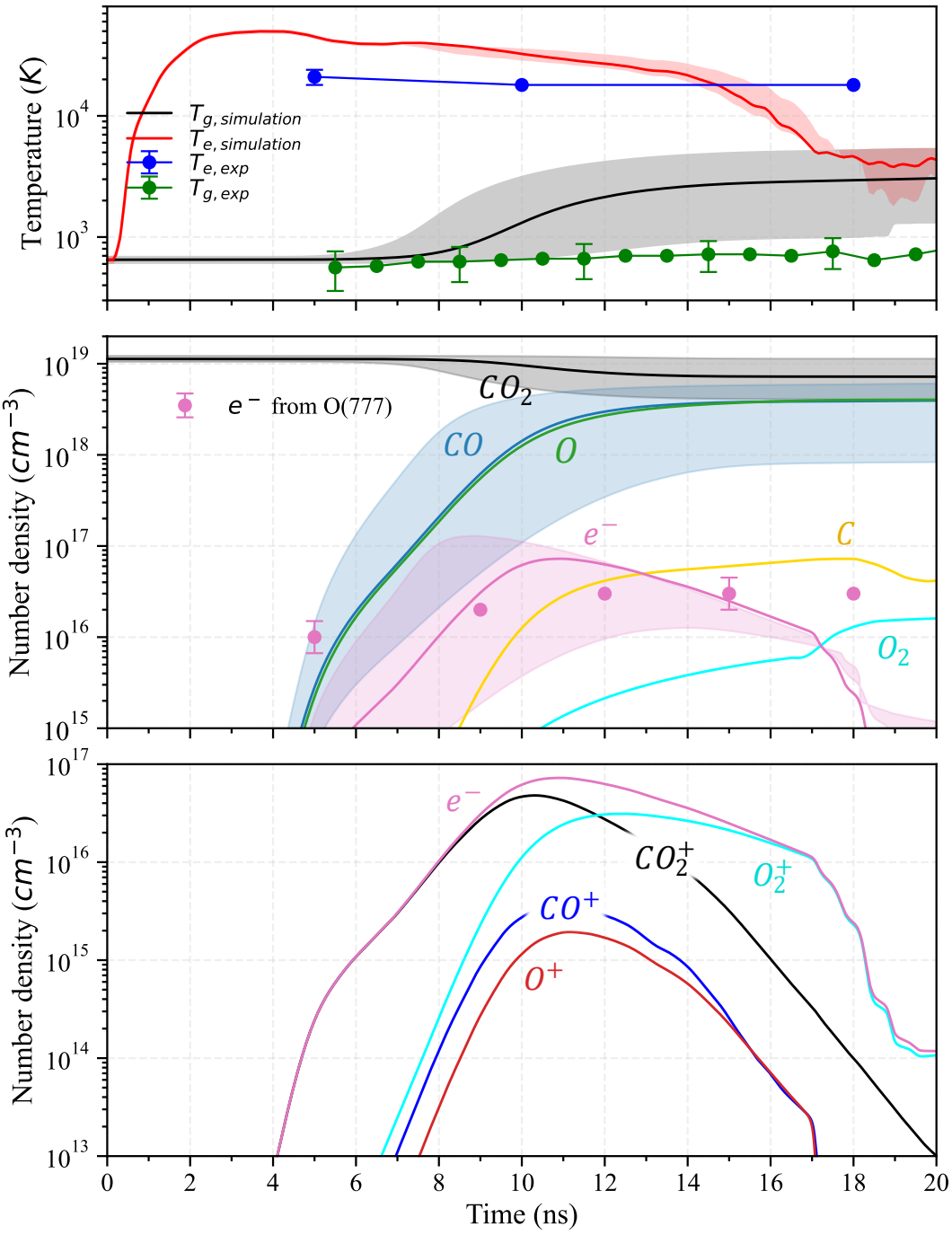

Figure 4-20. Non-thermal spark: comparison between model predictions (solid lines and colored areas) and experiments (symbols). The solid lines are the $T_0 = 650$ K case. The colored swaths indicate the limiting cases at $T_0 = 600$ and $T_0 = 700$ K. The electron density is measured using the Stark broadening of O(777) triplet, and the electron temperature from the O(716) and O(777) lines.

4.5.4 Thermal spark

In Chapter 3, we measured peak electron densities in the thermal spark ranging between $2{\cdot}10^{18}$ and $5{\cdot}10^{18}$ cm^{-3}, which corresponds to simulations with T_0 between 1000 and 1200 K.

In Figure 4-21, we report the temperatures (upper graph) and main species densities (bottom graph) of three simulations: the solid lines are computed at $T_0 = 1100\ K$, while the colored swaths represent the spread of the simulations at $T_0 = 1000\ K$ and $T_0 = 1200\ K$ (±10% variation compared to 1100 K). For readability, the colored swaths in the species graph are only shown for n_e and n_O. As can be seen in the figure, the transition to the thermal spark suddenly occurs 4 ns after the beginning of the pulse: the gas temperature jumps from 1000 K to 10,000 K, CO_2 is dissociated, and O, CO, and e^- appear in the plasma. 1 ns later, CO is dissociated in turn, and the O, C, O^+, and C^+ densities rise. At $t = 10\ ns$, the electron density reaches $4{\cdot}10^{18}$ cm^{-3}, and the plasma is in thermal equilibrium. In accordance with the findings of Chapter 3, T_e and T_g equilibrate at about 20,000 K (much higher than in the non-thermal spark) in a few ns. A similar thermalization phenomenon was shown by (Minesi et al. 2021; Shcherbanev et al. 2022) in NRP-sparks in air.

Additionally, we compare the simulation results to the n_e and T_e measurements of Chapter 3. As a reminder from this chapter, we obtained the electron density from the Stark broadening of the O(777) triplet, and the electron temperature from the measurements of C^+ and O^+ excited states. The calculated electron temperature underestimates the experimental values (blue points in the upper graph in Figure 4-21) by about 50%. By construction, the simulated and measured electron densities are in agreement.

Overall, the simulations reproduce the general behavior of the thermal sparks described in chapter 3. We note in particular the subnanosecond transition to a high ionization degree, the fully atomic composition, and the temperatures of approximately 20,000 – 30,000 K. We will show in Sec. 4.6.3 that for $T_0 = 1100$ K, the thermal spark reaches LTE. The CO production mechanism will be discussed in section 4.7.2.

Finally, as for the case of the NTS, our simulations highlight the sensitivity of the thermochemical conditions in the plasma to the initial temperature (i.e. the reduced electric field). The 20% variation of T_0 between 1000 and 1200 K results in a factor of 4 in the electron density, and 2 – 3 in the O, C, O^+, and C^+ densities.

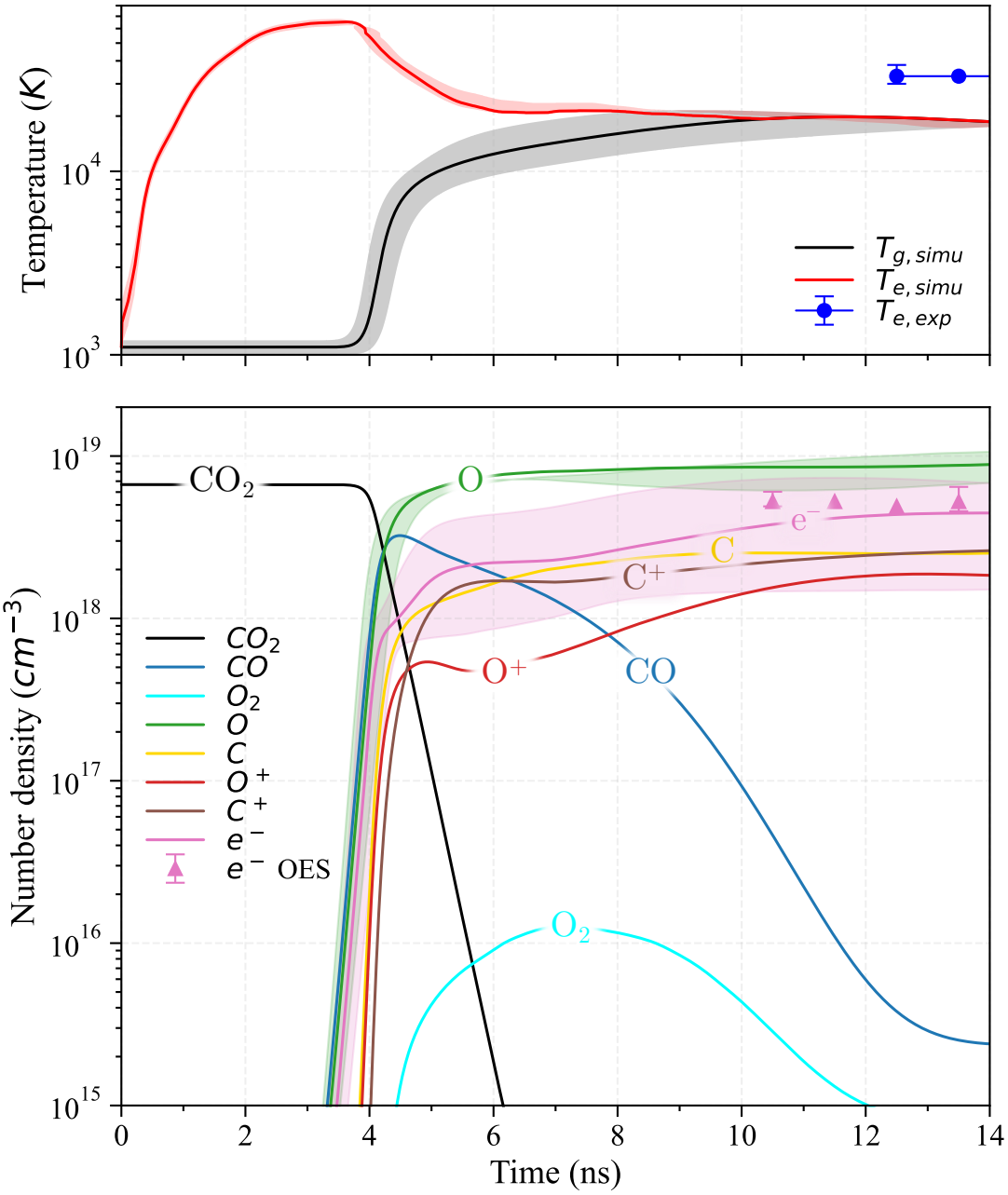

Figure 4-21. Temporal evolution of the temperatures and number densities of the main species in a *thermal* spark. Comparison between model predictions (solid lines and colored areas) and experiments (symbols). The measurements are taken in the bright region at the anode. The electron density is measured from the Stark broadening of the O(777) triplet. Calculations at $T_0 = 1000, 1100, 1200$ K are reported. The solid lines are the $T_0 = 1100$ K case. The colored swaths indicate the limiting cases at $T_0 = 1000$ and 1200 K ($\pm$ 10% on T_0).

4.5.5 Comparison with electrical measurements

In this section, we use the electrical measurements of Chapter 3 as an additional validation of the model.

The voltage pulse sent by the generator propagates toward the plasma in a cable of impedance $Z_{cable} = 75\ \Omega$. When the pulse encounters the plasma of impedance Z_{plasma}, a fraction of the power is reflected. The incident and reflected voltage pulses are measured 3 m away from the plasma, which allows the determination of the plasma impedance:

$$Z_{plasma} = \frac{U_i + U_r}{U_i - U_r} \cdot Z_{cable} \qquad \text{Eq. 4-8}$$

where U_i and U_r are the incident and reflected voltages. The voltage across the electrodes is $U_{plasma} = U_i + U_r$. Then, the total current in the plasma is $I_{plasma} = U_{plasma}/Z_{plasma} = (U_i - U_r)/Z_{cable}$.

According to Chapter 3, during the first pulse, more than 99% of the energy goes into the faint region due to the very small volume of the bright region compared to the faint region (during the first pulse, type a/b emission is dominant and $V_{a/b} \approx 2 \cdot 10^{-13}\ m^{-3}$, to be compared to $V_{faint} \approx 6 \cdot 10^{-10}\ m^{-3}$). The faint region can be approximated as a cylinder with a measured diameter of about 500 µm (Figure 3-10). The current density is obtained by dividing I_{plasma} by the cylinder cross-section area.

The current density measured in the faint region (which is in the non-thermal spark regime) is compared to the simulations in Figure 4-22. After about 10 ns, the current density qualitatively agrees with the simulations at $T_0 = 600 - 700\ K$.

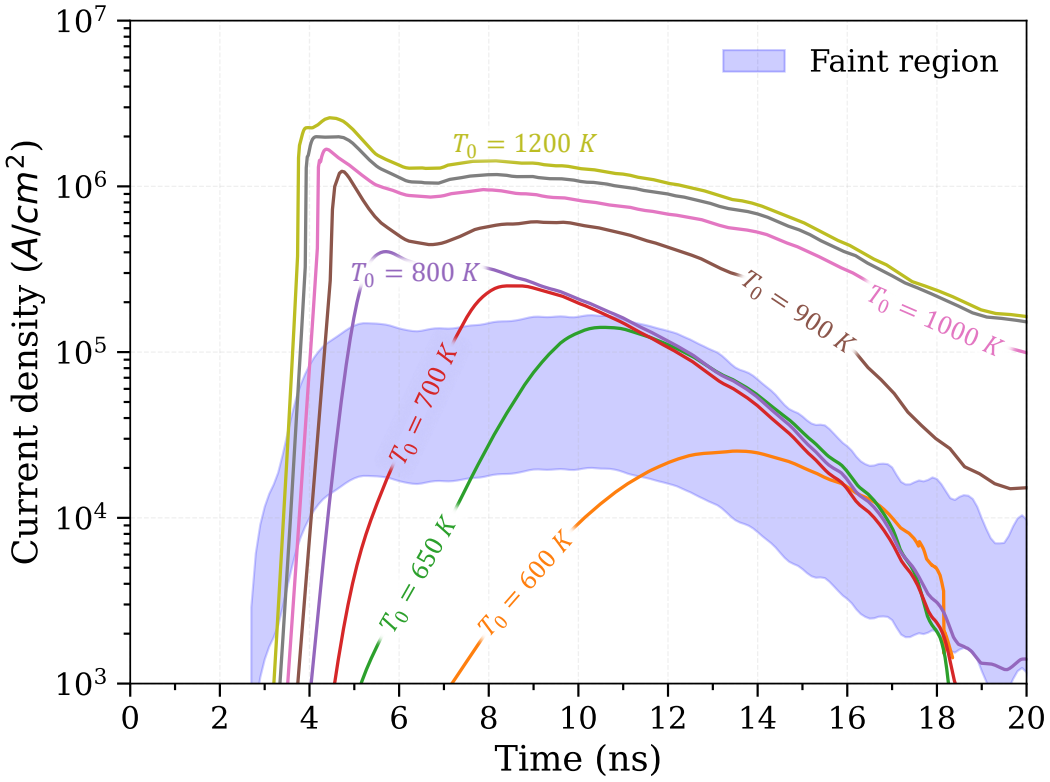

Figure 4-22. Current density in the faint region (blue area) compared to the simulation results. The uncertainty in the experimental data comes from the uncertainty on the diameter measurements. The faint region's current density is consistent with the simulations for T_0 between 600 and 700 K after 10 ns.

4.6 Mechanisms of formation of the thermal and non-thermal sparks

4.6.1 Ionization mechanism

The net rates of the main ionization reactions in the non-thermal and thermal sparks are reported in Figure 4-23 and Figure 4-24. We observe that ionization proceeds in 3 stages.

At first, CO_2 is ionized to CO_2^+ by electron impact ($e^- + CO_2 \rightarrow e^- + e^- + CO_2^+$). In the non-thermal spark, this reaction is the main contributor to the electron production. In the thermal spark, as CO_2 dissociates very quickly, the contribution of CO_2 ionization to the overall electron production is only important up to about 3 ns (i.e. before the transition).

Then, as the dissociation of CO_2 into CO and O becomes significant (at about 10 ns for the NTS and 4 ns for the TS), so does the ionization of CO, CO*, O, and O*. In this phase, the ionization of CO* is by far the most significant reaction. CO* ionization is the second electron producer in the non-thermal spark, and the first one in the thermal spark. In the

reference simulation of the thermal spark ($T_0 = 1100\ K$), it accounts for 30% of the total electron production.

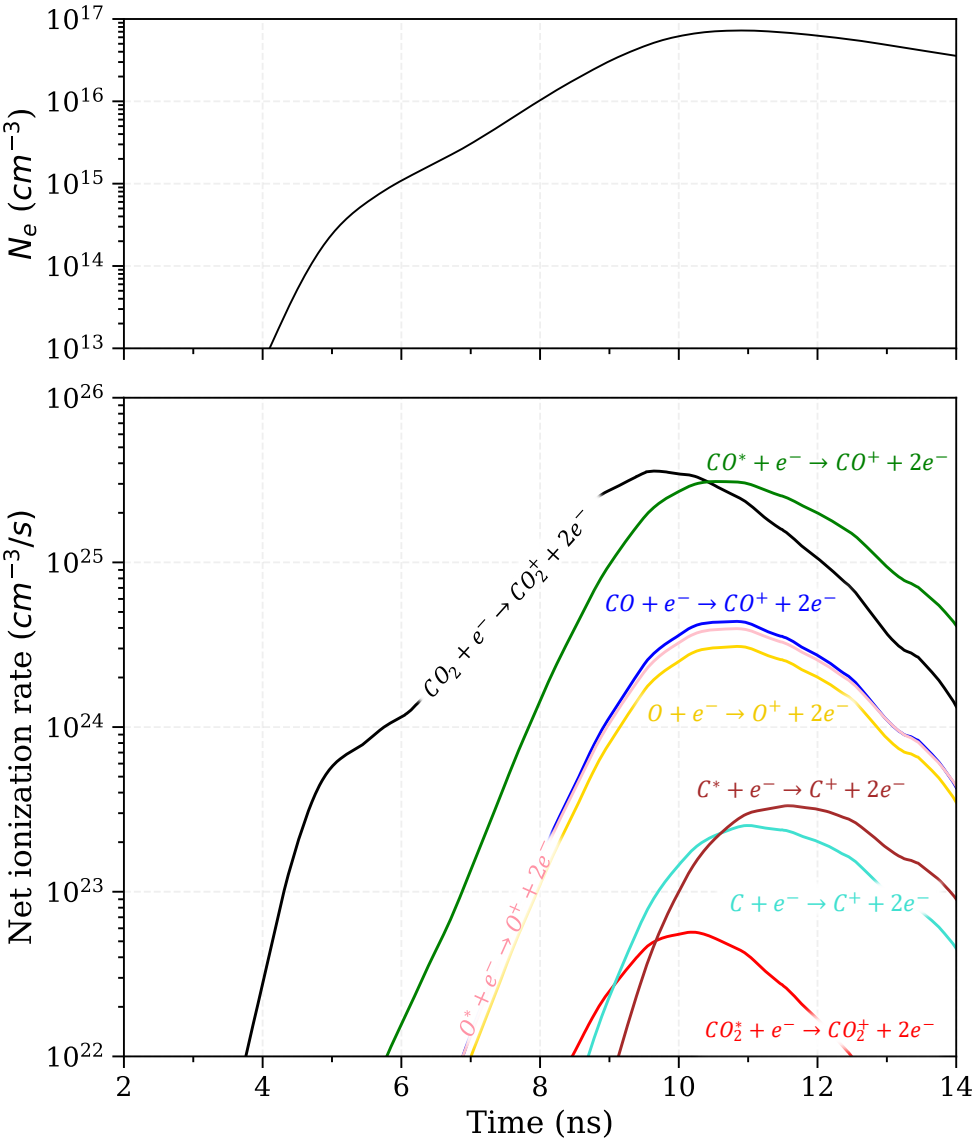

Figure 4-23. Electron density and net rate of the main ionization reactions, as a function of time, for $T_0 = 650\ K$.

The first two ionization stages are common to both NTS and TS. The third stage is unique to the TS. In the TS regime, the dissociative recombination of CO^+ and the electron-impact dissociation of CO produce C and O. In turn, C and C* are ionized to C^+. At the same time, O and O* ionization increases. Together, the ionization of C and C* accounts for 34% of the total electron production (in the reference TS simulation). The ionization of O and O* accounts for 35% of the total electron production. In the non-thermal spark, the excited states C* and O* do not play a significant role.

In the thermal spark, we note that the transition from $n_{e,0} \sim 10^{10}$ to 10^{18} cm^{-3} occurs in about 2 ns, i.e. faster than the pressure relaxation. Thus, the isochoric assumption (section 4.4.3) is justified for simulating this transition.

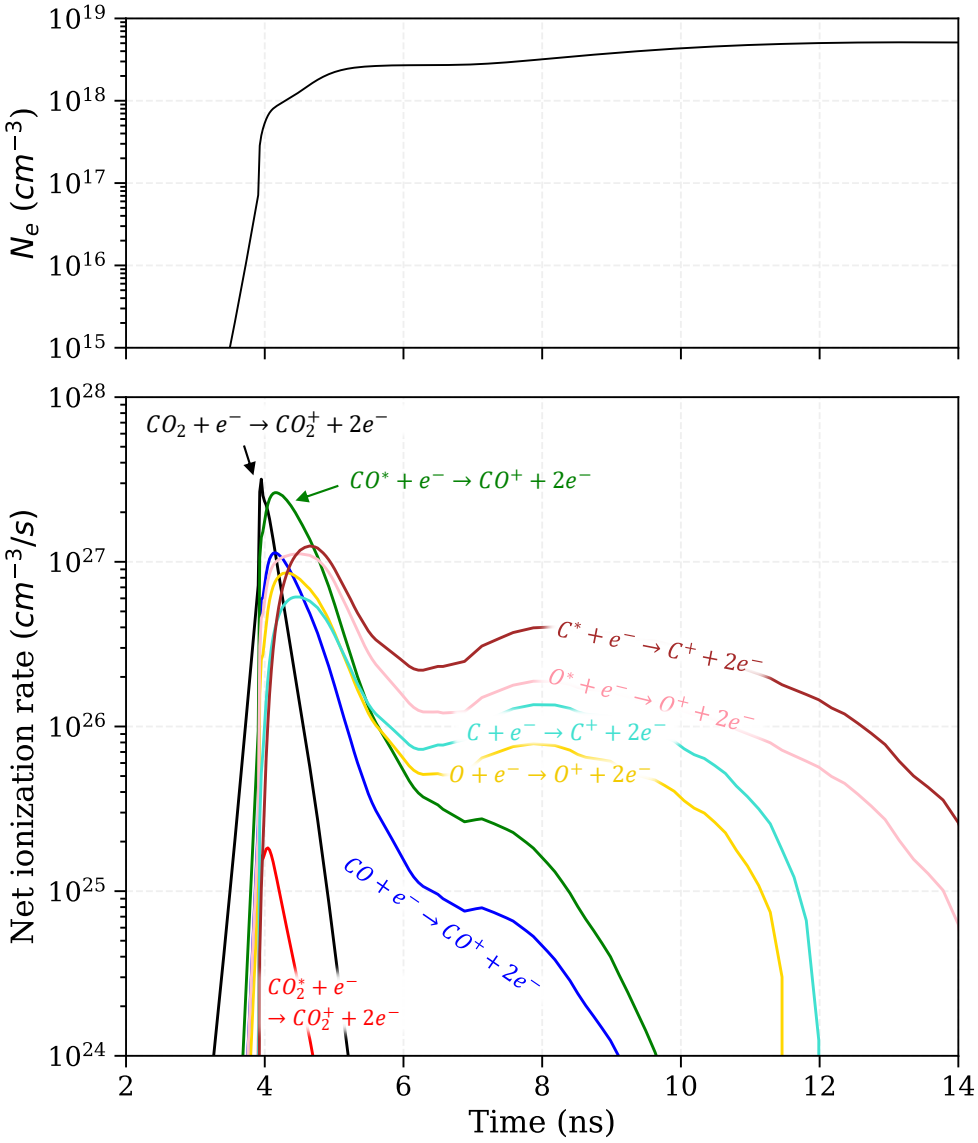

Figure 4-24. Electron density and net rate of the main ionization reactions, as a function of time, for $T_0 = 1100\ K$.

To confirm the importance of the excited electronic states of C and O in the thermal spark formation, we simulate the TS reference case ($T_0 = 1100\ K$) using two simplified versions of the kinetic scheme. The first has no excited electronic states at all, and the second has only the excited electronic states of molecules, namely CO_2*, O_2*, and CO*. In Figure 4-25, we report the electron density obtained with each model, compared to the complete model. Without the excited electronic states, n_e stays below 10^{18} cm^{-3}. Adding the excited electronic states of molecules brings n_e over 10^{18} cm^{-3}. Finally, adding the excited electronic states of atomic species brings n_e up to $5{\cdot}10^{18}$ cm^{-3}. These simulations underscore the key role of the

electronic states of atoms and molecule in the thermal spark formation in CO_2, as was also found to be the case for NRP discharges in air (Minesi et al. 2021).

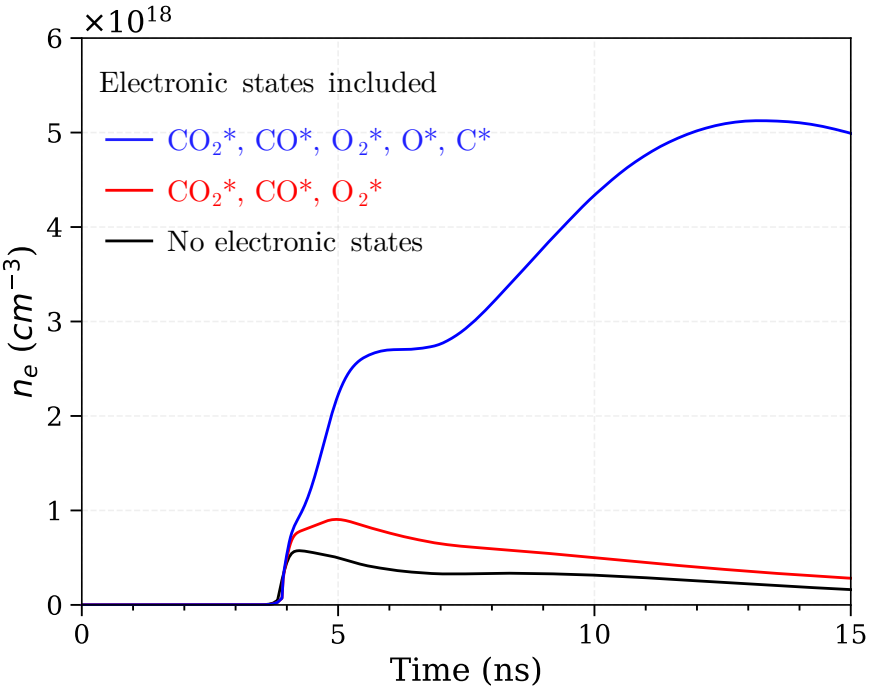

Figure 4-25. Temporal evolution of the electron density predicted by the model without any electronic states (black), with molecular excited electronic states (red), with molecular and atomic excited electronic states (blue). Simulation at $T_0 = 1100\ K$. The excitation of electronic states strongly enhances ionization.

4.6.2 Thermalization mechanism in the thermal and non-thermal sparks

For a thermal spark in air, Minesi *et al.* (Minesi 2020; Minesi et al. 2021) showed that electron-ion elastic collisions lead to the thermalization of the electrons and heavy species, i.e. to $T_g = T_e$. In Chapter 3, based on our OES measurements of n_e and T_e, we estimated the electron-ion thermalization time to be a few ns. As it is much shorter than the characteristic time of temperature variation, electron-ion collisions lead to the thermalization of the plasma. Here, we assess this assertion and the thermalization mechanism in thermal and non-thermal sparks.

In Figure 4-26, we report the temporal evolution of the reduced electric field, T_e, and T_g, as well as the main heating processes in the nominal TS simulation. The figure shows that, at first, the speedy increase of T_g is mainly due to the following inelastic processes: CO_2* dissociation, as well as CO_2^+ and CO^+ dissociative recombination. In 1 ns, T_g jumps from 1,100 K to 10,000 K, which corresponds to a heating rate of about 10^{13} K/s. Then, T_g

increases from 10,000 K to 20,000 K in about 5 ns, which corresponds to $2 \cdot 10^{12}$ K/s, mainly due to electron-ion elastic collisions but also with a significant contribution of O* and C* quenching.

Thus, the electron-ion elastic collisions contribute to the gas thermalization in the thermal spark but they are not the only mechanism. Dissociative recombination of the molecular ions and quenching of the electronic states of atomic species are the other significant contributors.

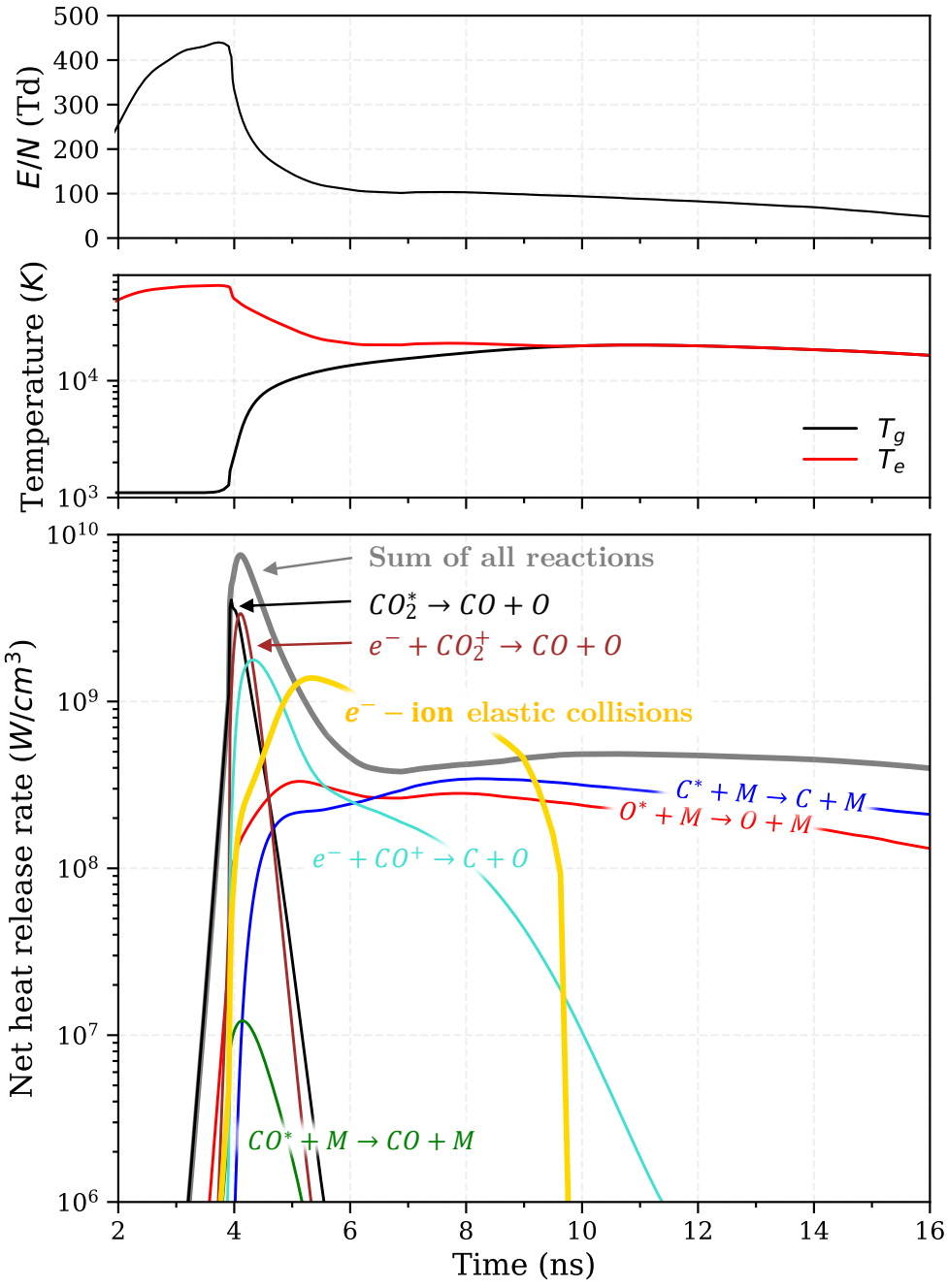

Figure 4-26. Gas and electron temperature, and main heating processes as a function of time, in a thermal spark. $T_0 = 1100\ K$.

Figure 4-27 shows the main heating mechanisms in a non-thermal spark. CO_2* predissociation, quenching of O and CO electronic states, and CO_2^+ dissociative recombination are the main contributors. Electron-heavy elastic collisions account for less than 1% of the heating. The gas temperature increases to 2000 K at a rate of about $3{\cdot}10^{11}$ K/s. For comparison, a heating rate of $5{\cdot}10^{10}$ K/s was measured in non-thermal sparks in air (Rusterholtz et al. 2013).

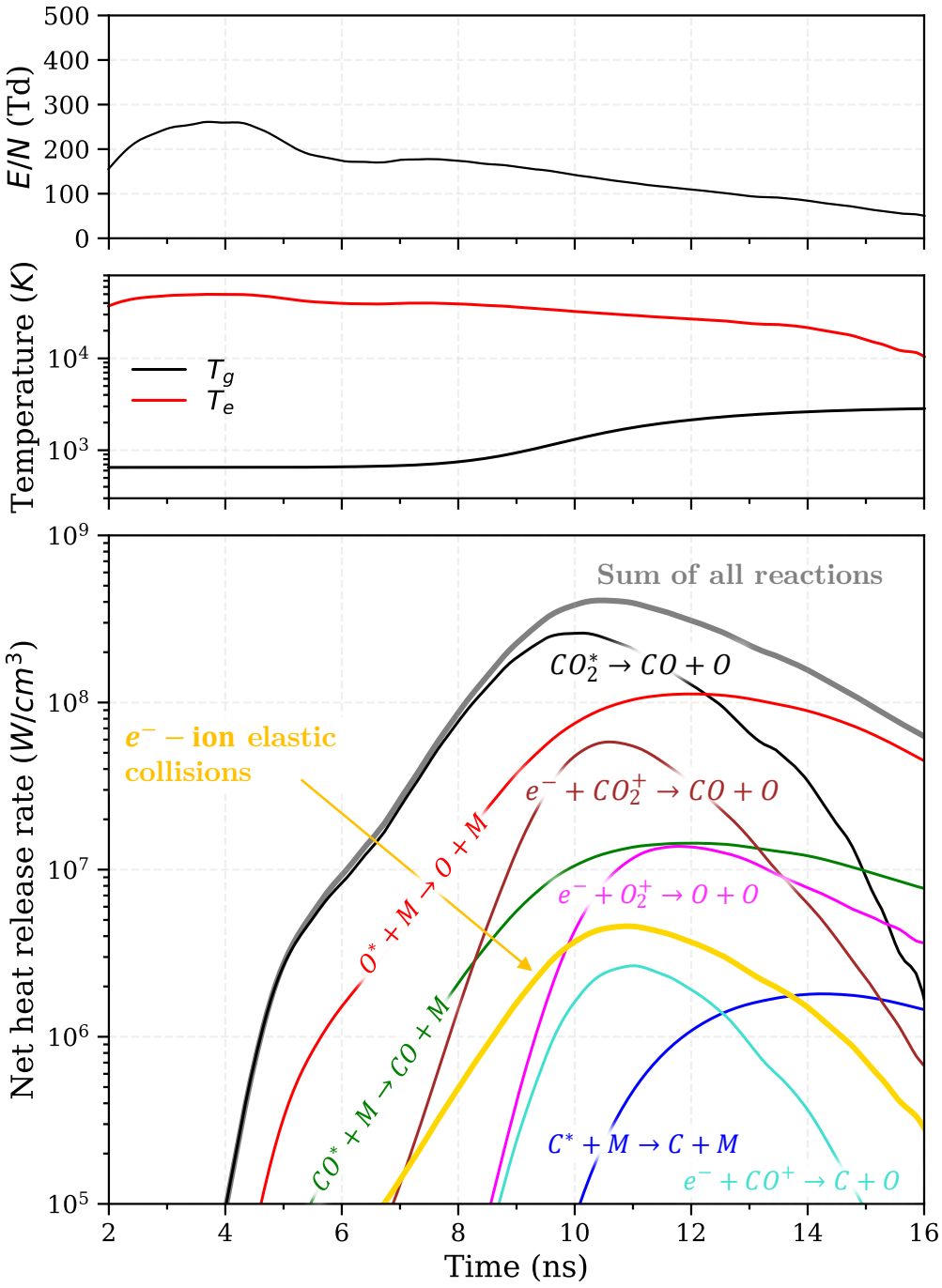

Figure 4-27. Gas and electron temperatures, and main heating processes as a function of time, in the non-thermal spark. $T_0 = 650\ K$.

4.6.3 LTE or not LTE?

We compute the gas composition at chemical equilibrium at the pressure and temperature obtained in the TS simulation ($T_0 = 1100$ K). In Figure 4-28, we report the simulated-over-LTE density ratios for the main species. After the transition (i.e. between 5 and 10 ns), the ratios are close to unity (within a factor of two), i.e the simulated densities are near their LTE values. This result supports the results of Chapter 3, showing that the thermal sparks reach near-LTE conditions.

In Figure 4-29, we show the same graph for the NTS simulation ($T_0 = 650$ K). As expected, the chemical composition is very far from the equilibrium.

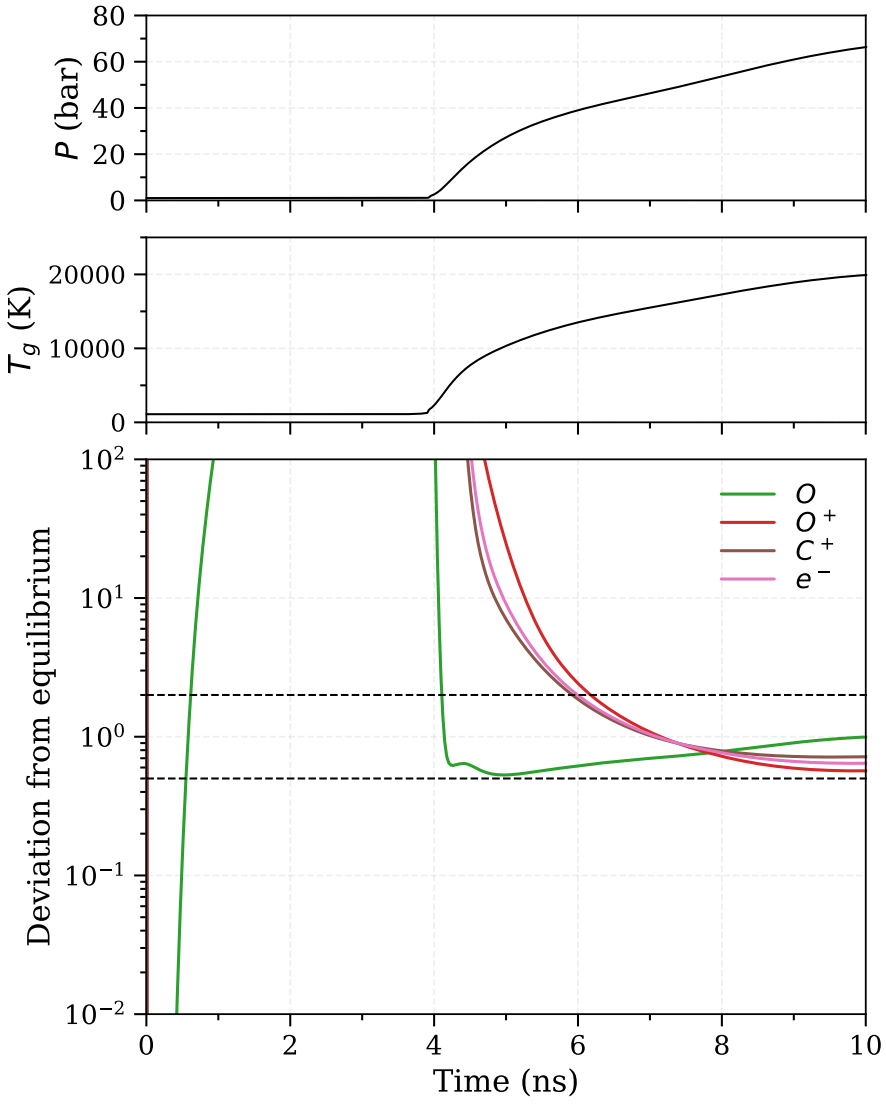

Figure 4-28. Deviation of the simulated densities from the LTE, as a function of time, for the TS conditions. $T_0 = 1100$ K.

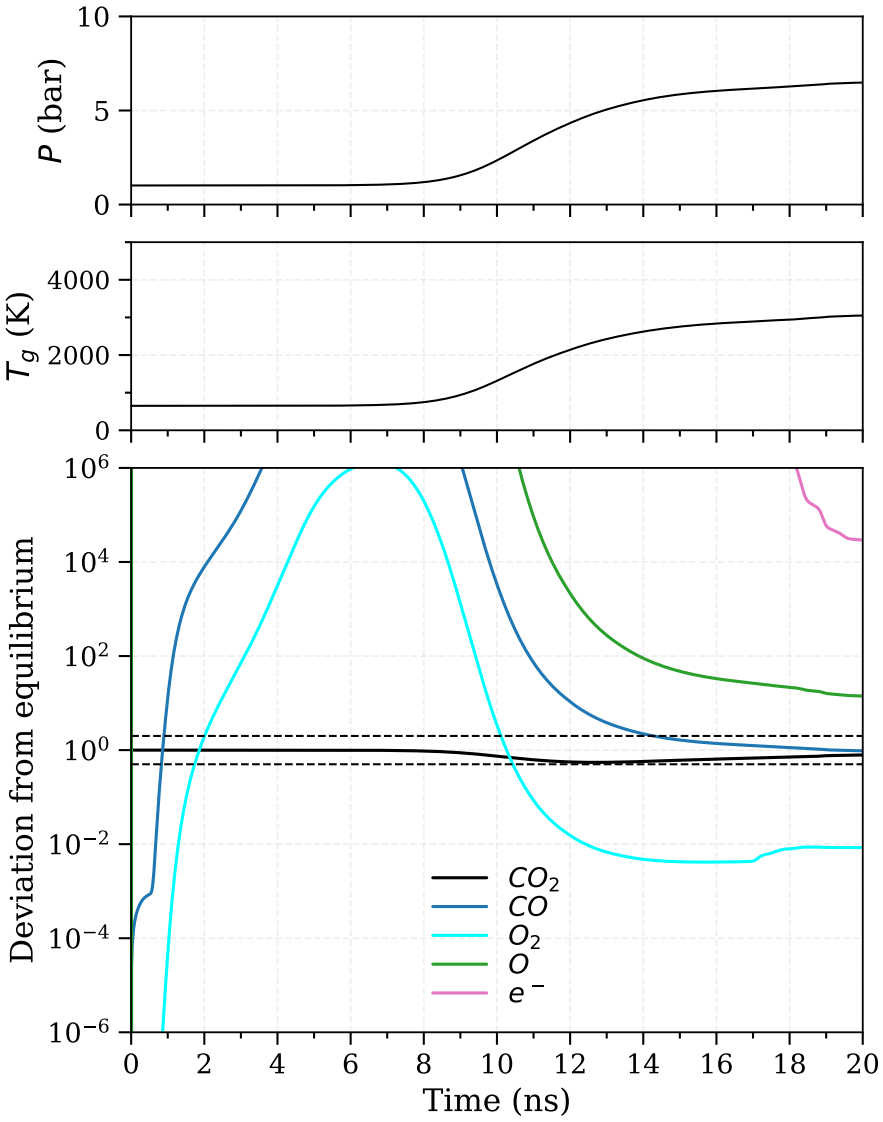

Figure 4-29. Departure of the simulated densities from LTE, as a function of time, for the NTS conditions. $T_0 = 650$ K.

4.7 CO production mechanism

4.7.1 Non-thermal spark

Figure 4-30 shows the cumulated density of CO produced in the NTS for $T_0 = 650$ K. The colors indicate different production pathways. Like the models of (Heijkers et al. 2019; Pannier 2019), for the NTS our model predicts that most CO production occurs through the predissociation of CO_2 electronic states during the 20 ns pulse (for $T_0 = 650$ K, the conversion to CO reaches 36% at the end of the pulse). As mentioned in Section 4.5.3, the energy efficiency of CO production at the end of the 20 ns simulations of the NTS is 18 -

21%, precisely the EE range calculated in Chapter 2 for the electronic dissociation pathway at 200 – 300 Td (Figure 2-12).

At t = 20 ns, the gas temperature is high (about 3,000 K for the case T_0 = 650 K) and a high density of atomic species is produced ($n_O(20\ ns) = 4 \cdot 10^{18}\ cm^{-3}$, $n_C(20\ ns) = 4 \cdot 10^{16}\ cm^{-3}$). Thus, additional CO is expected to be produced with this level of heat and atomic species. Pannier calculated that, over the first µs following the pulse, approximately 33% additional CO is produced by thermal dissociation, leading to a total EE of 23%. In our experiments, we showed that most CO is produced by the NTS, and we measured an overall EE of approximately 25-35%. Since it is higher than the 18-21% EE at t = 20 ns predicted by our model, this confirms that a significant amount of CO is produced after the pulse.

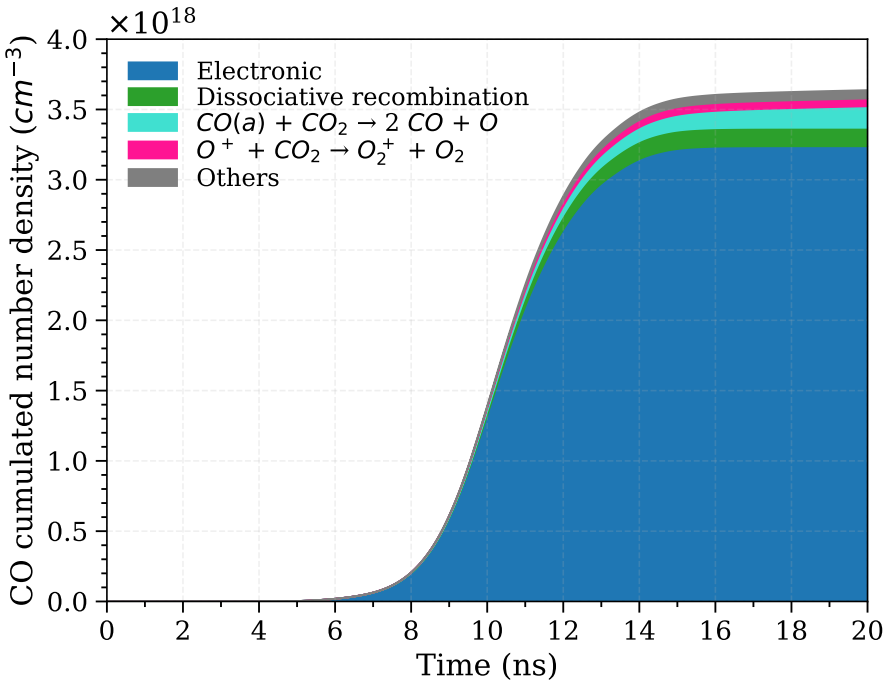

Figure 4-30. Cumulated CO number density produced by the main channels, in non-thermal spark conditions (T_0 = 650 K, P_0 = 1 atm).

4.7.2 Thermal spark

For the thermal spark, we showed in Section 4.3.6 that the characteristic times of CO production and of mass and energy transfer are comparable. To simulate CO production in this regime, these transfers must be accounted for. This is the objective of this section. We will use a simplified version of the kinetic model presented in Section 4.4 (Model 4), and a simple physical model for the post-discharge. We will refer to the model of this section as Model 5.

4.7.2.1 Modeling the CO production induced by a thermal spark

Main assumptions

We use a simplified 0D kinetic model to understand the filament-induced CO production. The model is described in the discharge diagram shown in Figure 4-14. On this diagram, t' = 0 ns corresponds to the end of the voltage pulse, i.e. approximately 20 ns *after* the beginning of the pulse. Thus, at t' = 0 ns, the thermal filament is formed and begins to exchange energy and particles with the surrounding gas, which 1 µs – 1 ms after will result in CO production.

Once the filament has sufficiently cooled down, we expect atomic species to recombine to CO. But more importantly, mixing the atomic species produced in the filament with the surrounding gas can also produce CO, and thus recycle the excess energy in the filament. The mixing rate (or dilution rate) of the filament species with the surrounding gas is crucial to achieving high energy efficiency (EE). Species diffusion and convection around the discharge govern this mixing rate. Here, the first assumption is to model this mixing rate by a constant input of CO_2 at a given temperature T_s (the "s" letter stands for "surrounding"). We consider the system formed by the thermal filament (initially at T_f) into which a constant flow of CO_2 at T_s enters.

The second major assumption is that this system is considered adiabatic. The energy from the hot filament is transferred to the cold regions. Concretely, this results in a lower T_f and higher T_s. Only after the heat is transferred to the reactor walls, it is considered a loss. In our model, there are no energy losses at the wall. We account for the energy fluxes between the hot and cold regions of the plasma by varying the T_f and T_s parameters.

Although this model is a highly simplified representation of the actual species and energy exchange process, it is useful to gain a qualitative understanding of the phenomena at play, and insight into the optimization levers.

Physical model description

We consider a thermal filament at an initial gas temperature T_f in the range 5000-30,000 K. The upper limit of this range (30,000 K) corresponds to our temperature measurement in the filament (cf Chapter 3). The lower limit (5000 K) corresponds to the temperature expected at about 200-300 ns, based on an extrapolation of the temperature measurements of Chapter 3 (Figure 3-25). We do not consider T_f values lower than this limit because we already simulated the recombination of CO_2 below 5000 K in Chapter 2.

We assume that the initial pressure in the filament is $P_f = 50\ bar$, and the filament volume is $V_f = 2 \cdot 10^{-11}\ m^3$. These pressure and volume correspond to a type-f pulse measured at 20 ns. The filament composition is obtained by assuming the LTE.

We showed in Section 4.2.2 that the pressure in the thermal spark decreases with a characteristic time of about 10 ns (see also Figure 4-4). Thus, we approximate the evolution of the filament pressure as a decreasing exponential with a characteristic time $\tau_P = 10$ ns:

$$P(t) = P_f e^{-t/\tau_P} \qquad \text{Eq. 4-9}$$

where the initial pressure in the filament is $P_f = 50\ bar$. Note that varying τ_P between 10 and 100 ns has a negligible impact on the calculation results.

After 5 τ_P, i.e. when the pressure in the filament has relaxed to 1 atm, we assume that a constant flow of CO_2 at T_s enters the system and is instantly mixed. This input CO_2 flow (q_{CO2}) cools the plasma, and the reactive species of the filament dissociate the fresh CO_2. To quantify this flow, we define the dilution frequency parameter as:

$$\nu_{dilu} = \frac{q_{CO2}}{m_f} \qquad \text{Eq. 4-10}$$

where m_f is the initial mass of the filament, and q_{CO2} is the input mass flow rate of CO_2. We vary ν_{dilu} in the range $[10^3;\ 10^8]\ s^{-1}$, which correspond to characteristic dilution times τ_{dilu} of 10 ns to 1 ms. A dilution time of 10 ns corresponds to the situation just after breakdown when the gas expands rapidly and the very high temperature (~ 30,000 K) causes rapid species diffusion. After the shock attenuation, at lower temperature (~ 1000 K), the dilution time is approximately the diffusion time, i.e. about 10 µs (corresponding to $\nu_{dilu} \sim 10^5\ s^{-1}$)

The temperature profile (averaged from 0 to 30 µs) measured by Pannier (Pannier 2019) peaks at 2,300 K at $r = 0$ µm, and falls to 600 K at $r = 900$ µm. According to our kinetic model, the temperature in the faint region, just after the pulse, is about 3,000 K (see Figure 4-20). Thus, to assess the impact of these temperatures on CO production, we vary the temperature T_s of the diluting gas in the range 300-3000 K.

We summarize the main characteristics of the model in Table 4-4, and we sketch in Figure 4-31 the system considered in the simulations.

Kinetic model

For t > 50 ns, we simulate this system using a simplified version of Model 4 (presented in Section 4.4.2 and Appendix C). We remove all electronic states and thus, the excitation and quenching reactions. We consider the electron impact dissociation of CO_2 as a single step process. The cross-section of CO_2 dissociation is the sum of the cross-sections of CO_2

electronic excitation (equivalent to assuming an infinitely quick predissociation rate). We assume that the plasma stays in thermal equilibrium: $T_e = T_g$. We use the same set of cross-sections presented in Section 4.4.2, but we integrate them over a Maxwellian EEDF to get rate constants in Arrhenius form.

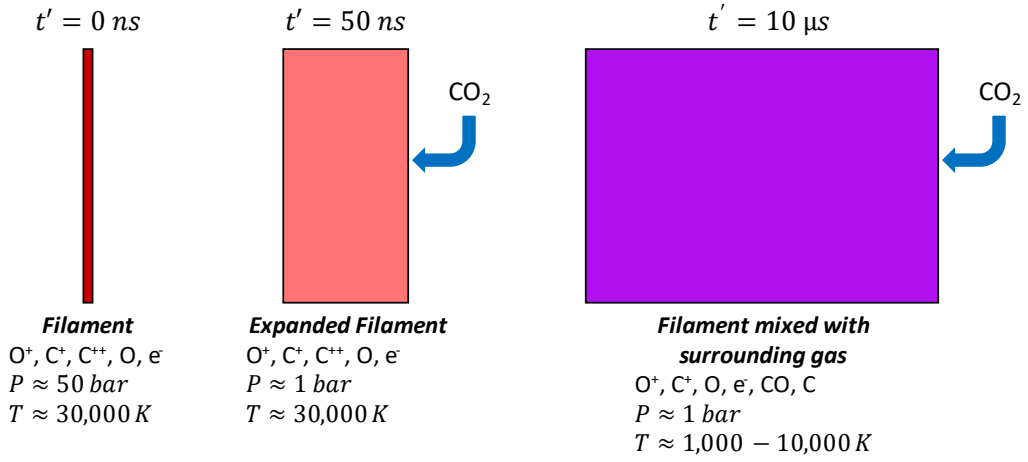

Figure 4-31. Diagram of the system considered in the simulation and its temporal evolution.

Implementation in CANTERA

The calculations are performed with CANTERA (Goodwin et al. 2017). We use the *IdealGasConstantPressureReactor* object for the plasma (P,T). Initially, $P = P_f$, $T = T_f$, and $V = V_f$. In the pressure relaxation phase, we impose the exponential decay of the pressure. The reactor object is connected to a *Reservoir* (containing CO_2 at T_s) via a *MassFlowController*. When, $(P - P_{atm})/P_{atm} < 1\%$, CO_2 at T_s enters the system at the mass flow rate q_{CO_2}, the volume of the system increases, the temperature T decreases, and CO starts to form.

Table 4-4. Parameters of the model of thermal filament recombination.

P	• Initial value at 50 bar • Exponential relaxation to 1 atm with $\tau_P = 10$ ns			
Initial composition	LTE composition at P, T_s			
Initial volume	$2 \cdot 10^{-11}$ m^3			
Thermal model	$T_e = T_v = T_g$			
Kinetic model	Reactions of Appendix C, without the state-specific reactions. The rates of e-impact reactions are obtained by assuming Maxwellian distributions at T_g=T_e			
Variable parameter	**Min value**	**Max value**	**Number of points**	**Scale**
ν_{dilu} (s^{-1})	10^3	10^8	30	log
T_f (K)	5,000	30,000	6	linear
T_s (K)	300	3000	10	linear

Outputs

The main outputs of the model are the conversion degree (to CO) and the energy efficiency (of CO production).

The conversion degree is the ratio of the CO amount in the system over the total CO_2 input: $N_{CO}/N_{CO_2}^{in}$. The total CO_2 input is the sum of the initial CO_2 quantity converted to O^+, C^+, O, C, and e^- by the discharge, and the cumulated CO_2 quantity that entered the system after the pressure relaxation: $N_{CO_2}^{in} = N_{CO_2}^0 + q_{CO2} \cdot t$ (in this equation, $N_{CO_2}^{in}$ is the number of molecules, and q_{CO2} is the number of molecules entering the system per unit of time).

The energy efficiency is defined as in Chapter 2: $\eta = \Delta_r H \cdot N_{CO}/E_{cost}$, where $\Delta_r H = 2.93\ eV$, N_{CO} is the number of CO molecules produced, and E_{cost} is the energy cost of the process. Here, the energy cost is the sum of (i) the enthalpy of the filament ($m_f \cdot (h_f - h_0)$) and (ii) the enthalpy of the diluting CO_2 ($m_f \cdot \nu_{dilu} t \cdot (h_s - h_0)$). We obtain:

$$E_{cost} = m_f \cdot \left(h_f - h_0 + \nu_{dilu} t \cdot (h_s - h_0)\right) \qquad \text{Eq. 4-11}$$

where h_f and h_s are the specific enthalpies of the filament and of the surrounding gas.

4.7.2.2 Study of some illustrative cases

Illustrative case of $\nu_{dilu} = 10^6\ s^{-1}$

We first consider a case representative of the conditions measured in the TS of Chapter 3: $T_f = 30{,}000\ K$ and $T_s = 300\ K$. In a TS, the characteristic time of species diffusion calculated immediately after the pulse is 1 – 10 µs (Sec. 4.3), which by definition means that, during this time, the species produced in the discharge are transported over a distance

of the order of the filament radius. Thus, the species produced in the filament modeled as a cylinder of radius r, are comprised in a cylinder of radius $2r$ after 1-10 µs, i.e. in a 4 times bigger volume. Assuming that the number density of this volume is constant during the diffusion – which is true from $t = 30$ ns, since the pressure relaxation time is about 10 ns – we obtain a dilution α_{dilu} of the order of 4 during 1-10 µs. The dilution is related to ν_{dilu} by $\alpha_{dilu} = \nu_{dilu} \cdot t + 1$. If $\alpha_{dilu}(1\ \mu s) = 4$, we obtain $\nu_{dilu} = 3 \cdot 10^6$ s^{-1}. Thus, diffusion characteristic times of the order of 1-10 µs are equivalent to dilution rates of $3{\cdot}10^5$-$3{\cdot}10^6$ s^{-1}. We choose $\nu_{dilu} = 10^6$ s^{-1} as an estimation of the dilution rate induced by the TS.

Figure 4-32 shows the temporal evolution of the mass of the main species, the temperature, pressure, conversion degree, and CO production energy efficiency obtained in the simulation. The pressure relaxes to 1 atm in about 30 ns. After 100 ns, the temperature decreases as fresh CO_2 enters the system. Atomic species (O and C) are produced around 1 µs, followed by molecular species (CO after 3 µs and O_2 after 10 µs).

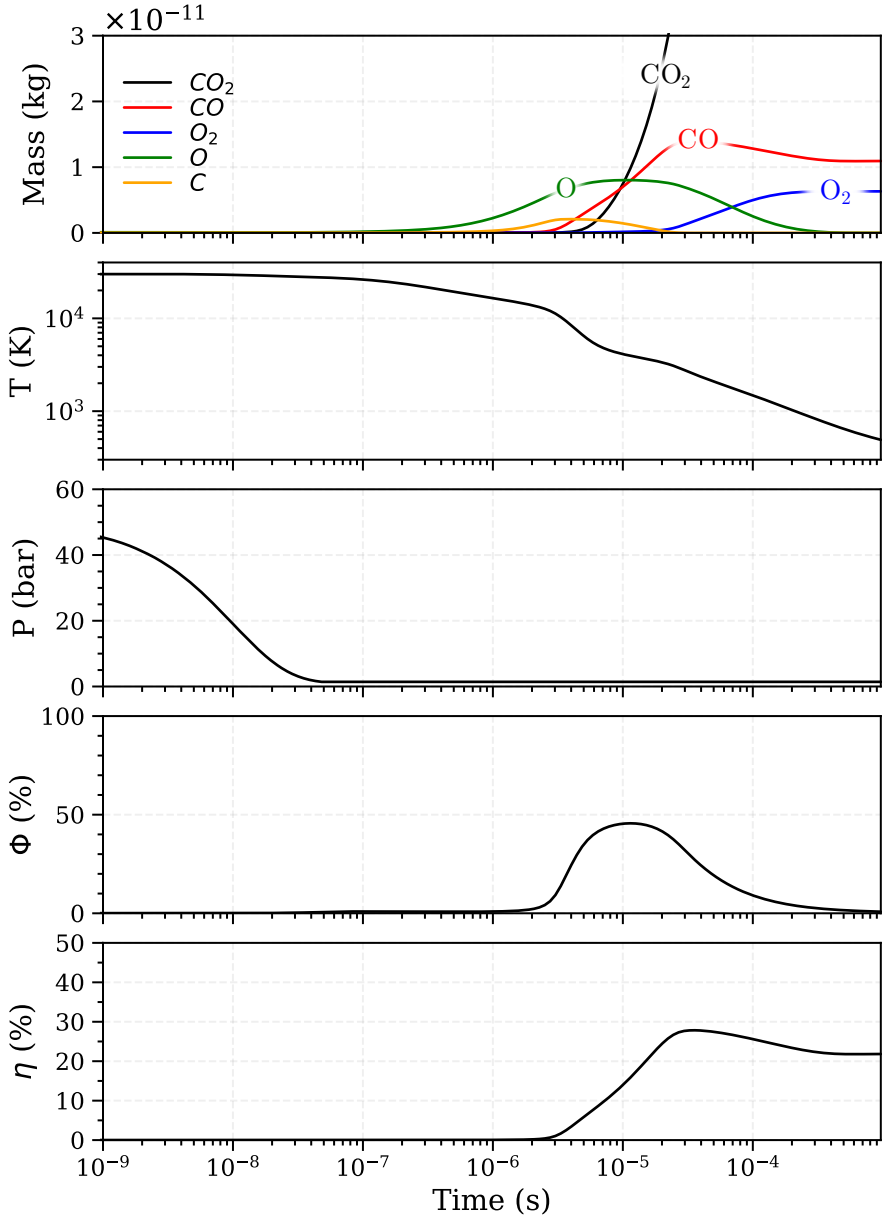

Figure 4-32. Temporal evolution of the mass of main species, temperature (T), pressure (P), conversion degree into CO (Φ), and energy efficiency (η), for the case $T_s = 30,000\ K$, $T_s = 300\ K$, $\nu_{dilu} = 10^6\ s^{-1}$.

Figure 4-33 zooms on the species density temporal evolution. Initially, the LTE plasma at 30,000 K and 50 bar is composed of e^-, O^+, and C^+, and a little C^{++} and O. In the first 1 µs, the decreasing temperature favors the increase of O, C^+, and C. After 1 µs, the temperature falls below 15,000 K, making O^+ and C^+ recombine. O and C become the main species during a few µs. After 10 µs, the molecular species are dominant.

The CO formed in the dilution process makes the conversion degree (Φ) increase to 44% around 10 µs. At 30 µs, the CO amount peaks at about $1.4{\cdot}10^{-11}$ kg, and the EE peaks at 27%. Then, the temperature decreases to 1,000 K, causing CO to recombine with the

remaining O atoms. Finally, after 400 µs, the temperature falls below 1000 K, so the CO amount is frozen at 10^{-11} kg and the EE at 21%.

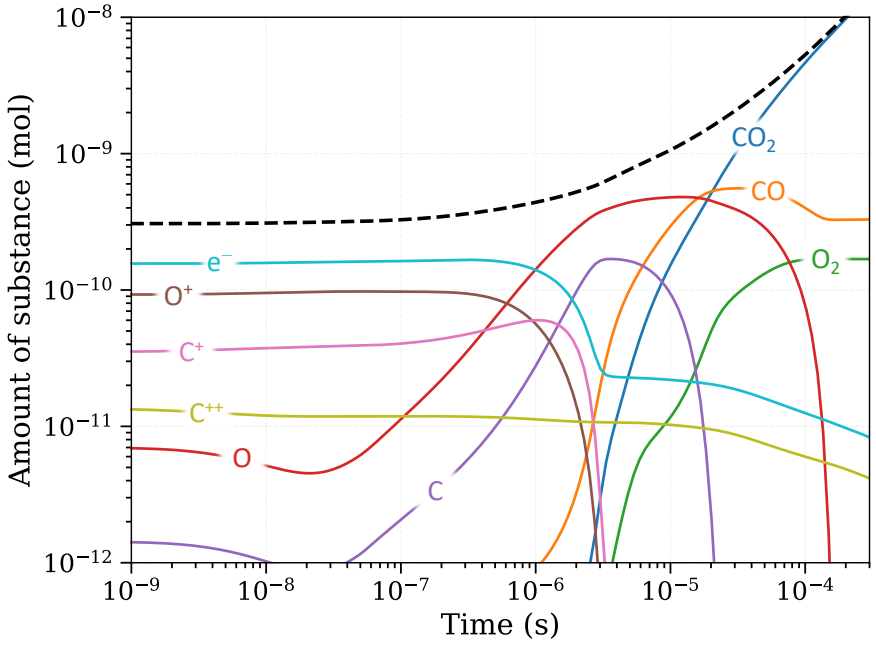

Figure 4-33. Temporal evolution of the species (number of moles) in the case $T_s = 30,000\ K$, $T_s = 300\ K$, $\nu_{dilu} = 10^6\ s^{-1}$. The dotted line is the total number of moles.

Effect of the dilution rate

Now, we investigate the effect of the dilution frequency on the EE. We report in Figure 4-34 the simulation results obtained for $\nu_{dilu} = 10^4\ s^{-1}$. We find that (i) a conversion degree (to CO) of 100% is reached at about 1 ms, and a EE of 46% at 2 ms. However, (ii) by the time the composition is frozen, the EE drops to 30%. This last point (ii) is easy to understand: in our model, the cooling rate is proportional to the dilution rate. Thus, at lower dilution rate, the mixture spends more time in the "CO recombination zone", i.e. $1{,}000 < T < 3{,}000\ K$. This leads to more CO losses. This is shown in Figure 4-35, superimposing the temperature and main species amount obtained at $\nu_{dilu} = 10^4, 10^6, 10^7\ s^{-1}$. The red area indicates the temperature conditions of CO recombination. At $\nu_{dilu} = 10^6\ s^{-1}$, the time spent in this area is about 200 µs, whereas it is about 10 ms at $\nu_{dilu} = 10^4\ s^{-1}$. The lost CO amount is about $0.3 \cdot 10^{-11}\ kg$ and $0.9 \cdot 10^{-11}\ kg$, respectively.

The first point (i) suggests that, the lower the dilution rate, the more CO is produced (before its recombination). To understand this, we plot in Figure 4-36 the cumulated CO density produced from the different channels at each dilution rate. At $\nu_{dilu} = 10^4\ s^{-1}$, the major CO production channels are CO_2 thermal dissociation (N1) ($CO_2 + M \rightarrow CO + O + M$), O-$CO_2$ association (N2) ($CO_2 + O \rightarrow CO + O_2$), and C^+-CO_2 dissociative charge exchange (I3) ($C^+ + CO_2 \rightarrow CO + CO^+$). At $\nu_{dilu} = 10^6\ s^{-1}$, the C-$O_2$ association reaction (N4) (C

+ $O_2 \rightarrow CO + O$) is also significant. At very high dilution rate ($\nu_{dilu} = 10^7\ s^{-1}$), the neutral exchange reactions (N2) ($CO_2 + O \rightarrow CO + O_2$) and (N4) ($C + O_2 \rightarrow CO + O$) do not contribute anymore. At thermodynamic equilibrium, CO production is favored for temperatures between 3000 and 7000 K. At high dilution rates, the plasma does not spend enough time in this favorable temperature region (about 1 µs at $\nu_{dilu} = 10^7\ s^{-1}$ and 20 µs at $\nu_{dilu} = 10^6\ s^{-1}$) to enable reactions (N2) and (N4), which results in a limited CO production.

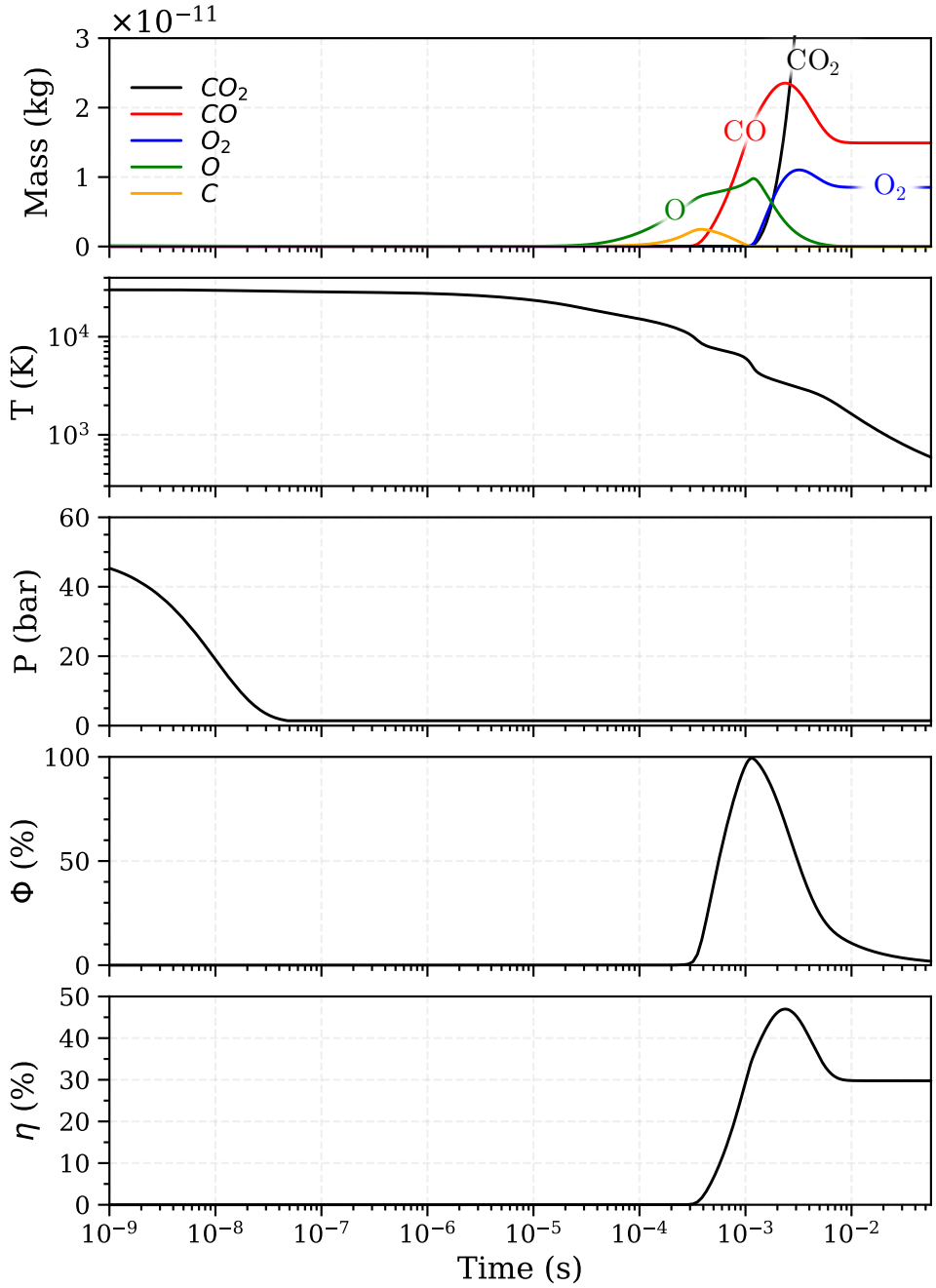

Figure 4-34. Temporal evolution of the mass of main species, temperature (T), pressure (P), conversion degree into CO (Φ), and energy efficiency (η), for the case $T_s = 30,000\ K$, $T_s = 300\ K$, $\nu_{dilu} = 10^4\ s^{-1}$

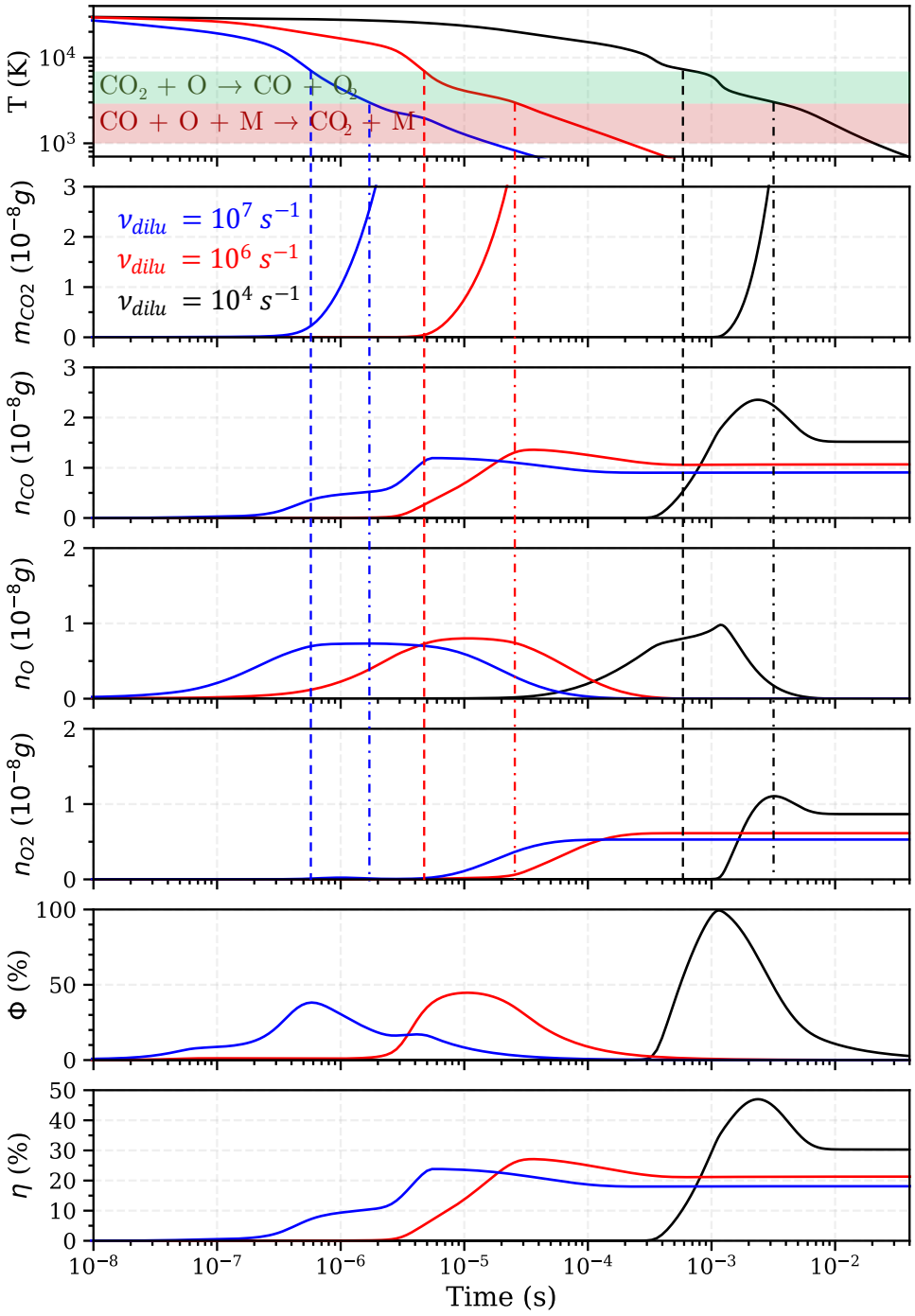

Figure 4-35. Temporal evolution of the main species (number of moles), temperature (T), pressure (P), conversion degree (Φ), and energy efficiency (η), for the case $T_s = 30,000\ K$, $T_s = 300\ K$, at $\nu_{dilu} = 10^4, 10^6, 10^7\ s^{-1}$. The green area represents the favorable temperature conditions for O-CO_2 association, and the red area for CO-O recombination. The vertical dashed lines indicate the time spent in these areas.

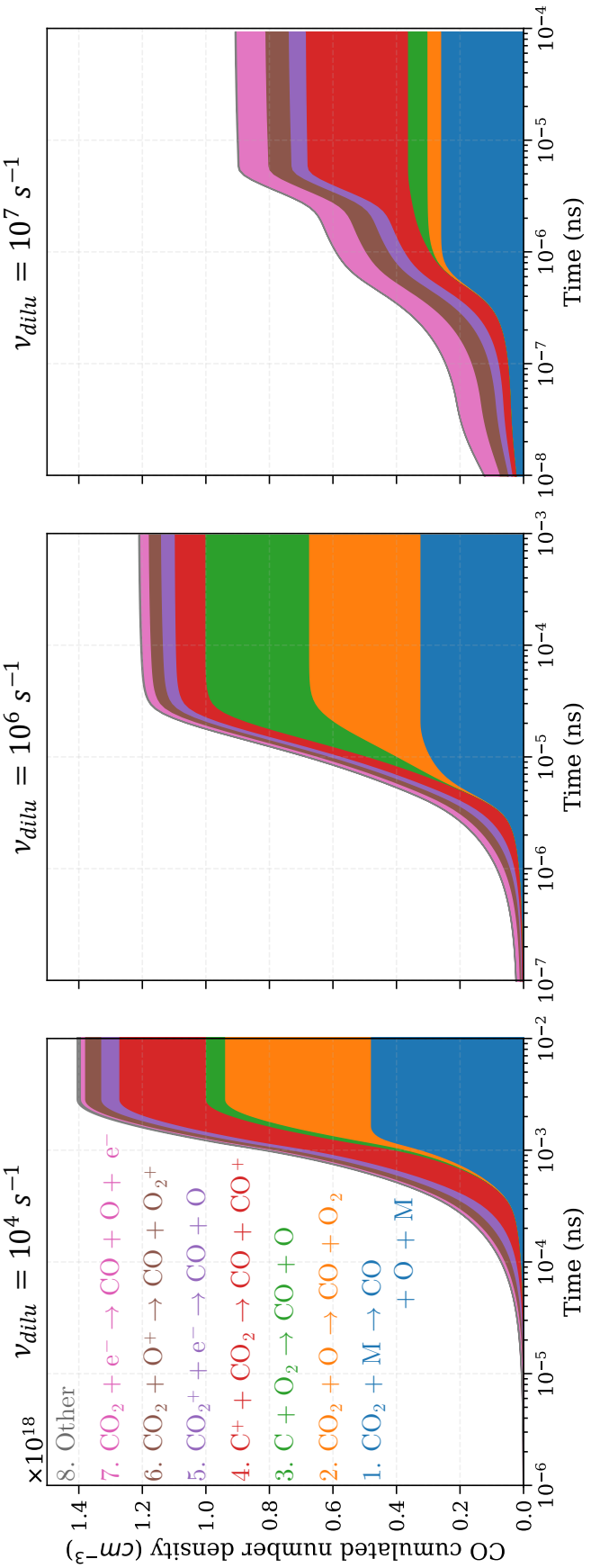

Figure 4-36. Cumulated CO number density produced via the main channels at $\nu_{dilu} = 10^4, 10^6, 10^7\ s^{-1}$.

4.7.2.3 Energy efficiency as a function of model parameters

The analysis of some simulation examples in the previous section illustrates how the dilution rate impacts the temperature, the amount of CO_2 present in the mixture, and thus the CO production mechanism and overall EE. In this section, we present a systematic evaluation of the EE as a function of the dilution rate, filament temperature, and surroundings temperature.

Impact of the dilution rate

We vary the dilution rate in the range $[10^3;\ 10^8]\ s^{-1}$ while the parameters T_f and T_s are fixed at 30,000 K and 300 K, respectively. Figure 4-37 shows the maximal and final EE obtained. The maximal EE is the peak of EE obtained during the simulation. It is relevant to report the maximal EE because, in real conditions, some cooling processes could be implemented (other than dilution) to accelerate the cooling and achieve absolute quenching (AQ is defined as a sufficiently fast quenching of the products to prevent CO recombination to CO_2). Examples of such cooling processes include cooling the reactor wall, expanding the gas, or spraying liquid water. The final EE is the EE achieved when the mixture is frozen (i.e. when the gas temperature decreases below 700 K).

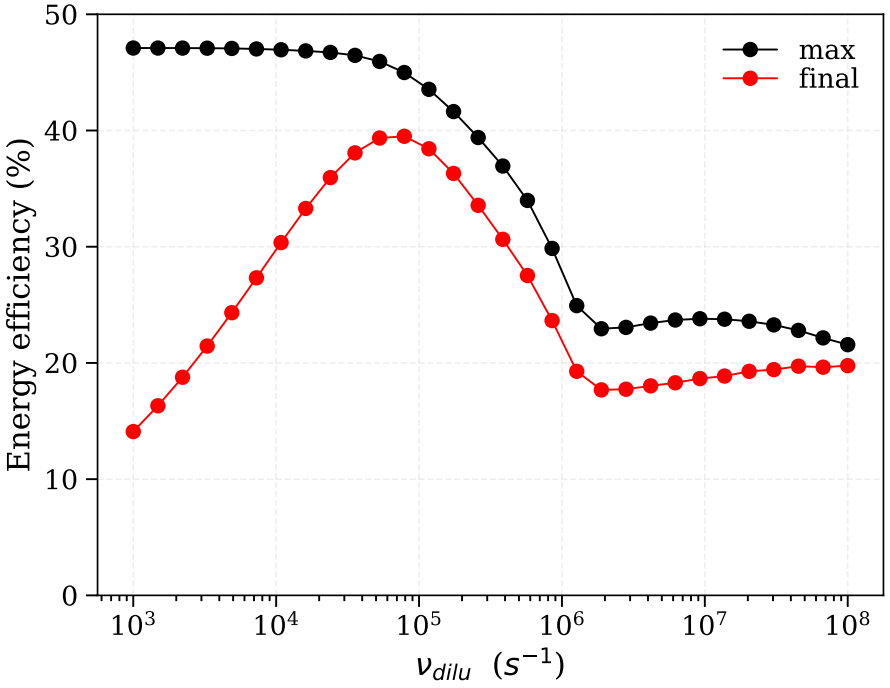

Figure 4-37. Energy efficiency of the thermal-spark-induced CO production as a function of the dilution rate, at T_f = 30,000 K and T_s = 300 K. The black symbols correspond to the maximal EE that could be obtained by using absolute quenching, and the red symbols to the EE obtained at the end of the process (i.e. when the kinetics are frozen).

The maximal-EE is maximal at low dilution rates: it reaches 46% below $\nu_{dilu} < 3 \cdot 10^4\ s^{-1}$ (which is slightly below the EE thermodynamic limit, as expected from Chapter 2). As explained in Section 4.7.2.2, at higher ν_{dilu} the cooling is too fast for CO production, i.e., the mixture does not spend enough time in the favorable temperature-composition conditions to produce CO.

However, if we now consider the final EE, at low ν_{dilu} a significant amount of CO is lost in recombination to CO_2. This was already shown and explained in Section 4.7.2.2: the gas does not cool fast enough to prevent recombination. At $\nu_{dilu} > 10^5\ s^{-1}$, the maximal and final EE are close to each other: the cooling is now sufficiently fast to prevent significant recombination of CO. Therefore, the final EE is maximal at $\nu_{dilu} = 10^5\ s^{-1}$ and an EE of 40% is reached.

Impact of T_f and T_s

We vary the initial temperature of the filament T_f and the temperature of the surrounding gas T_s. First, in Figure 4-38, we keep $T_s = 300\ K$ and plot the maximal and final EE for $T_f = 5000, 10000, 20000, 30000\ K$. Whatever the filament temperature, η_{max} reaches 46% when ν_{dilu} is low enough. Thus, the highest EE in a thermal spark should be obtained with a rather slow dilution rate ($\nu_{dilu} \leq 10^5\ s^{-1}$ for $T_f = 20{,}000 - 30{,}000\ K$ for instance), followed by fast quenching of the products.

If dilution is the predominant quenching mechanism (it is the only one in our model), it is relevant to consider η_{final}. Whatever the filament temperature, η_{final} reaches the same maximum, 40%, but at different dilution rates (Figure 4-38). Logically, the higher T_f, the higher the optimal dilution rate. We can compare the optimal dilution rates obtained in Figure 4-38 to the dilution rate expected in a thermal spark. According to the characteristic times calculation of Table 4-1, in the first tens of ns after the thermal spark formation, the advection time can be as low as 10 ns, and the diffusion 1 µs. This is equivalent to dilution rates of 10^8 – 10^6 s^{-1}, whereas it should be 10^4 - 10^5 s^{-1} for an initial filament temperature of 10,000 – 30,000 K. Nevertheless, as the pressure decreases, so is the intensity of the shock, and thus the advection slows down. The diffusion also slows down as the pressure decreases. It is then too early to conclude on the EE induced by the thermal spark. The hydrodynamics following the TS formation should be calculated to obtain the actual dilution rate and its temporal evolution. Here, we only indicate the dilution rate to target in order to achieve the best EE possible.

In Figure 4-39, we report calculations at fixed T_f = 30,000 K and T_s = 300, 600, 900 K. T_s has almost no impact on η_{max}: as long as the dilution rate is slower than $10^4\ s^{-1}$, the same upper limit of 46% is reached. However, T_s has a strong impact on η_{final}. Higher T_s implies a slower cooling, thus more CO recombination to CO_2, i.e. a lower EE.

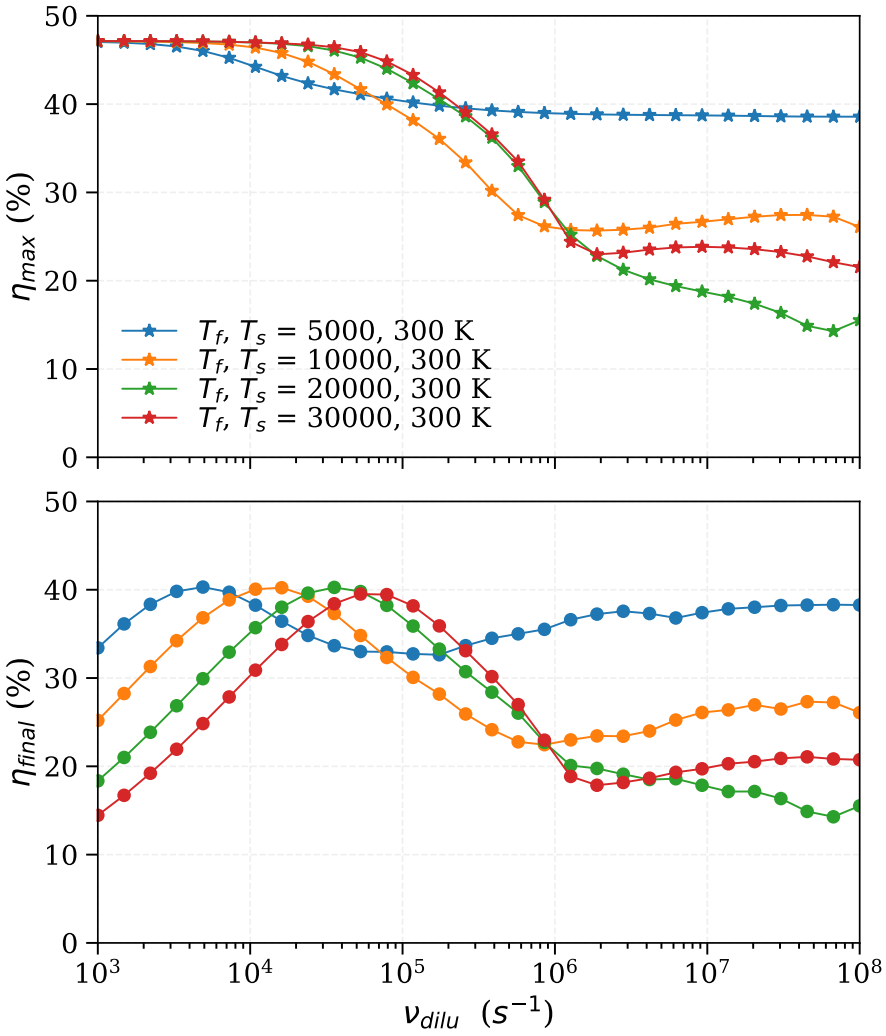

Figure 4-38. Energy efficiency of the thermal-spark-induced CO production as a function of the dilution rate at different initial temperatures of the filament (T_f). The maximal EE is plotted in the upper graph, and the final EE in the bottom graph. Whatever T_f, η_{max} reaches 46% when ν_{dilu} is low enough. As T_f increases, η_{final} can still reach 40% but the optimal ν_{dilu} increases as well.

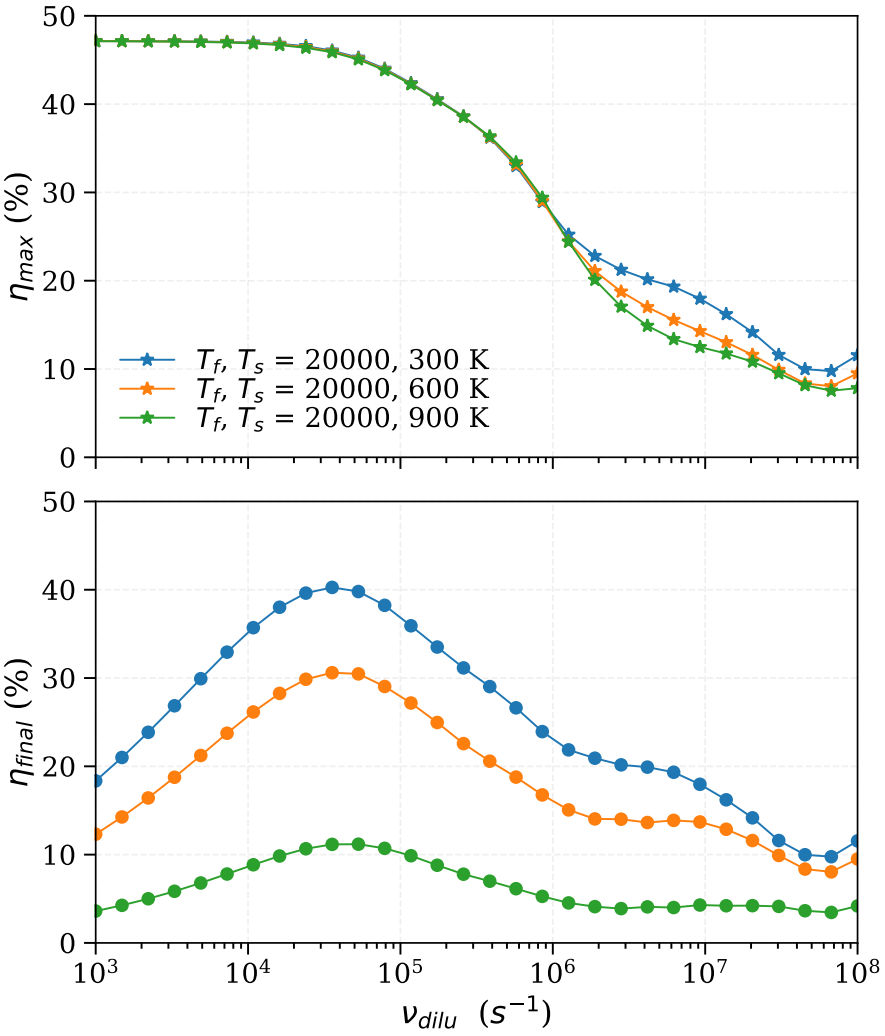

Figure 4-39. Energy efficiency of the thermal-spark-induced CO production as a function of the dilution rate, at different temperatures of the surrounding gas (T_s). The maximal EE is plotted in the upper graph, and the final EE in the bottom graph. T_s has very little impact on η_{max} which reaches 46% at low ν_{dilu}. On the contrary, η_{final} drops as T_s increases: the cooling is not fast enough at high T_s.

Conclusion on the EE of the thermal spark

To conclude, this section showed that the EE of CO production induced by a thermal spark is in the 10% - 40% range. If dilution is the only cooling mechanism, 40% EE is reached for ν_{dilu} between 10^4 and $7{\cdot}10^4$ s^{-1} when the spark reaches peak temperatures of 10,000 – 30,000 K.

With optimized mixing and quenching rates, the thermal spark could bring the EE to the thermodynamic limit (48% at atmospheric pressure), and thus, significantly outperform the NTS. Achieving the maximal EE requires a slow dilution of the filament, followed by fast cooling. In our simple model, dilution and cooling are correlated, but they can be decorrelated in a real system. On one hand, in a real system the dilution rate can be adjusted

by controlling the hydrodynamics. Some control parameters are easily tunable: varying the electric field would change the pressure and temperature conditions in the filament, whereas modifying the pulse repetition frequency and the reactor geometry would change the temperature of the surrounding gas. In the end, these parameters change the Mach number of the shock (therefore the advection) and the speed of the diffusion processes, that is, the dilution rate of the filament. On the other hand, the cooling rate could be increased by the addition of a cooling process, such as expanding the gas, spraying liquid water, or flowing the gas in a heat exchanger once CO is formed.

There are also some limits to exploiting the thermal spark regime to produce CO. First, the shock heats the gas in a wide volume (a cylinder of a few mm diameter, cf section 4.3.4). Thus, the temperature of the diluting gas is likely higher than 300 K by hundreds of kelvins, which would slow the cooling of the products, thus leading to significant CO losses (i.e. lower EE, cf Figure 4-39). Second, if dilution is the only cooling mechanism, a high EE is achieved at the expense of the conversion rate (whereas conversion is also important from an industrial point of view).

4.7.3 CO production mechanism in our experiments and in the literature

In light of the EE calculations of this chapter, we can now estimate the relative contribution to CO production of the non-thermal and thermal regions observed in the experiments of Chapter 3.

As stated in Section 4.5.3, the EE of CO production after 20 ns stays approximately constant in the different non-thermal spark conditions simulated: for T_0 between 600-800 K, the EE is around 20%. Since the heat and reactive species remaining in the plasma may create additional CO in the following µs, 20% is a lower bound for the EE of the NTS.

Regarding the EE of the thermal spark in our conditions, we point out that no additional cooling technology is used in our experiments, so they are within the framework of our model. Thus, the EE should remain in the range calculated for the final EE in previous sections, i.e. 10 – 40%. In the following calculations, we will use 40% for the EE of the TS to estimate an upper bound of its contribution to CO production (and thus, a lower bound of the contribution of the non-thermal region).

Let us recall the results from Chapter 3. Following the initial pulse of 4 mJ, in 90% of the cases, the thermal regions are limited to small spheres near the electrodes, and 99% of the energy goes to the non-thermal region. By multiplying the energy deposited in each region by the EE, we obtain the useful energy in each region, i.e. the energy actually used for CO

production. Thus, at least 98% of the CO production occurs in the non-thermal region, and less than 2% in the thermal region.

In the 10% of cases where the thermal region occupies half of the interelectrode gap, between 6 and 24% of the pulse energy goes to that region. Based on the upper value of this range, we obtain an upper bound of 39% for the relative contribution of the TS to CO production.

During the reflected pulse of 0.5 mJ, we estimate that approximately half of the energy goes to the filament. Thus, at most 67% of the CO production resulting from the reflected pulse is due to the thermal region.

Finally, the total average contribution of the non-thermal and thermal regions can be estimated by summing the initial and reflected pulses production, and by weighting the production by their occurrence frequency. We find that the contribution of the thermal region to the overall CO production in our experiment is lower than 16%.

4.8 Conclusions

To conclude, let us summarize the contributions of this chapter. First, we developed a 0D kinetic model to simulate a thermal spark (Model 4). The model is based on previous work from our laboratory (Pannier 2019). The major additions are the ionization reactions for all electronic states. The model shows that the spark thermalization is driven by the initial temperature in the interelectrode gap: a non-thermal spark (NTS) is predicted for $T_0 \leq 700\ K$, and a thermal spark (TS) for $T_0 \geq 950\ K$. This result, added to the non-uniform and fluctuant temperature field in NRP discharges, explains the measurements of thermal and non-thermal regions in Chapter 3. This explains the local presence of thermal filaments near the electrodes after the first pulse and their fluctuation from pulse to pulse. Also, it explains why the reflected pulse generates a thermal spark despite its lower voltage (Chapter 3): T_0 is much higher in the gas before the reflection than before the first pulse.

The NTS and TS simulations were then compared with the OES and electrical measurements of Chapter 3. The TS simulation correctly reproduces (i) the full dissociation and ionization of CO_2 and (ii) the thermalization of the electron and gas temperatures. It predicts that, 10 ns after the pulse, the plasma reaches near-LTE conditions at 20,000 K, which is consistent with the OES measurements of Chapter 3.

The model also shows that the ionization in the thermal spark proceeds in three stages: at first, CO_2 is ionized to CO_2^+; then, the nascent O and CO and their respective electronic states are ionized to O^+ and CO^+; finally, while CO dissociates, the C atoms, the extra O atoms, and their electronic states are ionized. In the whole process, the ionization of electronic states is critical. In the non-thermal spark, only the first two stages play a role.

In the thermal spark, the model shows that the thermalization of the electron and heavy species proceeds through the dissociation of CO_2 electronic states, the dissociative recombination of molecular species, the quenching of O and C electronic states, and the electron-ion elastic collisions. This complements the explanation of (Minesi et al. 2021).

Finally, we investigated the CO production mechanisms in non-thermal and thermal sparks.

In the non-thermal spark, we find the same results as (Heijkers et al. 2019; Pannier 2019): during the pulse, CO_2 is quickly converted via CO_2* predissociation. The model yields an EE of CO production of 18 – 21%. The post-discharge likely increases CO production, as predicted by Pannier and Heijkers *et al.* and suggested by the higher EE measured in the experiments of Chapter 3. To accurately describe the dissociation during the post-discharge, a 2D simulation is needed.

In the thermal spark, because of the extremely fast transport processes, the 0D modelling approach is approximate. Nevertheless, we captured the spatial phenomena by introducing a dilution rate, and we qualitatively discussed the EE that could be achieved in this regime. In our model (Model 5), the EE is in the 10% - 40% range. The optimal dilution rate is a balance between a slow mixing while $T_g > 3{,}000$ K (leaving time for the CO production reactions to occur), and a fast quenching from 3,000 to 700 K to preserve the CO molecules. For initial filament temperature between 10,000 K and 30,000 K, the optimal dilution rate is between 10^4 and $7{\cdot}10^4$ s^{-1}.

In the thermal spark, an EE of 46% could be reached with a slow dilution rate ($\nu_{dilu} \leq 10^5\ s^{-1}$) and an additional cooling stage. Thus, the process could significantly outperform the non-thermal spark. To confirm this result, more work should be devoted to the hydrodynamics of the post-discharge (e.g. 2D simulations) given the sensitivity of the TS results to the dilution rate, filament temperature and surrounding gas temperature.

In our experiments (Chapter 3), the thermal spark accounts for less than 16% of the overall CO production. Nevertheless, its sensitivity to the initial temperature in the interelectrode gap suggests that its formation could be fostered (or prevented) by playing on experimental parameters, such as the electrode geometry, pulse frequency, shape and amplitude of the input voltage. Being able to isolate the TS or NTS regime would be an important step to allow their experimental study and understanding their effect on the EE.

Take-away messages of Chapter 4

- The development of the plasma toward a *non-thermal* or *thermal* spark is controlled by the initial temperature of the gas at a given applied electric field. The temperature non-uniformities in NRP-spark discharges result in *non-thermal* and *thermal* regions, as measured in Chapter 3.
- During the pulse of a *non-thermal* spark, we confirm that CO is mostly produced by predissociation of CO_2 electronic states, following their electron-impact excitation. The EE at the end of the pulse is approximately 20%, but it can be higher after a few µs, if the heat and reactive species produce additional CO.
- In the *thermal* spark, we estimate an EE of 10 – 40% depending on the dilution rate. The optimal dilution rate is a balance between a slow cooling down to 3,000 to produce CO, and fast quenching from 3,000 to 700 K to preserve the CO production. For a thermal spark at 30,000 K, the optimal dilution rate is $\nu_{dilu} \sim 7{\cdot}10^4$ s^{-1}.
- In the thermal spark, an EE of 46% could be reached with a slow dilution rate ($\nu_{dilu} \leq 10^5\ s^{-1}$) and an additional cooling stage. Thus, the process could significantly outperform the non-thermal spark and provide some of the best results for CO_2 plasmalysis.
- For the conditions of the experiments of Chapter 3, more than 84% CO is produced in the *non-thermal* regions.

Chapter 5

Conclusion and recommendations for future work

5.1 Contribution of this thesis

In this thesis, we investigated experimentally and numerically the conversion of CO_2 by a plasmalysis technique using Nanosecond Repetitively Pulsed (NRP) discharges. Our goal was to evaluate the potential of NRP discharges at atmospheric pressure in terms of their energy efficiency (EE).

In Chapter 1, we discussed the potential of CO_2 plasmalysis as a method to produce low-carbon fuels in the context of global warming. We emphasized the importance of the energy efficiency of this process, which is the focus of this thesis.

In Chapter 2, we began by summarizing the main CO production pathways in CO_2 plasmas and analyzing their respective energy efficiency. We recalled that the EE is intrinsically limited by thermodynamics. In local thermodynamic equilibrium (LTE) conditions, CO cannot be produced with an EE above 48% at 1 bar and 52% at 0.01 bar, because part of the energy is spent in gas heating and the production of O atoms. To achieve EEs above 53%, the O atoms must be recycled, which, according to our definition, means that their chemical energy must be reused to produce additional CO molecules at a reduced energy cost.

We then developed a simple but exhaustive kinetic model to study O recycling in CO_2 plasma discharges. Using this model, we showed that O recycling is impossible in a non-LTE, but thermal equilibrium process, i.e. a process where all temperatures are equal. This result was obtained for any gas composition resulting from the discharge and a dilution stage. Even if the O-CO_2 association reaction does occur, it does not allow to overcome the EE thermodynamic limit, because of the high energy cost of maintaining the high

temperatures that promote O-CO_2 association and the competing recombination and reverse reactions.

We extended this model to thermal nonequilibrium processes, considering vibrationally enhanced O-recycling. Although Vibrational-Translational (VT) nonequilibrium does accelerate O-CO_2 association, we showed that this reaction is still slower than heavy-particle impact dissociation of CO_2 and VT relaxation. Electronic excitation of O and CO_2 does not promote O-recycling either.

Finally, whatever the electronic, vibrational, and translational temperature conditions, and whatever the gas composition, O-recycling cannot occur in a CO_2 plasma. Consequently, the EE of a catalyst-free plasma process cannot exceed 53%.

In accordance with these findings, we showed that the overwhelming majority of the CO_2 plasmalysis studies of the past decade did not achieve energy efficiencies above 50%. Cold plasma discharges were limited to an EE of 10%. The best results (of about 50%) were obtained in MW discharges at temperatures above 3,000 K, where CO production is dominated by thermal reactions. Although the 50% EE of hot plasmas (with $T_g > 3000$ K) cannot be significantly exceeded, reproducing it at lower temperatures would be beneficial to industrialize the process. For example this would facilitate the cooling phase, reduce heat losses and material stress. NRP discharges are a promising candidate to do so. They can produce vibrational and electronic nonequilibrium conditions allowing CO_2 to be converted below 3,000 K. They also operate in a wide temperature range, and generate powerful hydrodynamic effects that could rapidly and efficiently quench the products.

In the literature, energy efficiencies of 20-58% have been reported for NRP-sparks, with the highest EEs reported by (Montesano et al. 2020). The electron density above 10^{18} cm^{-3} measured by (Ceppelli et al. 2021) for the conditions of (Montesano et al. 2020) differed from the predictions of recent 0D-kinetic models (Heijkers et al. 2019; Pannier 2019) where the electron density was found to be limited to 10^{16}–10^{17} cm^{-3} for similar conditions. An electron density above 10^{18} cm^{-3} could lead the plasma to thermalize, as shown in air discharges (Minesi et al. 2020, 2021, 2023), thus completely changing the CO production mechanism. In order to assess the potential improvements in EE that could be achieved in NRP discharges, it is necessary to understand the CO production mechanisms that they activate. This was the focus of Chapters 3 and 4 of this thesis.

In Chapter 3, we experimentally investigated CO_2 plasmalysis with NRP discharges. We began by exploring a wide range of conditions similar to those of the experiments of (Montesano et al. 2020): specific energy inputs from 0.1 to 1.6 eV/molecule, electric fields from 20 to 80 kV/cm, pulse repetition frequencies from 3 to 50 kHz, using continuous and burst modes. We obtained an EE in the 20 – 36% range.

A detailed study of the NRP discharges was then conducted, using optical emission spectroscopy (OES) and ns-imaging to reassess the thermophysical conditions in NRP discharges in CO_2 at atmospheric pressure. In particular, we devoted considerable effort to the analysis of Stark-broadened atomic lines and excited electronic populations to disentangle the complex spatio-temporal phenomena. With these measurements, we evidenced the coexistence of bright, highly-ionized ($n_e \geq 10^{18}\ cm^{-3}$), atomic regions, and faint, moderately ionized ($n_e \sim 10^{16} - 10^{17}\ cm^{-3}$), molecular regions.

We compared our measurements with those of (Matteo Ceppelli et al. 2021), and showed that in both setups the discharge proceeds in two similar phases: a breakdown phase (temporal region I in (Matteo Ceppelli et al. 2021) and $t < 70\ ns$ in this work), followed by several reignition events (temporal regions II, III, IV in (Matteo Ceppelli et al. 2021), $t \geq 70\ ns$ in this work). In the breakdown phase, Ceppelli *et al.* and this work reported the same spectral features (CO Angström, C_2 Swan, $CO_2^+(A^2\Pi_u - X^2\ \Pi_g)$, and O lines) in the center of the interelectrode gap, in what we called the "faint region". During the first 20 ns, the presence of these bands and our various measurements of electron density (10^{16}-10^{17} cm^3), electron temperature ($T_e \sim$ 20,000 K), and gas temperature ($T_g \sim$ 600-800 K) indicate a non-thermal spark. In the reignition phase, both works obtained the same spectra, this time composed of O^+, C^+, and O lines. We measured $n_e \sim$ 1-5·10^{18} cm^{-3}, $T_e \approx$ 30,000 K and showed that the "bright region" is thermal and can even reach local thermodynamic equilibrium (LTE) at 30,000 K. To our knowledge, this is the first identification of a thermal spark in CO_2.

Based on thermodynamic calculations, we estimated that in our conditions most CO is produced in the non-thermal region of the breakdown phase. In the general case, however, both non-thermal and thermal spark regimes could contribute to CO_2 dissociation. These results motivated the modeling studies of Chapter 4.

In Chapter 4, we studied the formation of thermal and non-thermal sparks at 1 bar. To estimate their EE, we developed a new kinetic model for warm CO_2 plasmas. This model starts from the model of Pannier and supplements it with the ionization reactions of the electronic states of atoms and molecules. It is used in conjunction with a simplified 0D thermophysical model of the discharge where we neglect all transport phenomena (closed, adiabatic, and isochore system). This assumption holds as long as the simulation time is small compared to the characteristic time of the fastest transport phenomenon. Thus, we showed that the simulation time must stay below 10 ns for a Thermal Spark (TS), and 1 µs for a Non-Thermal Spark (NTS). Also, since the discharge is highly non-uniform, several simulations starting with different initial conditions must be performed to obtain a representative description of the discharge. Each simulation describes the local thermo-kinetics of the discharge before transport phenomena come into play.

Starting from different temperatures measured in NRP-sparks, we showed that both non-thermal and thermal sparks can be obtained for a given electric field: a Non-Thermal Spark (NTS) is predicted for an initial temperature $T_0 \leq 700\ K$, and a Thermal Spark (TS) for $T_0 \geq 950\ K$. A transition between the non-thermal and thermal regimes is observed in between. This result, added to the non-uniform and fluctuant temperature field in NRP discharges, explains the observation of co-existing thermal and non-thermal regions in Chapter 3. It suggests that thermal or non-thermal sparks could be promoted by playing on the initial temperature field.

The NTS and TS simulations were then compared with the OES and electrical measurements of Chapter 3. The TS simulation correctly reproduces (i) the full dissociation and ionization of CO_2 and (ii) the thermalization of the electron and gas temperatures. It predicts that, 10 ns after the pulse, the plasma reaches near-LTE conditions consistent with the OES measurements of Chapter 3.

The model also explains the ionization and thermalization mechanisms in the TS: ionization proceeds mainly through the ionization of electronic excited states of CO, O, and C. The thermalization proceeds equally through inelastic (the dissociation of CO_2 electronic states, the dissociative recombination of molecular species, the quenching of O and C electronic states), and elastic (electron-ion collisions) processes.

Finally, we investigated the CO production mechanisms in non-thermal and thermal sparks. In the NTS, we found the same results as (Heijkers et al. 2019; Pannier 2019): during the pulse, CO_2 is quickly converted via CO_2* predissociation. The model yields an EE of CO production of 18-21%. The post-discharge likely enhances CO production, as predicted by Pannier and Heijkers *et al.* This may explain the EE of 30% obtained in our experiments of Chapter 3. In the TS, since no CO is produced at the end of the pulse, we had to account for the transport phenomena that take place in the post-discharge. We captured these effects by introducing a dilution rate, allowing to qualitatively estimate the EE that could be achieved in this regime. We obtained an EE in the 10-40% range. We found that the optimal dilution rate is a balance between a slow cooling while $T_g > 3{,}000$ K – leaving time for the radicals to react with fresh CO_2 and produce CO –, and a fast cooling from 3,000 to 700 K to preserve the CO produced. For initial filament temperatures between 10,000 K and 30,000 K, the optimal dilution rate was found to be between 10^4 and $7{\cdot}10^4$ s^{-1}. An EE of 46% could be achieved if cooling could be accelerated with an additional cooling stage.

Based on the estimation of the EE of the non-thermal and thermal mechanisms (Chapter 4), and on the quantification of the energy deposited in each region (Chapter 3), we calculated that more than 84% of the CO production comes from the non-thermal region in our reference experimental conditions.

In summary, we showed the existence of non-thermal and thermal sparks in NRP discharges in CO_2. On the one hand, the non-thermal spark regime achieves an EE of about 30%, but has no room for improvement because it relies on the electronic dissociation pathway, which has an EE limit of 25%. The temperature in the NTS is on the order of 1000-2000 K. On the other hand, the thermal spark regime could achieve higher EEs, but reaches much higher temperatures and requires the addition of a cooling stage to be efficient.

5.2 Recommendations for future work

We aimed to evaluate the potential of NRP discharges at atmospheric pressure in terms of energy efficiency (EE). As shown throughout this thesis, the EE of the NTS and TS regimes critically relies on the post-discharge. Therefore, the post-discharge dynamics should now be studied experimentally and numerically to estimate the mixing and cooling rates and refine our prediction of the EE achievable in NTS and TS regimes. Consequently, future work should focus on (i) isolating the non-thermal and thermal regimes, and (ii) studying the post-discharge phase for both regimes.

The thermal spark sensitivity to the electric field and the initial temperature in the interelectrode gap suggests that its formation could be prevented (or fostered) by playing on experimental parameters, such as the electrode geometry, pulse frequency, shape and amplitude of the input voltage. Thus, for objective (i), we recommend conducting a parametric study to find the conditions favoring one regime or the other, and measuring the initial 2D spatial distribution of the temperature in the interelectrode gap, using Rayleigh or Raman scattering for example.

For objective (ii), we recommend conducting Schlieren measurements and 2D measurements of the temperature (Rayleigh or Raman scattering), O, and CO in the post-discharge (by laser-induced fluorescence, for example). Also, we recommend extending the OES measurements to the UV region, where characteristic species of the thermal spark such as O^+, C^+, or C^{++} can be more readily observed. Then, 2D simulations of the post-discharge hydrodynamics coupled with the kinetics should be carried out. The coupling between hydrodynamics and kinetics is expected to be significant in the post-discharge of the TS, as the recombination reactions are highly exothermic. These simulations, validated by measurements, would be extremely useful to provide a final assessment of the most efficient regime (or superposition of regimes) to produce CO.

5.3 Global conclusion

CO_2 plasmalysis still has some way to go before it becomes an industrial process, but returning to the plasma typology presented in Table 2-9, several conclusions can be drawn from the present work regarding its future path to viable industrialization.

First, the cold plasma path should be closed because 10 years of experiments have shown that its EE is limited to a maximum of 10%.

Second, in warm plasmas, efficient nonequilibrium vibrational dissociation does not appear feasible. Basically, the high power density required to climb the vibrational ladder cannot be maintained without heating the gas, or in other words, the high ionization degree and low temperature conditions required to maintain faster vibrational excitation than VT cannot be achieved simultaneously. This is due to (i) the high VT transfer at temperatures above 1000 K, and (ii) exothermic recombination of the dissociation products. Since O recycling does not occur, the O chemical energy ends up in heat, which amounts to 2.6 eV / CO molecule produced. Thus, vibrational nonequilibrium cannot be maintained simultaneously with vibrational dissociation. Then, the dominant dissociation mechanisms in warm plasmas are the electronic and thermal dissociation. The electronic dissociation pathway is limited to an EE of 25%. The lower the gas temperature, the smaller the contribution of thermal dissociation, and the closer the EE would be to this limit. Choosing this path means sacrificing the 48% EE target (at 1 bar) to maintain moderate operating temperatures (~1000-2000 K).

Third, in plasmas above 3000 K, EEs close to 50% could be achieved, provided that the challenges of cooling, material constraints, and heat losses are solved.

Finally, as mentioned in Chapter 2, the coupling of plasma with catalysts is a promising alternative that has been increasingly studied in the community. Another alternative is CO_2 electrolysis, which has achieved high energy efficiencies at low temperatures. The exploration of these various pathways, and the understanding of the physico-chemical phenomena at play in each of them, remain challenging but essential tasks in the race toward the replacement of fossil fuels.

Appendix A Degree of equilibrium estimation using Cristoforetti's three criteria

We showed in Section 3.4.4 that the high electron density in the bright region leads to a high frequency of electron-ion collisions, allowing thermalization of the electron energy with the heavy species. Under certain conditions, the plasma can reach Local Thermodynamic Equilibrium (LTE), thus achieving the thermal spark regime (Minesi et al. 2020, 2021). The McWhirther criterion defines the electron number density above which electron-collision processes prevail over radiative processes. It can be written as:

$$n_e(cm^{-3}) > 1.6 \cdot 10^{12} \cdot T^{0.5} \cdot \Delta E^3 \qquad \text{Eq. 5-1}$$

where n_e $[cm^{-3}]$ is the electron number density, T $[K]$ the gas temperature, and ΔE $[eV]$ the energy gap between the ground state and the first resonant excited state. We evaluate an upper bound of this electron density threshold. The highest temperature condition in the bright region is $T \sim 40{,}000\ K$. Given the species present in the bright region – O, C, O^+, C^+ – the highest energy gap for an optical allowed transition is the energy of the first O^+ resonant transition, $\Delta E_{nm} = 14.9\ eV$. Thus, the McWhirter criterion becomes $n_e > 10^{18}\ cm^{-3}$. This condition is fulfilled in the bright region.

To assess the validity of LTE for transient and non-homogeneous plasmas, (Cristoforetti et al. 2010) extended the McWhirter criterion. They pointed out that the thermochemical conditions must vary much slower than the plasma relaxes to the LTE. Thus, they added the following criteria:

$$\frac{T(t+\tau_{rel})-T(t)}{T(t)} \ll 1 \qquad \frac{N_e(t+\tau_{rel})-N_e(t)}{N_e(t)} \ll 1 \qquad \text{Eq. 5-2}$$

where τ_{rel} is the time needed for the plasma to relax to LTE. Equivalently, we can write:

$$\tau_{rel} \ll \frac{T_e(t)}{\frac{\partial T_e}{\partial t}(t)} \qquad \tau_{rel} \ll \frac{n_e(t)}{\frac{\partial n_e}{\partial t}(t)} \qquad \text{Eq. 5-3}$$

Based on the OES measurements between t = 20 ns and t = 60 ns presented in Figure 3-21 (for n_e) and Figure 3-25 (for T_e), we obtain:

$$\frac{T_e(t)}{\frac{\partial T_e}{\partial t}(t)} \approx 200\ ns \qquad \frac{n_e(t)}{\frac{\partial n_e}{\partial t}(t)} \approx 50\ ns \qquad \text{Eq. 5-4}$$

Cristoforetti *et al.* estimated the time needed to relax to LTE as the characteristic time of collisional excitation from the ground state to the first resonant state. Thus, we estimate τ_{rel} as:

$$\tau_{rel} = \frac{6.3 \cdot 10^4}{n_e f_{12} \langle \bar{g} \rangle} \cdot \Delta E_{21} \cdot (kT)^{\frac{1}{2}} \cdot e^{\frac{\Delta E_{21}}{kT}} \cdot \eta_i \qquad \text{Eq. 5-5}$$

with n_e $[cm^{-3}]$ the electron density, f_{12} the oscillator strength for the selected transition, $\langle \bar{g} \rangle$ the Gaunt factor, ΔE_{21} $[eV]$ the transition energy, kT [eV] the electron temperature, and η_i the ionization fraction of the species i considered (for example, for O: $\eta_O = n_{O^+}/(n_O + n_{O^+})$).

We compute the relaxation time of the first resonant transition of O and O^+: $\mathbf{O}(2s^2 2p^4\ ^3P)$(0 eV) ↔ $\mathbf{O}(2s^2 2p^3(^4S^0)3s\ ^3S^0)$(9.5 eV) and $\mathbf{O^+}(\ 2s^2 2p^3\ ^4S^0)$(0 eV) ↔ $\mathbf{O^+}(\ 2s2p^4\ ^4P)$(14.9 eV). The oscillator strengths for these two transitions are 0.052 and between 0.045 and 0.14 (depending on the J of the upper level) (Kramida, Ralchenko, et al. 2023), respectively. We need to estimate the ionization fractions $\eta_O = n_{O^+}/(n_O + n_{O^+})$ and $\eta_{O^+} = n_{O^{++}}/(n_{O+} + n_{O^{++}})$. Since we are looking for an upper bound of τ_{rel}, we choose upper bounds for the ionization fractions by taking the equilibrium composition at 30,000 K and 20 bar (already given in Figure 3-29). This yields approximately 90% and 10% for the ionization fractions of O and O^+, respectively.

Finally, we use the electron density measured from the O(777) triplet (Figure 3-21) and the electron temperature from the O^+(455 – 475) lines (Figure 3-25). These calculations yield the temporal evolution of the relaxation times of O and O^+, shown in Figure 5-1.

Just after the first pulse, the relaxation time of O is small compared to the n_e variation time during approximately 10 ns, at every location. Then, it increases above the n_e variation time. During the reflection, the relaxation time falls again below the n_e variation time. This is particularly pronounced at the anode and midgap. These equilibration times are consistent with the plasma being close to LTE conditions but not fully achieving it.

The equilibration time of the distribution of the O^+ electronic states is much faster than for the O states: it is always much smaller than the n_e and T_e variation times. Thus, the O^+ electronic states (including the ground state) should all follow a Saha-Boltzmann distribution with the electrons.

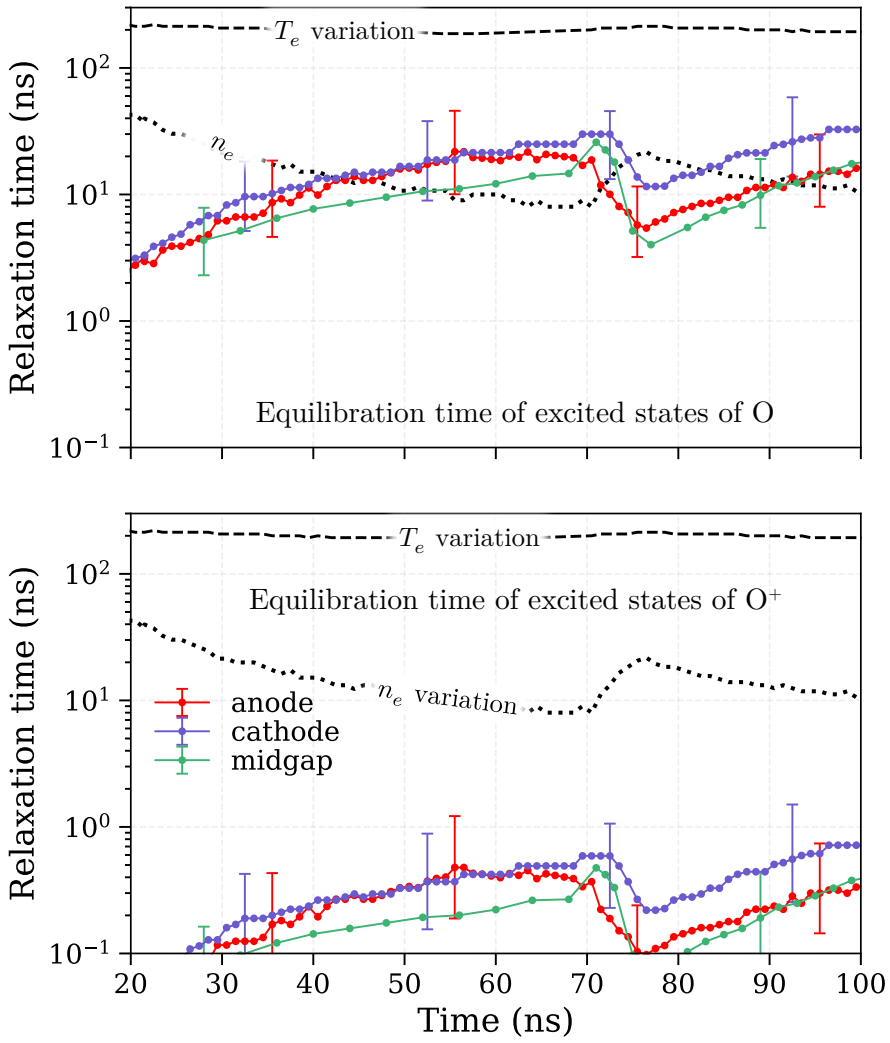

Figure 5-1. Temporal evolution of the O electronic states equilibration time (center), and O^+ electronic states equilibration time (bottom). The dashed and dotted lines are the T_e and and n_e variation characteristic times. Just after the first pulse, the O equilibration time is small compared to the n_e variation time, but it quickly decreases to the same order of magnitude. This does not allow to conclude on the LTE. O^+ equilibrates much faster suggesting that it is in Saha equilibrium with the electrons.

For a heterogeneous plasma, Cristoforetti mentions a last criterion: for the plasma to be in LTE, the diffusion length of the species during the relaxation time must be shorter than the characteristic length of variation of temperature and electron number density. Put another way: during the relaxation time of the plasma, the species diffuse; the thermochemical quantities must remain constant in the distance they cover during this time. If not, they will not have the time to equilibrate. This translates into:

$$\frac{T(x)-T(x+\lambda)}{T(x)} \ll 1 \qquad \frac{n_e(x)-n_e(x+\lambda)}{n_e(x)} \ll 1$$

with $\lambda = (D \cdot \tau_{rel})^{\frac{1}{2}}$ the diffusion length during τ_{rel} and D the diffusion coefficient of the fastest species.

According to (Cristoforetti et al. 2010), the diffusion coefficient of the fastest heavy species – the atoms, essentially O in our case – can be estimated as $D \approx 3 \cdot 10^{19} \cdot kT[eV]/(n_{II}[cm^{-3}]\ M_A)$ with n_{II} the absolute number density of ions and M_A the relative mass of the species and of the ion. In our case, O^+ and C^+ are the main ions, so we use $M_A = 1$. The total ion number density is equal to the electron density. Thus, the O diffusion length can be determined using the electron density and electron temperature measurements from Figure 3-21 and Figure 3-25, respectively. The resulting diffusion length varies between 1 – 10 µm, which is well below the 100 µm plasma diameter. Therefore, during the relaxation time, the species diffuse in a constant temperature and electron density field. The plasma heterogeneity does not prevent it from reaching equilibrium.

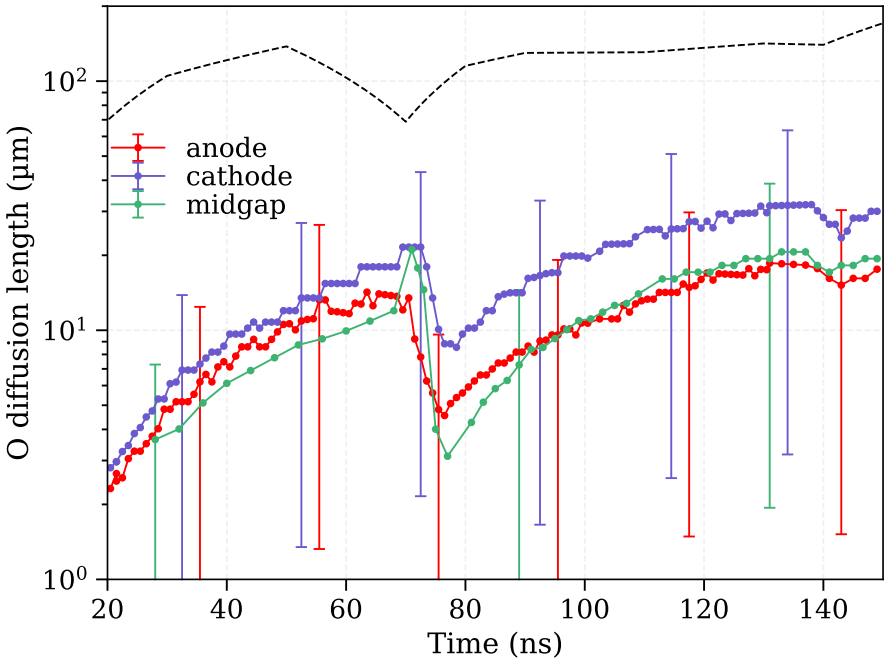

Figure 5-2. Temporal evolution of the O diffusion length, calculated in Cristoforetti's way. The bright region diameter is plotted for comparison. We show that the diffusion length varies between 1 – 10 µm, which is well below the 100 µm plasma diameter. Therefore, during the relaxation time the species move in a constant temperature and electron density field.

Appendix B Single shot measurements of the O(777) triplet: simultaneity or "successivity" of the broad and narrow components?

The single-shot images of the plasma (cf Figure 3-5 and Figure 3-7) showed the existence of simultaneous bright and faint emission regions. The spectra of each region (Figure 3-11, and Figure 3-13) revealed an atomic and highly ionized plasma on one side and a molecular and moderately ionized plasma on the other. The double-component spectra of the O(777) triplet (Figure 3-19) allowed us to measure the electron density in each region.

Based on the single-shot images of Figure 3-5 and the energy calculations of Section 3.5.2, we have shown that the bright and faint regions appear simultaneously. However, the broad and narrow components measured in Section 3.4.2 are not necessarily simultaneous because the spectra are averaged over thousands of pulses. There are three potential scenarios leading to the observation of two superimposed components in the same spectra:

(i) The spectral lines emitted by the filament and the faint region are of the same order of magnitude. Thus, the resulting double-component spectrum can be observed in a single-shot measurement. Averaging over several spectra would naturally conserve the same double-Lorentzian shape. This interpretation was already mentioned in (Maillard et al. 2022).

(ii) In some pulses, the filament emission overshadows the faint region emission. In others, the observed region has no filament emission (for example, a type a pulse has no bright region near the cathode). A single-shot spectrum would have only one component. However, the spectrum obtained by averaging thousands of pulses would show a double Lorentzian lineshape.

(iii) Initially, the faint region dominates. Then, between 10 and 25 ns, the filament appears and instantly dominates the spectrum. Since our spectra are averaged over 4 ns and the transition to a thermal filament may occurs in less than 1 ns (according to (Minesi et al. 2021) and Chapter 4 of this work), an opening period of the ICCD camera straddling the transition would result in a double-component spectrum. In this case, we would also observe double-component lineshapes in single shot.

Discriminating scenarios (i) and (iii) would require sub-ns, single-shot emission measurements. This is not possible with our equipment. In this section, we will simply observe double-component spectra in single-shot to evaluate scenario (ii) against scenarios (i),(iii).

First, the single-shot measurements are made over the first 50 ns of the discharge, and we use the parallel mirror configuration for spatial resolution. Figure 5-3 shows the spatial distribution of the lineshape types for 100 single-shot measurements. A broad component is often observed near the electrodes (revealing a filament), and a single narrow component in the middle of the gap (revealing the faint region). We do observe two-component spectra near the electrodes and at the interface between the filament and the faint region.

Figure 5-4 shows the statistical distribution of the various lineshapes (narrow, wide, and double) along the inter-electrode axis before the reflection. This distribution quantifies the observations about Figure 5-3. During the 0-50 ns period, at the cathode, a broad component appears about 40% of the time, a narrow component about 35% of the time, and a two-component lineshape about 25% of the time. In the middle of the gap, a narrow component is seen about 90% of the time. The remaining 10% are split between two-component lineshapes and single broad components. At the anode, a single broad component is seen 80% of the time, and a two-component lineshape 20% of the time. Thus, we show that the three scenarios (i), (ii) and (iii) occur.

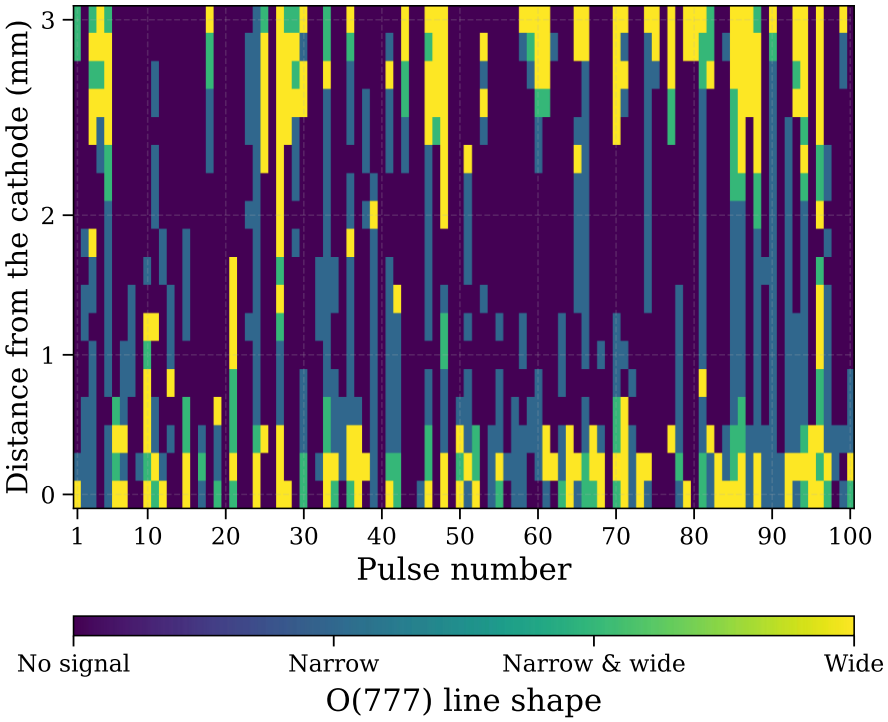

Figure 5-3. Shape of the O(777) line measured in single-shot (integrated from 0 to 50 ns) as a function of the distance from the cathode (along the inter-electrode axis) and the measurement number. Yellow stands for a broad component, light blue for a narrow component, and green for the superposition of the two. Dark blue indicates a signal too low to be interpreted.

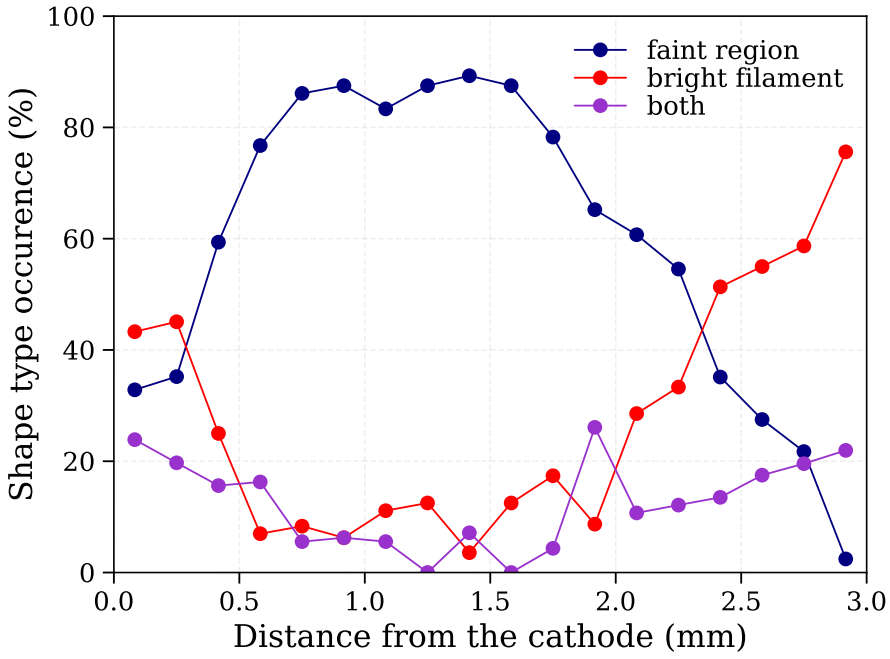

Figure 5-4. Shape type occurrence as a function of distance from the cathode across the inter-electrode gap. The spectra are integrated from 0 to 50 ns.

Single-shot spectra measured with a 50 ns gate width are more likely to lead to scenario (iii) than scenario (i). To refine the measurements, we use a PI-MAX4 camera (1024i, Princeton Instruments) equipped with a Super Red (SR) intensifier – much more sensitive at 777 nm. The higher sensitivity allows us to perform single-shot measurements with a narrow 6-ns gate width. Again, we measure two-component spectra in single-shot, an example of which is shown in Figure 5-5. Although it does not entirely eliminate scenario 3 (a sub-ns gate width would be needed), this measurement brings credibility to scenario (i).

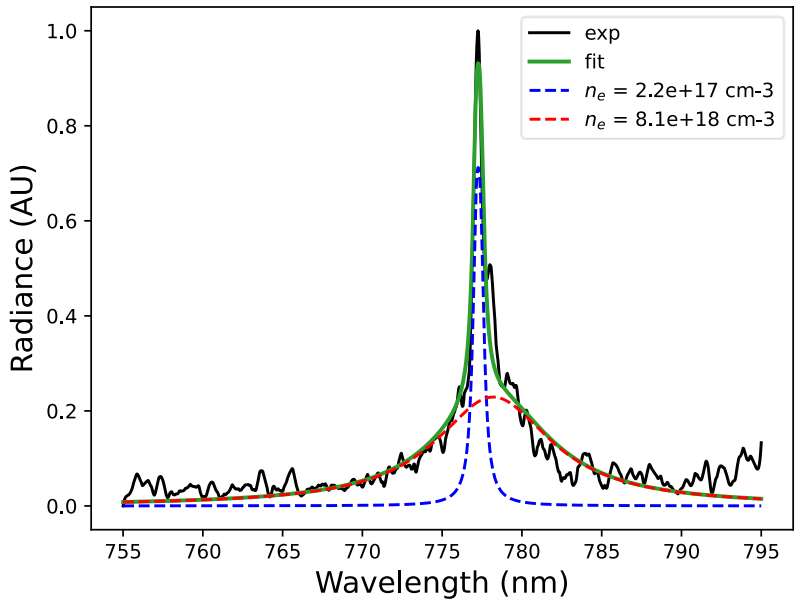

Figure 5-5. Single-shot oxygen triplet emission measured at midgap, integrated from 14 to 20 ns. The double-Lorentzian fit yields electron densities of $2{\cdot}10^{17}$ and $8{\cdot}10^{18}$ cm^{-3}.

Appendix C Kinetic model

This appendix lists the reation and rate constants of Model 4.

Table C-1. Electron-neutral reactions. The rate constants are calculated by solving the EEDF using BOLSIG+ and the cross-sections reported in the rightmost column. When double arrows are indicated, the backward rate constant is calculated by detailed balance.

(E1)	$e^- + CO_2 \rightarrow e^- + CO_2$	IST-Lisbon database (Grofulović, Luís L Alves, et al. 2016)
(E2)	$e^- + CO_2 \rightarrow e^- + e^- + CO_2^+$	Idem
(E7)	$e^- + CO_2 \leftrightarrow e^- + CO_2(^3\Sigma_u^+)$	Idem, CO_2(7 eV)
(E8)	$e^- + CO_2 \leftrightarrow e^- + CO_2(^1\Sigma_u^+)$	Idem, CO_2(10 eV)
(E9)	$e^- + CO_2 \leftrightarrow e^- + CO_2(^1\Pi_u)$	Idem, CO_2(10 eV)
(E10)	$e^- + CO_2 \leftrightarrow e^- + CO_2(^1A')$	Idem, CO_2(10 eV)
(E11)	Elastic collisions $e^- + CO_2^* \rightarrow e^- + CO_2^*$ with $CO_2^* = CO_2(^3\Sigma_u^+)$, $CO_2(^1\Sigma_u^+)$, $CO_2(^1\Pi_u)$, $CO_2(^1A')$	Same cross section as ground state
(E12)	Excitation collisions $e^- + CO_2^* \rightarrow e^- + e^- + CO_2^+$ with $CO_2^* = CO_2(^3\Sigma_u^+)$, $CO_2(^1\Sigma_u^+)$, $CO_2(^1\Pi_u)$, $CO_2(^1A')$	Calculated from (Drawin 1967)
(E13)	$e^- + CO \rightarrow e^- + CO$	IST-Lisbon database (Grofulović, Luís L Alves, et al. 2016)
(E14)	$e^- + CO \rightarrow e^- + e^- + CO^+$	Itikawa database (Itikawa 2015)
(E15)	$e^- + CO \rightarrow e^- + e^- + C^+ + O$	Itikawa database (Itikawa 2015)
(E16)	$e^- + CO \rightarrow e^- + e^- + C + O^+$	Itikawa database (Itikawa 2015)
(E17)	$e^- + CO \leftrightarrow e^- + CO(A^3\Pi)$	IST-Lisbon database (Grofulović, Luís L Alves, et al. 2016)
(E18)	$e^- + CO(A^3\Pi) \rightarrow e^- + CO(A^3\Pi)$	Same cross section as the ground state
(E19)	$e^- + CO(A^3\Pi) \leftrightarrow e^- + e^- + CO^+$	Calculated from (Drawin 1967)
	$e^- + C \rightarrow e^- + C$	(Wang et al. 2013)
	$e^- + C \leftrightarrow e^- + C(^1D)$	Idem
	$e^- + C \leftrightarrow e^- + C(^1S)$	Idem
	$e^- + C \leftrightarrow e^- + C(^5S_0)$	Idem
	$e^- + C \rightarrow e^- + e^- + C^+$	Idem
	Elastic and excitation collisions[1] of C* $e^- + C^* \leftrightarrow e^- + C^*$ with $C^* = C(^1D)$, $C(^1S)$, $C(^5S_0)$	Idem
	Ionization of C*	Idem

	$e^- + C^* \leftrightarrow e^- + e^- + C^+$ with $C^* = C(^1D)$, $C(^1S)$, $C(^5S_0)$	
	$e^- + O_2 \rightarrow e^- + O_2$	IST-Lisbon database (Grofulović, Luís L Alves, et al. 2016)
	$e^- + O_2 \rightarrow e^- + O + O$	Idem
	$e^- + O_2 \rightarrow e^- + O + O(^1D)$	Idem
	$e^- + O_2 \rightarrow e^- + O + O(^1S)$	Idem
	$e^- + O_2 \rightarrow e^- + O + O(^5P)$	Idem
	$e^- + O_2 \rightarrow e^- + O + O(3p^3P)$	Idem
	$e^- + O_2 \rightarrow e^- + e^- + O_2^+$	Idem
	$e^- + O_2 \rightarrow e^- + e^- + O + O^+$	Idem
	$e^- + O_2 \rightarrow e^- + O_2(a_1)$	Idem
	$e^- + O_2 \rightarrow e^- + O_2(a_2)$	Idem
	$e^- + O_2 \rightarrow e^- + O_2(4.5\ eV)$	Idem
	Elastic and excitation collisions[1] $e^- + O_2^* \leftrightarrow e^- + O_2^*$ with $O_2^* = O_2(a_1)$, $O_2(a_2)$, $O_2(4.5\ eV)$	(Ionin et al. 2007)
	Dissociation $e^- + O_2^* \rightarrow e^- + O + O^*$ with $O_2^* = O_2(a_1)$, $O_2(a_2)$ and $O^* = O$, $O(^1D)$	Idem
	Ionization $e^- + O_2^* \rightarrow e^- + e^- + O_2^+$ with $O_2^* = O_2(a_1)$, $O_2(a_2)$	Idem
	Dissociative ionization $e^- + O_2^* \rightarrow e^- + e^- + O + O^+$ with $O_2^* = O_2(a_1)$, $O_2(a_2)$	Idem
	$e^- + O_2(4.5\ eV) \leftrightarrow e^- + O_2(4.5\ eV)$	Same as the ground state
	$e^- + O_2(4.5\ eV) \leftrightarrow e^- + e^- + O_2^+$	Calculated from (Drawin 1967)
	$e^- + O \rightarrow e^- + O$	(Tayal and Zatsarinny 2016)
	$e^- + O \rightarrow e^- + e^- + O^+$	Idem
	$e^- + O \leftrightarrow e^- + O(^1D)$	Idem
	$e^- + O \leftrightarrow e^- + O(^1S)$	Idem
	Elastic and excitation collisions[1] of O* $e^- + O^* \leftrightarrow e^- + O^*$ with $O^* = O(^1D)$, $O(^1S)$	Idem
	Ionization of O* $e^- + O^* \leftrightarrow e^- + e^- + O^+$ with $O^* = O(^1D)$, $O(^1S)$	Idem

[1]Elastic if the excited state is the same on both sides of the reaction, inelastic otherwise.

Table C-2. Other electron-ion reactions

	$e^- + O^+ \leftrightarrow e^- + e^- + O^{++}$	$9.42 \cdot 10^{-14} \cdot T_e^{0.98} \cdot \exp(-381{,}240/T_e)$ integrated from (Tawara and Kato 1987) assuming a Maxwellian EEDF
	$e^- + C^+ \leftrightarrow e^- + e^- + C^{++}$	$4.3 \cdot 10^{-15} \cdot T_e^{0.89} \cdot \exp(-279{,}733/T_e)$ integrated from (Tawara and Kato 1987) assuming a Maxwellian EEDF
	$e^- + CO_2^+ \leftrightarrow CO + O$	$4.2 \cdot 10^{-7} \cdot \left(\frac{T_e}{300}\right)^{-0.75}$ (Viggiano et al. 2005)
	$e^- + CO^+ \leftrightarrow C + O$	$3.68 \cdot 10^{-8} \cdot \left(\frac{T_e}{11{,}605}\right)^{-0.55}$ (Kozàk and Bogaerts 2014)
	$e^- + O_2^+ \leftrightarrow O + O^*$ with $O^* = O\ O(^1D)\ O(^1S)$	$4.3 \cdot 10^{-15} \cdot \left(\frac{300}{T_e}\right)^{0.7}$ (Capitelli et al. 2000)

Table C-3. Neutral reactions

(N1)	$CO_2 + M \leftrightarrow CO + O + M$	$1.15 \cdot 10^{-2} \cdot (T_g T_v)^{-1.5} \exp\left(-\frac{63{,}275}{\sqrt{T_g T_v}}\right)$ (Park et al. 1994)
(N2)	$CO_2 + O \leftrightarrow CO + O_2$	$2.80 \cdot 10^{-11} \cdot \exp(-\frac{26{,}500}{T_g})$ (Kozàk and Bogaerts 2014)
(N3)	$CO_2 + C \leftrightarrow CO + CO$	10^{-15} (Kozàk and Bogaerts 2014)
(N4)	$CO + O \leftrightarrow C + O_2$	$6.5 \cdot 10^{-11} \cdot T_g^{-0.18} \cdot \exp(-\frac{69{,}200}{T_g})$ (Park et al. 1994)
(N5)	$CO + M \leftrightarrow O + C + M$	$3.82 \cdot 10^{-4} \cdot (T_g T_v)^{-1} \cdot \exp(-\frac{129{,}000}{\sqrt{T_g T_e}})$ (Park et al. 1994)
(N6)	$O_2 + M \leftrightarrow O + O + M$	$3.32 \cdot 10^{-3} \cdot (T_g T_v)^{-1.5} \cdot \exp(-\frac{59{,}750}{\sqrt{T_g T_e}})$ (Park et al. 1994)

Table C-4. Excited states reactions

CO_2 electronic states predissociation		
(P1)	$CO_2(^3\Sigma_u^+) \rightarrow CO + O$	$5 \cdot 10^{13}$ (Wright et al. 2017)
(P2)	$CO_2(^1\Sigma_u^+) \rightarrow CO + O(^1S)$	$5 \cdot 10^{13}$ (Wright et al. 2017)
(P3)	$CO_2(^1\Pi_u) \rightarrow CO + O(^1D)$	$5 \cdot 10^{13}$ (Wright et al. 2017)
(P4)	$CO_2(^1A') \rightarrow CO(A^3\Pi) + O$	$5 \cdot 10^{13}$ (Wright et al. 2017)
$O_2(a_1)$ quenching		
	$O_2(a_1) + O_2 \leftrightarrow O_2 + O_2$	$3.8 \cdot 10^{-18} \cdot \exp(-\frac{205}{T_g})$ (Capitelli et al. 2000)

	$O_2(a_1) + CO_2 \leftrightarrow O_2 + CO_2$	$2 \cdot 10^{-14}$ (Torbin et al. 2018)
	$O_2(a_1) + CO \leftrightarrow O_2 + CO$	$3.7 \cdot 10^{-15}$ (Dunlea and Ravishankara 2004) (see 4.4.2)
	$O_2(a_1) + O \leftrightarrow O_2 + O$	$7 \cdot 10^{-16}$ (Capitelli et al. 2000)
	$O_2(a_1) + C \leftrightarrow O_2 + C$	$7 \cdot 10^{-16}$ (see 4.4.2)
	$O_2(a_1) + O^+ \leftrightarrow O_2 + O^+$	$7 \cdot 10^{-16}$ (see 4.4.2)
	$O_2(a_1) + C^+ \leftrightarrow O_2 + O^+$	$7 \cdot 10^{-16}$ (see 4.4.2)
$O_2(b_1)$ quenching		
	$O_2(b_1) + O_2 \leftrightarrow O_2(a_1) + O_2$	$k_{b1-O2} = 4.3 \cdot 10^{-22} \cdot T_g^{2.4} \cdot \exp\left(-\frac{241}{T_g}\right)$ (Kossyi et al. 1992)
	$O_2(b_1) + O_2 \leftrightarrow O_2 + O_2$	$4 \cdot 10^{-17} - k_{b1-O2}$ (Sander et al. 2003) (see 4.4.2)
	$O_2(b_1) + CO_2 \leftrightarrow O_2(a_1) + CO_2$	$3.5 \cdot 10^{-15}$ (Kirillov 2013)
	$O_2(b_1) + CO \leftrightarrow O_2(a_1) + CO$	$3.7 \cdot 10^{-15}$ (Dunlea and Ravishankara 2004) (see 4.4.2)
	$O_2(b_1) + O \leftrightarrow O_2(a_1) + O$	$8.1 \cdot 10^{-14}$ (Capitelli et al. 2000)
	$O_2(b_1) + O \leftrightarrow O_2 + O(^1D)$	$3.4 \cdot 10^{-11} \cdot \left(\frac{300}{T_g}\right)^{0.1} \cdot \exp\left(-\frac{4{,}200}{T_g}\right)$ (Capitelli et al. 2000)
	$O_2(b_1) + C \leftrightarrow O_2(a_1) + C$	$8.1 \cdot 10^{-14}$ (see 4.4.2)
	$O_2(b_1) + O^+ \leftrightarrow O_2(a_1) + O^+$	$8.1 \cdot 10^{-14}$ (see 4.4.2)
	$O_2(b_1) + C^+ \leftrightarrow O_2(a_1) + C^+$	$8.1 \cdot 10^{-14}$ (see 4.4.2)
O_2(4.5 eV) quenching		
	$O_2(4.5\text{ eV}) + O_2 \leftrightarrow O_2 + O_2$	$3 \cdot 10^{-12}$ (Kirillov 2014)
	$O_2(4.5\text{ eV}) + CO_2 \leftrightarrow O_2 + CO_2$	$5.5 \cdot 10^{-11}$ (Kirillov 2014)
	$O_2(4.5\text{ eV}) + CO \leftrightarrow O_2 + CO$	$3 \cdot 10^{-12}$ (Kirillov 2014)
	$O_2(4.5\text{ eV}) + O \leftrightarrow O_2 + O$	$9 \cdot 10^{-12}$ (Kenner and Ogryzlo 1980)
	$O_2(4.5\text{ eV}) + C \leftrightarrow O_2 + C$	$9 \cdot 10^{-12}$ (see 4.4.2)
	$O_2(4.5\text{ eV}) + O^+ \leftrightarrow O_2 + O^+$	$9 \cdot 10^{-12}$ (see 4.4.2)
	$O_2(4.5\text{ eV}) + C^+ \leftrightarrow O_2 + C^+$	$9 \cdot 10^{-12}$ (see 4.4.2)
Quenching of CO*: $CO(A^3\Pi)$		
	$CO^* + O_2 \leftrightarrow CO + O_2$	$0.4 \times 6 \cdot 10^{-11}$ (A. F. Silva et al. 2020)
	$CO^* + O_2 \leftrightarrow CO + O + O$	$0.4 \times 6 \cdot 10^{-11}$(A. F. Silva et al. 2020)
	$CO^* + O_2 \leftrightarrow CO_2 + O$	$0.2 \times 6 \cdot 10^{-11}$(A. F. Silva et al. 2020)
	$CO^* + CO_2 \leftrightarrow CO + CO_2$	$0.5 \cdot 10^{-11}$ (A. F. Silva et al. 2020)
	$CO^* + CO_2 \leftrightarrow CO + CO + O$	$0.5 \cdot 10^{-11}$(A. F. Silva et al. 2020)
	$CO^* + CO \leftrightarrow CO + CO$	$5.7 \cdot 10^{-11}$ (A. F. Silva et al. 2020)
	$CO^* + O \leftrightarrow CO + O$	$1.9 \cdot 10^{-16}$ (A. F. Silva et al. 2020)
	$CO^* + C \leftrightarrow CO + C$	$1.9 \cdot 10^{-16}$ (see 4.4.2)
	$CO^* + O^+ \leftrightarrow CO + O^+$	$1.9 \cdot 10^{-16}$ (see 4.4.2)
	$CO^* + C^+ \leftrightarrow CO + C^+$	$1.9 \cdot 10^{-16}$ (see 4.4.2)

Quenching of $O(^1D)$		
	$O(^1D) + O_2 \leftrightarrow O + O_2(a_1)$	10^{-12} (Capitelli et al. 2000)
	$O(^1D) + O_2 \leftrightarrow O + O_2$	$3.2 \cdot 10^{-11} \cdot \exp(\frac{70}{T_g})$ (Sander et al. 2003)
	$O(^1D) + CO_2 \leftrightarrow CO + O_2$	$2.4 \cdot 10^{-13}$ (Sedlacek et al. 1989)
	$O(^1D) + CO_2 \leftrightarrow O + CO_2$	$7.4 \cdot 10^{-11} \cdot \exp(\frac{120}{T_g})$ (Sander et al. 2003)
	$O(^1D) + CO \leftrightarrow O + CO$	$3.2 \cdot 10^{-11} \cdot \exp(\frac{70}{T_g})$ (see 4.4.2)
	$O(^1D) + O \leftrightarrow O + O$	$8 \cdot 10^{-12}$ (Capitelli et al. 2000)
	$O(^1D) + C \leftrightarrow O + C$	$8 \cdot 10^{-12}$ (see 4.4.2)
	$O(^1D) + O^+ \leftrightarrow O + O^+$	$8 \cdot 10^{-12}$ (see 4.4.2)
	$O(^1D) + C^+ \leftrightarrow O + C^+$	$8 \cdot 10^{-12}$ (see 4.4.2)
Quenching of $O(^1S)$		
	$O(^1S) + O_2 \leftrightarrow O + O_2$	$2.76 \cdot 10^{-12} \cdot \exp(-\frac{208}{T_g})$ (T G Slanger and Black 1978b; Slanger, Wood, and Black 1972)
	$O(^1S) + O_2 \leftrightarrow O(^1D) + O_2$	$1.24 \cdot 10^{-12} \cdot \exp(-\frac{208}{T_g})$ (T G Slanger and Black 1978b; Slanger et al. 1972)
	$O(^1S) + O_2(a_1) \leftrightarrow O + O_2(4.5\ eV)$	$1.1 \cdot 10^{-10}$ (Capitelli et al. 2000)
	$O(^1S) + O_2(a_1) \leftrightarrow O(^1D) + O_2(b_1)$	$2.9 \cdot 10^{-11}$ (Capitelli et al. 2000)
	$O(^1S) + O_2(a_1) \leftrightarrow O + O + O$	$3.2 \cdot 10^{-11}$ (Capitelli et al. 2000)
	$O(^1S) + CO_2 \leftrightarrow O + CO_2$	$0.37 \times 3.6 \cdot 10^{-13}$ (Filseth et al. 1970; T G Slanger and Black 1978a)
	$O(^1S) + CO_2 \leftrightarrow O(^1D) + CO_2$	$0.63 \times 3.6 \cdot 10^{-13}$ (Filseth et al. 1970; T G Slanger and Black 1978a)
	$O(^1S) + CO \leftrightarrow O + CO$	$0.69 \cdot 10^{-14}$ (Filseth et al. 1970)
	$O(^1S) + CO \leftrightarrow O(^1D) + CO$	$0.31 \cdot 10^{-14}$ (Filseth et al. 1970)
	$O(^1S) + O \leftrightarrow O + O$	$2.5 \times 5 \cdot 10^{-11} \cdot \exp(-\frac{73.4}{T_g})$ (Slanger and Black 1976)
	$O(^1S) + O \leftrightarrow O(^1D) + O$	$2.5 \times 5 \cdot 10^{-11} \cdot \exp(-\frac{73.4}{T_g})$ (Slanger and Black 1976)
	$O(^1S) + C \leftrightarrow O + C$	$2.5 \times 5 \cdot 10^{-11} \cdot \exp(-\frac{73.4}{T_g})$ (see 4.4.2.4)
	$O(^1S) + C \leftrightarrow O(^1D) + C$	$2.5 \cdot 10^{-11} \cdot \exp(-\frac{73.4}{T_g})$ (see 4.4.2.4)
	$O(^1S) + O^+ \leftrightarrow O + O^+$	$2.5 \cdot 10^{-11} \cdot \exp(-\frac{73.4}{T_g})$ (see 4.4.2.4)
	$O(^1S) + O^+ \leftrightarrow O(^1D) + O^+$	$2.5 \cdot 10^{-11} \cdot \exp(-\frac{73.4}{T_g})$ (see 4.4.2.4)
	$O(^1S) + C^+ \leftrightarrow O + C^+$	$2.5 \cdot 10^{-11} \cdot \exp(-\frac{73.4}{T_g})$ (see 4.4.2.4)
	$O(^1S) + C^+ \leftrightarrow O(^1D) + C^+$	$2.5 \cdot 10^{-11} \cdot \exp(-\frac{73.4}{T_g})$ (see 4.4.2.4)
Quenching of C*: $C(^1D)$, $C(^1S)$, $C(^5S_0)$		
	$C^* + O_2 \leftrightarrow C + O_2$	$4 \cdot 10^{-12} \cdot \exp(-\frac{208}{T_g})$ (see 4.4.2.4)
	$C^* + CO_2 \leftrightarrow C + CO_2$	$3.6 \cdot 10^{-13}$ (see 4.4.2.4)

	$C^* + CO \leftrightarrow C + CO$	10^{-14} (see 4.4.2.4)
	$C^* + O \leftrightarrow C + O$	$5 \cdot 10^{-11} \cdot \exp(-\frac{73.4}{T_g})$ (see 4.4.2.4)
	$C^* + C \leftrightarrow C + C$	$5 \cdot 10^{-11} \cdot \exp(-\frac{73.4}{T_g})$ (see 4.4.2.4)
	$C^* + O^+ \leftrightarrow C + O^+$	$5 \cdot 10^{-11} \cdot \exp(-\frac{73.4}{T_g})$ (see 4.4.2.4)
	$C^* + C^+ \leftrightarrow C + C^+$	$5 \cdot 10^{-11} \cdot \exp(-\frac{73.4}{T_g})$ (see 4.4.2.4)

Table C-5. Charge transfer reactions (ion – neutral reactions).

(I1)	$O^+ + CO_2 \leftrightarrow O_2^+ + CO$	$9.4 \cdot 10^{-10}$ (Kozàk and Bogaerts 2014)
(I2)	$O + CO_2^+ \leftrightarrow O^+ + CO_2$	$9.62 \cdot 10^{-11}$ (McElroy et al. 2013)
(I3)	$C^+ + CO_2 \leftrightarrow CO^+ + CO$	$9.62 \cdot 10^{-9}$ (McElroy et al. 2013)
(I4)	$CO^+ + CO_2 \leftrightarrow CO_2^+ + CO$	10^{-9} (Kozàk and Bogaerts 2014)
(I5)	$O + CO^+ \leftrightarrow O^+ + CO$	$1.4 \cdot 10^{-10}$ (Kozàk and Bogaerts 2014)
(I6)	$C^+ + CO \leftrightarrow C + CO^+$	$1.66 \cdot 10^{-11} \cdot \exp(-\frac{31{,}400}{T_g})$ (Park et al. 1994)
(I7)	$O_2^+ + C \leftrightarrow CO^+ + O$	$5.2 \cdot 10^{-11}$ (Kozàk and Bogaerts 2014)
(I8)	$O_2^+ + C \leftrightarrow C^+ + O_2$	$5.2 \cdot 10^{-11}$ (Kozàk and Bogaerts 2014)
(I9)	$CO_2^+ + O \leftrightarrow CO + O_2^+$	$1.64 \cdot 10^{-10}$ (Kozàk and Bogaerts 2014)
(I10)	$CO_2^+ + O_2 \leftrightarrow CO_2 + O_2^+$	$5.3 \cdot 10^{-11}$ (Kozàk and Bogaerts 2014)
(I11)	$CO^+ + O_2 \leftrightarrow CO + O_2^+$	$1.2 \cdot 10^{-10}$ (Kozàk and Bogaerts 2014)
(I12)	$C^+ + O_2 \leftrightarrow CO + O^+$	$4.54 \cdot 10^{-10}$ (McElroy et al. 2013)
(I13)	$C^+ + O_2 \leftrightarrow CO^+ + O$	$3.42 \cdot 10^{-10}$ (McElroy et al. 2013)
(I14)	$O + O_2^+ \leftrightarrow O^+ + O_2$	$6.64 \cdot 10^{-12} \cdot T_g^{-0.09} \cdot \exp(-\frac{18{,}000}{T_g})$ (Park et al. 1994)
(I15)	$C + O^+ \leftrightarrow C^+ + O$	$1.16 \cdot 10^{-9}$ Langevin reaction rate coefficient (Haynes et al. 2016)

Table C-6. Optical transitions.

	$O^+ + e^- + h\nu \rightarrow O$	$1.78 \cdot 10^{-13} \cdot T_e^{-0.52}$ (Park et al. 1994)
	$C^+ + e^- + h\nu \rightarrow C$	$3.35 \cdot 10^{-13} \cdot T_e^{-0.46}$ (Park et al. 1994)

Appendix D Sensitivity analysis of the kinetic model

In this section, we evaluate the impact of some important assumptions made in Model 4 (presented in Sections 4.4 and 4.5), which was used to simulate the TS and NTS formation. At first, we assess the impact of the $T_v = T_g$ assumption, by comparing with the results obtained with the opposite assumption, $T_v = T_e$. Then, we assess the sensitivity of our results to the initial electron density ($n_{e,0}$). Finally, we implement a pressure relaxation term to assess the validity of the isochore hypothesis.

T_v assumption

In our model, T_v impacts the dissociation reactions (N1) $CO_2 + M \rightarrow CO + O + M$, (N5) $CO + M \rightarrow O + C + M$, (N6) $O_2 + M \rightarrow O + O + M$. In Figure 5-6, we compare the simulation results at $T_v = T_g$ and $T_v = T_e$ in the NTS ($T_0 = 650$ K). At the beginning of the discharge, the case $T_v = T_e$ results in a higher CO_2 dissociation and lower gas temperature. Nevertheless, after 8 ns, the densities of both cases agree within 20%, and the gas temperature within 30%. The energy efficiency of CO production is 20% in the case $T_v = T_g$, and 24% in the case $T_v = T_e$. Therefore, even when accelerated by a highly nonequilibrium vibrational excitation, the dissociation reactions by heavy collisions have a negligible impact on the NTS during the first 20 ns.

In Figure 5-7, we compare the simulation results at $T_v = T_g$ and $T_v = T_e$ in the TS ($T_0 = 1100$ K). As for the NTS, at the beginning of the discharge, the case $T_v = T_e$ results in a higher CO_2 dissociation and lower gas temperature. Nevertheless, after 4 ns, the densities of both cases agree within 10%, and after 7 ns the gas temperatures are equal. Thus, the vibrational temperature has a negligible impact on the TS formation.

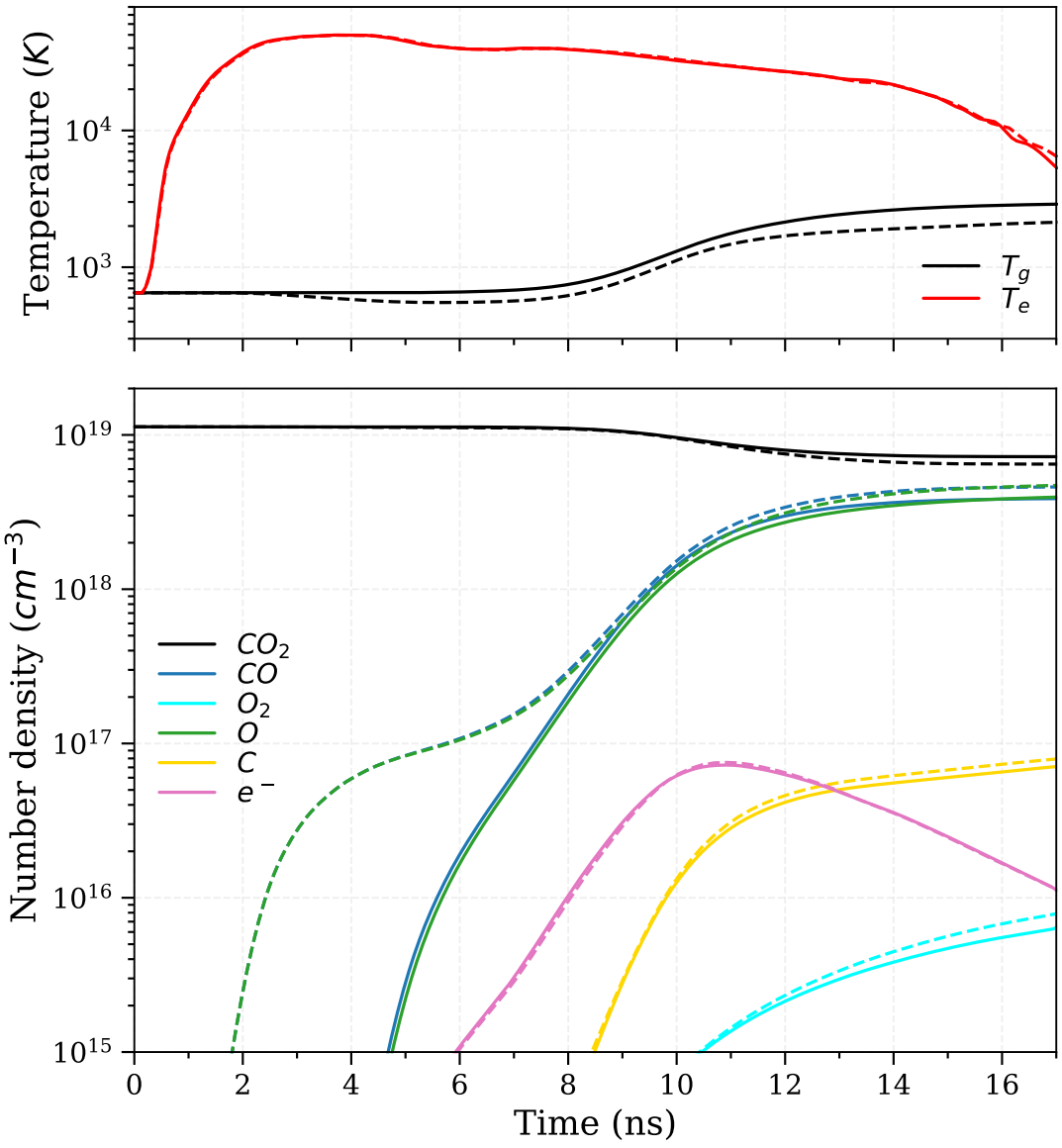

Figure 5-6. Comparison of the non-thermal spark simulations (T_0 = 650 K) for $T_v = T_g$ (solid lines) and $T_v = T_e$ (dashed lines).

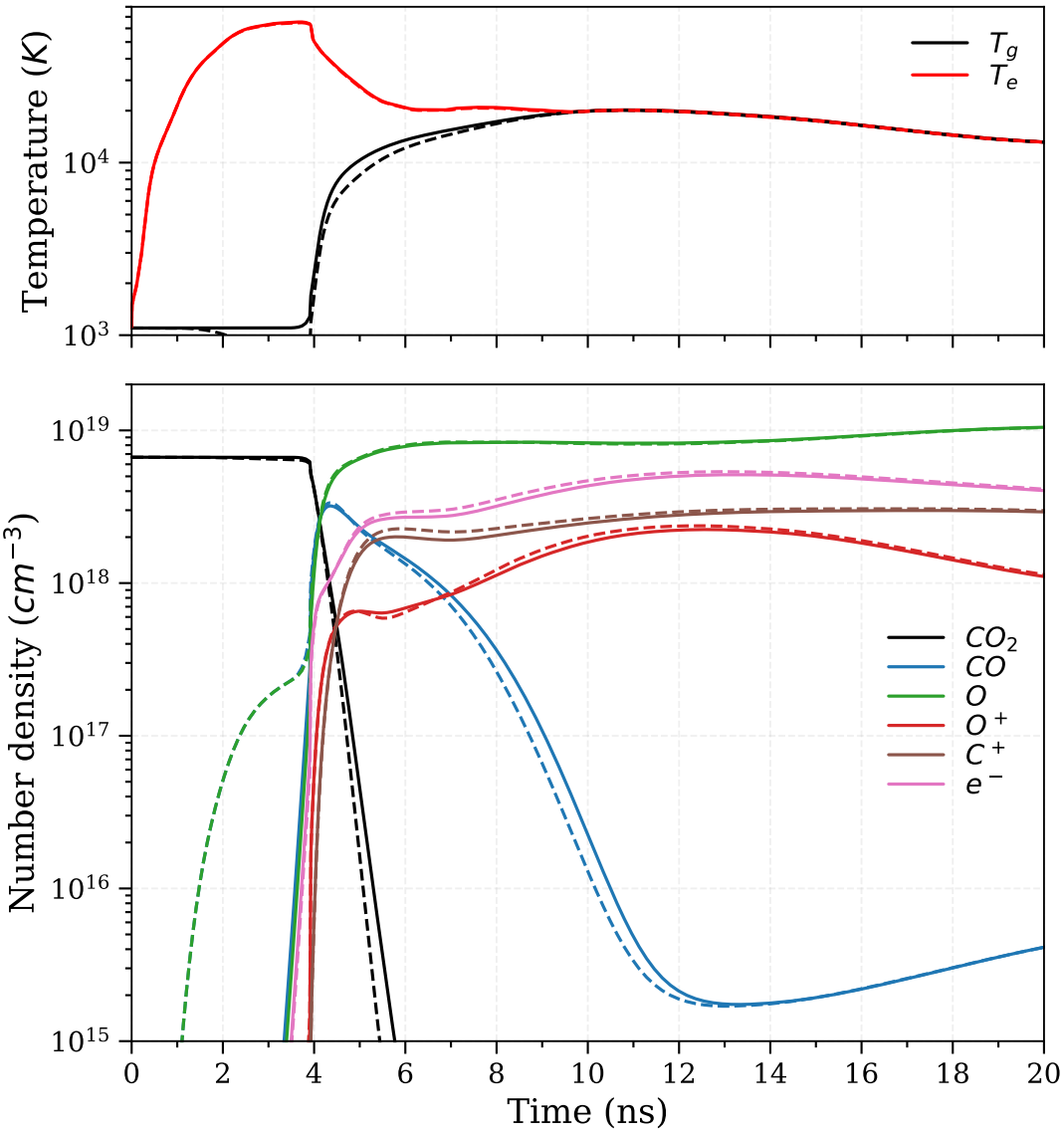

Figure 5-7. Comparison of the thermal spark simulations (T_0 = 1100 K) for $T_v = T_g$ (solid lines) and $T_v = T_e$ (dashed lines).

Sensitivity to the initial electron density

The initial electron density in our conditions was not measured, but estimated to be around 10^{10} cm^{-3}. To assess the impact of this initial density on the transition, we show in Figure 5-8 the calculated peak electron density as a function of T_0 and $n_{e,0}$. At $T_0 \leq 600$ K, the initial electron density has a significant impact on the peak electron density reached: Changin n_{e0} from 10^8 to 10^{10} cm^{-3} increases n_e^{peak} from 10^{14} to 10^{16} cm^{-3}. Nevertheless, for $T_0 \geq 700$ K, n_{e0} has little influence on the peak electron density. Thus, whatever the initial electron density between 10^8 and 10^{12} cm^{-3}, the transition to the thermal spark occurs around $T_0 \geq 900$ K.

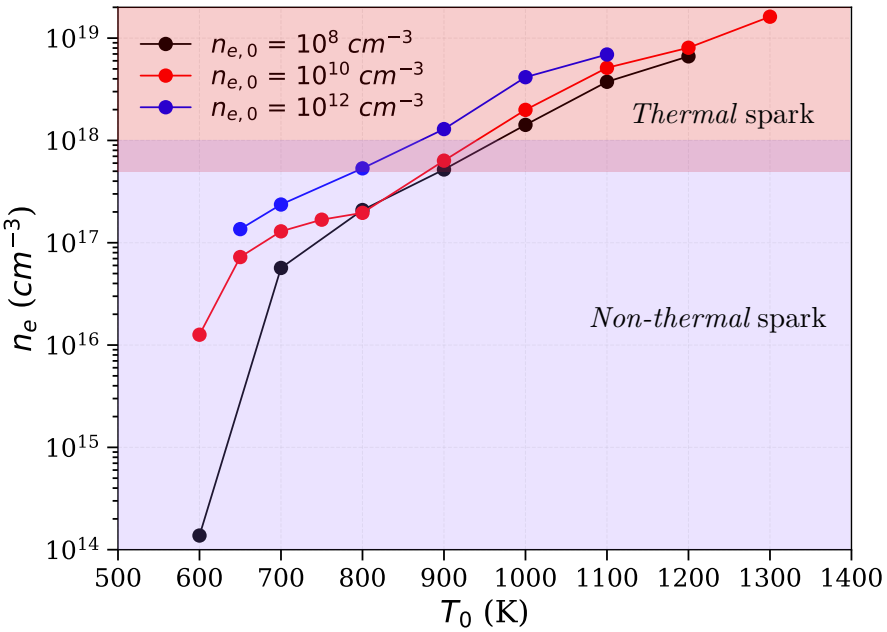

Figure 5-8. Peak electron density given by the simulations for different T_0 and $n_{e,0}$ inputs.

References

Aerts, Robby, Wesley Somers, and Annemie Bogaerts. 2015. "Carbon Dioxide Splitting in a Dielectric Barrier Discharge Plasma: A Combined Experimental and Computational Study." *ChemSusChem* 8(4):702–16. doi: 10.1002/cssc.201402818.

Albrecht, H., W. H. Bloss, W. Herden, R. Maly, B. Saggau, and E. Wagner. 1977. "New Aspects on Spark Ignition." in *SAE Technical Papers*. Vol. 9.

Allah, Zaenab Abd, and J. Christopher Whitehead. 2015. "Plasma-Catalytic Dry Reforming of Methane in an Atmospheric Pressure AC Gliding Arc Discharge." *Catalysis Today* 256(P1):76–79. doi: 10.1016/j.cattod.2015.03.040.

Appel, Aaron M., John E. Bercaw, Andrew B. Bocarsly, Holger Dobbek, Daniel L. DuBois, Michel Dupuis, James G. Ferry, Etsuko Fujita, Russ Hille, Paul J. A. Kenis, Cheryl A. Kerfeld, Robert H. Morris, Charles H. F. Peden, Archie R. Portis, Stephen W. Ragsdale, Thomas B. Rauchfuss, Joost N. H. Reek, Lance C. Seefeldt, Rudolf K. Thauer, and Grover L. Waldrop. 2013. "Frontiers, Opportunities, and Challenges in Biochemical and Chemical Catalysis of CO 2 Fixation." *Chemical Reviews* 113(8):6621–58. doi: 10.1021/cr300463y.

Aresta, Michele, Angela Dibenedetto, and Antonella Angelini. 2014. "Catalysis for the Valorization of Exhaust Carbon: From CO2 to Chemicals, Materials, and Fuels. Technological Use of CO2." *Chemical Reviews* 114(3):1709–42. doi: 10.1021/cr4002758.

Ashford, Bryony, and Xin Tu. 2017. "Non-Thermal Plasma Technology for the Conversion of CO2." *Current Opinion in Green and Sustainable Chemistry* 3:45–49. doi: 10.1016/j.cogsc.2016.12.001.

Azizov, R. ~I., A. ~K. Vakar, V. ~K. Zhivotov, M. ~F. Krotov, O. ~A. Zinov'ev, B. ~V. Potapkin, A. ~A. Rusanov, V. ~D. Rusanov, and A. ~A. Fridman. 1983. "The Nonequilibrium Plasmachemical Process of Decomposition of CO2 in a Supersonic SHF Discharge." *Soviet Physics Doklady* 28:567.

Bacri, J., and A. Medani. 1980. "Electron Diatomic Molecule Weighted Total Cross Section Calculation." *Physica B+C* 101(3):399–409. doi: 10.1016/0378-4363(80)90037-6.

Bacri, J., and A. Medani. 1982. "Electron Diatomic Molecule Weighted Total Cross Section Calculation. III. Main Inelastic Processes for N2 and N+2." *Physica B+C* 112(1):101–18. doi: 10.1016/0378-4363(82)90136-X.

Bak, Moon Soo, Seong-kyun Im, and Mark A. Cappelli. 2015. "Nanosecond-Pulsed Discharge Plasma Splitting of Carbon Dioxide." *IEEE Transactions on Plasma Science* 43(4):1–6. doi: 10.1109/TPS.2015.2408344.

Van Den Bekerom, D. C. M., J. M. Palomare. Linares, T. Verreycken, E. M. Van Veldhuizen, S. Nijdam, G. Berden, W. A. Bongers, M. C. M. Van De Sanden, and G. J. Van Rooij. 2019. "The Importance of Thermal Dissociation in CO2 Microwave Discharges Investigated by Power Pulsing and Rotational Raman Scattering." *Plasma Sources Science and Technology* 28(5):055015. doi: 10.1088/1361-6595/aaf519.

Belov, Igor, Jens Vanneste, Morteza Aghaee, and Sabine Paulussen. 2016. "Synthesis of Micro- and

Nanomaterials in CO2 and CO Dielectric Barrier Discharges." *Plasma Processes and Polymers* 14(1600065):1–14.

Belov, Igor, Vincent Vermeiren, Sabine Paulussen, and Annemie Bogaerts. 2018. "Carbon Dioxide Dissociation in a Microwave Plasma Reactor Operating in a Wide Pressure Range and Different Gas Inlet Configurations." *Journal of CO2 Utilization* 24. doi: 10.1016/j.jcou.2017.12.009.

Berthelot, Antonin, and Annemie Bogaerts. 2017. "Modeling of CO2 Splitting in a Microwave Plasma: How to Improve the Conversion and Energy Efficiency." *Journal of Physical Chemistry C* 121(15):8236–51. doi: 10.1021/acs.jpcc.6b12840.

Biberman, LM, VS Vorob'ev, and IT Yakubov. 1987. *Kinetics of Ionization and Recombination.* Springer New York, NY.

Biondo, Omar, Chloé Fromentin, Tiago Silva, Vasco Guerra, Gerard van Rooij, and Annemie Bogaerts. 2022. "Insights into the Limitations to Vibrational Excitation of CO 2 : Validation of a Kinetic Model with Pulsed Glow Discharge Experiments." *Plasma Sources Science and Technology* 31(7):074003. doi: 10.1088/1361-6595/ac8019.

Blauer, J., and G. Nickerson. 1974. "A Survey of Vibrational Relaxation Rate Data for Processes Important to CO2-N2-H2O Infrared Plume Radiation." in *7th Fluid and PlasmaDynamics Conference*. American Institute of Aeronautics and Astronautics.

Bogaerts, Annemie, Xin Tu, J. Christopher Whitehead, Gabriele Centi, Leon Lefferts, Olivier Guaitella, Federico Azzolina-Jury, Hyun Ha Kim, Anthony B. Murphy, William F. Schneider, Tomohiro Nozaki, Jason C. Hicks, Antoine Rousseau, Frederic Thevenet, Ahmed Khacef, and Maria Carreon. 2020. "The 2020 Plasma Catalysis Roadmap." *Journal of Physics D: Applied Physics* 53(44). doi: 10.1088/1361-6463/ab9048.

Bongers, Waldo, Henny Bouwmeester, Bram Wolf, Floran Peeters, Stefan Welzel, Dirk van den Bekerom, Niek den Harder, Adelbert Goede, Martijn Graswinckel, Pieter Willem Groen, Jochen Kopecki, Martina Leins, Gerard van Rooij, Andreas Schulz, Matthias Walker, and Richard van de Sanden. 2017. "Plasma-Driven Dissociation of CO2 for Fuel Synthesis." *Plasma Processes and Polymers* 14(6):1–8. doi: 10.1002/ppap.201600126.

Britun, Nikolay, Tiago Silva, Guoxing Chen, Thomas Godfroid, Joost van der Mullen, and Rony Snyders. 2018. "Plasma-Assisted CO2 Conversion: Optimizing Performance via Microwave Power Modulation." *Journal of Physics D: Applied Physics* 51(14):144002. doi: 10.1088/1361-6463/AAB1AD.

Butylkin, I. P., V. K. Zhivotov, E. G. Krasheninnikov, M. F. Krotov, V. D. Rusanov, Iu. V. Tarasov, and A. A. Fridman. 1981. "Plasma-Chemical Process of CO2 Dissociation in a Nonequilibrium Microwave Discharge." *Zhurnal Tekhnicheskoi Fiziki* 51:925–31. doi: 1981ZhTFi..51..925B.

Calvin, Katherine, Dipak Dasgupta, Gerhard Krinner, Aditi Mukherji, Peter W. Thorne, Christopher Trisos, José Romero, Paulina Aldunce, Ko Barrett, Gabriel Blanco, William W. L. Cheung, Sarah Connors, Fatima Denton, Aïda Diongue-Niang, David Dodman, Matthias Garschagen, Oliver Geden, Bronwyn Hayward, Christopher Jones, Frank Jotzo, Thelma Krug, Rodel Lasco, Yune-Yi Lee, Valérie Masson-Delmotte, Malte Meinshausen, Katja Mintenbeck, Abdalah Mokssit, Friederike E. L. Otto, Minal Pathak, Anna Pirani, Elvira Poloczanska, Hans-Otto Pörtner, Aromar Revi, Debra C. Roberts, Joyashree Roy, Alex C. Ruane, Jim Skea, Priyadarshi R. Shukla, Raphael Slade, Aimée Slangen, Youba Sokona, Anna A. Sörensson, Melinda Tignor, Detlef van Vuuren, Yi-Ming Wei,

Harald Winkler, Panmao Zhai, Zinta Zommers, Jean-Charles Hourcade, Francis X. Johnson, Shonali Pachauri, Nicholas P. Simpson, Chandni Singh, Adelle Thomas, Edmond Totin, Andrés Alegría, Kyle Armour, Birgit Bednar-Friedl, Kornelis Blok, Guéladio Cissé, Frank Dentener, Siri Eriksen, Erich Fischer, Gregory Garner, Céline Guivarch, Marjolijn Haasnoot, Gerrit Hansen, Mathias Hauser, Ed Hawkins, Tim Hermans, Robert Kopp, Noëmie Leprince-Ringuet, Jared Lewis, Debora Ley, Chloé Ludden, Leila Niamir, Zebedee Nicholls, Shreya Some, Sophie Szopa, Blair Trewin, Kaj-Ivar van der Wijst, Gundula Winter, Maximilian Witting, Arlene Birt, and Meeyoung Ha. 2023. *IPCC, 2023: Climate Change 2023: Synthesis Report. Contribution of Working Groups I, II and III to the Sixth Assessment Report of the Intergovernmental Panel on Climate Change [Core Writing Team, H. Lee and J. Romero (Eds.)]. IPCC, Geneva, Switzerland.* edited by P. Arias, M. Bustamante, I. Elgizouli, G. Flato, M. Howden, C. Méndez-Vallejo, J. J. Pereira, R. Pichs-Madruga, S. K. Rose, Y. Saheb, R. Sánchez Rodríguez, D. Ürge-Vorsatz, C. Xiao, N. Yassaa, J. Romero, J. Kim, E. F. Haites, Y. Jung, R. Stavins, A. Birt, M. Ha, D. J. A. Orendain, L. Ignon, S. Park, Y. Park, A. Reisinger, D. Cammaramo, A. Fischlin, J. S. Fuglestvedt, G. Hansen, C. Ludden, V. Masson-Delmotte, J. B. R. Matthews, K. Mintenbeck, A. Pirani, E. Poloczanska, N. Leprince-Ringuet, and C. Péan. doi: 10.59327/IPCC/AR6-9789291691647.

Capitelli, M., G. Colonna, D. Giordano, L. Marraffa, A. Casavola, P. Minelli, D. Pagano, L. D. Pietanza, and F. Taccogna. 2005. *Tables of Internal Partition Functions and Thermodynamic Properties of High-Temperature Mars-Atmosphere Species from 50K to 50000K.*

Capitelli, Mario, Carlos M. Ferreira, Boris F. Gordiets, and Alexey I. Osipov. 2000. *Plasma Kinetics in Atmospheric Gases.* Vol. 31. Berlin, Heidelberg: Springer Berlin Heidelberg.

Carbone, Emile, Federico D'Isa, Ante Hecimovic, and Ursel Fantz. 2020. "Analysis of the C2 (D3 Πg-A3 Πu) Swan Bands as a Thermometric Probe in CO2 Microwave Plasmas." *Plasma Sources Science and Technology* 29(5). doi: 10.1088/1361-6595/ab74b4.

Castela, Maria, Sergey Stepanyan, Benoit Fiorina, Axel Coussement, Olivier Gicquel, Nasser Darabiha, and Christophe O. Laux. 2017. "A 3-D DNS and Experimental Study of the Effect of the Recirculating Flow Pattern inside a Reactive Kernel Produced by Nanosecond Plasma Discharges in a Methane-Air Mixture." *Proceedings of the Combustion Institute* 36(3):4095–4103. doi: 10.1016/j.proci.2016.06.174.

Centi, Gabriele, Elsje Alessandra Quadrelli, and Siglinda Perathoner. 2013. "Catalysis for CO2 Conversion: A Key Technology for Rapid Introduction of Renewable Energy in the Value Chain of Chemical Industries." *Energy & Environmental Science* 6(6):1711. doi: 10.1039/c3ee00056g.

Ceppelli, M., T. P. W. Salden, L. M. Martini, G. Dilecce, and P. Tosi. 2021. "Time-Resolved Optical Emission Spectroscopy in CO2 Nanosecond Pulsed Discharges." *Plasma Sources Science and Technology* 30(11). doi: 10.1088/1361-6595/ac2411.

Chen, Francis F., and Jane P. Chang. 2003. *Lecture Notes on Principles of Plasma Processing.* Springer Science & Business Media.

Chen, Guoxing, Thomas Godfroid, Nikolay Britun, Violeta Georgieva, Marie Paule Delplancke-Ogletree, and Rony Snyders. 2017. "Plasma-Catalytic Conversion of CO2 and CO2/H2O in a Surface-Wave Sustained Microwave Discharge." *Applied Catalysis B: Environmental* 214:114–25. doi: 10.1016/j.apcatb.2017.05.032.

Chen, Guoxing, Rony Snyders, and Nikolay Britun. 2021. "CO2 conversion Using Catalyst-Free and Catalyst-Assisted Plasma-Processes: Recent Progress and Understanding." *Journal of CO2*

Utilization 49(March):101557. doi: 10.1016/j.jcou.2021.101557.

Chen, Zhichao, Fuchun Liu, Bo Jiang, Xueming Yang, and David H. Parker. 2010. "Imaging CO2 Photodissociation at 157 Nm: State-to-State Correlations between CO(ν) and O(3Pj =0,1,2)." *Journal of Physical Chemistry Letters* 1(12):1861–65. doi: 10.1021/jz100356f.

Cossart-Magos, Claudina, Sydney Leach, Michèle Eidelsberg, Françoise Launay, and François Rostas. 1982. "Rotationally Resolved Rydberg Absorption of CO 2 at 1106 Å. Assignment and Analysis of the Π3g3pπu 3Σu- ← X1Σg+ Transition." *J. Chem. Soc., Faraday Trans. 2* 78(8):1477–87. doi: 10.1039/F29827801477.

Cristoforetti, G., A. De Giacomo, M. Dell'Aglio, S. Legnaioli, E. Tognoni, V. Palleschi, and N. Omenetto. 2010. "Local Thermodynamic Equilibrium in Laser-Induced Breakdown Spectroscopy: Beyond the McWhirter Criterion." *Spectrochimica Acta - Part B Atomic Spectroscopy* 65(1):86–95. doi: 10.1016/j.sab.2009.11.005.

Delikonstantis, Evangelos, Marco Scapinello, Varun Singh, Hilde Poelman, Cesare Montesano, Luca Matteo Martini, Paolo Tosi, Guy B. Marin, Kevin M. Van Geem, Vladimir V. Galvita, and Georgios D. Stefanidis. 2022. "Exceeding Equilibrium CO2Conversion by Plasma-Assisted Chemical Looping." *ACS Energy Letters* 7(6):1896–1902. doi: 10.1021/acsenergylett.2c00632.

Drawin, H. W. 1967. *COLLISION AND TRANSPORT CROSS-SECTIONS*.

Dubuet, U., E. Pannier, and C. O. Laux. 2022. "Uncertainties in Multi-Temperature Nonequilibrium Partition Functions and Application to CO2." *Journal of Quantitative Spectroscopy and Radiative Transfer* 290:108314. doi: 10.1016/j.jqsrt.2022.108314.

Dumitrache, Ciprian, Arnaud Gallant, Nicolas Minesi, Sergey Stepanyan, Gabi D. Stancu, and Christophe O. Laux. 2019. "Hydrodynamic Regimes Induced by Nanosecond Pulsed Discharges in Air: Mechanism of Vorticity Generation." *Journal of Physics D: Applied Physics* 52(36). doi: 10.1088/1361-6463/ab28f9.

Dunlea, Edward J., and A. R. Ravishankara. 2004. "Kinetic Studies of the Reactions of O(1D) with Several Atmospheric Molecules." *Physical Chemistry Chemical Physics* 6(9):2152–61. doi: 10.1039/b400247d.

Eremin, A. V, V. S. Ziborov, V. V Shumova, and D. Voiki. 1997. "Formation of O (1D) Atoms in Thermal Decomposition of CO2." *Kinetics And*.

European Parliament. 2018. "Directive (EU) 2018/2001 of the European Parliament and of the Council of 11 December 2018 on the Promotion of the Use of Energy from Renewable Sources (Recast)." *Official Journal of the European Union* 2018(L 328):82–209.

Filseth, S. V., F. Stuhl, and K. H. Welge. 1970. "Collisional Deactivation of O(1S)." *The Journal of Chemical Physics* 52(1):234–38. doi: 10.1063/1.1672671.

Fridman, Alexander. 2008. *Plasma Chemistry*. Vol. 9780521847. Cambridge University Press.

Fromentin, C., T. Silva, T. C. Dias, A. S. Morillo-Candas, O. Biondo, O. Guaitella, and V. Guerra. 2023. "Study of Vibrational Kinetics of CO2 and CO in CO2-O2 Plasmas under Non-Equilibrium Conditions." *Plasma Sources Science and Technology* 32(2). doi: 10.1088/1361-6595/acb665.

George, Adwek, Boxiong Shen, Michael Craven, Yaolin Wang, Dongrui Kang, Chunfei Wu, and Xin

Tu. 2021. “A Review of Non-Thermal Plasma Technology: A Novel Solution for CO2 Conversion and Utilization.” *Renewable and Sustainable Energy Reviews* 135(December 2019):109702. doi: 10.1016/j.rser.2020.109702.

Goodwin, David G., Harry K. Moffat, and Raymond L. Speth. 2017. “Cantera: An Object-Oriented Software Toolkit for Chemical Kinetics, Thermodynamics, and Transport Processes.”

Grebenshchikov, Sergy Yu. 2013. “Photodissociation of Carbon Dioxide in Singlet Valence Electronic States. I. Six Multiply Intersecting Ab Initio Potential Energy Surfaces.” *Journal of Chemical Physics*. doi: 10.1063/1.4808369.

Grebenshchikov, Sergy Yu, and Raffaele Borrelli. 2012. “Crossing Electronic States in the Franck−Condon Zone of Carbon Dioxide.” *The Journal of Physical Chemistry*.

Griem, Hans R. 1963. “Validity of Local Thermal Equilibrium in Plasma Spectroscopy.” *Physical Review* 131(3):1170–76. doi: 10.1103/PhysRev.131.1170.

Griem, Hans R. 1964. *Plasma Spectroscopy*. McGraw-Hill Book Company.

Grimaldi, C. 2023. “Experimental Study and Modeling of a Recombining CO2 Plasma”, PhD Thesis, Université Paris-Saclay.

Grofulović, M., T. Silva, B. L. M. Klarenaar, A. S. Morillo-Candas, O. Guaitella, R. Engeln, C. D. Pintassilgo, and Guer. 2018. “Kinetic Study of CO2 Plasmas under Non-Equilibrium Conditions. II. Input of Vibrational Energy.” *Plasma Sources Science & Technology*. doi: 10.1016/j.cej.2007.09.011.

Grofulović, Marija, Luís L Alves, and Vasco Guerra. 2016. “Electron-Neutral Scattering Cross Sections for CO2 : A Complete and Consistent Set and an Assessment of Dissociation.” *Journal of Physics D: Applied Physics* 49(39):395207. doi: 10.1088/0022-3727/49/39/395207.

Gupta, Roop N., Jerrold M. Yos, Richard A. Thompson, and Kam-Pui Lee. 1990. “A Review of Reaction Rates and Thermodynamic and Transport Properties for an 11-Species Air Model for Chemical and Thermal Nonequilibrium Calculations to 30 000 K.”

Hagelaar, G. J. M. 2015. “Coulomb Collisions in the Boltzmann Equation for Electrons in Low-Temperature Gas Discharge Plasmas.” *Plasma Sources Science and Technology* 25(1):15015. doi: 10.1088/0963-0252/25/1/015015.

Hagelaar, G. J. M., and L. C. Pitchford. 2005. “Solving the Boltzmann Equation to Obtain Electron Transport Coefficients and Rate Coefficients for Fluid Models.” *Plasma Sources Science and Technology* 14(4):722–33. doi: 10.1088/0963-0252/14/4/011.

Hake, R. D., and A. V Phelps. 1967. “Momentum-Transfer and Inelastic-Collision Cross Sections for Electrons in O2, CO, and CO2.” *Physical Review* 158(1):70–84. doi: 10.1103/PhysRev.158.70.

Hao, Leiduan, Qineng Xia, Qiang Zhang, Justus Masa, and Zhenyu Sun. 2021. “Improving the Performance of Metal-Organic Frameworks for Thermo-Catalytic CO2 Conversion: Strategies and Perspectives.” *Chinese Journal of Catalysis* 42(11):1903–20. doi: 10.1016/S1872-2067(21)63841-X.

den Harder, Niek, Dirk van den Bekerom, Richard S. Al, Martijn Graswinckel, Jose M. Palomares, Floran J. J. Peeters, Srinath Ponduri, Teofil Minea, Waldo A. Bongers, Mauritius van de Sanden, and Gerard J. van Rooij. 2016. “Homogeneous CO2 Conversion by Microwave Plasma : Wave Propagation and Diagnostics.” *Plasma Processes and Polymers* (September):1–24. doi:

10.1002/ppap.201600120.

Haynes, W. M., D. R. Lide, and T. J. Bruno. 2016. *CRC Handbook of Chemistry and Physics: A Ready-Reference Book of Chemical and Physical Data*. 97th ed. Boca Raton, Florida: CRC Press.

Heijkers, Stijn, and Annemie Bogaerts. 2017. "CO2 Conversion in a Gliding Arc Plasmatron: Elucidating the Chemistry through Kinetic Modeling." *Journal of Physical Chemistry C* 121(41):22644–55. doi: 10.1021/acs.jpcc.7b06524.

Heijkers, Stijn, Luca Matteo Martini, Giorgio Dilecce, Paolo Tosi, and Annemie Bogaerts. 2019a. "Nanosecond Pulsed Discharge for CO2 Conversion: Kinetic Modeling To Elucidate the Chemistry and Improve the Performance." *The Journal of Physical Chemistry C* 123(19):12104–16. doi: 10.1021/acs.jpcc.9b01543.

Herzberg, Gerhard. 1966. "Molecular Spectra & Molecular Structure III (Polyatomic Molecules)." *Molecular Spectra & Molecular Structure III (Polyatomic Molecules)* 307.

Ibragimova, L. B., G. D. Smekhov, O. P. Shatalov, A. V. Eremin, and V. V. Shumova. 2000. "Dissociation of CO2 Molecules in a Wide Temperature Range." *High Temperature* 38(1):33–36. doi: 10.1007/BF02755563.

Ibraguimova, L. B., B. F. Minaev, and I. S. Irgibaeva. 2014. "Spin-Orbit Coupling and Dissociation of CO2 Molecules." *Optics and Spectroscopy (English Translation of Optika i Spektroskopiya)* 117(5):695–702. doi: 10.1134/S0030400X14110095.

Ionin, A. A., I. V. Kochetov, A. P. Napartovich, and N. N. Yuryshev. 2007. "Physics and Engineering of Singlet Delta Oxygen Production in Low-Temperature Plasma." *Journal of Physics D: Applied Physics* 40(2). doi: 10.1088/0022-3727/40/2/R01.

IPCC. 2023. "Summary for Policymakers: Synthesis Report." *Climate Change 2023: Synthesis Report. Contribution of Working Groups I, II and III to the Sixth Assessment Report of the Intergovernmental Panel on Climate Change* 1–34.

Isa, F. A. D., E. A. D. Carbone, A. Hecimovic, and U. Fantz. 2020. "Performance Analysis of a 2.45 GHz Microwave Plasma Torch for CO2." *Plasma Sources Science and Technology* 29(105009).

IST-Lisbon. "IST-Lisbon Database." Retrieved from (www.lxcat.net).

Itikawa, Yukikazu. 2015. "Cross Sections for Electron Collisions with Carbon Monoxide." *Journal of Physical and Chemical Reference Data* 44(1). doi: 10.1063/1.4913926.

Jeswani, Harish K., Andrew Chilvers, and Adisa Azapagic. 2020. "Environmental Sustainability of Biofuels: A Review: Environmental Sustainability of Biofuels." *Proceedings of the Royal Society A: Mathematical, Physical and Engineering Sciences* 476(2243). doi: 10.1098/rspa.2020.0351.

Jouny, Matthew, Wesley Luc, and Feng Jiao. 2018. "General Techno-Economic Analysis of CO2 Electrolysis Systems." *Industrial and Engineering Chemistry Research* 57(6):2165–77. doi: 10.1021/acs.iecr.7b03514.

Kenner, R. D., and E. A. Ogryzlo. 1980. "Deactivation of O2(A3?U+) by O2, O, and Ar." *International Journal of Chemical Kinetics* 12(7):501–8. doi: 10.1002/kin.550120706.

Kirillov, A. S. 2013. "The Calculations of Quenching Rate Coefficients of O2(b 1σg+,v) in Collisions

with O2, N2, CO, CO2 Molecules." *Chemical Physics* 410:103–8. doi: 10.1016/j.chemphys.2012.11.012.

Kirillov, A. S. 2014. "The Calculation of Quenching Rate Coefficients of O2 Herzberg States in Collisions with CO2, CO, N2, O2 Molecules." *Chemical Physics Letters* 592:103–8. doi: 10.1016/j.cplett.2013.12.009.

Klarenaar, B. L. M., R. Engeln, D. C. M. van den Bekerom, M. C. M. van de Sanden, A. S. Morillo-Candas, and O. Guaitella. 2017. "Time Evolution of Vibrational Temperatures in a CO 2 Glow Discharge Measured with Infrared Absorption Spectroscopy." *Plasma Sources Science and Technology* 26(11):115008. doi: 10.1088/1361-6595/aa902e.

Klarenaar, B. L. M., M. Grofulović, A. S. Morillo-Candas, D. C. M. Van Den Bekerom, M. A. Damen, M. C. M. Van De Sanden, O. Guaitella, and R. Engeln. 2018. "A Rotational Raman Study under Non-Thermal Conditions in a Pulsed CO2 Glow Discharge." *Plasma Sources Science and Technology* 27(4). doi: 10.1088/1361-6595/aabab6.

Klarenaar, B. L. M., A. S. Morillo-Candas, M. Grofulović, M. C. M. Van De Sanden, R. Engeln, and O. Guaitella. 2019. "Excitation and Relaxation of the Asymmetric Stretch Mode of CO2 in a Pulsed Glow Discharge." *Plasma Sources Science and Technology* 28(3). doi: 10.1088/1361-6595/aada5e.

Knowles, Peter J., Pavel Rosmus, and Hans Joachim Werner. 1988. "On the Assignment of the Electronically Excited Singlet States in Linear CO2." *Chemical Physics Letters* 146(3–4):230–35. doi: 10.1016/0009-2614(88)87436-0.

Kossyi, I. A., A. Yu Kostinsky, A. A. Matveyev, and V. P. Silakov. 1992. "Kinetic Scheme of the Non-Equilibrium Discharge in Nitrogen-Oxygen Mixtures." *Plasma Sources Science and Technology* 1(3):207–20. doi: 10.1088/0963-0252/1/3/011.

Koyano, I., T. S. Wauchop, and K. H. Welge. 1975. "Relative Efficiencies of O(^{1} S) Production from Photodissociation of Co $_{2}$ between 1080 and 1160 Å." *The Journal of Chemical Physics* 63(1):110–13. doi: 10.1063/1.431061.

Kozák, Tomáš, and Annemie Bogaerts. 2015. "Evaluation of the Energy Efficiency of CO2 Conversion in Microwave Discharges Using a Reaction Kinetics Model." *Plasma Sources Science and Technology* 24(1):15024. doi: 10.1088/0963-0252/24/1/015024.

Kozàk, Tomàš, and Annemie Bogaerts. 2014. "Splitting of CO2by Vibrational Excitation in Non-Equilibrium Plasmas: A Reaction Kinetics Model." *Plasma Sources Science and Technology* 23(4). doi: 10.1088/0963-0252/23/4/045004.

Kramida, A., K. Olsen, and Yu. Ralchenko. 2023. "NIST LIBS Database." Retrieved (physics.nist.gov/PhysRefData/ASD/LIBS/libs-form.html).

Kramida, A., Yu. Ralchenko, J. Reader, and NIST ASD Team. 2023. "NIST Atomic Spectra Database." Retrieved (https://physics.nist.gov/asd).

Kruger, Charles H., Christophe O. Laux, Lan Yu, Denis M. Packan, and Lauent Pierrot. 2002. "Nonequilibrium Discharges in Air and Nitrogen Plasmas at Atmospheric Pressure." *Pure and Applied Chemistry* 74(3):337–47. doi: 10.1351/pac200274030337.

Laux, C. O., T. G. Spence, C. H. Kruger, and R. N. Zare. 2003. "Optical Diagnostics of Atmospheric Pressure Air Plasmas." *Plasma Sources Science and Technology* 12(2):125–38. doi: 10.1088/0963-

0252/12/2/301.

Lebouvier, Alexandre, Samuel A. Iwarere, Philippe D'Argenlieu, Deresh Ramjugernath, and Laurent Fulcheri. 2013. "Assessment of Carbon Dioxide Dissociation as a New Route for Syngas Production: A Comparative Review and Potential of Plasma-Based Technologies." *Energy and Fuels* 27(5):2712–22. doi: 10.1021/ef301991d.

Legasov, V. A., V. K. Zhivotov, E. G. Krasheninnikov, M. F. Krotov, B. I. Patrushev, V. D. Rusanov, G. V Rykunov, A. M. Spektor, A. A. Fridman, and G. V Sholin. 1978. "A Nonequilibrium Plasma-Chemical Process of CO2 Dissociation in HF and UHF Discharges." *Akademiia Nauk SSSR* 238:66–69.

Liang, Jun, Qiao Wu, Yuan Biao Huang, and Rong Cao. 2021. "Reticular Frameworks and Their Derived Materials for CO2 Conversion by Thermo−catalysis." *EnergyChem* 3(6):100064. doi: 10.1016/j.enchem.2021.100064.

Lieberman, Michael A., and Allan J. Lichtenberg. 2005. *Principles of Plasma Discharges and Materials Processing*. Vol. 30. Wiley.

Lin, Roger, Jiaxun Guo, Xiaojia Li, Poojan Patel, and Ali Seifitokaldani. 2020. *Electrochemical Reactors for CO2 Conversion*. Vol. 10.

Liu, Jing-lin, Xue Wang, Xiao-song Li, Blaž Likozar, and Ai-min Zhu. 2020. "CO 2 Conversion, Utilisation and Valorisation in Gliding Arc Plasma Reactors." *Journal of Physics D: Applied Physics* 53(25):253001. doi: 10.1088/1361-6463/ab7c04.

Lo, A., A. Cessou, C. Lacour, B. Lecordier, P. Boubert, D. A. Xu, C. O. Laux, and P. Vervisch. 2017. "Streamer-to-Spark Transition Initiated by a Nanosecond Overvoltage Pulsed Discharge in Air." *Plasma Sources Science and Technology* 26(4):045012. doi: 10.1088/1361-6595/aa5c78.

Lu, Na, Ning Liu, Chuke Zhang, Yan Su, Kefeng Shang, Nan Jiang, Jie Li, and Yan Wu. 2021. "CO2 Conversion Promoted by Potassium Intercalated G-C3N4 Catalyst in DBD Plasma System." *Chemical Engineering Journal* 417(October 2020). doi: 10.1016/j.cej.2021.129283.

Lu, Zhou, Yih Chung Chang, Yanice Benitez, Zhihong Luo, Adel Ben Houria, Tarek Ayari, Muneerah Mogren Al Mogren, M. Hochlaf, W. M. Jackson, and C. Y. Ng. 2015. "State-to-State Vacuum Ultraviolet Photodissociation Study of CO2 on the Formation of State-Correlated CO(X1Σ+; V) with O(1D) and O(1S) Photoproducts at 11.95-12.22 EV." *Physical Chemistry Chemical Physics* 17(17):11752–62. doi: 10.1039/c5cp01321f.

Luque, Alejandro. 2014. "BOLOS."

Maillard, Jean, Thomas van den Biggelaar, Erwan Pannier, and Christophe O. Laux. 2022. "Time-Resolved Optical Emission Spectroscopy Measurements of Electron Density and Temperature in CO2 Nanosecond Repetitively Pulsed Discharges." in *AIAA SCITECH 2022 Forum*. Reston, Virginia: American Institute of Aeronautics and Astronautics.

Maly, Rudolf R., and Rüdiger Herweg. 2008. "Spark Ignition and Combustion in Four-Stroke Gasoline Engines." Pp. 1–66 in *Flow and Combustion in Reciprocating Engines*. Berlin, Heidelberg: Springer Berlin Heidelberg.

Manion, J. A., R. R. Huie, E, D. Levin, D. R. Burgess Jr., V. L. Orkin, W. Tsang, W. S. McGivern, J. W. Hudgens, V. D. Knyazev, D. B. Atkinson, E. Chai, A. M. Tereza, C. Y. Lin, T. C. Allison, W.

G. Mallard, F. Westley, J. T. Herron, R. F. Hampson, and D. H. Frizzell. 2008. *NIST Chemical Kinetics Database, NIST Standard Reference Database 17, Version 7.0 (Web Version), Release 1.6.8, Data Version 2015.12, National Institute of Standards and Technology, Gaithersburg, Maryland, 20899-8320. Web Address:*

Martin-del-Campo, Jennifer, Marianna Uceda, Sylvain Coulombe, and Jan Kopyscinski. 2021. "Plasma-Catalytic Dry Reforming of Methane over Ni-Supported Catalysts in a Rotating Gliding Arc – Spouted Bed Reactor." *Journal of CO2 Utilization* 46:101474. doi: 10.1016/j.jcou.2021.101474.

Martin, William, and Wolfgang Wiese. 2006. "Atomic Spectroscopy." Pp. 175–98 in *Springer Handbook of Atomic, Molecular, and Optical Physics*. New York, NY: Springer New York.

Martini, L. M., N. Gatti, G. Dilecce, M. Scotoni, and P. Tosi. 2018. "Laser Induced Fluorescence in Nanosecond Repetitively Pulsed Discharges for CO2 Conversion." *Plasma Physics and Controlled Fusion* 60(1). doi: 10.1088/1361-6587/aa8bed.

Martini, Luca Matteo, Sara Lovascio, Giorgio Dilecce, and Paolo Tosi. 2018. "Time-Resolved CO_2 Dissociation in a Nanosecond Pulsed Discharge." *Plasma Chemistry and Plasma Processing* https://doi.org/10.1007/s11090-018-9893-3. doi: 10.1007/s11090-018-9893-3.

Masel, Richard I., Zengcai Liu, Hongzhou Yang, Jerry J. Kaczur, Daniel Carrillo, Shaoxuan Ren, Danielle Salvatore, and Curtis P. Berlinguette. 2021. "An Industrial Perspective on Catalysts for Low-Temperature CO2 Electrolysis." *Nature Nanotechnology* 16(2):118–28. doi: 10.1038/s41565-020-00823-x.

McBride, B. J., M. J. Zehe, and S. Gordon. 2002a. "NASA Glenn Coeefficients for Calculating Thermodynamic Properties of Individual Species." *NASA*. doi: NASA/TP—2002-211556.

McElroy, D., C. Walsh, A. J. Markwick, M. A. Cordiner, K. Smith, and T. J. Millar. 2013. "The UMIST Database for Astrochemistry 2012." *Astronomy and Astrophysics* 550:1–13. doi: 10.1051/0004-6361/201220465.

Mercer, E. R., S. Van Alphen, C. F. A. M. van Deursen, T. W. H. Righart, W. A. Bongers, R. Snyders, A. Bogaerts, M. C. M. van de Sanden, and F. J. J. Peeters. 2023. "Post-Plasma Quenching to Improve Conversion and Energy Efficiency in a CO2 Microwave Plasma." *Fuel* 334(P2):126734. doi: 10.1016/j.fuel.2022.126734.

Minesi, N., P. Mariotto, E. Pannier, G. D. Stancu, and C. O. Laux. 2021. "The Role of Excited Electronic States in Ambient Air Ionization by a Nanosecond Discharge." *Plasma Sources Science and Technology* 30(3):35008. doi: 10.1088/1361-6595/abe0a3.

Minesi, N., S. Stepanyan, P. Mariotto, G. D. Stancu, and C. O. Laux. 2020. "Fully Ionized Nanosecond Discharges in Air: The Thermal Spark." *Plasma Sources Science and Technology* 29(8). doi: 10.1088/1361-6595/ab94d3.

Minesi, Nicolas. 2020. "Thermal Spark Formation and Plasma-Assisted Combustion by Nanosecond Repetitive Discharges", PhD Thesis, Université Paris-Saclay.

Minesi, Nicolas Q., Pierre B. Mariotto, Erwan Pannier, Axel Vincent-Randonnier, Gabi Daniel Stancu, and Christophe O. Laux. 2023. "Kinetic Mechanism and Sub-Ns Measurements of the Thermal Spark in Air." *Plasma Sources Science and Technology* 32(4):44005. doi: 10.1088/1361-6595/acc9da.

Montesano, Cesare, Sara Quercetti, Luca Matteo Martini, Giorgio Dilecce, and Paolo Tosi. 2020. "The Effect of Different Pulse Patterns on the Plasma Reduction of CO2 for a Nanosecond Discharge." *Journal of CO2 Utilization* 39(February):101157. doi: 10.1016/j.jcou.2020.101157.

Montesano, Cesare, Toine P. W. Salden, Luca Matteo Martini, Giorgio Dilecce, and Paolo Tosi. 2023. "CO 2 Reduction by Nanosecond-Plasma Discharges: Revealing the Dissociation's Time Scale and the Importance of Pulse Sequence." *The Journal of Physical Chemistry C*. doi: 10.1021/acs.jpcc.3c02547.

Morillo-Candas, A S, C. Drag, J. P. Booth, T. C. Dias, V. Guerra, and O. Guaitella. 2020. "Oxygen Atom Kinetics in CO2 Plasmas Ignited in a DC Glow Discharge." *Plasma Sources Science & Technology* 2:0–31.

Morillo-Candas, A. S., B. L. M. Klarenaar, C. Amoedo, V. Guerra, and O. Guaitella. 2021. "Effect of Oxygen Atoms on the Vibrational Kinetics of CO 2 and CO Revealed by the Use of a Large Surface Area Material." *Journal of Physics D: Applied Physics* 54(9):095208. doi: 10.1088/1361-6463/abc992.

Morillo-Candas, A. S., T. Silva, B. L. M. Klarenaar, M. Grofulović, V. Guerra, and O. Guaitella. 2020. "Electron Impact Dissociation of CO2." *Plasma Sources Science and Technology* 29(1). doi: 10.1088/1361-6595/ab6075.

Morillo-Candas, Ana Sofia, Vasco Guerra, and Olivier Guaitella. 2020. "Time Evolution of the Dissociation Fraction in Rf CO2Plasmas: Impact and Nature of Back-Reaction Mechanisms." *Journal of Physical Chemistry C* 124(32):17459–75. doi: 10.1021/acs.jpcc.0c03354.

Naidis, G. V, and N. Yu Babaeva. 2022. "Modeling of Vibrational Excitation Dynamics in a Nanosecond CO 2 Discharge." *Journal of Physics D: Applied Physics* 55(1):015202. doi: 10.1088/1361-6463/ac9c10.

Nunnally, T., K. Gutsol, A. Rabinovich, A. Fridman, A. Gutsol, and A. Kemoun. 2011. "Dissociation of CO2 in a Low Current Gliding Arc Plasmatron." *Journal of Physics D: Applied Physics* 44(27):274009. doi: 10.1088/0022-3727/44/27/274009.

Okabe, H. 1978. "Photochemistry of Small Molecules."

Oloman, Colin, and Hui Li. 2008. "Electrochemical Processing of Carbon Dioxide." *ChemSusChem* 1(5):385–91. doi: 10.1002/cssc.200800015.

Pai, David Z., Deanna A. Lacoste, and Christophe O. Laux. 2010. "Transitions between Corona, Glow, and Spark Regimes of Nanosecond Repetitively Pulsed Discharges in Air at Atmospheric Pressure." *Journal of Applied Physics* 107(9). doi: 10.1063/1.3309758.

Pai, David Z, Deanna a Lacoste, and Christophe O. Laux. 2010. "Nanosecond Repetitively Pulsed Discharges in Air at Atmospheric Pressure—the Spark Regime." *Plasma Sources Science and Technology* 19(6):65015. doi: 10.1088/0963-0252/19/6/065015.

Pai, David Z., Gabi D. Stancu, Deanna A. Lacoste, and Christophe O. Laux. 2009. "Nanosecond Repetitively Pulsed Discharges in Air at Atmospheric Pressure—the Glow Regime." *Plasma Sources Science and Technology* 18(4):45030. doi: 10.1088/0963-0252/18/4/045030.

Pancheshnyi, S., S. Biagi, M. C. Bordage, G. J. M. Hagelaar, W. L. Morgan, A. V. Phelps, and L. C. Pitchford. 2012. "The LXCat Project: Electron Scattering Cross Sections and Swarm Parameters

for Low Temperature Plasma Modeling." *Chemical Physics* 398(1):148–53. doi: 10.1016/j.chemphys.2011.04.020.

Pancheshnyi, S., B. Eismann, G. J. M. Hagelaar, and L. C. Pitchford. 2008. "Computer Code ZDPlasKin." *University of Toulouse, LAPLACE, CNRS-UPS-INP, Toulouse, France.*

Pancheshnyi, Sergey. 2015. "Photoionization Produced by Low-Current Discharges in O2, Air, N2 and CO2." *Plasma Sources Science and Technology* 24(1):15023. doi: 10.1088/0963-0252/24/1/015023.

Pannier, Erwan. 2019. "Conversion of Carbon Dioxide with Nanosecond Pulsed Discharges.", PhD Thesis Université Paris Saclay.

Pannier, Erwan, Taemin Yong, Christophe Laux, and Mark A. Cappelli. 2022. "High-Pressure CO2 Dissociation with Nanosecond Pulsed Discharges." *Plasma Sources Science and Technology.* doi: https://doi.org/10.48550/arXiv.2211.00592.

Park, Chul, John T. Howe, Richard L. Jaffe, and Graham V. Candler. 1994. "Review of Chemical-Kinetic Problems of Future NASA Missions, II: Mars Entries." *Journal of Thermophysics and Heat Transfer* 8(1):9–23. doi: 10.2514/3.496.

Parkevich, E. V, M. A. Medvedev, G. V Ivanenkov, A. I. Khirianova, A. S. Selyukov, A. V Agafonov, Ph A. Korneev, S. Y. Gus'kov, and A. R. Mingaleev. 2019. "Fast Fine-Scale Spark Filamentation and Its Effect on the Spark Resistance." *Plasma Sources Science and Technology* 28(9):095003. doi: 10.1088/1361-6595/ab3768.

Pavan, Colin A., and Carmen Guerra-Garcia. 2023. "Modeling Flame Speed Modification by Nanosecond Pulsed Discharges to Inform Experimental Design." in *AIAA SCITECH 2023 Forum.* Reston, Virginia: American Institute of Aeronautics and Astronautics.

Pietanza, L. D., G. Colonna, and M. Capitelli. 2020. "Kinetics versus Thermodynamics on CO2 Dissociation in High Temperature Microwave Discharges." *Plasma Sources Science and Technology* 29(3). doi: 10.1088/1361-6595/ab6e5a.

Pietanza, L. D., G. Colonna, and M. Capitelli. 2022. "Non-Equilibrium Plasma Kinetics of CO2 in Glow Discharges: A Comparison with Existing Modeling and Experimental Results." *Plasma Sources Science and Technology* 31(10). doi: 10.1088/1361-6595/ac9083.

Pietanza, Lucia Daniela, Gianpiero Colonna, and Mario Capitelli. 2023. "Activation of Vibrational-Induced CO2 Dissociation in Cold Non-Equilibrium Plasma." *Plasma Physics and Controlled Fusion* 65(4). doi: 10.1088/1361-6587/acb843.

Pietanza, Lucia Daniela, Olivier Guaitella, Vincenzo Aquilanti, Iole Armenise, Annemie Bogaerts, Mario Capitelli, Gianpiero Colonna, Vasco Guerra, Richard Engeln, Elena Kustova, Andrea Lombardi, Federico Palazzetti, and Tiago Silva. 2021. "Advances in Non-Equilibrium CO2 Plasma Kinetics: A Theoretical and Experimental Review." *European Physical Journal D* 75(9):1–55. doi: 10.1140/epjd/s10053-021-00226-0.

Pitchford, Leanne C., Luis L. Alves, Klaus Bartschat, Stephen F. Biagi, Marie Claude Bordage, Igor Bray, Chris E. Brion, Michael J. Brunger, Laurence Campbell, Alise Chachereau, Bhaskar Chaudhury, Loucas G. Christophorou, Emile Carbone, Nikolay A. Dyatko, Christian M. Franck, Dmitry V. Fursa, Reetesh K. Gangwar, Vasco Guerra, Pascal Haefliger, Gerjan J. M. Hagelaar,

Andreas Hoesl, Yukikazu Itikawa, Igor V. Kochetov, Robert P. McEachran, W. Lowell Morgan, Anatoly P. Napartovich, Vincent Puech, Mohamed Rabie, Lalita Sharma, Rajesh Srivastava, Allan D. Stauffer, Jonathan Tennyson, Jaime de Urquijo, Jan van Dijk, Larry A. Viehland, Mark C. Zammit, Oleg Zatsarinny, and Sergey Pancheshnyi. 2017. "LXCat: An Open-Access, Web-Based Platform for Data Needed for Modeling Low Temperature Plasmas." *Plasma Processes and Polymers* 14(1–2). doi: 10.1002/ppap.201600098.

Pokrovskiy, Georgy. 2021. "Dissociation of Carbon Dioxide in Pulsed Plasma at High Electric Fields : Role of Energy Exchange with Electronically Excited Species."

Pokrovskiy, Georgy Vadimovich, Nikolay A. Popov, and Svetlana M. Starikovskaia. 2022. "Fast Gas Heating and Kinetics of Electronically Excited States in a Nanosecond Capillary Discharge in CO 2." *Plasma Sources Science and Technology* 149(3):543–47. doi: 10.1088/1361-6595/ac5102.

Qiao, Jinli, Yuyu Liu, Feng Hong, and Jiujun Zhang. 2014. *A Review of Catalysts for the Electroreduction of Carbon Dioxide to Produce Low-Carbon Fuels*. Vol. 43.

Qin, Yue, Guanghui Niu, Xu Wang, Daibing Luo, and Yixiang Duan. 2020. "Conversion of CO2 in a Low-Powered Atmospheric Microwave Plasma: In-Depth Study on the Trade-off between CO2 Conversion and Energy Efficiency." *Chemical Physics* 538(March):110913. doi: 10.1016/j.chemphys.2020.110913.

Raizer, Yuri P. 1991. "Gas Discharge Physics" edited by J. E. Allen. doi: 10.1007/978-3-642-61247-3.

Raposo, G., A. W. Van De Steeg, E. R. Mercer, C. F. A. M. Van Deursen, H. J. L. Hendrickx, W. A. Bongers, G. J. Van Rooij, M. C. M. Van De Sanden, and F. J. J. Peeters. 2021. "Flame Bands: CO + O Chemiluminescence as a Measure of Gas Temperature." *Journal of Physics D: Applied Physics* 54(37). doi: 10.1088/1361-6463/ac0924.

Ray, Debjyoti, Piu Chawdhury, and Ch Subrahmanyam. 2020. "A Facile Method to Decompose CO2 Using a G-C3N4-Assisted DBD Plasma Reactor." *Environmental Research* 183(October 2019):109286. doi: 10.1016/j.envres.2020.109286.

Ray, Debjyoti, and Ch Subrahmanyam. 2016. "CO2 Decomposition in a Packed DBD Plasma Reactor: Influence of Packing Materials." *RSC Advances* 6(45):39492–99. doi: 10.1039/c5ra27085e.

Ren, Shaoxuan, Dorian Joulié, Danielle Salvatore, Kristian Torbensen, Min Wang, Marc Robert, and Curtis P. Berlinguette. 2019. "Molecular Electrocatalysts Can Mediate Fast, Selective CO2 Reduction in a Flow Cell." *Science* 365(6451):367–69. doi: 10.1126/science.aax4608.

Renninger, Stephan, Maike Lambarth, and Kai Peter Birke. 2020. "High Efficiency CO2-Splitting in Atmospheric Pressure Glow Discharge." *Journal of CO2 Utilization* 42(October). doi: 10.1016/j.jcou.2020.101322.

Roger, E. 2023. "Kinetic and Hydrodynamic Modeling of Active Species in NRP Discharges." Université Paris-Saclay.

van Rooij, G. J., H. N. Akse, W. A. Bongers, and M. C. M. van de Sanden. 2018. "Plasma for Electrification of Chemical Industry: A Case Study on CO2 Reduction." *Plasma Physics and Controlled Fusion* 60(1):14019. doi: 10.1088/1361-6587/aa8f7d.

van Rooij, G. J., D. C. M. M. van den Bekerom, N. Den Harder, T. Minea, G. Berden, W. A. Bongers,

R. Engeln, M. F. Graswinckel, E. Zoethout, and M. C. M. M. Van De Sanden. 2015. “Taming Microwave Plasma to Beat Thermodynamics in CO2 Dissociation.” *Faraday Discussions* 183:233–48. doi: 10.1039/C5FD00045A.

Rusanov, V. D., A. A. Fridman, and G. V. Sholin. 1981a. “The Physics of a Chemically Active Plasma with Nonequilibrium Vibrational Excitation of Molecules.” *Soviet Physics Uspekhi* 24(6):447–74. doi: 10.1070/PU1981v024n06ABEH004884.

Rusterholtz, D. L., D. a Lacoste, G. D. Stancu, D. Z. Pai, and C. O. Laux. 2013. “Ultrafast Heating and Oxygen Dissociation in Atmospheric Pressure Air by Nanosecond Repetitively Pulsed Discharges.” *Journal of Physics D: Applied Physics* 46(46):464010. doi: 10.1088/0022-3727/46/46/464010.

Sainct, Florent P., Keiichiro Urabe, Erwan Pannier, Deanna A. Lacoste, and Christophe O. Laux. 2020. “Electron Number Density Measurements in Nanosecond Repetitively Pulsed Discharges in Water Vapor at Atmospheric Pressure.” *Plasma Sources Science and Technology* 29(2). doi: 10.1088/1361-6595/ab681b.

Salden A, Budde M, Garcia-Soto C A, Biondo O, Barauna J, Faedda M, Musig B, Guaitella O, et al., Meta-analysis of CO2 conversion, energy efficiency and other performance data of plasma-catalysis reactors with the open access PIONEER database, *Journal of Energy Chemistry* (2023) 10.1016/j.jechem.2023.07.022

Sander, S. P., R. R. Friedl, A. R. Ravishankara, D. M. Golden, C. E. Kolb, M. J. Kurylo, R. E. Huie, V. L. Orkin, M. J. Molina, G. K. Moortgat, and B. J. Finlayson-Pitts. 2003. “Chemical Kinetics and Photochemical Data for Use in Atmospheric Studies, Evaluation Number 14, JPL Publication 02-25.” (14).

Schmidt, Johan A, Matthew S. Johnson, and Reinhard Schinke. 2013. “Carbon Dioxide Photolysis from 150 to 210 Nm: Singlet and Triplet Channel Dynamics, UV-Spectrum, and Isotope Effects.” *Proceedings of the National Academy of Sciences of the United States of America* 110(44):17691–96. doi: 10.1073/pnas.1213083110.

Sedlacek, Arthur J., David R. Harding, Ralph E. Weston, Thomas G. Kreutz, and George W. Flynn. 1989. “Probing the O(1 D)+CO2 Reaction with Second-Derivative Modulated Diode Laser Spectroscopy.” *The Journal of Chemical Physics* 91(12):7550–56. doi: 10.1063/1.457278.

Shcherbanev, S. A., Ch Ding, S. M. Starikovskaia, and N. A. Popov. 2019. “Filamentary Nanosecond Surface Dielectric Barrier Discharge. Plasma Properties in the Filaments.” *Plasma Sources Science and Technology* 28(6). doi: 10.1088/1361-6595/ab2230.

Shcherbanev, Sergey A., Tanguy Krzymuski, Yuan Xiong, and Nicolas Noiray. 2022. “Jetting Axial Flow Induced by Nanosecond Repetitively Pulsed Discharges in Quiescent Ambient Air.” *Journal of Physics D: Applied Physics* 55(38). doi: 10.1088/1361-6463/ac7dcd.

Silva, A. F., A. S. Morillo-Candás, A. Tejero-Del-Caz, L. L. Alves, O. Guaitella, and V. Guerra. 2020. “A Reaction Mechanism for Vibrationally-Cold Low-Pressure CO2 plasmas.” *Plasma Sources Science and Technology* 29(12). doi: 10.1088/1361-6595/abc818.

Silva, T., M. Grofulović, B. L. M. Klarenaar, A. S. Morillo-Candas, O. Guaitella, R. Engeln, C. D. Pintassilgo, and V. Guerra. 2018. “Kinetic Study of Low-Temperature CO2 Plasmas under Non-Equilibrium Conditions. I. Relaxation of Vibrational Energy.” *Plasma Sources Science and*

Technology 27(1). doi: 10.1088/1361-6595/aaa56a.

Silva, T., M. Grofulović, L. Terraz, C. D. Pintassilgo, and V. Guerra. 2020. "Dynamics of Gas Heating in the Afterglow of Pulsed CO2 and CO2–N2 Glow Discharges at Low Pressure." *Plasma Chemistry and Plasma Processing* 40(3):713–25. doi: 10.1007/s11090-020-10061-7.

Silva, Tiago, Nikolay Britun, Thomas Godfroid, and Rony Snyders. 2014a. "Optical Characterization of a Microwave Pulsed Discharge Used for Dissociation of CO2." *Plasma Sources Science and Technology* 23(2):25009. doi: 10.1088/0963-0252/23/2/025009.

Silva, Tiago, Ana Sofia Morillo-Candas, Olivier Guaitella, and Vasco Guerra. 2021. "Modeling the Time Evolution of the Dissociation Fraction in Low-Pressure CO2 Plasmas." *Journal of CO2 Utilization* 53(September):101719. doi: 10.1016/j.jcou.2021.101719.

Slanger, T. G., and G. Black. 1978. " CO 2 Photolysis Revisited ." *The Journal of Chemical Physics* 68(4):1844–49. doi: 10.1063/1.435905.

Slanger, T G, and G. Black. 1978a. "O(1 S) Interactions—the Product Channels." *The Journal of Chemical Physics* 68(3):989–97. doi: 10.1063/1.435838.

Slanger, T G, and G. Black. 1978b. "Products of the O(1S) – O2 Interaction." *The Journal of Chemical Physics* 68(3):998–1000. doi: 10.1063/1.435839.

Slanger, T. G., R. L. Sharpless, and G. Black. 1977. "CO 2 Photodissociation, 1060–1175 Å." *The Journal of Chemical Physics* 67(11):5317–23. doi: 10.1063/1.434710.

Slanger, T. G., Bernard J. Wood, and Graham Black. 1972. "The Temperature Dependence of O(1S) Quenching by O2." *Chemical Physics Letters* 17(3):401–3. doi: 10.1016/0009-2614(72)87106-9.

Slanger, Tom G., and Graham Black. 1976. "O(1S) Quenching by O(3P)." *The Journal of Chemical Physics* 64(9):3763–66. doi: 10.1063/1.432691.

Smith, Gregory P., David M. Golden, Michael Frenklach, Nigel W. Moriarty, Boris Eiteneer, Mikhail Goldenberg, C. Thomas Bowman, Ronald K. Hanson, Soonho Song, William C. Gardiner Jr, and others. 1999. "GRI 3.0 Mechanism." *Gas Research Institute (Http://Www. Me. Berkeley. Edu/Gri_mech).*

Snoeckx, Ramses, and Annemie Bogaerts. 2017. "Plasma Technology – a Novel Solution for CO 2 Conversion?" *Chemical Society Reviews* 46(19):5805–63. doi: 10.1039/C6CS00066E.

Soldatov, S., E. Carbone, A. Kuhn, G. Link, J. Jelonnek, R. Dittmeyer, and A. Navarrete. 2022. "Efficiency of a Compact CO2 Coaxial Plasma Torch Driven by Ultrafast Microwave Power Pulsing: Stability and Plasma Gas Flow Dynamics." *Journal of CO2 Utilization* 58(December 2021):101916. doi: 10.1016/j.jcou.2022.101916.

Soldatov, Sergey, Guido Link, Lucas Silberer, Clara Marie Schmedt, Emile Carbone, Federico D. Isa, John Jelonnek, Roland Dittmeyer, and Alexander Navarrete. 2021. "Time-Resolved Optical Emission Spectroscopy Reveals Nonequilibrium Conditions for CO2 Splitting in Atmospheric Plasma Sustained with Ultrafast Microwave Pulsation." doi: 10.1021/acsenergylett.0c01983.

Song, Yu, Hong Gao, Yih Chung Chang, Zhou Lu, C. Y. Ng, and William M. Jackson. 2014. "Photodissociation of CO2 between 13.540 EV and 13.678 EV." *Physical Chemistry Chemical Physics* 16(2):563–69. doi: 10.1039/c3cp53250j.

Spencer, L. F., and A. D. Gallimore. 2013. “CO2 Dissociation in an Atmospheric Pressure Plasma/Catalyst System: A Study of Efficiency.” *Plasma Sources Science and Technology* 22(1):15019. doi: 10.1088/0963-0252/22/1/015019.

Spesyvtsev, R., T. Horio, Y. I. Suzuki, and T. Suzuki. 2015. “Observation of the Wavepacket Dynamics on the 1B2(1Σu+) State of CS2 by Sub-20 Fs Photoelectron Imaging Using 159 Nm Probe Pulses.” *Journal of Chemical Physics* 142(7):074308. doi: 10.1063/1.4907749.

Spielfiedel, A., N. Feautrier, G. Chabaud, N. Feautrier, and H. J. Werner. 1993. “The First Dipole-Allowed Electronic Transition 11Σ+u-X1Σ+gof CO2.” *Chemical Physics Letters* 216(1–2):162–66. doi: 10.1016/0009-2614(93)E1261-E.

Spielfiedel, A., N. Feautrier, G. Chambaud, P. Rosmus, and H. J. Werner. 1991. “Interactions of Rydberg and Valence States in CO2.” *Chemical Physics Letters* 183(1–2):16–20. doi: 10.1016/0009-2614(91)85091-A.

Spielfiedel, A., N. Feautrier, C. Cossart-Magos, G. Chambaud, P. Rosmus, H. J. H. -J. Werner, P. Botschwina, C. Cossart-Magos, G. Chambaud, P. Rosmus, H. J. H. -J. Werner, and P. Botschwina. 1992. “Bent Valence Excited States of CO2.” *The Journal of Chemical Physics* 97(11):8382. doi: 10.1063/1.463408.

van de Steeg, A. W., T. Butterworth, D. C. M. van den Bekerom, A. F. Silva, M. C. M. van de Sanden, and G. J. van Rooij. 2020. “Plasma Activation of N2, CH4 and CO2: An Assessment of the Vibrational Non-Equilibrium Time Window.” *Plasma Sources Science and Technology* 29(11). doi: 10.1088/1361-6595/abbae4.

Van De Steeg, Alex, Pedro Viegas, Ana Silva, Tom Butterworth, Alexander Van Bavel, Joost Smits, Paola Diomede, Mauritius Van De Sanden, and Gerard Van Rooij. 2021. “Redefining the Microwave Plasma-Mediated CO2reduction Efficiency Limit: The Role of O-CO2association.” *ACS Energy Letters* 6:2876–81. doi: 10.1021/acsenergylett.1c01206.

Stepanyan, Sergey, Jun Hayashi, Arthur Salmon, Gabi D. Stancu, and Christophe O. Laux. 2017. “Large-Volume Excitation of Air, Argon, Nitrogen and Combustible Mixtures by Thermal Jets Produced by Nanosecond Spark Discharges.” *Plasma Sources Science and Technology* 26(4). doi: 10.1088/1361-6595/aa5a2b.

Sun, Hojoong, Jungwun Lee, Hyungrok Do, Seong Kyun Im, and Moon Soo Bak. 2017. “Experimental and Numerical Studies on Carbon Dioxide Decomposition in Atmospheric Electrodeless Microwave Plasmas.” *Journal of Applied Physics* 122(3):1–11. doi: 10.1063/1.4994008.

Tawara, H., and T. Kato. 1987. “Total and Partial Ionization Cross Sections of Atoms and Ions by Elecrton Impact.” *Atomic Data and Nuclear Data Tables* 36(2):167–353.

Tayal, S. S., and Oleg Zatsarinny. 2016. “B -Spline R -Matrix-with-Pseudostates Approach for Excitation and Ionization of Atomic Oxygen by Electron Collisions.” *Physical Review A* 94(4):1–15. doi: 10.1103/PhysRevA.94.042707.

Teulet, P., J. P. Sarrette, and A. M. Gomes. 1999. “Calculation of Electron Impact Inelastic Cross Sections and Rate Coefficients for Diatomic Molecules. Application to Air Molecules.” *Journal of Quantitative Spectroscopy and Radiative Transfer* 62(5):549–69. doi: 10.1016/S0022-4073(98)00129-0.

Tholin, Fabien. 2012. “Numerical Simulation of Nanosecond Repetitively Pulsed Discharges in Air at Atmospheric Pressure: Application to Plasma-Assisted Combustion.”, PhD Thesis, Ecole Centrale Paris.

Torbin, A. P., A. A. Pershin, A. M. Mebel, M. V. Zagidullin, M. C. Heaven, and V. N. Azyazov. 2018. “Collisional Relaxation of O2(A1Δ $\Upsilon = 1, 2, 3$) by CO2.” *Chemical Physics Letters* 691:456–61. doi: 10.1016/j.cplett.2017.11.052.

Trenchev, G., A. Nikiforov, W. Wang, St Kolev, and A. Bogaerts. 2019. “Atmospheric Pressure Glow Discharge for CO2 Conversion: Model-Based Exploration of the Optimum Reactor Configuration.” *Chemical Engineering Journal* 362(December 2018):830–41. doi: 10.1016/j.cej.2019.01.091.

Tsang, W., and R. F. Hampson. 1986. “Chemical Kinetic Data Base for Combustion Chemistry. Part I. Methane and Related Compounds.” *Journal of Physical and Chemical Reference Data* 15(3):1087–1279. doi: 10.1063/1.555759.

Vialetto, L., A. W. Van De Steeg, P. Viegas, S. Longo, G. J. Van Rooij, M. C. M. Van De Sanden, J. Van Dijk, and P. Diomede. 2022. “Charged Particle Kinetics and Gas Heating in CO2microwave Plasma Contraction: Comparisons of Simulations and Experiments.” *Plasma Sources Science and Technology* 31(5). doi: 10.1088/1361-6595/ac56c5.

Viggiano, A. A., A. Ehlerding, F. Hellberg, R. D. Thomas, V. Zhaunerchyk, W. D. Geppert, H. Montaigne, M. Larsson, M. Kaminska, and F. Österdahl. 2005. “Rate Constants and Branching Ratios for the Dissociative Recombination of CO 2+.” *Journal of Chemical Physics* 122(22):13–16. doi: 10.1063/1.1926283.

Vincenti, W. G., and C. H. Kruger. 1965. *Introduction to Physical Gas Dynamics.*

Wang, Weizong, Danhua Mei, Xin Tu, and Annemie Bogaerts. 2017. “Gliding Arc Plasma for CO2 Conversion: Better Insights by a Combined Experimental and Modelling Approach.” *Chemical Engineering Journal* 330(April):11–25. doi: 10.1016/j.cej.2017.07.133.

Wang, Yang, Oleg Zatsarinny, and Klaus Bartschat. 2013. “B-Spline R-Matrix-with-Pseudostates Calculations for Electron-Impact Excitation and Ionization of Carbon.” *Physical Review A* 87(1):012704. doi: 10.1103/PhysRevA.87.012704.

Warnatz, Jürgen. 1984. “Rate Coefficients in the C/H/O System.” *Combustion Chemistry* 197–360. doi: 10.1007/978-1-4684-0186-8_5.

Watanabe, Noboru, Tsukasa Hirayama, Daisuke Suzuki, and Masahiko Takahashi. 2013. “Vibronic Effects on the Low-Lying Electronic Excitations in CO2 Induced by Electron Impact.” *Journal of Chemical Physics* 138(18). doi: 10.1063/1.4804190.

Weekes, David M., Danielle A. Salvatore, Angelica Reyes, Aoxue Huang, and Curtis P. Berlinguette. 2018. “Electrolytic CO2 Reduction in a Flow Cell.” *Accounts of Chemical Research* 51(4):910–18. doi: 10.1021/acs.accounts.8b00010.

Whitham, GB. 1976. *Linear and Nonlinear Waves.* John Wiley & Sons.

Wolf, A. J., F. J. J. Peeters, P. W. C. Groen, W. A. Bongers, and M. C. M. van de Sanden. 2020. “CO 2 Conversion in Nonuniform Discharges: Disentangling Dissociation and Recombination Mechanisms.” *The Journal of Physical Chemistry C* 124(31):16806–19. doi: 10.1021/acs.jpcc.0c03637.

Wolf, A. J., T. W. H. Righart, F. J. J. Peeters, W. A. Bongers, and M. C. M. Van De Sanden. 2020. "Implications of Thermo-Chemical Instability on the Contracted Modes in CO2 Microwave Plasmas." *Plasma Sources Science and Technology* 29(2). doi: 10.1088/1361-6595/ab5eca.

Wright, Travis W., Elio G. Champenois, James P. Cryan, Niranjan Shivaram, Chan Shan Yang, and Ali Belkacem. 2017. "Ultrafast Dynamics of the Lowest-Lying Neutral States in Carbon Dioxide." *Physical Review A* 95(2). doi: 10.1103/PhysRevA.95.023412.

Wyndorps, Jan, Hesam Ostovari, and Niklas von der Assen. 2021. "Is Electrochemical CO2reduction the Future Technology for Power-to-Chemicals? An Environmental Comparison with H2-Based Pathways." *Sustainable Energy and Fuels* 5(22):5748–61. doi: 10.1039/d1se00975c.

Xu, D. a, M. N. Shneider, D. a Lacoste, and C. O. Laux. 2014. "Thermal and Hydrodynamic Effects of Nanosecond Discharges in Atmospheric Pressure Air." *Journal of Physics D: Applied Physics* 47(23):235202. doi: 10.1088/0022-3727/47/23/235202.

Yong, Taemin, Hongtao Zhong, Erwan Pannier, Christophe Laux, and Mark A. Cappelli. 2023. "High-Pressure CO 2 Dissociation with Nanosecond Pulsed Discharges." *Plasma Sources Science and Technology* 32(11):115012. doi: 10.1088/1361-6595/ad066e.

Zhang, Hao, Li Li, Ruiyang Xu, Jingying Huang, Ni Wang, Xiaodong Li, and Xin Tu. 2020. "Plasma-Enhanced Catalytic Activation of CO2 in a Modified Gliding Arc Reactor." *Waste Disposal and Sustainable Energy* 2(2):139–50. doi: 10.1007/s42768-020-00034-z.

Zhu, Fengsen, Hao Zhang, Xin Yan, Jianhua Yan, Mingjiang Ni, Xiaodong Li, and Xin Tu. 2017. "Plasma-Catalytic Reforming of CO2-Rich Biogas over Ni/Γ-Al2O3 Catalysts in a Rotating Gliding Arc Reactor." *Fuel* 199:430–37. doi: 10.1016/j.fuel.2017.02.082.